NTNU

Norwegian University of
Science and Technology

Cryptic Variations of Olivene and Clinopyroxene in the RF-4 Drill-Core:

A geochemical study of the Reinfjord
Ultramafic Complex, Norway.

Kim Rune Bragstad
Grannes

Geology
Submission date: August 2016
Supervisor: Rune Berg-Edland Larsen, IGB
Co-supervisor: Thomas Grant, IGB
Bjørn Eske Sørensen, IGB

Norwegian University of Science and Technology
Department of Geology and Mineral Resources Engineering

Abstract

The Reinfjord Ultramafic Complex (15 km^2) is part of the 5500 km^2 Seiland Igneous Province (SIP), in northern Norway. It is one of four major ultramafic complexes in SIP. The Reinfjord magmas intruded between 560-570 Ma into gabbro-norite and metasediment gneisses (Roberts 2006). The complex most likely represents a deep crustal conduit system for mantle derived melts en route to the surface, within a large igneous province (Larsen et al. 2012).The Reinfjord ultramafic complex consists of three pulses of melt generation that formed Websterite, Lherzolite-Wehrlite and dunite cumulates that are either modally or cryptically layered. Central parts of the intrusion are composed of cryptically layered dunite (Fo_{82-85}). Drilling found that the dunite hosts two Cu reefs with 800 to 900 ppm of Cu and a PGE reef containing 0,3 ppm of total Pt+Pd+Au. The lower Cu reef almost all Cu is found as native copper. A contact deposit is found in the lower contact of the CS towards a newly discovered pyroxenite containing 900 ppm Cu and traces of PGE.

The aim with this study is to present the evolution of the dunite and how the cryptic variations leading to formation of Cu and PGE reefs. We also investigate how much the magma fractionated and the magma chamber processes leading to the formation of the cumulate sequence through compositional variations in olivine. The Reinfjord area is excellent for this type of study as surfaces are extremely fresh and primary features are well preserved.

To improve our understanding of the evolution of intrusion, the entire area was re-mapped. Major revisions from previous work include a reinterpretation of a large part of the intrusion and fault zones. Fieldwork also unravelled what may be the roof zone of the intrusion in north east at 900 meters above sea level (m.a.s.l.) and a possible roof zone in SW at 800 m.a.s.l.

Sammendrag (Norwegian summary)

Reinfjord Ultramafiske Kompleks (15 km^2) er en del av det 5500 km^2 store Seiland Magmatiske Provins (SIP), Nord-Norge. Det er et av fire store ultramafiske komplekser i SIP. Reinfjord magmaen intruderte i tidsperioden 560-570 Ma inn i gabbro-noritt og metasedimentær gneis (Roberts 2006). Komplekset representerer sannsynligvis magma dypt nede i jordskorpen som stiger opp mot overflaten gjennom ett rørsystem for smelten på vei til en magmatisk provins (Larsen et al. 2012). Reinfjord ultramafiske kompleks består av tre pulser av smelte som danner kryptisk eller modal lagdelte websteritt, Lherzolitt-Wehrlitt og dunitt kumulater. De sentrale områdene av intrusjonen består av kryptisk lagdelt dunitt (Fo_{82-85}). Drilling av kjerneprøver har funnet 2 kopper årer med henholdsvis 800 og 900 ppm kopper og en PGE anrikning med totalt 0,3 ppm Pt+Pd+Au i dunitten. I det nederste kopper åren finnes nesten alt kopper som gedigent kopper. Et kontakt forekomst er funnet i den nedre dunitt kontakten mot en nylig oppdaget pyroksenitt, denne forekomsten inneholder 900 ppm Cu med spor av PGE.

Målet med denne studien er å presentere utviklingen til dunitten og hvordan de kryptiske variasjonene bidrar til dannelsen av kopper og PGE forekomstene. Oppgaven undersøker også hvor mye magmaen fraksjonerer and prosessene som leder til dannelsen av kumulatbergartene gjennom kjemiske variasjoner i olivin. Reinfjord intrusjonen er utmerket til denne typen studier da bergartene er udeformerte og originale kjennetegn er bevart.

For å øke forståelsen av intrusjonen og utviklingen til bergartene er hele området kartlagt på nytt. Store revideringer er gjort fra tidligere arbeider, dette inkluderer nytolkning av store deler av intrusjonen og forkastningssoner. Feltarbeid oppdaget det som kan vise seg å være taket til intrusjonen i nord øst 900 meter over havet (moh) og et annet mulig tak i sørvest 800 moh.

Acknowledgements

This thesis master thesis has been carried out at the Department of Geology and Mineral Resources Engineering (IGB) at the Norwegian University of Science and Technology (NTNU), Trondheim. My supervisors have been Professor Rune Berg-Edland Larsen , Postdoc. Thomas B. Grant and Associate professor Bjørn Eske Sørensen. I would like to express my gratitude to my supervisors for their advice, feedback and time throughout my master period.

I would like to thank all my classmates for the friendship and good times we have had during the last five years. A special thanks to Even Nikolaisen for all the great discussions and teamwork we have had the last two years.

Kim Rune Bragstad Grannes

03.08.2015, Trondheim

Note to reader: digital appendix with geochemical data is available for download at http://daim.id.ntnu.no. It contains 1) whole-rock and trace element data for the RF-4 drill core and all surface samples used in this thesis. 2) EPMA results of olivine, pyroxene and plagioclase from both the CS and the gabbro-CS contact zone. 3) Calculation of the fractionation in the CS.

Table of content

ABSTRACT **1**

SAMMENDRAG (NORWEGIAN SUMMARY) ..... **III**

ACKNOWLEDGEMENTS ..... **V**

TABLE OF CONTENT ..... **VII**

LIST OF FIGURES ..... **XI**

LIST OF TABLES ..... **XVII**

ABBREVIATIONS ..... **XIX**

1 INTRODUCTION **1**

1.1 BACKGROUND 1

1.2 GEOLOGICAL SETTING 1

1.2.1 Local Setting *2*

1.2.2 Garnet gneiss *3*

1.2.3 Langstrand Gabbro *3*

1.2.4 Lower Layered Series (LLS) *4*

1.2.5 Upper Layered Series (ULS) *5*

1.2.6 Central Series (CS) *6*

1.2.7 Marginal Zones (MZ) *7*

1.3 EARLIER WORK 7

2 THEORY **9**

2.1 CLASSIFICATION OF ULTRAMAFIC ROCKS 9

2.2 MAGMATIC PROCESSES 9

2.2.1 Partition coefficient and generation of magma *9*

2.2.2 Magma density and replenishment *10*

2.2.3 Immiscibility and sulphur solubility *13*

2.3 LAYERING 14

2.4 OTHER MAFIC INTRUSIONS 17

2.4.1 Skaergaard, Greenland *18*

2.4.2 Bushveld, South Africa *18*

3 METHODS 21

3.1 FIELDWORK 21

3.2 MAPPING 21

3.3 SAMPLING 22

3.4 SAMPLE PREPARATION 23

Crushing 23

3.5 PETROGRAPHY 23

3.6 GEOCHEMICAL ANALYSIS 24

3.6.1 Whole-rock geochemistry 24

3.6.2 X-ray Diffraction (XRD) 25

3.6.3 SEM 26

3.6.4 EPMA 26

3.7 SOURCE OF ERROR 28

3.7.1 Map 28

3.7.2 Sample preparation 28

3.7.3 Geochemical analysis 29

4 RESULT 31

4.1 FIELD OBSERVATIONS 31

4.1.1 Garnet Gneiss 31

4.1.2 Langstrand Gabbronorite 32

4.1.3 Lower Layered Series (LLS) 32

4.1.4 Upper Layered Series (ULS) 34

4.1.5 Central Series (CS) 39

4.1.6 Marginal Zones (MZ) 43

4.1.7 A local zone in north eastern part of the intrusion 45

4.2 A NEW MAP 49

4.2.1 Western area 49

4.2.2 Central parts of the intrusion and the lake district 53

4.2.3 The northern area 54

4.2.4 Southern parts of the intrusion 56

4.3 PROFILES 62
4.4 CHEMICAL VARIATION THROUGHOUT THE CENTRAL SERIES 70
4.4.1 Whole-rock analysis 70
4.4.2 EPMA 80
4.4.3 Native copper 85
4.4.4 XRD 92
4.5 CONTACT ZONE BETWEEN CENTRAL SERIES AND THE LANGSTRAND GABBRONORITE 94
4.5.1 Field observations 94
4.5.2 Whole-rock and trace element analysis 98
4.5.3 EPMA 101
4.5.4 Normative mineralogy 103
4.5.5 Finger 105
5 DISCUSSION 107
5.1 REINFJORD ULTRAMAFIC INTRUSION 107
5.2 EVOLUTION OF CENTRAL SERIES 114
5.3 RELATIONSHIP OF CENTRAL SERIES AND LANGSTRANDGABBRO 122
5.4 ORIGIN OF THE NATIVE COPPER 124
6 CONCLUSIONS 129
7 REFERENCES 133
APPENDIX 137

List of figures

Figure 1.1: Regional geological map over SIP. Four ultramafic intrusions (1) Melkevann intrusion, (2) Nordre Bumannsfjord, (3) Kvalfjord and (4) Reinfjord. 2

Figure 1.2: Gabbro found 200 meter from the ultramafic (UM) complex. 4

Figure 1.3: The intrusion seen from the village of Reinfjord (seen from SW), garnet gneiss in the lowest areas with the LLS above. The MZ covered by the scree, a thin line of gabbro separating the LLS and the ULS on the mountain top. 5

Figure 1.4: South west facing cliff showing the spatial relationship of the Gneiss, LLS, gabbro and ULS in the western part of the intrusion. Seen towards west. 6

Figure 1.5:Southern part of plateau (Seen towards east) 7

Figure 2.1: Classification of ultramafic rocks (Source: Mindat.org) 9

Figure 2.2:a) Batch melting where melt and residual solid are in equilibrium b) Fractional melting considering no reaction between melt and solid residue, melt are instantly removed from the system. 10

Figure 2.3:a) Dense magma injection. b) Lighter magma injection (Robb, 2009) 11

Figure 2.4:“R” factor 13

Figure 2.5: a) Magma injection (contamination) b) Magma recharge 16

Figure 2.6 Oscillatory nucleation and crystal growth forming layering 17

Figure 2.7: Cross section of Skaergaard 18

Figure 3.1: Mosaic visualisation of the digitalized and geo-referenced map by Emblin 1985, with water and river data lying on top for better visualisation. Marked on the map are also some place names and two locations as reference. 22

Figure 3.2: Revised Michel-Lèvy interference colour chart by Sørensen (2013). 24

Figure 4.1: a) Foliated gneiss with bands of plagioclase, biotite and garnet-rich plagioclase. b) Clear red to pink almandine garnet. 31

Figure 4.2: a) Gabbro intruded by CS melt in the NE part of the intrusion under the formation of a Marginal Zone (MZ). b) Gabbro with barren contact deposit east of the plateau. Seen towards NE. 32

Figure 4.3: a) The north facing contact of the LLS in the northen part of the outcro, a fracture zone seen at the contact. b) Pyroxene oikocryst with poikilitic wherlite c) The west facing cliff of the LLS with the MZ covered by scree. With gabbro separating the LLS and the ULS high up. 33

Figure 4.4: top) photo show the UM series on plateau from the ridge N of the fault valley, seen towards south. Bottom) Photo taken from the mountain top seen on the right side of figure a, showing the plateau seen towards ENE. 35

Figure 4.5: a) Distorted layering. b) Rhythmic repeated layering of olivine with gradually increasing amount of poikilitic pyroxene and pyroxene rich wehrlite, above a larger zone of pyroxene rich wehrlite c) Sub-horizontal layering marked by diopside rich pyroxene layers in dunitic cumulates, cut by sub vertical UM veins. d) Load structure with wehrlite sinking into dunite with coarse-grained pyroxene in the contact. 36

Figure 4.6: a) Slumping structure in 3D dipping towards NE. b) Slumping in 2D, pyroxene rich wehrlite slumping over less dense pyroxene poor wehrlite. c) Load structure with pyroxene rich wehrlite into dunite. d) Irregular dunite replacing wehrlite. 37

Figure 4.7: a) Ductile foliated layering marked by pyroxene and olivine rich layers (Photo by Lars Anker-Rasch) b) Two sheetlike gabbro xenoliths in the western part of ULS, rims of pyroxene surrounds the xenoliths with plagioclase appearing in the wehrlite close to the contact. c) Recharge and formation of pyroxene pegmatite within the wehrlite. 38

Figure 4.8:a) Dykes of dunite (5-10 m) intruding and replacing the ULS in west, crosscutting the ULS layering. b) Dyke complex on the ridge north of lake district. c) Poikilitic pyroxene in the CS dunite. d) Poikilitic plagioclase in the CS dunite 50m from the gabbro contact close to the ULS rafts and the finger. 40

Figure 4.9: Scanned thin section in plane and cross polarized light (Xpl). 41

Figure 4.10: a) CS dunites show two types of olivine. b) Less deformed subhedral to euhedral olivine type 2. c) Show the poikilitic clinopyroxene with reaction rim between the Ol and the Cpx. together with the Cpx, Ol_2 and Ilm exist interstitially between the larger Ol1 grains.. d) show poikilitic Cpx and Chromium spinel interstitial between the Ol_1 crystals. 42

Figure 4.11: a) MZ found in Isdalen in the contact between the gneiss and the ULS. b) patch of plagioclase and poikilitic plagioclase in the ULS on the east side of the plateau. c) irregular contact between the MZ (dark) and the gabbro (white). Note the large pyroxene porphyries in the gabbro. d) 2-3 cm large pyroxene porphyry with pyroxene rim in the gabbro. 44

Figure 4.12: Pegmatitic granite stoping gneiss south of Storvatnet. The pegmatite arguably formed from partial melting of the gneiss. 45

Figure 4.13: a) In the top left corner of the photo gabbro is seen. b) Ultramafic series with gabbro laying on top in the top of the picture, seen towards southeast c) Contact seen towards east, where a cover of gabbro is lying on top of the UM series. Note the gabbro in the distance to the right of this photo. 46

Figure 4.14: Gabbro xenoliths bellow the roof zone, photo taken by the lake south of the cliff phase. It is the same area seen on the next two figures at greater distances. 47

Figure 4.15:a) Xenoliths beneath the roof zone follow the layering of the CS. Seen towards E. b) Roof, xenoliths and intruding CS into the gabbro is seen on this photo. Seen towards NE. Arrow mark a long gabbro slab. 48

Figure 4.16: The western part of the intrusion above Storvatnet and the Northern cliff phase in Isdalen. 50

Figure 4.17: The new map. 51

Figure 4.18: The map by Emblin (1985). 52

Figure 4.19: The separate ULS rafts cut by the later intruding CS. The CS seems to cut the ULS almost horizontal, and at the same elevation for the two rafts. Photo taken from the finger toward west. 53

Figure 4.20: Finger seen in the West-face of Langfjellet. 54

Figure 4.21:The NE CS-Gabbro contact. Two gabbro xenoliths located in the CS cliff left of the shadow, the largest of these is the same one as in figure 4.14.. 55

Figure 4.22: A zoomed in figure of the remapped NE part of the intrusion. 56

Figure 4.23: a) Photo is taken from fault showing the west facing mountain side where the MZ perforate into the gabbro with a thickness of 20+meters. b) Sketch of the photo, the major fault dips toward north while two minor fault dips south. 57

Figure 4.24: The south eastern part of the intrusion with the fault. The gabbro layering is marked to demonstrate the difference on each side of the fault, and the difference in the east compared to the western part. Down to the right the layering is dragged down into a curve indicating a normal fault. 58

Figure 4.25: The southern part of the map. As mentioned previous, the south eastern fault is shifted into the gabbro to be visual, it is following the contact as seen on previous figures. .. 59

Figure 4.26: Figure from Øen (2013), that show the fault cutting the two small outcrops of MZ and CS, west fault presented. And that this fault continuous NW. 60

Figure 4.27: This map show the author of the boundaries in the intrusion. It give an indication of the area of the area that have been revised and remapped in this thesis. 61

Figure 4.28: The location of the different profiles and the location of surface samples used to describe the CS and samples used in chapter 0 to describe the CS-Gabbro contact. 63

Figure 4.29: The southernmost profile showing the relationship between the UM and the host rock. 64

Figure 4.30: Profile intersecting with the RF-3 and RF-4 drill cores. 65

Figure 4.31: Profile over the dyke complex and what is believed to be conduit feeder for the parental melts. 66

Figure 4.32: Profile over the northern part of the intrusion. For legend see figure 4.28. 68

Figure 4.33: The N-S profile. Profile 1 to 4 is marked together with the RF-2 and RF-4 drill cores.. 69

Figure 4.34: Bulk rock chemistry of Mg# and Co/Cr 71

Figure 4.35: Loss on ignition (LOI) and Nd. 72

Figure 4.36: Bulk rock major element analysis of S (Wt%) and Ni (ppm). 74

Figure 4.37: Bulk rock major element analysis of Cu (ppm) and PGE (ppm). 75

Figure 4.38: Bulk rock major elements, showing Mg# and Co/Cr evolution in the CS above RF-4. 79

Figure 4.39: Volatiles shown in loss on ignition and base metal copper and nickel. 80

Figure 4.40: EPMA analysis showing the Fo content and NiO content in olivine 82

Figure 4.41: EPMA analysis showing the CaO content and NiO/MnO content in olivine 83

Figure 4.42: EPMA analysis showing the Mg# and CaO content in clinopyroxene. Points marked by yellow colour is analysed by one grain, therefore have low statistical significance 84

Figure 4.43 EPMA analysis showing the Cr_2O_3 content and SiO_2 content in clinopyroxene. Points marked by yellow colour is analysed by one grain, therefore have low statistical significance..... 85

Figure 4.44: a) Overview of the riches part of the 4-7550 sample. b) Native copper hosted in fractured and altered pyrrhotite. c) Native copper hosted in a pyrrhotite and chalcopyrite grain surrounded by iron oxide. d) Pyrrhotite hosts the native copper and an altered copper-iron phase. It is part of a larger sulphide grain consisting of pyrrhotite with pentlandite exsolutions. 87

Figure 4.45: SEM-EDS element map showing how the blue native copper is situated within a pyrrhotite grain. The yellow-red mix is dolomite, partially decomposing to brucite (red) and calcite (yellow). 88

Figure 4.46: SEM-EDS element map showing sulphur, nickle, copper and iron. Showing how the Native copper and other sulphide minerals coexisit Pure red colours is native copper, red spots mixed with pale orange and green is chalcopyrite, blue is pentlandite and bright green is pyrrhotite. 89

Figure 4.47: a-b) 2 cm pocket containing a wide range of copper minerals (Native copper, chalcopyrite, cubanite and covellite) and pyrrhotite in a matrix of serpentine, calcite and brucite. Red rectangle in a show the location of b. c-d)Large grain of native copper with a rim of iron oxide hosted in a fractured chalcopyrite. The chalcopyrite lies close to or is part of a larger grain of pyrrhotite with pentlandite exsolutions. 90

Figure 4.48: SEM-EDS maps. a) Shows the pocket of copper minerals pictured above. b) The same pocket showing how the copper is situated all over the pocket, green and blue colours show the total breakdown of dolomite to brucite (green) and calcite (blue) c) Breakdown of interstitial dolomite (mix of yellow and red) to brucite (red) and calcite (yellow) in olivine (pink) and clinopyroxene (purple)..... 91

Figure 4.49:The irregular gabbro-CS contact seen towards NE. 95

Figure 4.50: a) Cpx with a rim of Opx towards the Ol grains, seen in plane polarized light (ppl) in the MZ, 15 meters from the gabbro contact. b) Plagioclase with a rim of pyroxene in the MZ sample closest to the gabbro contact (KG14012). c) Ol inclusions at Cpx grain contact, in the centre of the M. d) Irregular grain contact between Cpx and Pl is observed in gabbro 15 meters from the contact. 97

Figure 4.51: Bulk rock chemistry of Mg#. Blue points is gabbro, yellow points is MZ and red points is CS samples..... 98

Figure 4.52: Trace elements over the CS-gabbro contact. 99

Figure 4.53: The samples are normalized to C1 chondrite and primitive mantle after Sun and McDonough (1989). Green, blue and pink samples are surface samples from the contact. The red samples are CS is from RF-4 (4-3950 and 4-24560), black is the pyroxenite in RF-4 (4-35970 and 4-36900). 100

Figure 4.54: The “Finger” marked with sample locations. 105

Figure 5.1:Possible faulting separating the ULS and gabbro in south-west. 108

Figure 5.2: Possible NE-SW striking fault north of Storvatnet in the Langstrandgabbro. Gabbro is rusted east of the possible fault..... 109

Figure 5.3: Major faults and possible major fault in the Reinfjord intrusion..... 110

Figure 5.4: Xenoliths hosted within the layering of the ULS, located in SW..... 111

Figure 5.5: Part of the map by Emblin (1985). Where he observed plagioclase left of the thin line marked by arrows, in the plagioclase free ULS 113

Figure 5.6: Fractionation of the CS from 440 to 590 m.a.s.l.. Numbered after depth from top down. 116

Figure 5.7: a) Large grained Cpx with twinning, and recrystallized Ol_2. b) 3-4 cm large Cpx twinned grain. c) Band of recrystallized olivine in the pyroxenite d) Interstitial ol_2 with Cpx and Ol cumulates..... 118

Figure 5.8: 3D model of the conductive field under the lake district..... 119

Figure 5.9: Native copper formation along cleavage or fracture planes in Chalcopyrite 125

List of Tables

Table 3.1: Overview over elements in the mineral programs used for EPMA. Note difference in detection limit, count time and Astimex standards on the same elements on different programs. 27

Table 3.2: Shows what minerals or compounds the Astimex standard is based on. 27

Table 4.1: Estimates on the stratigraphic elevation for the surface samples. 78

Table 4.2: XRD results of the four shallowest thin sections from the RF-4 drill core, showing the modal mineralogy. 93

Table 4.3: EPMA results showing the change in Mg# in Cpx, plagioclase and olivine composition throughout the gabbro-CS contact. 103

Table 4.4: CIPW normalized calculation after Hollocher, presented in percent. Meters from centre of MZ in brackets. 104

Table 4.5: EPMA results showing the change in Mg# in Cpx, plagioclase and forsterite content in olivine. Average data with number of analysis is brackets. 106

Abbreviations

The paper by Whitney and Evans (2010) have been used for mineral abbreviations in this thesis. Abbreviations used in this thesis are amphibole (Amp), brucite (Brc), calcite (Cal), chalcocite (Cct), chalcopyrite (Ccp), chromite (Chr) clinopyroxene (Cpx), covellite (Cv), cubanite (Cbn), digenite (Dg), dolomite (Dol), Enstatite (En), forsterite (Fo), , hematite (Hem), ilmenite (Ilm), magnesite (Mgs), magnetite (Mag), olivine (Ol), orthopyroxene (Opx), pentlandite (Pn), plagioclase (Pl), pyrite (Py), pyrrhotite (Po), serpentine (Srp) and spinel (Spl).

EBSD	Electron Back Scatter Diffraction
EPMA	Electron probe micro-analysis
LIP	Large igneous province
m.a.s.l.	Meters above sea level
SEM	Scanning electron microscope
SIP	Seiland Igneous Province
PPL	Plane polarized light
PPM	Parts per million
PPB	Parts per billion
UM	Ultramafic
XPL	Cross polarized light
XRD	X-Ray Diffraction

1 Introduction

1.1 Background

The Reinfjord ultramafic complex is one of four ultramafic intrusions in the 5500 km^2 Seiland Igneous Province (SIP). SIP is located in Northern Norway (Troms and Finnmark), was dated by Roberts et al. (2006) to 560-570 Ma and emplaced during only 10 Ma. The Reinfjord ultramafic complex represents a lower crustal magma chamber emplaced at a depth of 25-35 km, and is thought to represent a deep conduit system for mantle derived melts en route to shallower levels of a large igneous province (Grant et al., 2016). The entire SIP consists of 55% layered gabbro's, 30% ultramafic (UM) complexes, 10% diorites, granodiorites and granites and 5% alkalic rocks.

Reinfjord ultramafic complex is located in the southern part of the Seiland province in an alpine landscape. It is mainly exposed over a plateau region at 650-750 m.a.s.l.. The Reinfjord ultramafic complex covers an area of 15 km^2, and consists of fresh ultramafic rocks with a minimal of weathering and deformation. The ultramafic rocks are websterites, lherzolites, wehrlites and dunites.

The aim of this thesis is to understand the evolution of the Central Series dunitic cumulates that comprises recently found Ni-Cu-PGE deposit, and to study features of the cumulate chemistry and texture that may be associated with the ore-forming event. Detailed geological mapping of the Reinfjord ultramafic complex is combined with petrographic and geochemical studies throughout a drill core (RF-4) and is supplemented by surface samples. The deposits are formed by mantle derived magma, and may be linked to mantle plume activity. This is an unusual ore deposit, probably emplaced in a magma chamber located in the lower crust, that is connected the conduit system for an Large Igneous Province (LIP).

1.2 Geological setting

The 5500 km^2 Seiland Igneous Province covers the islands of Sørøya, Seiland and Stjernøya as well as the Øksfjord peninsula. SIP probably constitutes the roots of a deep-seated magmatic conduit system forming at depths of 25-35 km (Grant et al., 2016). Roberts et al. (2006) showed that SIP was emplaced at 570 - 560 Ma, with the majority of the magmatic activity occurring

within 4 Ma. They also argue, that the relatively short timeframe between emplacement of the main plutons indicated a single emplacement mechanism. That this correlated with an extensional tectonic event at the margins of the Rodinia supercontinent.

The Caledonian orogeny strongly affected the pre-Silurian Norwegian geology, from Rogaland in the south to Finnmark in the north. The Caledonian orogeny is dived into four allochthons: Lower-, Middle-, Upper- and Uppermost allochthons. All except the Uppermost Allochthon are present in Troms and Finnmark municipalities. The Seiland Igneous Province is emplaced into the Sørøy metasedimentary sequence which is the lowest sequence of the Kalak Nappe complex in the Middle Allochthon. All ultramafic complexes in SIP are situated in a "Right way up" position (figure 1.1). (Bennett et al., 1986, Griffin et al., 2013, Roberts, 2008).

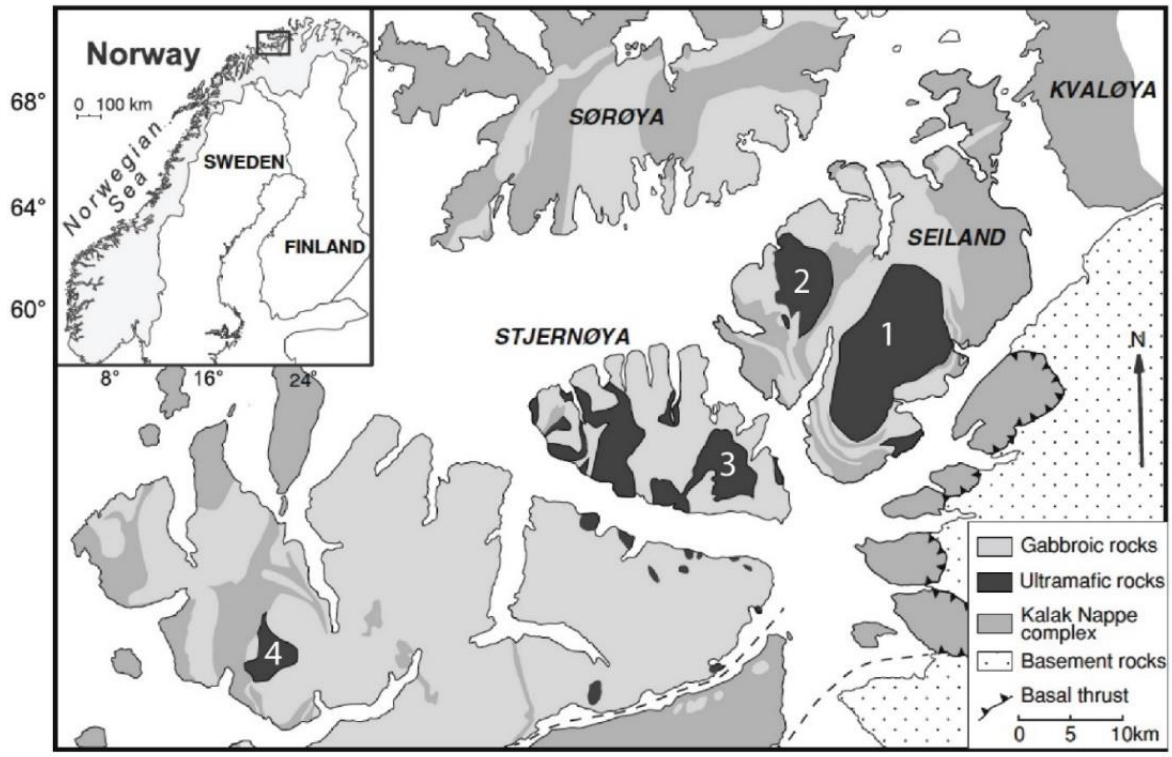

Figure 1.1: Regional geological map over SIP. Four ultramafic intrusions (1) Melkevann intrusion, (2) Nordre Bumannsfjord, (3) Kvalfjord and (4) Reinfjord. (Griffin et al., 2013)

1.2.1 Local Setting

Reinfjord ultramafic complex consists of three ultramafic series, the Lower Layered Series (LLS), the Upper Layered Series (ULS) and the Central Series (CS). These are separate phases with multiple magma recharges entering the magma chamber. The series show an increasing

olivine content from the LLS, ULS to CS, forming from progressively more primitive melt composition with time (Grant et al., 2016). Composition range from Websterite (LLS), Lherzolite-wehrlite (ULS) to dunite (CS). The ultramafic series has cumulate layering, showing a sub-horizontal cryptic or modal layering.

The country rocks consists of garnet gneiss and gabbronorite (Langstrandgabbro). Contact zones (MZ) between the ultramafic series and the country rocks, is a hybrid rock including contaminated ultramafic rock and partial melted host rock. The MZ have previously been divided into three and four separate zones (Bennett, 1974, Emblin, 1985). In this thesis all marginal zones are combined into one Marginal Zone (MZ). As stated in the introduction the focus of this thesis will be the Central Series dunite, and the north eastern contact between the CS and the gabbro. Names of the ultramafic series used in this thesis are based on the work by Emblin (1985), which revised the nomenclature after Bennett (1974).

1.2.2 Garnet gneiss

The emplacement of the Langstrand gabbronorite and the Reinfjord ultramafic complex in the Sørøy metasediments lead to a 2 km, high temperature metamorphic aureole belonging to the upper amphibolite facies (Emblin, 1985). This thermal aureole locally reached the granulite facies, resulting in partial melting of the gneisses forming a two-pyroxene granulites (Emblin, 1985). The metasedimentary rocks in Kalak nappe complex are from Neoproterozoic age. The deformation lead to formation of the garnet gneiss characterised by sillimanite, kyanite and K-feldspar (Bennett, 1974). Where the ultramafic complex is in direct contact with the gneiss a zone of intensive partial melting and mixing is produced. This is a 20-50 meter wide zone where the rocks gradually become less and less ultramafic with distance from the contact.

1.2.3 Langstrand Gabbro

The Langstrand gabbro cover an area of 100km^2. It is believed to be slightly older than the Reinfjord ultramafic complex, although it was still hot when the ultramafic melts were emplaced, seen by the lack of chilled margin (Emblin, 1985). The Reinfjord ultramafic complex intruded into the western part of the Langstrand gabbro. The Langstrand gabbronorite contains a mineral assemblage of plagioclase, pyroxenes and olivine, with biotite, amphibole, pyrrhotite, chrome spinel, zircon and apatite as accessory phases (figure 1.2). (Bennett et al., 1986, Grant

et al., 2016). In this thesis the Langstrand gabbronorite is addressed as the Langstrand gabbro, Langstrand gabbronorite, gabbro and gabbro-norite.

Figure 1.2: Gabbro found 200 meter from the ultramafic (UM) complex.

1.2.4 Lower Layered Series (LLS)

The Lower layered series seen in Figure 1.3 is located only in the cliff above the village of Reinfjord. The near vertical cliff-face limit the accessibility of the LLS and the lower contact to the gneiss is covered by scree. It is separated from the rest of the intrusion by only 50-100m, of gabbro. The LLS represent the earliest of the three ultramafic pulses, and consists of four modally layered cyclic units. These units consists of olive cumulates ($Fo_{79,9-83}$) at the base of each unit followed by olivine-clinopyroxene cumulates (Bennett et al., 1986, Emblin, 1985).

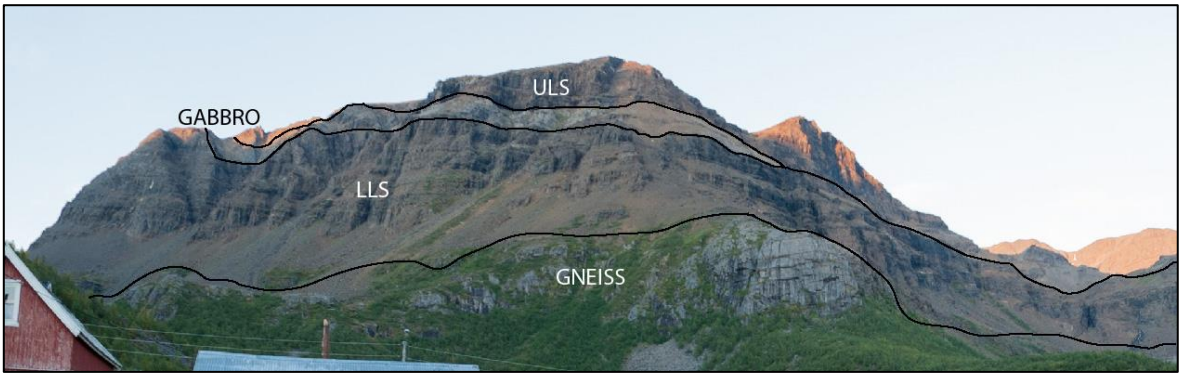

Figure 1.3: The intrusion seen from the village of Reinfjord (seen from SW), garnet gneiss in the lowest areas with the LLS above. The MZ covered by the scree, a thin line of gabbro separating the LLS and the ULS on the mountain top. (Photo by Lars Anker-Rasch)

1.2.5 Upper Layered Series (ULS)

The Upper Layered Series consists of several separate bodies throughout the Reinfjord complex (Figure 4.17). In the west 50-100 meters of gabbro separates ULS from the LLS (figure 1.4). On the plateau, the ULS is found on the western and eastern side of CS. The CS intrudes into the ULS and by melt-rock reactions replaces it forming a dunite. On the eastern side the ULS occur as “rafts”, lying as a thin layer (50cm to 2m thick) enclosed by CS.

The ULS consists of olivine cumulates of poikilitic wehrlite and olivine-clinopyroxenite, with an olivine composition of $Fo_{81\text{-}83,5}$ (Emblin, 1985). The modal layering varies in thickness from cm to meters (Figure 4.5c). The well preserved ULS shows magma chamber processes, such as load structures, replenishment events, bedding structures, etc (Figure 4.5 and figure 4.6).

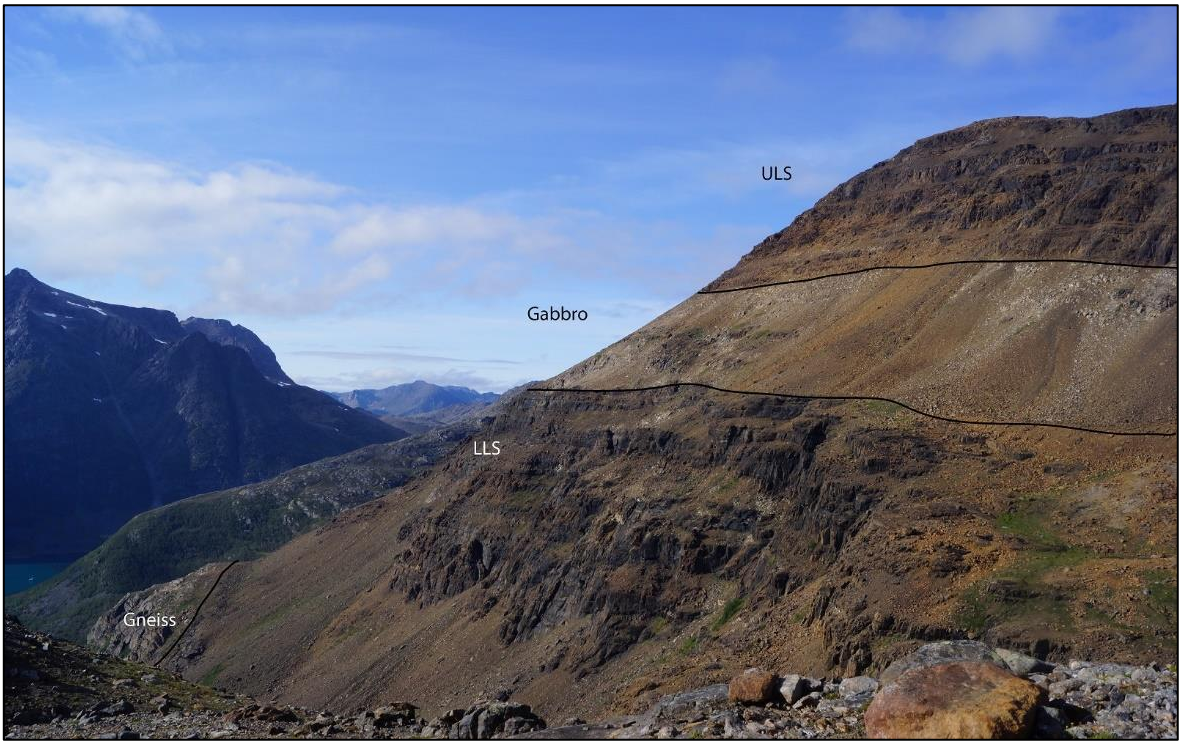

Figure 1.4: South west facing cliff showing the spatial relationship of the Gneiss, LLS, gabbro and ULS in the western part of the intrusion. Seen towards west.

1.2.6 Central Series (CS)

The central series is the youngest of the major magmatic events in the Reinfjord complex and consist of olivine cumulates ($Fo_{83-85,9}$), with varying amount of poikilitic clinopyroxene (often less than 10 percent, rare samples up to 30-40 percent). Compared to the LLS and the ULS the Central Series is only cryptically layered due to the high olivine content. (Emblin, 1985, Grant et al., 2016). The Central Series is found only on the plateau (Figure 1.5 and Figure 4.17). In the south of the intrusion it is cut by a fault at 500 m.a.s.l.. The northern part of the intrusion is covered by a glacier. In chapter 4.1.7 a possible exposure of a local roof zone of the CS will be discussed. Iljina (2013) and Nordic Mining ASA found two possible reefs in a drill core (RF-1), a Ni-Cu and a Ni-Cu-PGE reef. Field observations show that the CS is younger than the ULS (Figure 4.8a) and that it intruded into the ULS while it was still unconsolidated, crystal-melt mush. This can be seen in several parts of the contact zones where the CS melts assimilate or replace ULS.

The central series is the largest series in the Reinfjord complex, covering 45% of the intrusion, compared to the ULS (22,5%), the LLS (7,5%) and the MZ (25%). Calculated after the remapping using the new boundaries.

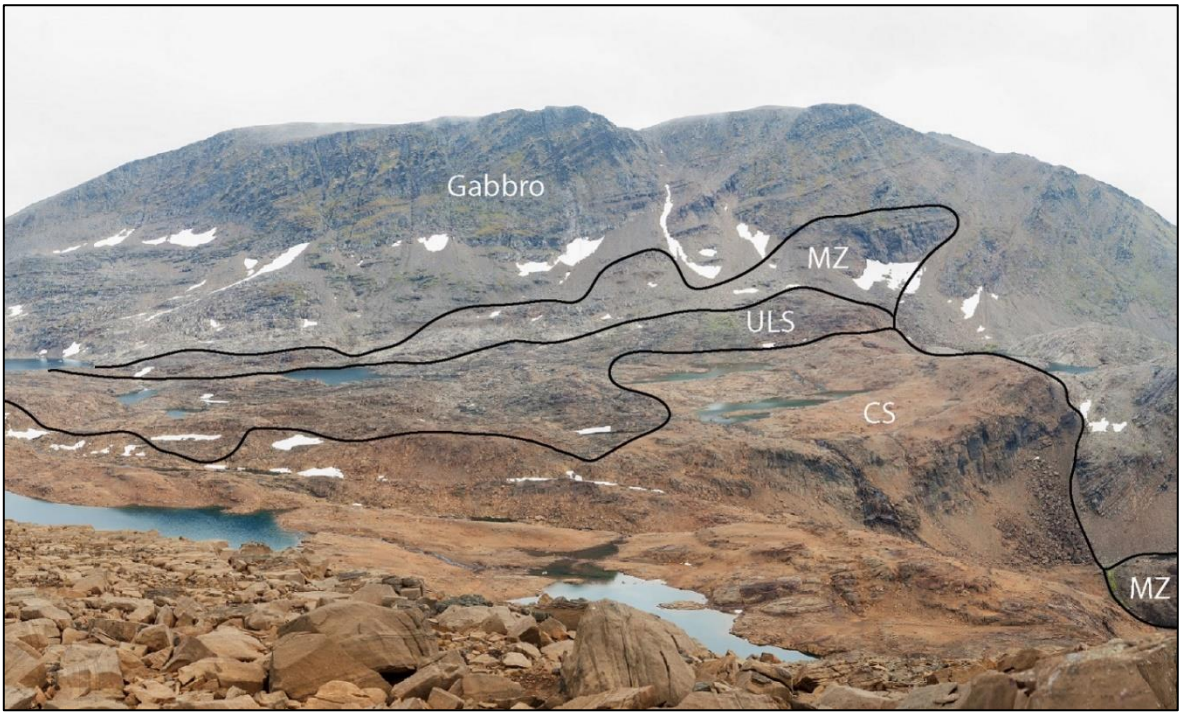

Figure 1.5:Southern part of plateau (Seen towards east) (Photo: Lars Anker Rasch).

1.2.7 Marginal Zones (MZ)

All around the complex where the ultramafic series have been in contact with the gabbro or the gneiss, a marginal zone is formed. The MZ is a hybrid, containing pyroxene rich rocks (websterite), plagioclase rich ultramafic rocks (often with plagioclase veins), pyroxene pegmatites and olivine gabbro.

Bennett (1974) and Emblin (1985) divided the marginal zones into several units, (northeast marginal zone, upper marginal zone and lower marginal zone). Due to the large variety and irregularity within each of these series, all marginal zones will be treated as one hybrid zone in this thesis. The MZ is a hybrid based on the UM series and type of host rock, and not distinguish by its locality.

1.3 Earlier work

Despite the special geological setting and well preserved rock, Reinfjord ultramafic complex is understudied. Geologist have been investigating the SIP since the late 1800s, especially after the 1950s when they found nepheline deposits on Stjernøya. The mafic-ultramafic rocks on Stjernøya were first described by Oosterom (1963) and the western areas of Øksfjord peninsula

by Hooper (1971). The Reinfjord area were first documented by Bennett (1971) and Bennett (1973) in which he described the intrusion and divided the intrusion into several series. At the same time Hansen (1971) described findings of a sulphide contact deposit in the western part of the intrusion, between the later classified LLS and the gneiss. Emblin (1984) reclassified the geology of Reinfjord, his classification is still in use today with some modifications. An overview of the four ultramafic intrusions within the Seiland Igneous Province was published by Bennett et al. (1986).

Robins and Gardner (1975) suggested that the Seiland igneous province was formed in a subduction zone, with subduction of oceanic crust under the Baltican plate. However later studies by Krill and Zwaan (1987) suggested that the SIP was formed in an extensional regime. This was later confirmed by Roberts et al. (2006), whose dating constrained the emplacement of the SIP to be 570-560 Ma. Other studies in the Seiland igneous province include the study on the Hasvik intrusion by Tegner et al. (1999) and Heredia et al. (2008), Melkevann intrusion by Yeo (1984), the Nordre Bumannsfjord intrusion by Griffin et al. (2013) and a series studies on gabbros and ultramafic nodules in Seiland by Robins and Gardner (1974), Robins and Gardner (1975), Robins (1975).

In recent years Reinfjord has gained renewed attention after Nordic Mining ASA in collaboration with NTNU found a possible Ni-Cu-PGE deposit (Iljina, 2013). This resulted in four drill cores and several publications including a map by Øen (2013) and Anker-Rasch (2013).

2 Theory

2.1 Classification of ultramafic rocks

A ultramafic rock must contain more than 90% mafic minerals (olivine, orthopyroxene, clinopyroxene and amphibole). The classification is based on the amount of these minerals: Olivine, clinopyroxene, orthopyroxene and hornblende (Winter, 2010), as seen in Figure 2.1.

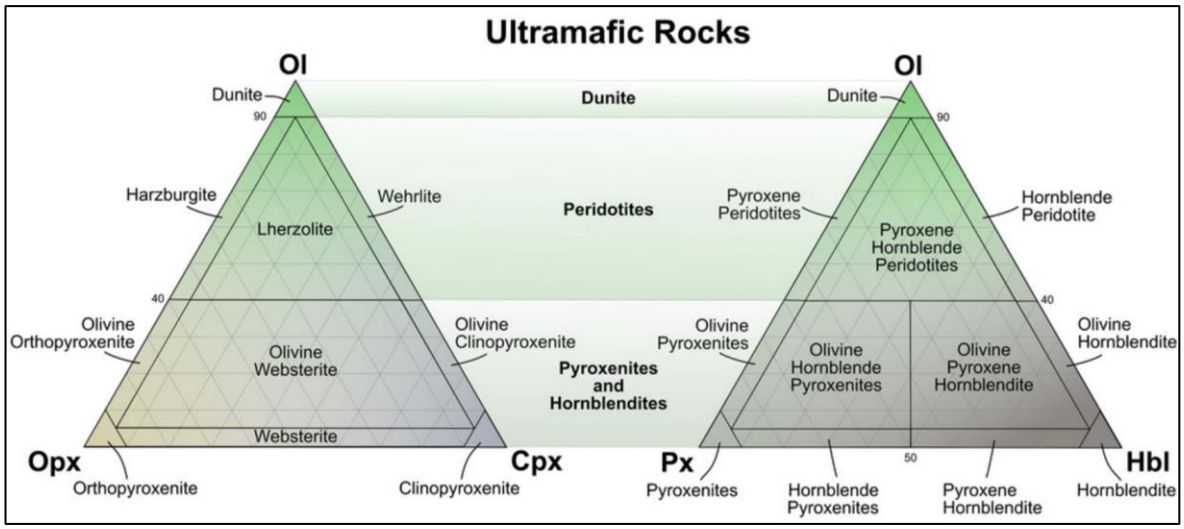

Figure 2.1: Classification of ultramafic rocks (Source: Mindat.org)

2.2 Magmatic processes

2.2.1 Partition coefficient and generation of magma

When crystals form from a melt, elements will partition into the crystal lattice (compatible) of the forming crystals or stay in the melt (incompatible). Elements that partition into the crystals are depleted in the melt, whereas incompatible elements are enriched by the ratio of crystals forming (Robb, 2009). This is an important ore-forming process to generate melts that may lead to the formation of an ore deposit, as the last portion of the liquid will be strongly enriched in incompatible elements. Several magma chamber events may facilitate ore-deposits for such melt. Reversing the process to melting of a rock. The first forming droplets of melt will be strongly enriched in incompatible elements, as these elements prefer to stay in the melt. The residual solid will gradually be more and more depleted in these incompatible elements leaving only the compatible elements. Figure 2.2 from Robb (2009) show how incompatible and compatible elements will behave during batch and fractional melting.

Two extremes exist for partial melting of a rock. Either the melts forming are instantaneously removed from the system (fractional melting) or the melt stays in equilibrium with the residual rock (batch melting). The effect this has on the melt composition with regards to incompatible and incompatible elements is shown in Figure 2.2.

During fractional melting, the melt is efficiently removed from the solid. The first increment of melt will be highly enriched in incompatible elements (i.e. D<1), depleting the residual solid in these elements. The next increment of melt will therefore be less enriched in this element. During batch melting, the solid and melt remain in constant equilibrium. A highly incompatible element (D=0.01) will become much less depleted in the melt than during fractional melting. When all the solid have melted (F=1) and the melt and the original solid have the same composition (Robb, 2009).

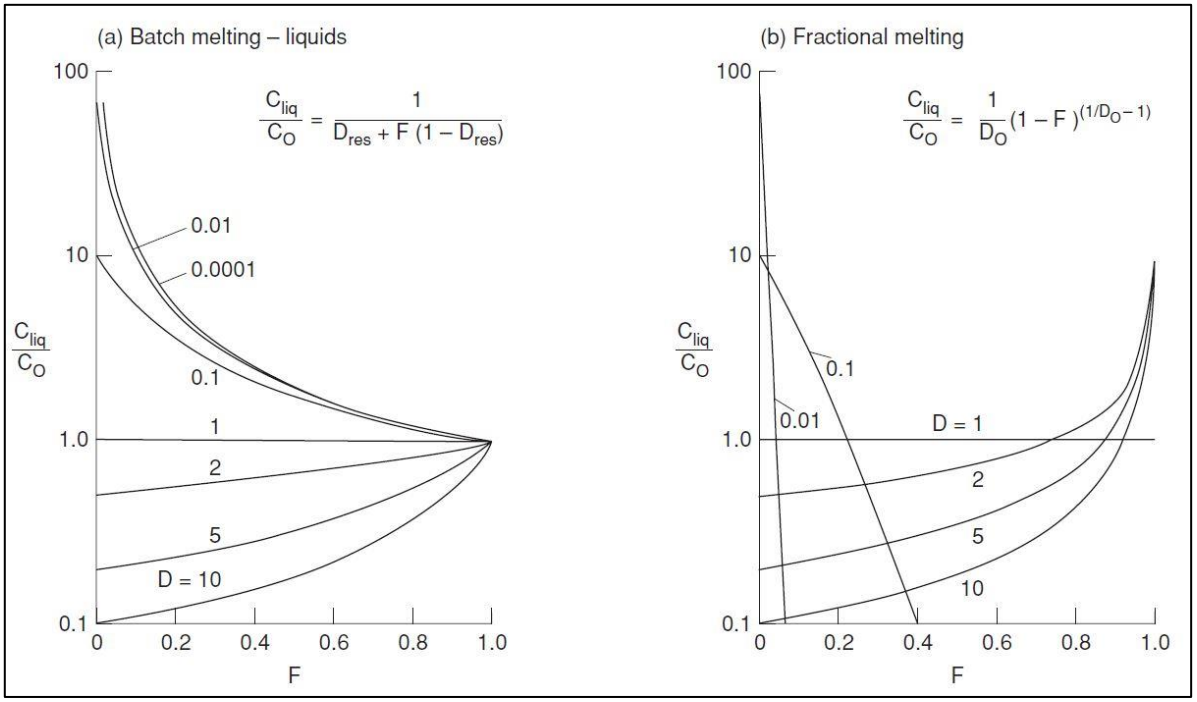

Figure 2.2:a) Batch melting where melt and residual solid are in equilibrium b) Fractional melting considering no reaction between melt and solid residue, melt are instantly removed from the system. (Robb, 2009)

2.2.2 Magma density and replenishment

Melt density varies with in a differentiating magma chamber during fractional crystallizatio. A mafic melt crystalizing pyroxene will become less dens due to the removal of heavy elements particularly iron in mafic minerals such as pyroxene. Alternatively, if the same melt crystalizes mostly plagioclase it becomes more dense due to the low density of the plagioclase components.

This effect will strongly affect the settling velocity of crystal in the melt. Melt density will also play a major role if a new pulse of magma is injected into the system, also referred to as replenishment or magma recharge. If the injected melt is more dense than the original melt in the magma chamber, it will rise up due to emplacement pressure and then sink to the floor of the chamber, this is referred to as a "fountain" event (Figure 2.3a). If the injected magma is less dense than the original magma, it will rise through the magma chamber. As it does so, the injected magma will mix with old magma. This is referred to as a "plume" (Figure 2.3b). (Robb, 2009)

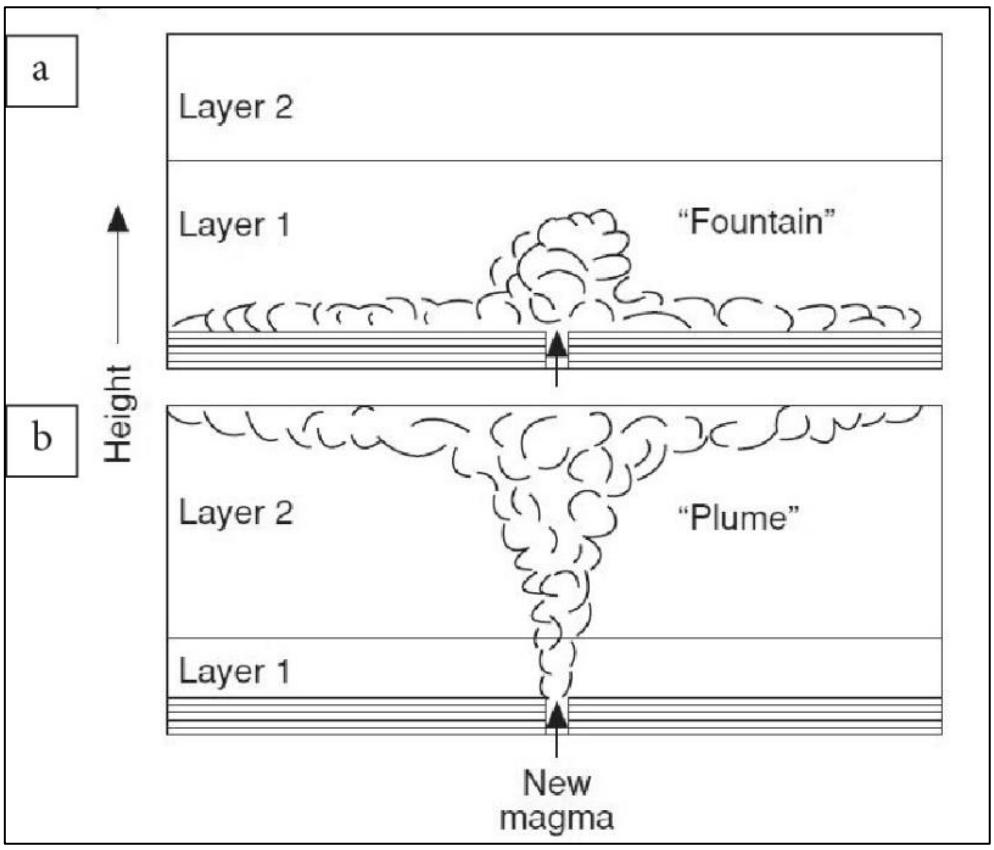

Figure 2.3:a) Dense magma injection. b) Lighter magma injection (Robb, 2009)

A replenishment event will cause mixing for both scenarios, but during a "fountain" event this mixing will be limited. A "plume" on the other hand will be more efficient at mixing and may lead to turbulent mixing between the injected magma and the magma already in the chamber. This process is very important from an ore-forming perspective, as this may lead to economic grade deposits. If a separate sulphide phase is present in the melt, it will react with nearby melt and scavenge the melt for chalcophile elements (that are compatible in sulphide melt). The "R" factor was defined by Campbell and Naldrett (1979), and is based on the melt/sulphide ratio where sulphide liquid is in equilibrium with the melt before removal. The "R" factor is the mass

of silicate liquid brought in contact with the sulphide liquid. So a “R” factor of 10 000 means that the sulphide liquid have been in contact with 10 000 times its own mass of silicate melt before been deposited.

Final concentration of an element in the sulphide liquid (Eq. 1) is controlled by the initial concentration (in melt – C_0), partition coefficient (D) of the chalcophile and siderophile elements and “R” value (Naldrett, 2004).

Figure 2.4 show the relationship of nickel and platinum in a melt with a sulphide phase. These elements have very different distribution coefficients (D) and initial concentration (X_i). The X-axis show the “R” factor while the Y-axis show the Ni concentration in the sulphide liquid on the left and Pt concentration on the right. At a “R” factor of 1000, the nickel starts to be saturated, while there is nearly no Pt in the sulphides. To form a PGE deposits a much higher “R” factor is required.

Eq. 1:The R factor (Campbell and Naldrett, 1979):

$$C_{Sul} = C_0 D(R+1)/(\mathrm{R}+\mathrm{D})$$

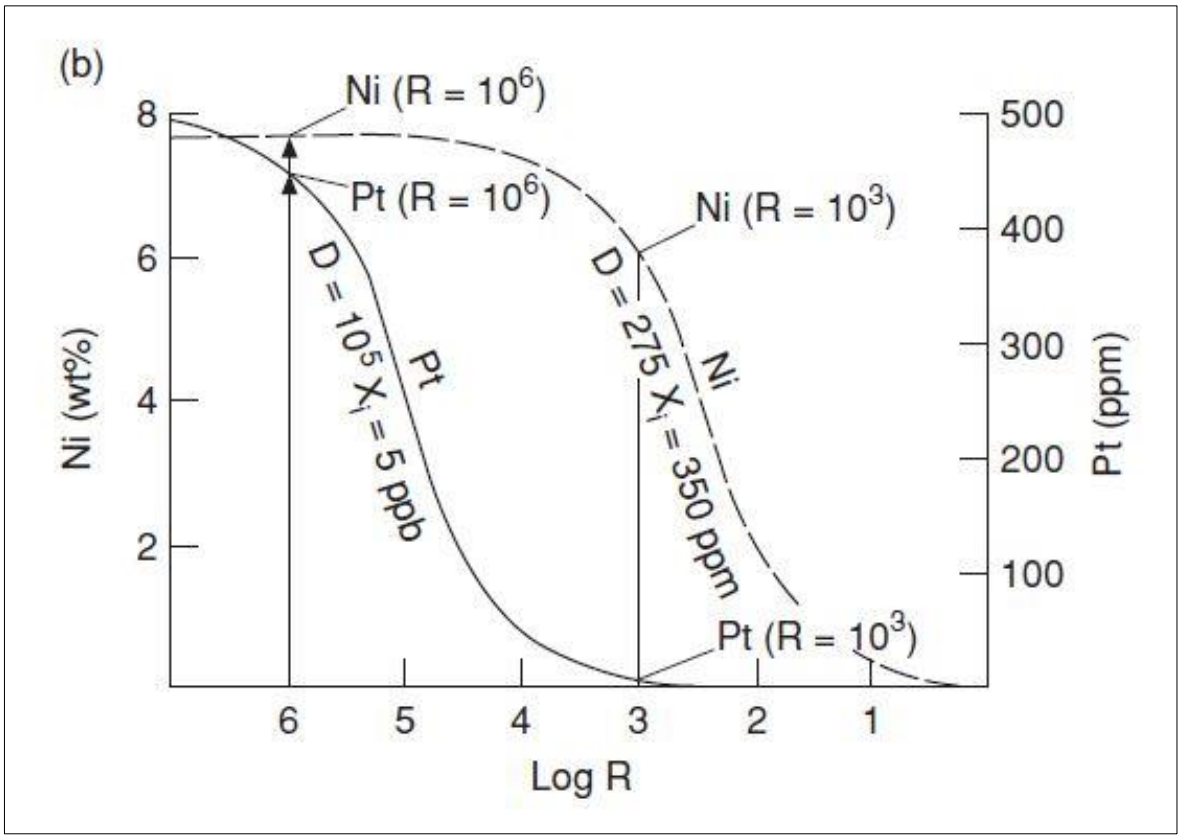

Figure 2.4:"R" factor (Robb, 2009)

2.2.3 Immiscibility and sulphur solubility

Liquid immiscibility is an important process forming sulphide deposits in mafic and ultramafic intrusions. Immiscibility is where a homogeneous liquid segregates into two liquid fractions. There are two types of liquid immiscibility, the fractions can be chemically similar such as silicate-silicate immiscibility or they can be very different such as in silicate-oxide or silicate-sulphide immiscibility (Robb, 2009).

Sulphur solubility in a melt is affected by a wide range of variables, such as temperature, pressure, melt composition and oxygen fugacity. Sulphur solubility increases with an increase in FeO, MgO and CaO content in the melt, while SiO_2 and Al_2O_3 decreases sulphide solubility. Increase in oxygen fugacity will also decrease sulphide solubility. Increasing temperature will increase sulphide solubility, whereas an increase in pressure will decreases sulphide solubility. Due to the strong pressure effect on the sulphide solubility in a rising magma, solubility will increases and therefore not reach sulphide saturation. Unless large amounts of fractional crystallization, contamination by assimilation of felsic rock or assimilation of large amounts of sulphides from country rocks occurs (Naldrett, 2004).

2.3 Layering

Layering is a feature found in many mafic and ultramafic layered intrusions. Irvine (1982) classified layering as the overall structure and fabric of cumulates through layers, laminae and laminations. “A layer is a sheetlike cumulate unit that is a distinctive entity in its compositional and/or textural features.” (Irvine, 1982, p 138). Layering can be modal (mineral variation), cryptic (chemical variation), textural (texture variation) and/or grain size variation.

Namur (2015) distinguished between two types of processes of magmatic layering: dynamic or non-dynamic. He defined dynamic processes as processes formed by melt, crystal mush or crystals in movement, caused by filling of a magma chamber or by crystallization. Non-dynamic processes are classified as layering formed by in-situ crystallization and without movement of large volume of melts. Dynamic layer-forming processes include crystal settling and crystal flotation, convection, replenishment, contamination and interstitial melt migration. Non-dynamic processes are processes controlling crystallization (such as pressure, oxygen fugacity), change in nucleation and crystal growth rate.

Crystal-settling and crystal-flotation are processes that contributes to layering, as crystals forming often will have different density compared to the melt. Crystals that are less dense will float through the melt and accumulate in the roof zone of the magma chamber, whereas more dense crystals will sink and accumulate on the floor of the magma chamber. For a magma (non-Newtonian fluid) this process will follow stokes law (Eq. 2)

Eq. 2: Stokes law:

$$V = \frac{2r^2 g(\rho_1 - \rho_2)}{9\eta}$$

Settling velocity depends on grain size (radius r), density contrasts ($\rho_1 - \rho_2$) and melt viscosity (9η). Given this equation, crystal settling and crystal flotation may lead to layering of both grain-size and modal variations caused by density variations. Large grains and dense minerals accumulate in floor zone and grading upward to small less dense minerals upwards. The settling velocity is strongly dependent on the viscosity, controlled by: temperature, amount of crystals,

SiO_2 and H_2O-content (Naslund and McBirney, 1996, Namur, 2015). Melt in a magma chamber is almost always in movement due to density, chemical and temperature gradients, which are the driving forces for convection cells in magma chambers. This may affect how the crystals settle, as convection may keep the crystals in suspension if the settling velocity is low. Due to this phenomena, crystals in suspension need to reach a critical concentration before settling, forming batches of crystals accumulation on the floor of the magma chamber (Namur, 2015).

Interstitial migration of residual melt or a free hydrous fluids-phase may form layers by dissolution. Migration of interstitial melt may form a chemical and thermal disequilibrium strong enough to partially dissolve pre-existing minerals, that replace with new minerals. Migration of fluids though cumulate rock can lead to dissolution of minerals and precipitation of hydrous minerals. By constant flow and a high fluid/rock ratio the dissolved minerals will be removed, leaving only the most resistant minerals, forming layering by dissolution (Namur, 2015). An example this processis given by Boudreau (1999) on the Stillwater complex, in the OB1 (olivine-bearing zone 1). He argue that the olivine-bearing rocks were formed by exsolving fluids from the cumulus pile, that partially melt the gabbronorite forming an olivine saturated liquid.

Magmatic layering by a convection magma is where crystals crystalizes in-situ at the walls and roof zones due to cooling, and on the floor by accumulation (Naslund and McBirney, 1996). The accumulation on the floor is mostly controlled by crystal settling. Temperature gradients are the dominating factor for developing continuous convection. Hot magma injected in a magma chamber is cooled from the walls and roof faster than from the floor creating a gradient from the centre towards walls and roof. In-situ crystallization on the floor is also suggested as a mechanism for forming layering in large convecting magma chamber. Naslund and McBirney (1996) suggested that the transfer of heat from floor section to the roof and walls may lead to melting of country rock and crystallization on the floor.

Figure 2.5 modified by Naslund and McBirney (1996) after Irvine (1977) show magma recharge and magma injection in the SiO_2-Mg_2SiO_4-Cr_2FeO_4 ternary diagram. Figure 2.5a shows an evolving primitive melt with composition A that will fractionate olivine, with minor chromite (around 1%), and follow the liquidus to point B. From B to C the melt will reach a peritectic

point, where olivine and chromite stop to crystalize, the melt then enters the orthopyroxene stability field, where orthopyroxene is the only phase to crystalize. If the melt in point C mixes with a new pulse of the primary magma A (Figure 2.5b), a new melt composition (M_2) will be created. This new melt is in the chromite stability field and will precipitate chromite until it reaches the cotectic. If a less evolved magma (point B) mixes with the primary magma A. However, the new melt composition (M_1) are closer to the liquidus line for olivine and chromite, the melt will therefore precipitate smaller fractions of chromite. Contamination by a felsic (F) rock of the primary magma will also push the new mix into the chromite stability field and precipitate chromite before following the same liquidus line (Figure 2.5a). Since the chemical difference between primary magma A and the felsic rock F is so large, only a small volume of felsic magma is required to stabilize chromite. (Naslund and McBirney, 1996)

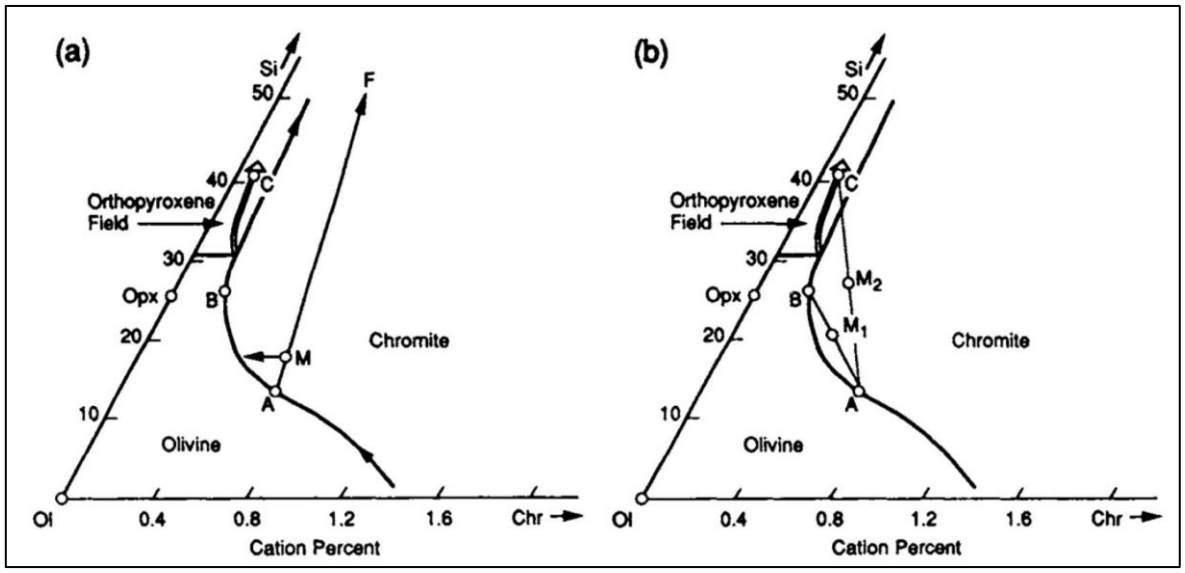

Figure 2.5: a) Magma injection (contamination) b) Magma recharge (modified by Naslund and McBirney (1996) after Irvine 1977)

The processes discussed above are all dynamic, using the terminology by Namur (2015). The other type of process he distinguishes were non-dynamic layering processes, such as changes in pressure and oxygen fugacity. The liquidus phases crystalizing at equilibrium melt conditions changes with composition, pressure, temperature and oxygen fugacity. Repeated fluctuation of pressure may form layering by controlling which minerals precipitate. The pressure may vary due to build up and release of hydrous phases in the melt, or by changing between lithostatic and hydrostatic conditions. Oxygen fugacity strongly affects which phases precipitate, especially the Fe-Ti oxides, which in turn control the Fe_2O_3/FeO in the melt. Increases in oxygen fugacity may put the melt in a state where only magnetite will precipitate, while under

more reducing conditions you may precipitate olivine and plagioclase (Naslund and McBirney, 1996). Variations in oxygen fugacity, may also be caused by assimilation of host rocks fluids (from Klemm et al. (1985) in Tegner et al. (2006)).

Oscillatory nucleation and crystal growth is a process also widely believed to form layering. As nucleation and crystal growth is depended on temperature, chemical components in the melt and free energy in order to grow and nucleate crystals, this may be an efficient process to form layering. One way to form layering by this method, is when one phase is crystallizing it depletes the nearby melt in these compatible elements forcing the surrounding melt into a new stability field where it begins to crystalize a new mineral. Figure 2.6 from Namur (2015) visualise this where a parent melt (a) starts by only crystalizing forsterite until this is locally depleted in the melt and starts to nucleate enstatite (Opx). If this continues over time, a rhythmic layering may form, untill the system reaches equilibrium and crystallizes forsterite and enstatite simultaneously.

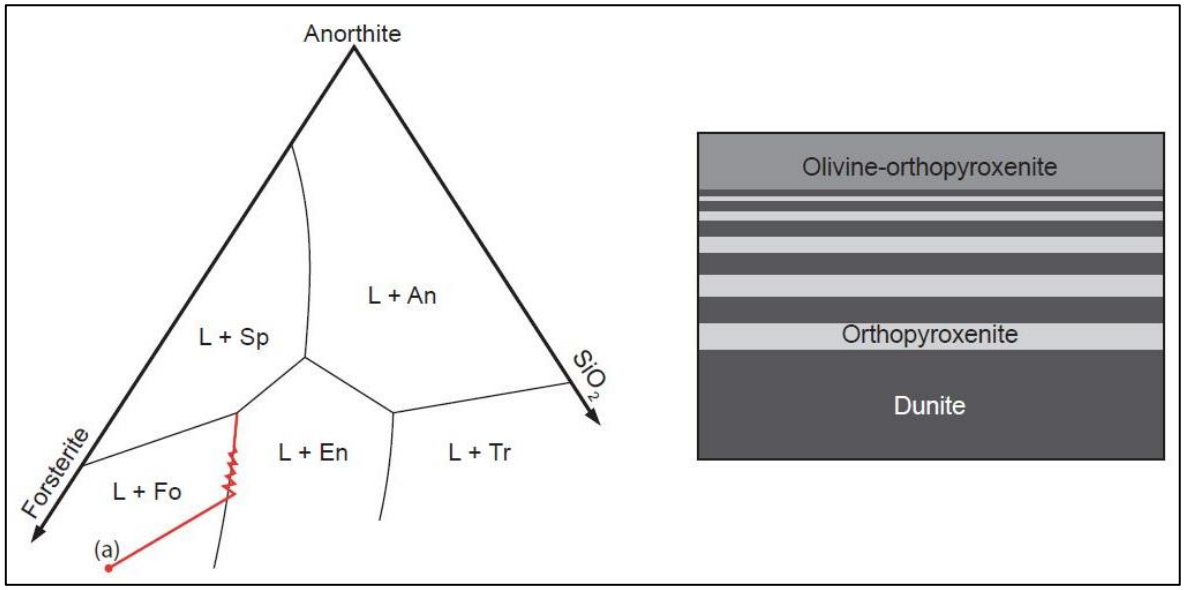

Figure 2.6 Oscillatory nucleation and crystal growth forming layering (Namur, 2015)

2.4 Other mafic intrusions

Two of the world's best known and most studied mafic-ultramafic intrusions, are the Bushveld and Skaergaard intrusions. Geologists have worked on these intrusions for decades, but they are still not fully understood. Even though they are not fully understood, they have given great insight in how mafic intrusions form and which magmatic processes are dominant in such environments.

2.4.1 Skaergaard, Greenland

The Skaergaard intrusion in the eastern part of Greenland, is one of the most studied mafic intrusions in the world. The relatively small intrusion measuring 11 km (N-S) and 8 km (E-W) was emplaced into Precambrian gneisses and Tertiary basalts at 55 Ma (Winter, 2010).

It is generally accepted that the Skaergaard intrusion were formed by one single magmatic event (Nielsen, 2004, Salmonsen and Tegner, 2013) . The intrusion is divided into three series, the Layered Series, the Upper Border Series and the Marginal Border Series (figure 2.7). These cumulate sequences fractionated inwards from the floor, roof and walls respectively (Salmonsen and Tegner, 2013 from Wagner and Deer, 1939). Where the Upper Border Series and the Layered Series meet, a zone containing the last and most evolved melt crystalized. This zone named the Sandwich Horizon (Winter, 2010). The Layered Series is divided into a Hidden Zone, Lower Zone, Middle Zone and a Upper Zone, with subdivisions marked by the appearance of cumulus phases. Salmonsen and Tegner (2013) showed that the Upper Border Series mirror the Layered Series and Marginal Border Series, and therefore is formed from the same melt that formed the Upper Border Series and the Marginal Border Series.

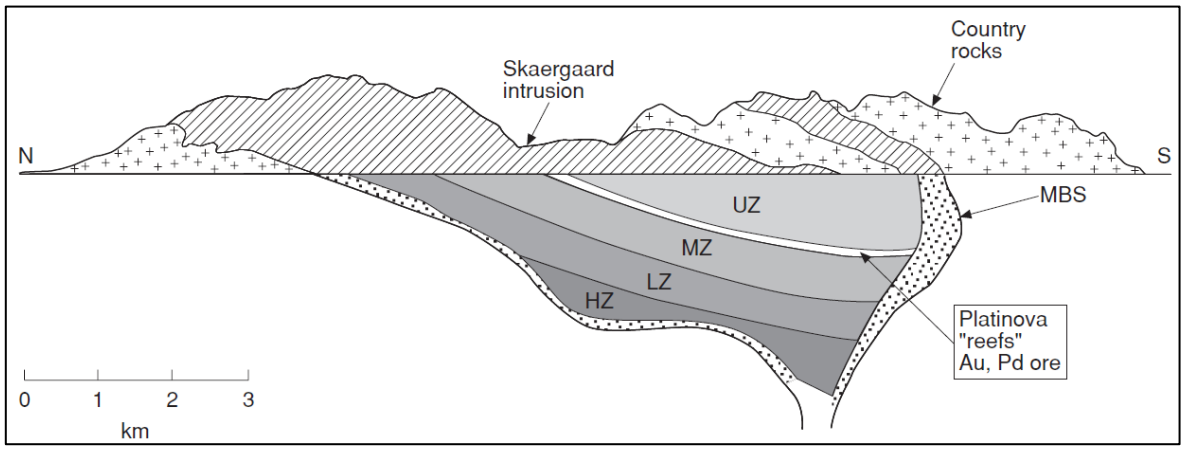

Figure 2.7: Cross section of Skaergaard (Robb, 2009)

2.4.2 Bushveld, South Africa

The Bushveld complex in South Africa is the world's largest layered mafic intrusion, it covers an area of more than 60,000 km^2 and has an estimated volume of 1 million km^3. The mafic rocks in the Bushveld complex are well preserved from deformation despite their age of 2,06 B.y. (Kinnaird, 2005, Cawthorn, 2015).

2.Theory

The mafic and ultramafic Rustenburg layered suite is where the main body of mafic and ultramafic rocks in Bushveld is located. It stretches for 300-400km with a thickness of 9km. From the base to the top, the Rustenburg suite is divided into a Marginal Zone (norites), Lower Zone (dunite cumulates), Critical Zone (norite, orthopyroxenite and anorthosite layers), Main Zone (homogenous norite and gabbro-norite) and the Upper Zone (anorthosite, gabbro and ferrodiorite). The Rustenburg suite show an differentiation sequence from olivine Fo_{90} at the base to olivine Fo_1 in top layers, and show the worlds most complete fractional crystallisation (Winter, 2010, Cawthorn, 2015).

Bushveld contains large world class deposits of PGE, chromite, iron and vanadium. The famous Merensky Reef is located between the critical zone and the main zone, it holds the Pt-Pd sulphide bearing unit, and is the largest distributor in the world of platinum (Winter, 2010, Cawthorn, 2015).

2.Theory

3 Methods

3.1 Fieldwork

A total of 23 days were spent in field over two field seasons. In the 2014 field season a total of 13 days were spent in field. The first days were used to explore the area and getting to know the different rocks types, four days of sampling and six days of mapping in the eastern part of lake district and the NE part of the intrusion. The 2015 field season consisted of a total of 10 days in field. This was a week less than planned, due to bad weather and sickness within the camp, which strongly affected the efficiency and time schedule of this field season. First four days were spent mapping the western parts of the intrusion, before the camp was set up on the plateau. Three days of mapping were conducted on the plateau before we had to evacuate due to bad weather. This is the reason why the Northern area close to the glacier is not mapped.

3.2 Mapping

Mapping was conducted digitally using handheld GPS with notebooks to register field observations. The GPSs used in field are Garmin GPSmap 62s (2014) and Garmin GPSmap 64st (2015).

The digital map presented in this thesis was created using the ArcMap software from ESRI. A set of geodatabases were set up with the ArcMap program to separate background information such as contour, rivers, lakes, etc. from geological observations. Separating raw data, background data and analysed data ensure good reliability on the data and dataset. It is a strong foundation, making adding and editing data easier and more secure. This also makes it easier for future work to make necessary corrections to the map.

With the database structure complete, background data and aerial photos from The Norwegian Mapping Authority (Kartverket) was added. Previous maps such as Emblin (1985), Øen (2013) and Anker-Rasch (2013) were also added to the database. Geo-referencing of paper maps such as Emblin (1985) (Figure 3.1) is done in the same ESRI software, assuring the best compatibility and accuracy. The ArcMap software allows the user to compare previous geological maps, old digitized and geo-referenced maps and geophysical maps with new data.

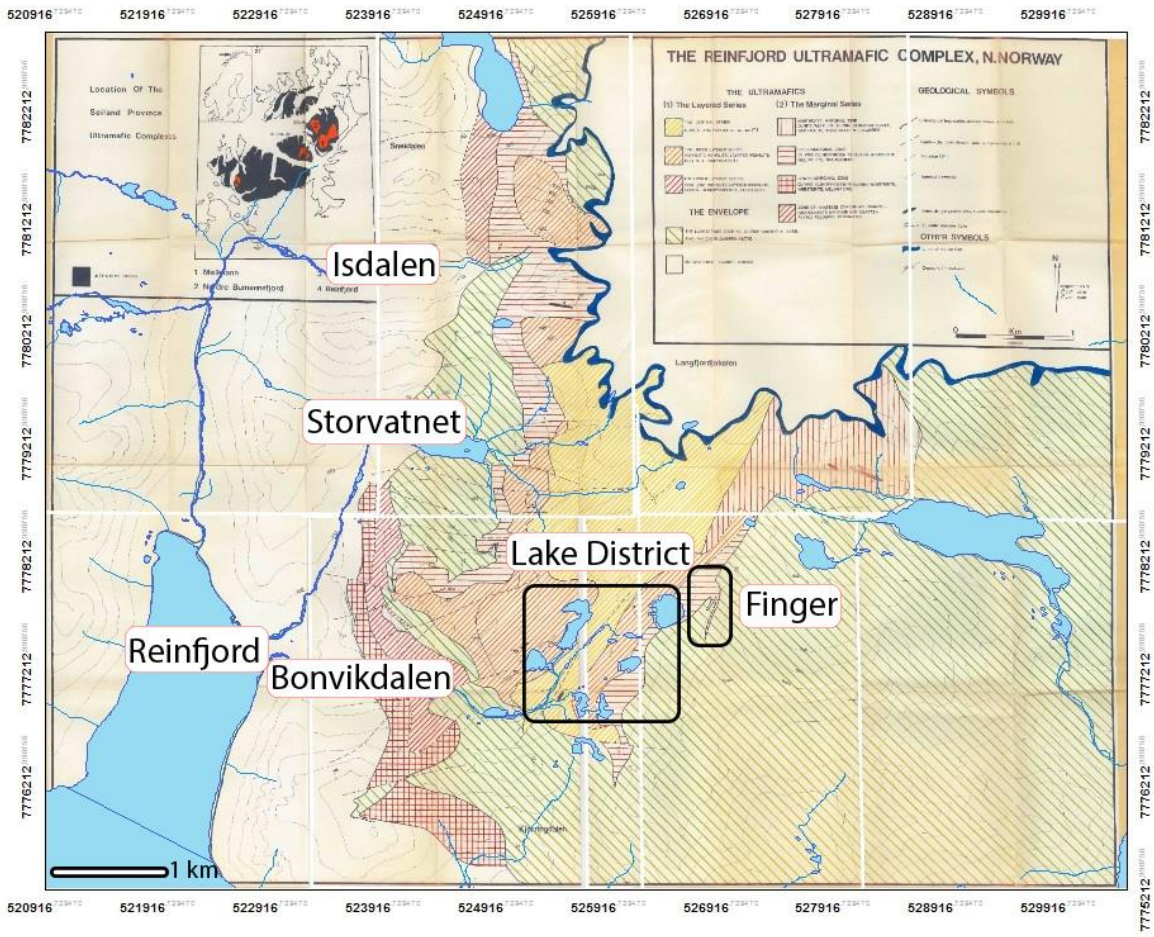

Figure 3.1: Mosaic visualisation of the digitalized and geo-referenced map by Emblin 1985, with water and river data lying on top for better visualisation. Marked on the map are also some place names and two locations as reference.

Since it was not possible to investigate the entire area, the map in this thesis is based on work done by Emblin (1985), with some revisions from Øen (2013) and Anker-Rasch (2013), along with some major reinterpretations by this author. Figure 4.27 show how much of the new map is based on previous work, and how much have been revised.

3.3 Sampling

In total 41 samples were collected during fieldwork. Of these 12 samples were taken from the RF-3 and RF-4 drill cores. A profile with 7 samples was collected to describe the CS-Gabbro contact. The rest of the samples were collected to give a better understanding of the intrusion as a whole. Of these samples, 15 are analysed and used in this thesis together with samples and analysis from the RF-4 drill core. Altogether 40 thin sections have been made for this thesis.

Of which 16 thin sections are from RF-4, 12 thin sections from CS surface samples, 12 thin sections are used to understand and describe the interaction between the Central Series and the Langstrandgabbro contact.

3.4 Sample preparation

All surface samples collected in the field, that are used in this thesis, were cut with a diamond saw at the Department of Geology and Mineral Resources Engineering, NTNU. The rock slices were then prepared for thin sections at the thin section laboratory at the Department of Geology and Mineral Resources Engineering, NTNU, where they were prepared into 30µm polished thin sections. A total of 16 quarter samples were collected from the drill core and prepared together with the surface samples.

Crushing

Samples that were chosen to be analysed were first crushed at the Department of Geology and Mineral Resources Engineering, NTNU. A hand crusher was used to reduce the sample size from 15-20 cm to 1-3 cm. The crushed samples were then crushed again in a Retsch Jaw Crusher using tungsten discs, reducing the sample size down to less than 0,5cm. The samples were then split into two sections, approximately 100 g for external whole-rock analysis at ALS Chemex and 20-50 g for X-Ray Diffraction (XRD) analysis (was not carried out). Four drill core samples was analysed on the XRD at the Department of Geology and Mineral Resources Engineering, NTNU. These samples were crushed by the hand crusher, before being milled on a Siebtechnik Disk Mill for 4 minutes using an agate grinding set.

3.5 Petrography

Polarized- and reflected light microscopy was performed using an Olympus BX51 microscopy with a Progress CT5 mounted camera. It was used to identify and document mineral phases present. Scans of thin sections presented in this thesis were captured using Epson Perfection V600 Photo Scanner with polarized filters.

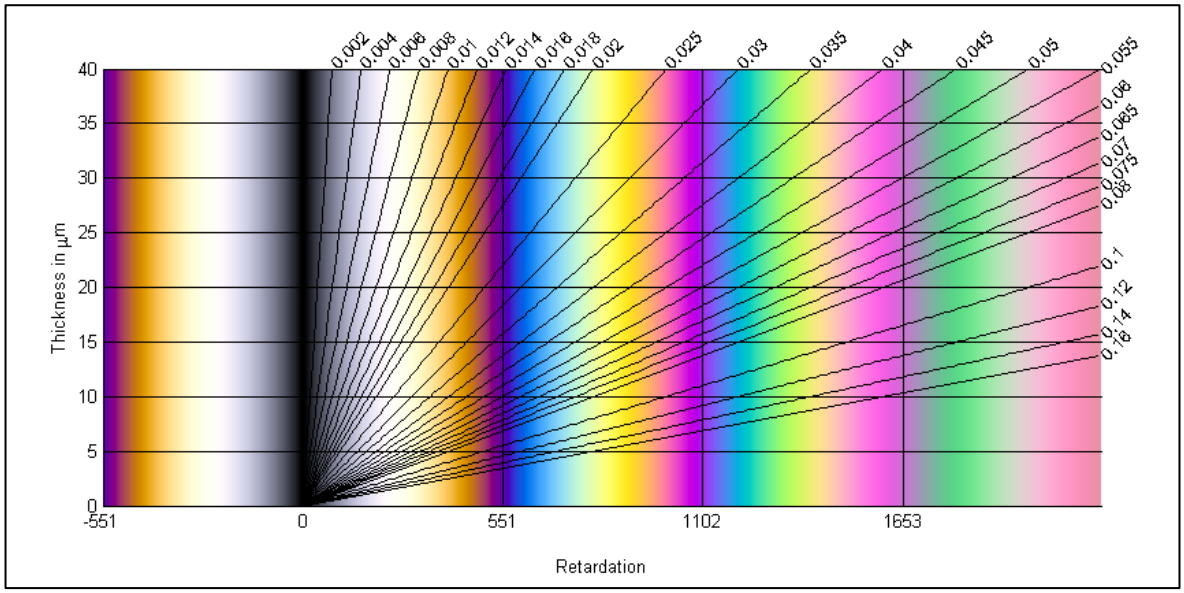

Figure 3.2: Revised Michel-Lèvy interference colour chart by Sørensen (2013).

3.6 Geochemical analysis

The Electron Probe Micro-Analysis (EPMA), and were performed at the Department of Geology and Mineral Resources Engineering, NTNU. Scanning Electron Microscope (SEM) was performed at the Department of Material Science and Engineering , NTNU. Whole-rock geochemistry, including trace element and PGE analysis, were performed by ALS Chemex. Descriptions of the tests run by ALS are based on the description brochure found on their website (www.alsglobal.com), where it can be found and downloaded.

3.6.1 Whole-rock geochemistry

Major oxides analysis, the ME- ICP06 method.

0,2g sample is added to 0,9g of lithium metaborate/lithium tetraborate, it is mixed and fused in a furnace at 1000°C. The melt is cooled and dissolved in 100mL of 4% nitric acid and 2% hydrochloric acid. The ME- ICP06 is analysed by inductively coupled plasma-atomic emission spectrometry (ICP-AES) and corrected for spectral inter-element interferences. Results are reported as weight percent (wt%).

Loss of ignition (LOI), the OA-GRA05 method.

1,0g sample is heated in an oven at 1000°C for one hour, cooled and measured. The loss on ignition is calculated by mass difference, this reveals the remaining volatiles (H_2O and $CO_{2,}$) in the sample.

Trace element analysis by fusion, the ME-MS81method.

The trace element analysis by fusion method is prepared the same way as the major oxides, but it is analysed by inductively coupled plasma – mass spectrometry (ICP-MS). Results are reported as parts per million (PPM).

Trace element by dissolution, the ME- ICP61 method.

A 0,25g sample is digested with perchloric, nitric, hydrofluoric and hydrochloric acids. The residue is diluted with dilute hydrochloric acid. The solution is analysed by ICP-AES.

Platinum group minerals analysis, the PGM- ICP23 method

The sample is fused with lead oxide, sodium carbonate and borax silica that are inquarted in silver. This is digested in a high power microwave for 2 minutes in dilute nitric acid, after cooling, hydrochloric acid is added before again digested for 2 minutes at half power. After cooling the mixture is diluted by 4mL 2% hydrochloride acid and homogenised. The sample is the analysed for Au, Pt and Pd by ICP-AES.

3.6.2 X-ray Diffraction (XRD)

X-ray powder diffraction is a fast and powerful analytical method to determine the physical and chemical characteristics of materials. The diffraction is a result from the X-ray interaction with the atoms in the crystalline structure (Will, 2006). Samples were analysed at the department of geology and Mineral Resources Engineering, NTNU, using a Bruker X-ray Diffractor D8 Advance, with 40 Kv, 40 mA and CuKα radiation of wavelength λ = 1,5406 Å. Diffractograms were recorded from 3-65 °2θ, in 0,009 °2θ increments with 0,6s count time per increment giving a total analysis time of 71 minutes per sample. Mineral identifications were based on optical

microscopy and SEM, confirmed by the software Bruker EVA using ICDD 4 database. Phase quantification was performed using Rietveld refinement software TOPAS 4.2.

3.6.3 SEM

The SEM work was performed on a Zeiss Ultra 55, using Bruker Quantax Esprit software. Samples investigated on SEM and EPMA were carbon coated to prevent charging of the samples. Working distance was set to 10mm with an acceleration voltage on 20kV. The main use of the SEM was to collect Electron Dispersive spectra (EDS). EDS is a method used to determine the mineralogy of the samples. It is used to determine chemistry of individual points for classifying minerals and to create EDS-maps to show mineralogical relationships of optically similar minerals.

3.6.4 EPMA

The EPMA analyses were conducted on a JEOL JXA-8500F Electron Probe Micro Analyser. It is a thermal field emission electron probe micro analyser. A total of 797 measurements were collected and analysed. 493 of these points are distributed over 18 thin sections in RF-4 and surface samples, where olivine (424 measurements) and pyroxene (72 measurements) are analysed with some amphibole (21 measurements). 280 measurements were conducted on the 7 thin sections from a CS-Gabbro contact zone, these samples olivine (84 measurements), pyroxene (117 measurements) and plagioclase (76 measurements) were analysed. The analyses were performed using standards for each mineral (Table 3.1). The elements measured, with the detection limit, count time and the Astimex standard used for each element in each of these programs is presented in Table 3.1. All analyses were performed with beam current at 20nA and 15kV acceleration voltage. The plagioclase was analysed with 5µm defocused beam, pyroxene with 2µm defocus beam and olivine was conducted without defocus, (i.e. spot analysis).

To have a statistically representative number of analyses the samples were analysed with >3 analysis per grain and >6 grains per sample, where possible. Due to the low content of accessory phases in the CS (dunite), the data with few measurements are marked due to low statistically significance.

Table 3.1: Overview over elements in the mineral programs used for EPMA. The first 8 elements are the same in all three programs and the last three are specific for each program. Note difference in detection limit, count time and Astimex standards on the same elements on different programs.

	Detection limit (ppm)			Count time (s)			Standard		
Element	**Ol**	**Px**	**Pl**	**Ol**	**Px**	**Pl**	**Ol**	**Px**	**Pl**
SiO_2	200	150	300	40	20	20	Ast34	Ast21	Ast35
Na_2O	100	150	150	40	10	10	Ast28	Ast28	Ast28
K_2O	100	150	150	40	10	10	Ast41	Ast41	Ast41
MnO	100	150	150	40	30	20	Ast39	Ast11	Ast11
MgO	100	150	150	40	20	20	Ast34	Ast21	Ast34
Al_2O_3	100	200	200	120	20	20	Ast28	Ast28	Ast35
CaO	100	150	150	40	20	20	Ast4	Ast21	Ast35
FeO	200	200	200	40	20	20	Ast34	Ast12	Ast34
NiO	200			40			Ast52		
Cr_2O_3		150			30			Ast17	
TiO_2		150	200		30	20		Ast40	Ast29

Table 3.2: Shows what minerals or compounds the Astimex standard is based on.

Astimex standard	Mineral standard	Astimex standard	Mineral standard
Ast4	Apatite	Ast34	Olivine
Ast11	Calcite	Ast35	Plagioclase
Ast12	Cassiterite	Ast39	Rhodonite
Ast17	Chromium Oxide	Ast40	Rutile
Ast21	Diopside	Ast41	Orthoclase
Ast28	Jadeite	Ast52	Nickel Silicide
Ast29	Kaersutite		

3.7 Source of error

3.7.1 Map

The background data used to create the new map are assembled mainly from The Norwegian Mapping Authorities ("Kartverket"), and are based mostly on free available sources, such as the website "Norge i Bilder" which supplies aerial photos of Norway. High resolution data are available through a deal between NTNU and The Norwegian Mapping Authorities and have been used to ensure the best possible geo-referencing of old maps. Even with this geo-referencing old paper maps bring an extra inaccuracy, especially if the map is split into several parts (as needed for the Emblin map).

The reported accuracy of a handheld GPS is >3m depending of the number and geometry of connected satellites (Source: U.S. Geological Survey). In the field we experienced higher inaccuracy when close to mountains or had bad weather, due to losing contact with some of the available satellites. Aerial photos from "Norge I Bilder" were used to map the extent of the glacier. The latest update of aerial photos for the Reinfjord area was in 2008.

3.7.2 Sample preparation

The first step after field work was to select samples for geochemical analyses, based on their relevance for the thesis, the alteration of the samples (which often could only be seen after cutting) and how representative they were for the rock type. When the selected samples were crushed, all equipment used was vacuumed, washed with alcohol and dried with compressed air between each crushing to prevent contamination. When using the disk mill, the equipment was first washed with water, then washed with alcohol and dried.

Tungsten Carbide was used in the jaw crusher. This is because the samples contain almost no tungsten. Tungsten contamination will not affect the geochemical interpretation. In the disk mill, agate was preferred over steel, since steel might contaminate the sample.

The drill core samples (one quarter of the drill core) were collected in Løkken (National drill core storage) and sent directly to ALS, where the samples then were crushed and analysed in 5 meter sections.

3.7.3 Geochemical analysis

EPMA

The EPMA is thought of as an accurate method giving reliable data. The 797 analysis in this thesis range between a total 97-103%, this gives a small extra inaccuracy to the measurements. On the pyroxene standard the measurements were run with a defocused 2µm beam width, this was not enough to include much of the exsolutions. This was because of a misunderstanding at the lab, the intended beam width was a defocus at 20µm. The 20 µm would minimize the loss of Na and Mg and give a less elevated value on Ca, due to the analyses would have included the Opx exsolutions in the Cpx measurements. However the 2 µm defocused beam width is more precise but less accurate.

Scanning Electron Microscope

Some elements have overlapping photon peak intensity in the SEM spectra. This has to be taken into consideration when preforming EDS analysis. This overlapping problem is countered with an evaluation of all EDS maps and spot analysis. SEM was performed in an early stage, and before preforming EPMA, so any wrong classifications are corrected in any later stage.

X-ray Diffraction

The XRD analysis is based on random distribution of crystals of an equal size. Too much pressing when crushing the sample into powder may cause preferred orientation of the crystals, thereby giving inaccurate results. The four samples analysed were only crushed using a disk mill for four minutes, so this should not be a source for error. Another source of error using XRD, is overlapping diffraction peaks, which makes the classification of minerals more difficult. This should not be a major problem for the samples analysed, since the minerals present were already were classified using optical microscopy and SEM. XRD analysis is only a semi-quantitative method, and hence the results are rounded to the nearest percentage and for results less than 1% should be reported as such, due to the inaccuracy.

3.Methods

4 Result

4.1 Field observations

The following rock descriptions will focus on the ultramafic series, but will also include some field observations from the gneiss and the gabbro-norite.

4.1.1 Garnet Gneiss

Gneiss is only found on the western side of the intrusion. It consists of quartz, plagioclase, garnet and biotite, with minor amounts of rutile, ilmenite and magnetite. It is strongly foliated, especially close to the UM contacts (Figure 4.1a). Isdalen is where the contact with the UM can be best studied due to the sub vertical contact. Close to the LLS the gneiss is mostly overgrown and covered by scree. In Isdalen, high temperature deformation and partial melting have occurred, Emblin (1985) argue that the gneiss have experienced granulite facies metamorphism based on the the degree of partial melting. This is also observed south of Storvatnet, where stoping is observed in an area north of an east-west striking fault. The gneiss is stoped by a pegmatitic granite, indicating a high degree of partial melting (Figure 4.12).

Figure 4.1: a) Foliated gneiss with bands of plagioclase, biotite and garnet-rich plagioclase. b) Clear red to pink almandine garnet.

4.1.2 Langstrand Gabbronorite

The Langstrand gabbro have not been studied in detail by this or previous authors, and is the focus of this thesis. The Langstrand gabbro cumulates have a tholeiitic affinity with an upward enrichment in Fe (Bennett, 1973, Robins and Gardner, 1975). The Langstrand gabbro is the main host rock for the Reinfjord intrusion. Emblin (1985) observed that the cumulate stratigraphy of the gabbro changed in modal mineralogy. The lower units contain Ol-Pl-Cpx and Pl-Cpx cumulates that changed to Pl-Cpx-Opx and Pl-Opx cumulates in the upper levels of the gabbro.

In close contact with the Reinfjord intrusion, it is recrystallized into a leucogabbro with plagioclase, clinopyroxene, orthopyroxene and olivine as main phases (figure 4.2). Accessory phases include biotite, amphibole, ilmenite, magnetite and apatite. The overall cryptic variations are $Fo_{74\text{-}76}$, $An_{48,1\text{-}70,3}$ and $Di_{70,7\text{-}80,4}$ (Emblin, 1985)

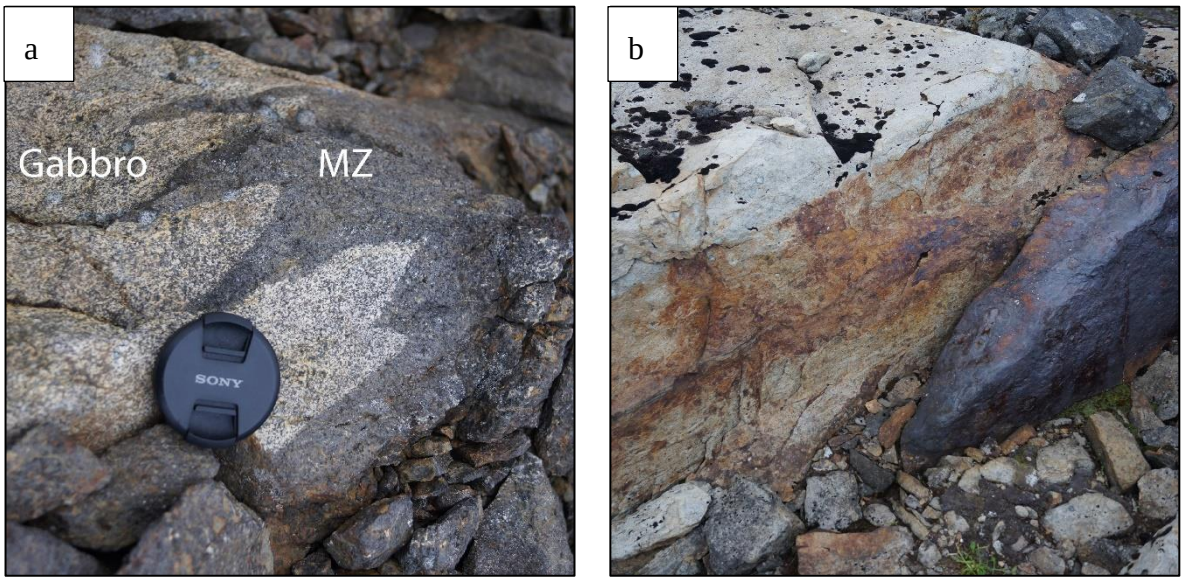

Figure 4.2: a) Gabbro intruded by CS melt in the NE part of the intrusion under the formation of a Marginal Zone (MZ). b) Gabbro with barren contact deposit east of the plateau. Seen towards NE.

4.1.3 Lower Layered Series (LLS)

The LLS is located in the western parts of the intrusion. It is long and narrow in geometry and is situated between the gabbro in east and the gneiss in west. The near vertical cliff limits the accessibility of the LLS to the lowest 100m (Figure 4.3a and c). As first reported by Hansen (1971) the LLS hosts sulphide contact deposits towards the gneiss. This deposit contain chalcopyrite, pyrrhotite and pentlandite. The LLS is modally layered, and consists of dunites

with large orthopyroxene oikocrysts, wehrlites and pyroxenites (Figure 4.3b). In the upper contact, towards the gabbro a small part of the LLS have intruded or been faulted into the gabbro. In the southern parts of the LLS it hosts a lot of gabbro xenoliths.

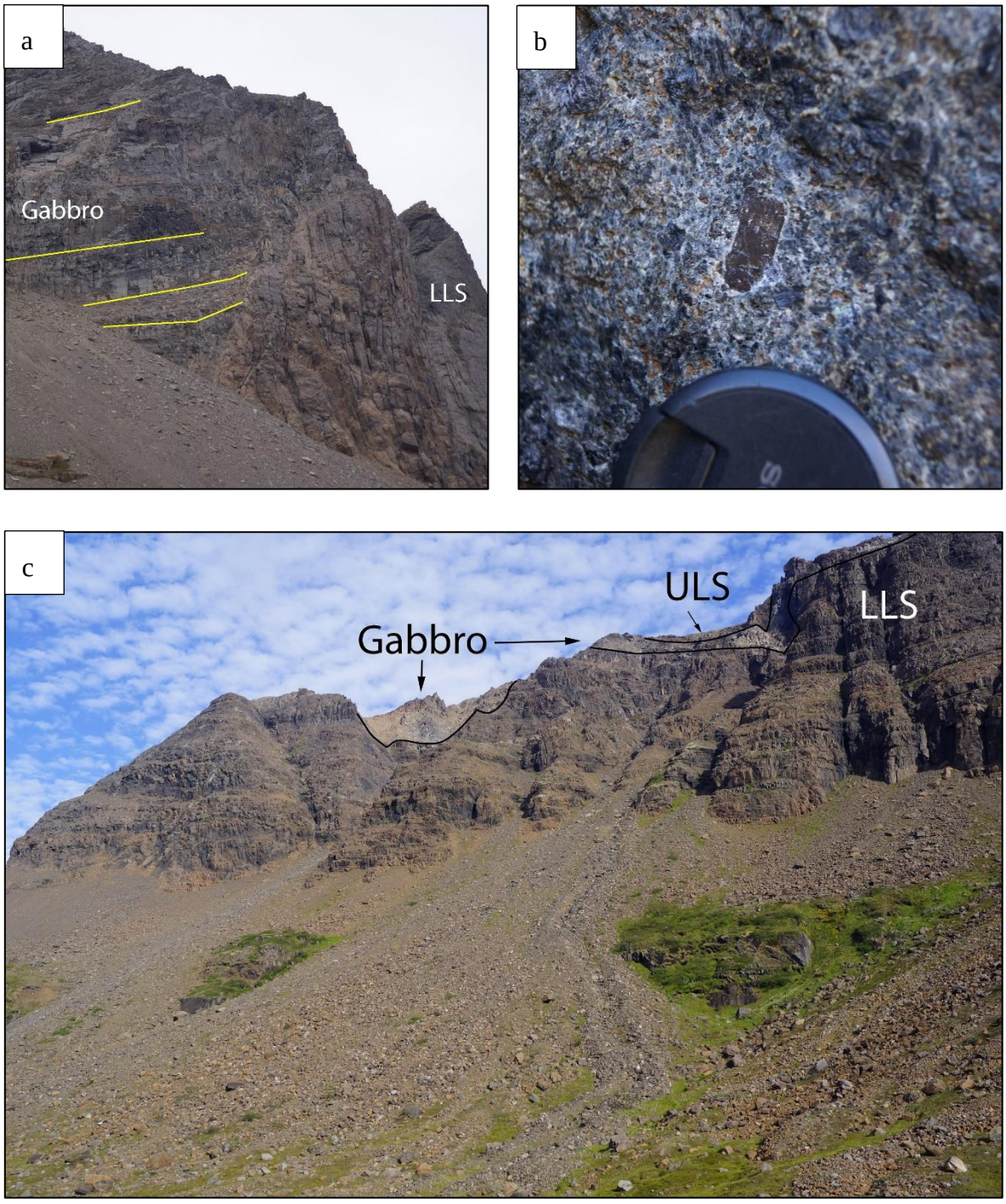

Figure 4.3: a) The north facing contact of the LLS in the northen part of the outcro, a fracture zone seen at the contact. b) Pyroxene oikocryst with poikilitic wherlite c) The west facing cliff of the LLS with the MZ covered by scree. With gabbro separating the LLS and the ULS high up.

4.1.4 Upper Layered Series (ULS)

The ULS is mainly located on the plateau, where it lies on both sides of the CS (Figure 4.4). The ULS is also found in the NW area in two outcrops, these are almost inaccessible by foot due to their location in the rough landscape, and therefore have not been investigated.

The ULS is modally layered, it appears as mostly olivine and pyroxen dominated cumulates of dunite, wehrlite and olivine clinopyroxenite. On the east side of the plateau several patches of pure pyroxene pegmatite can be found, where crystals up to 20 cm long and 10 cm wide were observed. The sub horizontal layering dip 10-25° towards NE. Sub vertical veins often cut the layering, and these range from dunitic to gabbroic in composition (Figure 4.5c). Figure 4.7a (and Figure 4.5a) shows that the layering is distorted in an ductile way, indicating that the magma chamber may have been exposed to stress while still hot. Multiple recharge events of new magma into the crystal-melt mush (referred to as crystal mush and mush). This forms different mineralogy due to the density contrasts and is forming the structures seen Figure 4.5d and Figure 4.6a,b and c.

In the ULS, west of the CS, numerous gabbro xenoliths are observed (Figure 4.7b). This is in the same area that Emblin (1985) observed plagioclase in the ULS. He suggested that these features indicate that this area is close to a floor zone of the intrusion close to a contact with the gabbro. This is because the majority of the intrusion do not contain any plagioclase, except the Marginal Zones close to the gabbro or gneiss.

Figure 4.4: Top) photo show the UM series on plateau from the ridge N of the fault valley, seen towards south. Bottom) Photo taken from the mountain top seen on the right side of figure a, showing the plateau seen towards ENE.

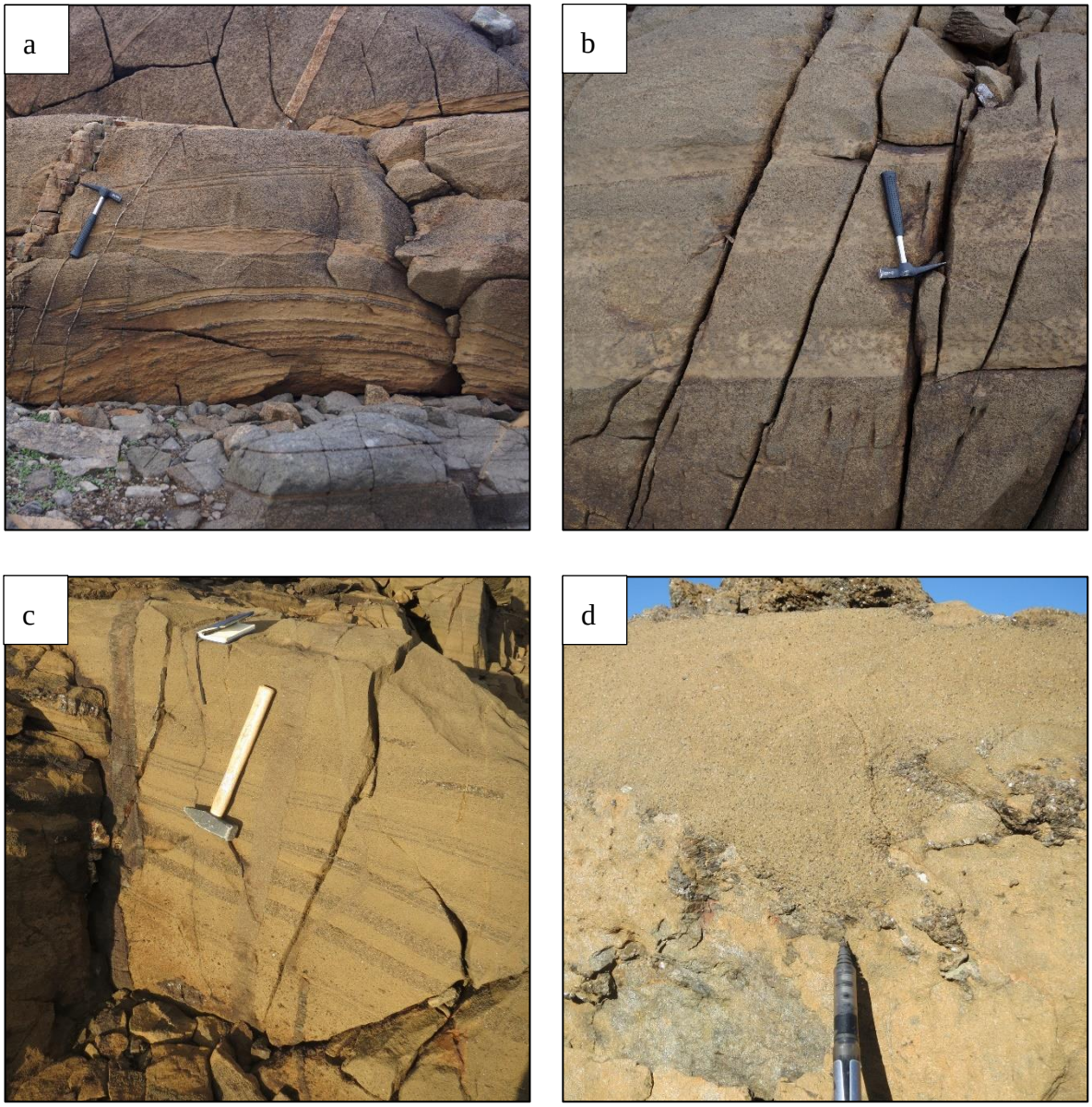

Figure 4.5: a) Distorted layering. b) Rhythmic repeated layering of olivine with gradually increasing amount of poikilitic pyroxene and pyroxene rich wehrlite, above a larger zone of pyroxene rich wehrlite c) Sub-horizontal layering marked by diopside rich pyroxene layers in dunitic cumulates, cut by sub vertical UM veins. d) Load structure with wehrlite sinking into dunite with coarse-grained pyroxene in the contact.

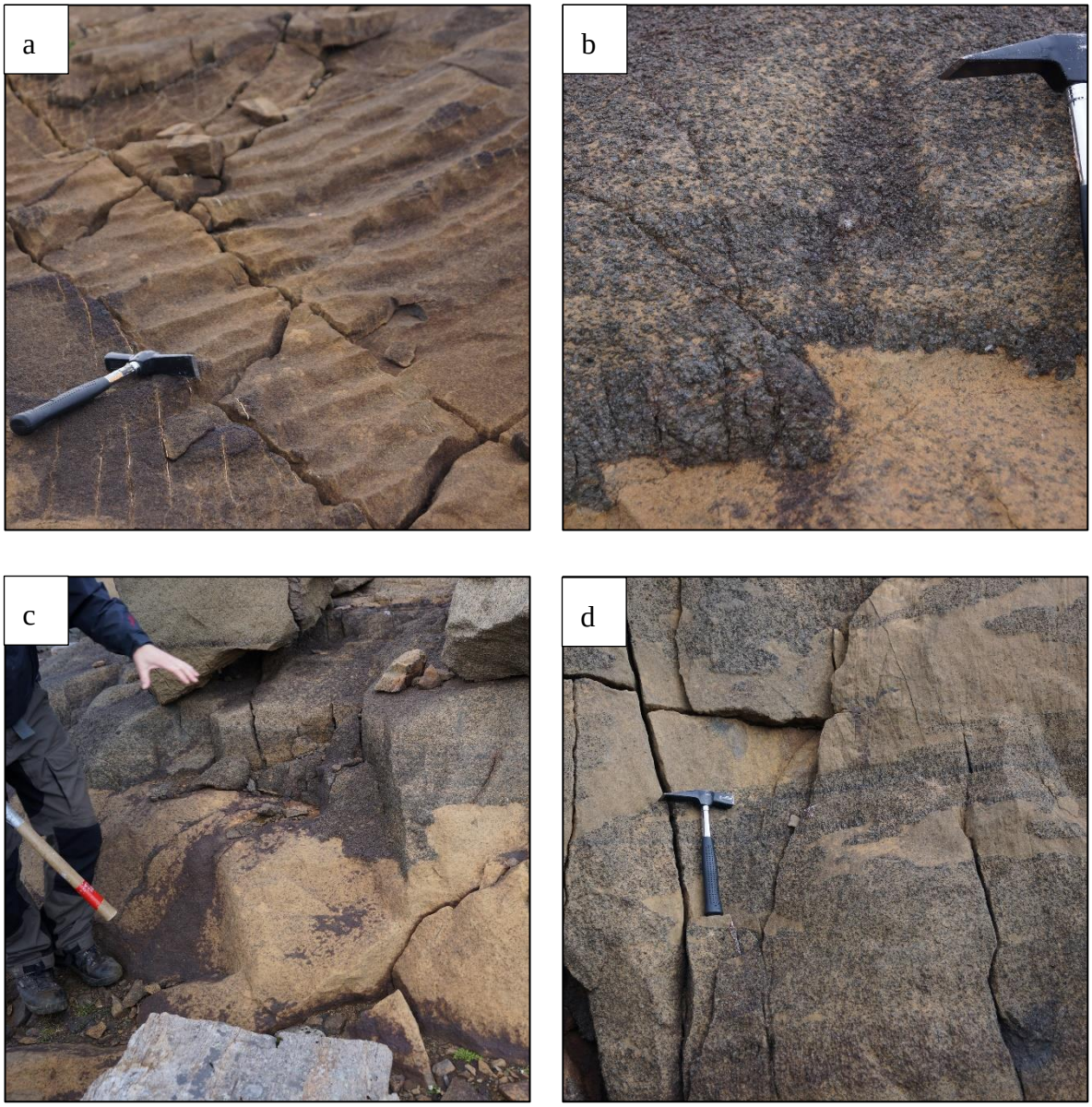

Figure 4.6: a) Slumping structure in 3D dipping towards NE. b) Slumping in 2D, pyroxene rich wehrlite slumping over less dense pyroxene poor wehrlite. c) Load structure with pyroxene rich wehrlite into dunite. d) Irregular dunite replacing wehrlite.

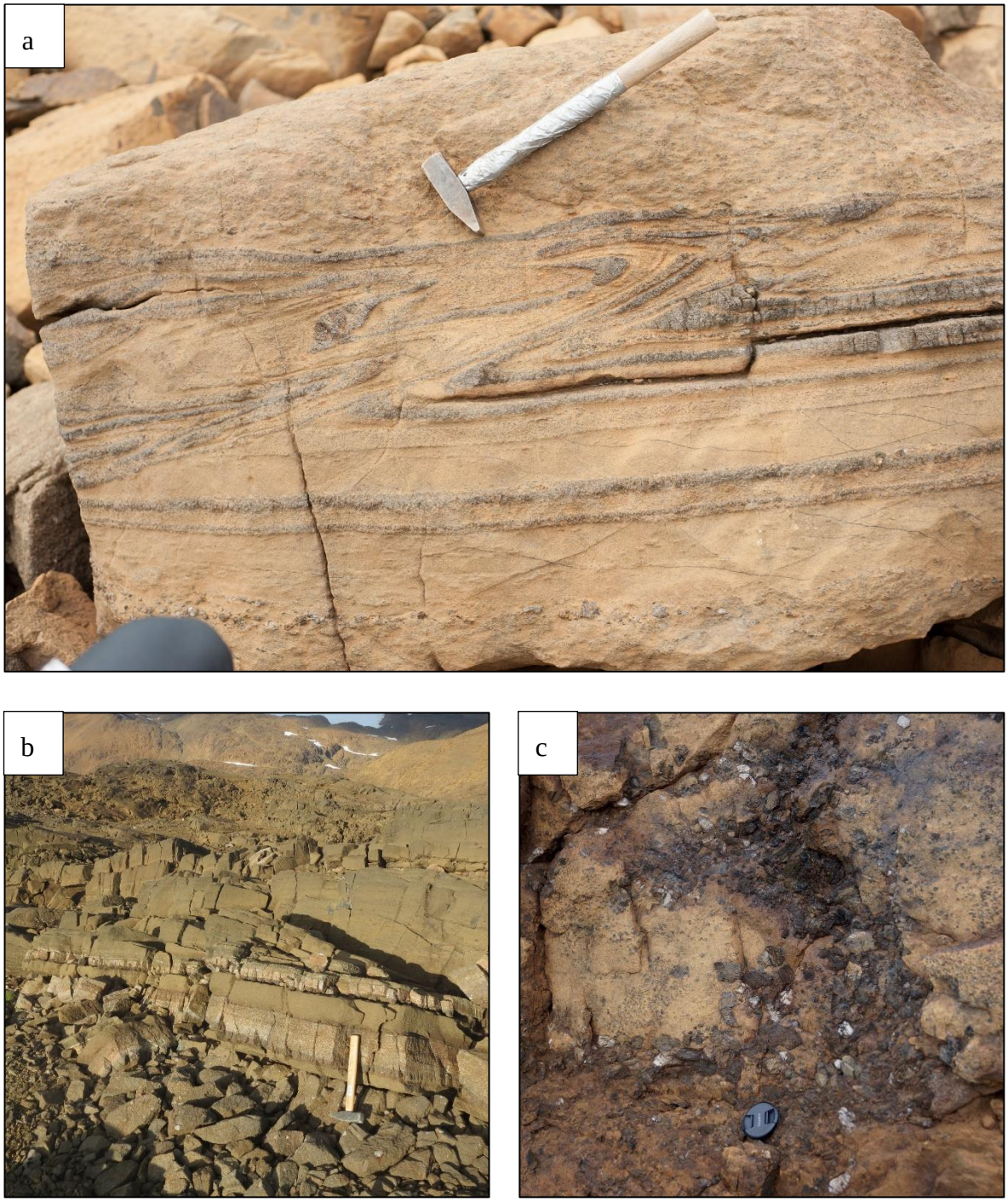

Figure 4.7: a) Ductile foliated layering marked by pyroxene and olivine rich layers (Photo by Lars Anker-Rasch) b) Two sheetlike gabbro xenoliths in the western part of ULS, rims of pyroxene surrounds the xenoliths with plagioclase appearing in the wehrlite close to the contact. c) Recharge and formation of pyroxene pegmatite within the wehrlite.

4.1.5 Central Series (CS)

The CS is the youngest of the UM series. It is located in the central parts of the intrusion. It thins towards the south away from the conduit system (from1 km to 500 meter wide) with the ULS on either side, separating it from the gabbro. North of the lake district it widens to approximately 2 km. In the northernmost part of the intrusion, the CS widens drastically to a width of 3,5 km.

The CS is mainly composed of dunite and minor wehrlite, consisting of cumulus olivine with or without poikilitic clinopyroxene (Figure 4.8c) and secondary serpentine. The CS is cryptically layered. The low amount of accessory phases make changes in the CS difficult to spot in field. Cryptic variations are presented in chapter 4.4.

Figure 4.8a and Figure 4.19 show the intrusive relationship between the CS and the ULS, and gives clear indications that the CS formed last and intruded into the ULS. The replacive dunite (CS) dykes and veins found in ULS can be traced back to the CS, indicating that they originated from the parental melts forming the CS. Around these replacive dunite dykes the ULS is often influenced in a ductile manner, indicating that it was unconsolidated during infiltration of CS-forming melts. The intrusive behaviour of the CS is also observed towards the gabbro. The CS intrudes into the gabbro as small sills or dykes (Figure 4.21), one such sill is presented in chapter 4.2.2.

The CS is cut by scattered dykes all over the intrusion. On the hill north of the lake district, the density of dykes is particularly high and is referred to as a dyke swarm (Figure 4.8b). The dyke swarm covers an area of approximately 300x300m.

In south, the CS is cut by a NE-SW striking normal fault, dipping east with a conspicuous throw (B.E. Sørensen, personal communication, 13 January 2016). Not much data exists on the fault, and it is currently studied in by Sørensen and co-workers.

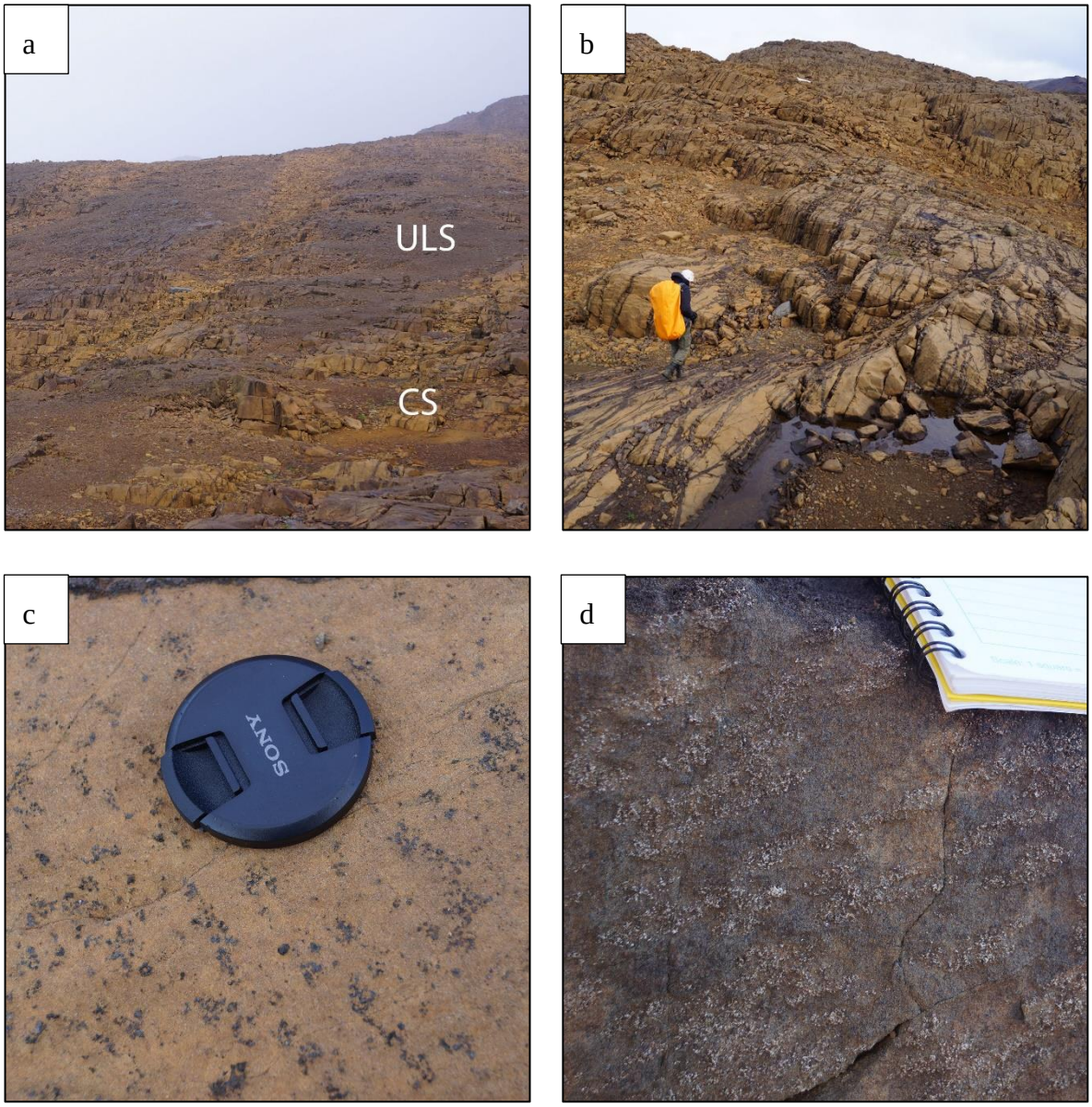

Figure 4.8:a) Dykes of dunite (5-10 m) intruding and replacing the ULS in west, crosscutting the ULS layering. b) Dyke complex on the ridge north of lake district. c) Poikilitic pyroxene in the CS dunite. d) Poikilitic plagioclase in the CS dunite 50m from the gabbro contact close to the ULS rafts and the finger.

Thin section microscopy shows two types of olivine, first described in Grant et al. (2016). Type 1 (Ol_1) is large anhedral to subhedral irregular shaped crystals, with internal deformation, type 2 (Ol_2) is smaller euhedral to subhedral grains with little or no internal deformation (Figure 4.10).

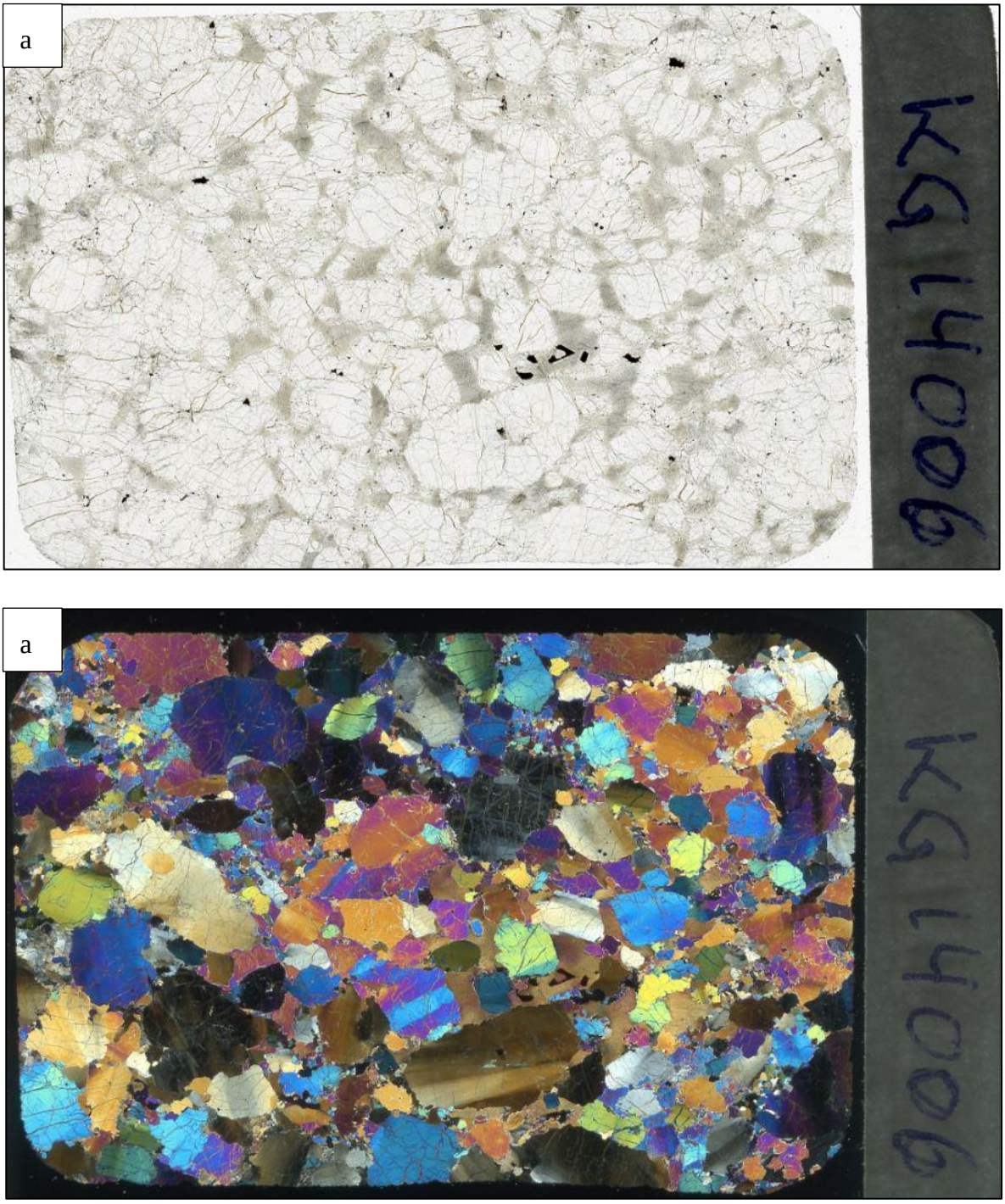

Figure 4.9: Scanned thin section in plane and cross polarized light (Xpl). This is the sample KG14006, it shows Central Series dunite with poikilitic pyroxene.

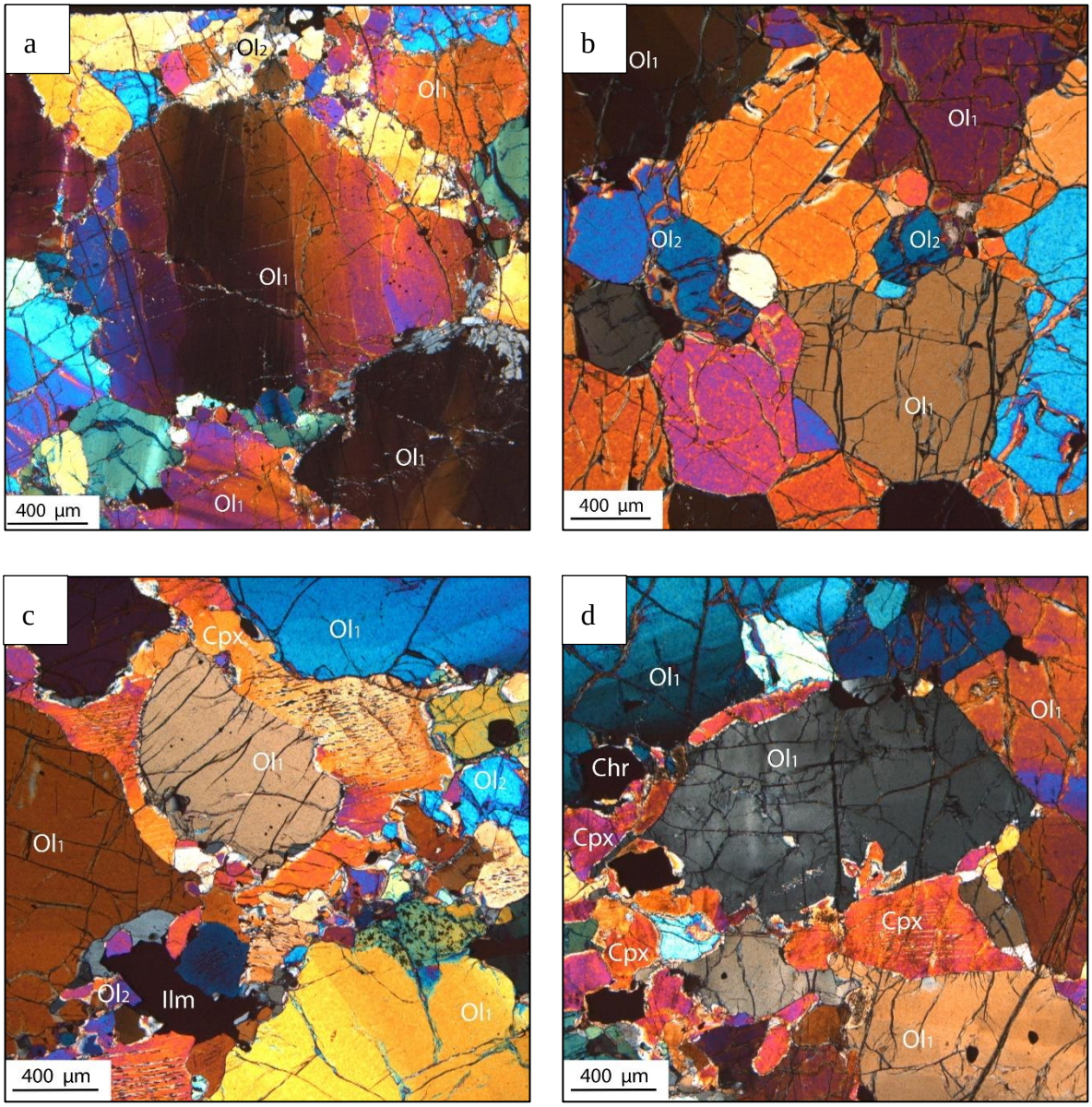

Figure 4.10: a) CS dunites show two types of olivine. From sample KG14005, 547 m.a.s.l. b) Sample 4-19900 from the RF-4 drill core (416 m.a.s.l.) showing the less deformed subhedral to euhedral olivine type 2. c) Sample KG14006 (577 m.a.s.l.) shows the poikilitic clinopyroxene with reaction rim between the Ol and the Cpx. together with the Cpx, Ol_2 and Ilm exist interstitially between the larger Ol1 grains. Same sample as Figure 4.9. d) Sample KG14007 (606 m.a.s.l.) show poikilitic Cpx and Chromium spinel interstitial between the Ol_1 crystals.

4.1.6 Marginal Zones (MZ)

Marginal Zones are several different hybrid zones, occurring in the contact between country rocks and the Reinfjord Complex. Previous work by Bennett (1971), Emblin (1985), Øen (2013) and Anker-Rasch (2013) all mapped and described the MZ as separate zones, depending on their location around the complex and rock types. As stated in the introduction, all variations in the MZ are now combined into one zone. This has been done to show that the contact zones share many common features unrelated to their position in the complex. Previous mapping of the MZ was incorrect in certain areas, such as the NE-part of the intrusion (see chapter 4.2.3).

The MZ formed where UM melts (forming LLS, ULS and CS respectively) intrude and assimilate the country rocks (gneiss and gabbro) and form pyroxenites (websterites and olivine websterites), plagioclase bearing UM to olivine rich gabbronorite, recrystallized gneisses and mafic pegmatites of pyroxene in plagioclase matrix (Emblin, 1985, Bennett et al., 1986, Grant et al., 2016).

In the south on the eastern side of the intrusion, the MZ is dominated by websterites and pegmatitic pyroxene in a plagioclase matrix where the ULS is in contact with the gabbro. Further north, where the CS melt have intruded into the gabbro, the MZ changes into plagioclase bearing UM rocks and olivine rich gabbronorite. The latter is intruded by alkali veins, forming patches of plagioclase in the CS (Figure 4.11b).

On the west side of the intrusion, where the gneiss is in contact with the LLS and the ULS Marginal Zones. The gneiss is increasingly metamorphosed towards the contact, and is increasingly partial melted towards the contact (Figure 4.12). The MZ is dominated by a gradual transition from recrystallized granite to gabbro to plagioclase bearing UM. Emblin (1985) observed a pyroxenite as the dominating phase of the MZ in this area, he named it two pyroxene granulites. The pyroxenes consists of large grained pyroxenes in a matrix of plagioclase (Figure 4.11c and d).

Figure 4.11: a) MZ found in Isdalen in the contact between the gneiss and the ULS. b) patch of plagioclase and poikilitic plagioclase in the ULS on the east side of the plateau. c) irregular contact between the MZ (dark) and the gabbro (white). Note the large pyroxene porphyries in the gabbro. d) 2-3 cm large pyroxene porphyry with pyroxene rim in the gabbro.

Figure 4.12: Pegmatitic granite stoping gneiss south of Storvatnet. The pegmatite arguably formed from partial melting of the gneiss.

4.1.7 A local zone in north eastern part of the intrusion

In the North eastern part of the intrusion a roof zone can be seen (figure 4.15). It is located at the mountain top that is approximately on 900 m.a.s.l (See map Figure 4.22). The sub horizontal CS-Gabbro contact can be followed for over 1200 m, where it follows the topographic contour with a gentle dip towards the NE (5-15°).

The area was observed by helicopter, and therefore only documented though photographs and long distance observations (figure 4.13). However, the evidence for this zone is clear, with two separate roofs (separated by a small depression in relief) connected to the main host in the east cap the CS. The MZ is not observed on the photos or in field, this might be due to distance of the observations, and is therefore not mapped. However, MZ is believed to exist. Based on the contact zones around the intrusion.

Underneath this zone, the CS hosts several large sheet-like gabbro xenoliths (over 100 m long and 1-5 m thick) and several smaller xenoliths (10-20 m long and 0,5-3m thick) (Figure 4.14

and Figure 4.15). The sheet-like xenoliths have the same orientation as the CS layering. Indicating that they were stoped from the gabbro in the roof zone, where CS melts have intruded fractures and weakness zones following the layering in the gabbro. Figure 4.15b show such a feature, where a large slab of gabbro is seen separating by the intruding CS melt. The xenoliths are located from the roof contact down to 300 meters beneath the roof zone. The smaller xenoliths is more irregular in shape and might either be from the wall which is close by or have been entrained into the roof zone.

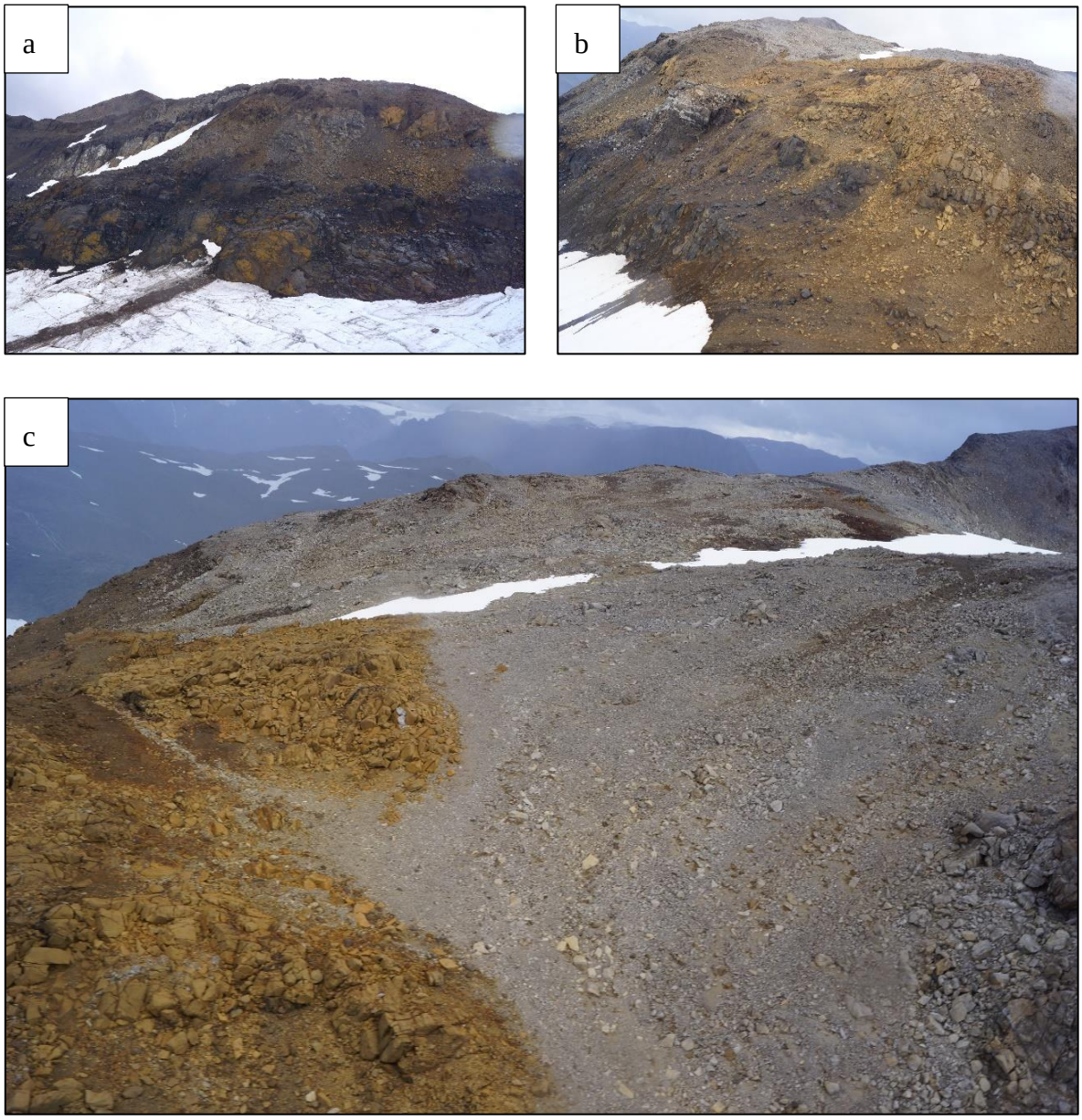

Figure 4.13: a) The light and the wet surface of the rock make the classification of the series difficult, but in the top left corner of the photo gabbro is seen. Photo seen towards south b) Ultramafic series with gabbro laying on top in the top of the picture, seen towards southeast c) Contact seen towards east, where a cover of gabbro is lying on top of the UM series. Note the gabbro in the distance to the right of this photo.

Figure 4.14: Gabbro xenoliths (greyish white) bellow the roof zone, photo taken by the lake south of the cliff phase. It is the same area seen on the next two figures at greater distances. (Photo: Lars Anker-Rasch)

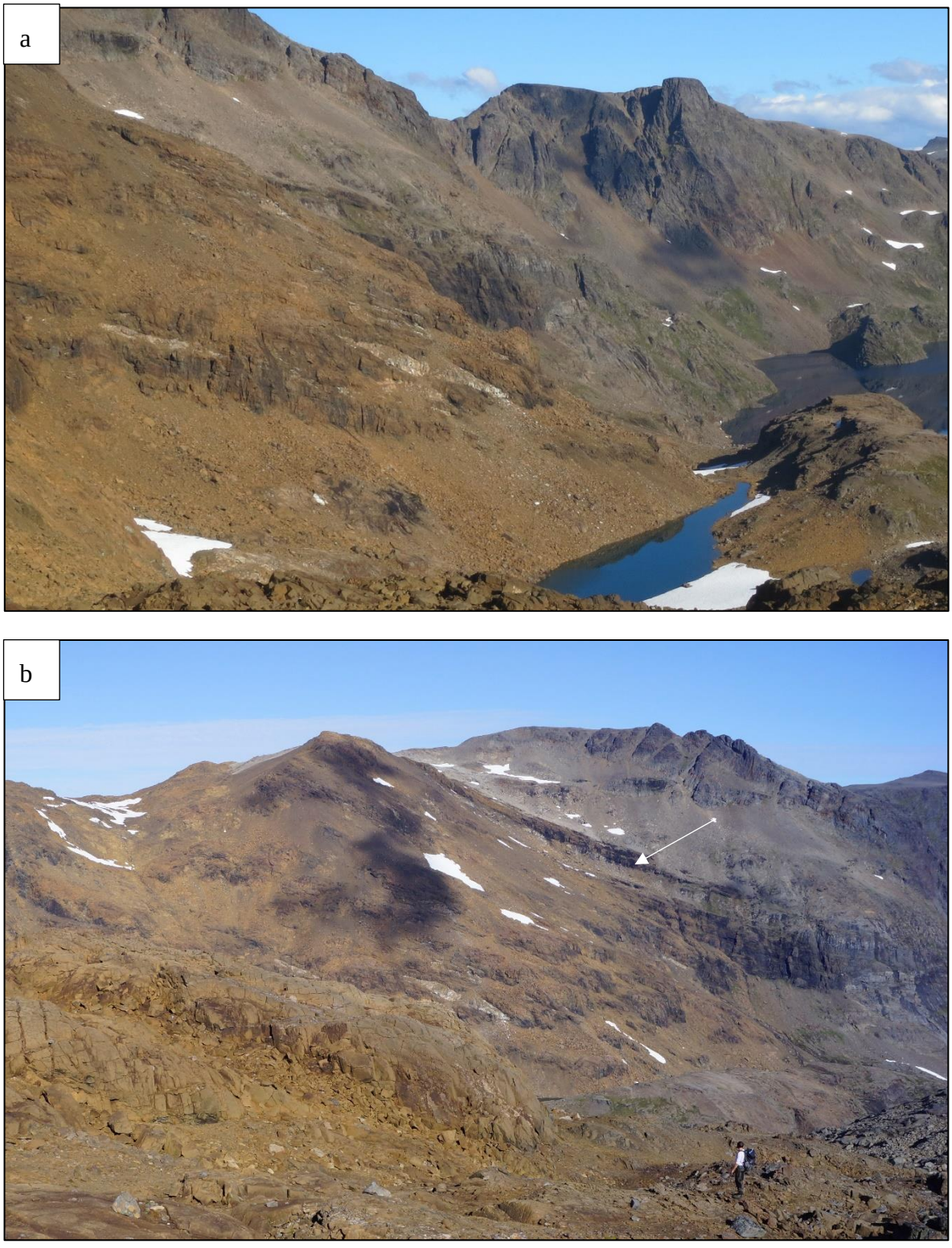

Figure 4.15:a) Xenoliths beneath the roof zone follow the layering of the CS. Seen towards E. b) Roof, xenoliths and intruding CS into the gabbro is seen on this photo. Seen towards NE. Arrow mark a long gabbro slab.

4.2 A new map

As mentioned previously, the area was first mapped by Bennett (1971), but the area was reinterpreted and re-mapped by Emblin (1985) (Figure 4.18), further reinterpretations were presented in the work by Anker-Rasch (2013) and Øen (2013). After the first two days in the field it was clear that the existing needed some revision. Especially the eastern and north eastern contacts needed re-mapping. In the map created by Anker-Rasch (2013) and Øen (2013), which was based on the work by Emblin (1985), some major errors was found in the south and north eastern area. An example of this is found on the MZ in the south west where the contact was approximately 500m off, it is believed that this error occurred during geo-referencing (Øen 2015, personal communication, 14 September).

The new map is presented in this thesis is Figure 4.17. Main changes from previous work on Reinfjord is the revision of the Marginal Zones and NE part of the intrusion, where the area was previous mapped as a large marginal zone. Other changes include the removal of faults, changing of magmatic contacts to be more irregular, a reinterpretation and an update of boundary location by GPS mapping. A preliminary version of this map was published in Grant et al. (2016) and in the master thesis by Nikolaisen (2016).

4.2.1 Western area

In the valley of Isdalen the garnet gneiss is strongly metamorphosed and foliated (Figure 4.1). The garnet gneiss show signs of partial melting, and recrystallization. Ultramafic veins are found in the gneiss some hundred meters from the contact. Previously mapped LLS in Isdalen is removed, as fieldwork proved it not to exist further north than the valley south of Storvatnet. The MZ in Isdalen is heterogenic with altered gabbro and pyroxenites that is formed in the contact with UM and gneiss,

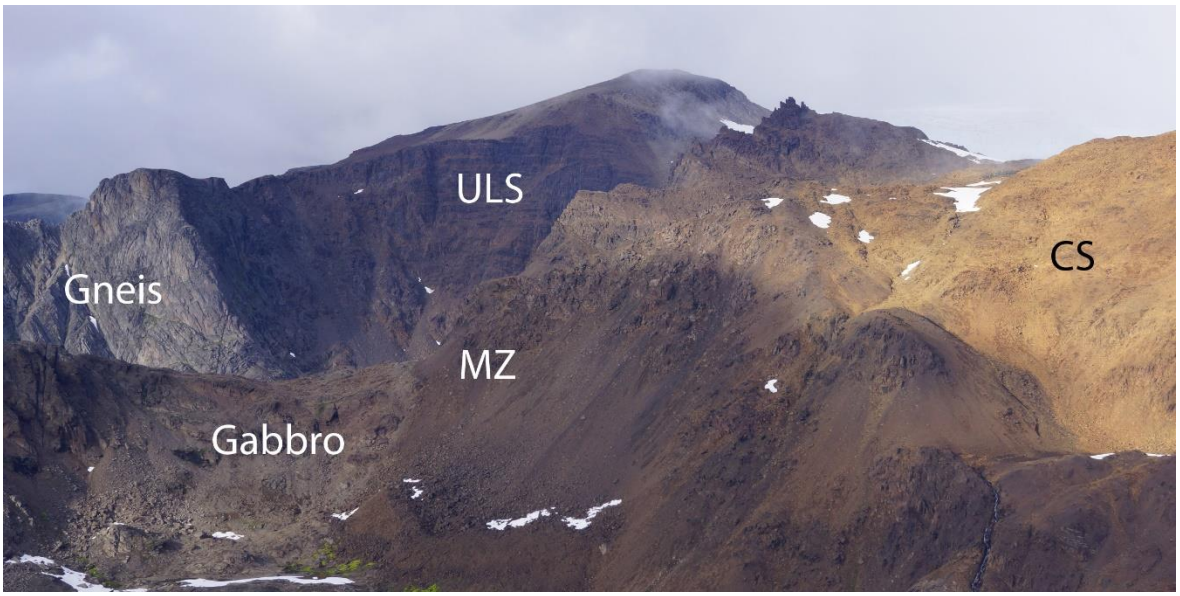

Figure 4.16: The western part of the intrusion above Storvatnet and the Northern cliff phase in Isdalen.

By Storvatnet, only minor reinterpretations were conducted. On the eastern side of Storvatnet repetition of the ULS and gabbro in the contact have been explained by faulting by previous authors. Our interpretation is that this is caused by an irregular contact and intrusive UM melt into the gabbro, as no faulting was observed in this area.

South of Storvatnet in the ULS, a zone of gabbro xenoliths are mapped, this is in the same area that Emblin (1985) (figure 5.5) observed a zone of plagioclase in the otherwise plagioclase free ULS. The Lower Layered Series was only revised in the lower areas due to the vertical cliff face and lack of time to investigate the mountain above the LLS. As seen in Figure 4.3c most of the contacts towards the gneiss and lower part of the LLS are covered by scree material and are therefore are difficult to map.

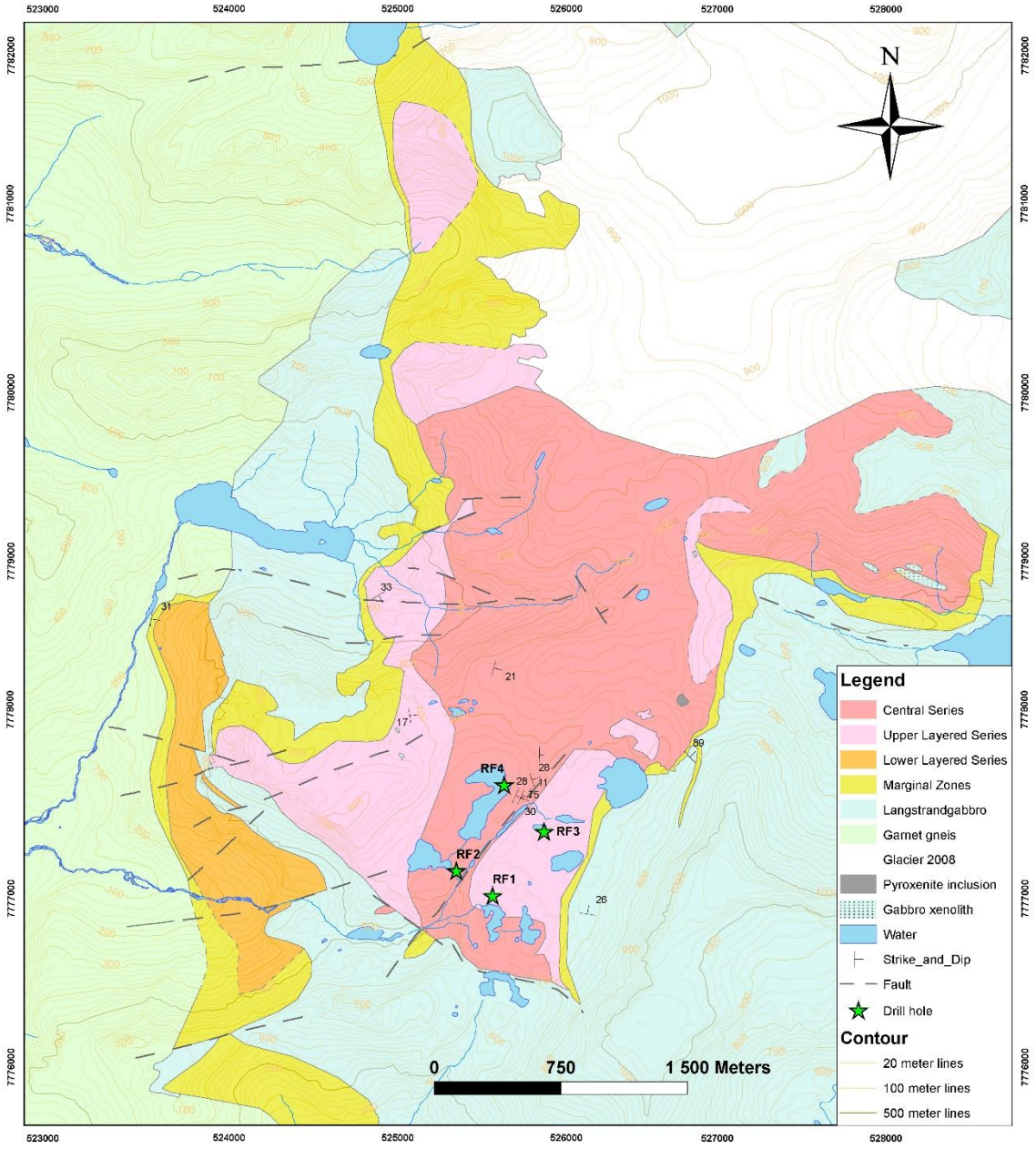

Figure 4.17: The new map.

Faults following certain contacts are shifted or exaggerated to be visible on the map. All these changes are thorough marked and presented in the next subchapters. Some faults have a slip that may be seen in the cliff faces or on flat surfaces but are too small to be mapped out.

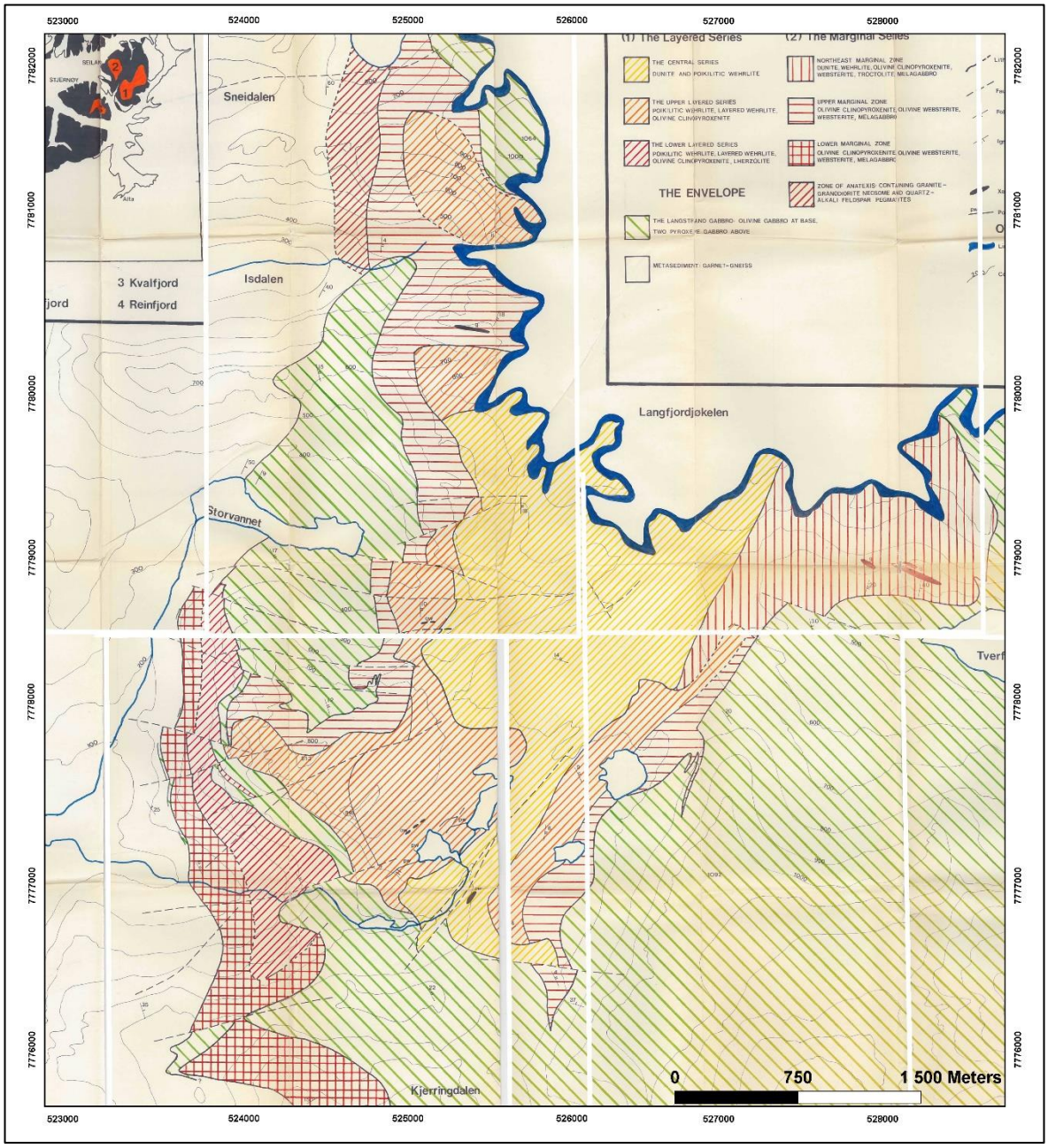

Figure 4.18: The map by Emblin (1985).

4.2.2 Central parts of the intrusion and the lake district

The central area around the Lake District was the main focus for Anker-Rasch (2013) and Øen (2013) in their theses. This area was confirmed by our own observations and did not need much revision. Figure 4.20 shows the CS penetrating the gabbro as a small sill following the layering, this feature is referred to as the *finger* (for location see Figure 3.1). An attempt was made at remapping this feature, but the steep cliff and slippery surface made this unsafe, so the mapping is based on Emblin's work with revisions. West of the *Finger* the ULS is mapped as one coherent series in previous work. Field work proved that the ULS is cut by the CS which interfingers underneath and around the ULS. Creating two "rafts" of ULS which are only between 0,5-2m thick (Figure 4.19). The MZ was redrawn on the basis of the presence of plagioclase in the ultramafic rocks.

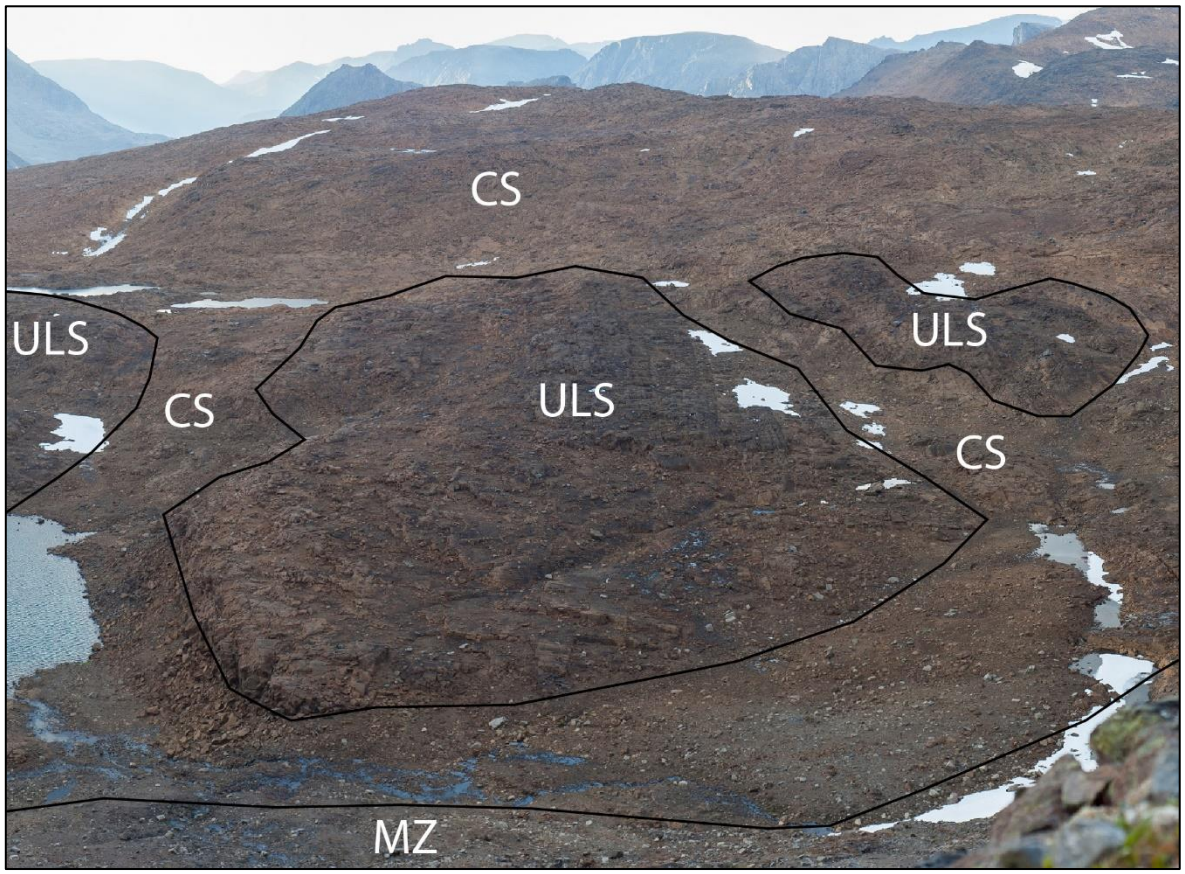

Figure 4.19: The separate ULS rafts cut by the later intruding CS. The CS seems to cut the ULS almost horizontal, and at the same elevation for the two rafts. Photo taken from the finger toward west.

Figure 4.20: Finger seen in the West-face of Langfjellet.

4.2.3 The northern area

Northwest of the *Finger*, on the same ridge a pyroxenite inclusion is found and mapped. Due to weathering no samples could be collected and therefore it is not studied. North of this pyroxene inclusion, the ULS reappears. This is where previous workers have mapped MZ (North Eastern Marginal Zone).This fieldwork proves that it does not exist. However the Marginal Zone changes in this area, it widens and become more pyroxene rich. Where the CS turns east, patches of bronzite pyroxenite, massive pegmatitic pyroxenite and plagioclase rich areas appear. West of the small lake in this area the MZ is difficult to map on the account of the topography. The boundary between the CS and the gabbro in NE is impossible to follow in the east because of a steep cliff face. This area is very complex and needs further investigation.

At the mountain peaks above this complex area, at approximately 900 m.a.s.l, the gabbro reappears as a thin cover. As discussed previously, this is believed to be a roof zone. A helicopter trip documenting the intrusion during the 2014 field season, revealed a gabbro zone lying on top of the UM in this part of the intrusion. In the south facing cliff underneath the roof zone, several gabbroic xenoliths are hosted within the CS (Figure 4.21). They are inaccessible

due to the location in the steep cliff, so they are mapped from distance, by calculating their approximate location.

Figure 4.21:The NE CS-Gabbro contact. Two gabbro xenoliths located in the CS cliff left of the shadow, the largest of these is the same one as in Figure 4.14. Picture taken towards N from 750m.

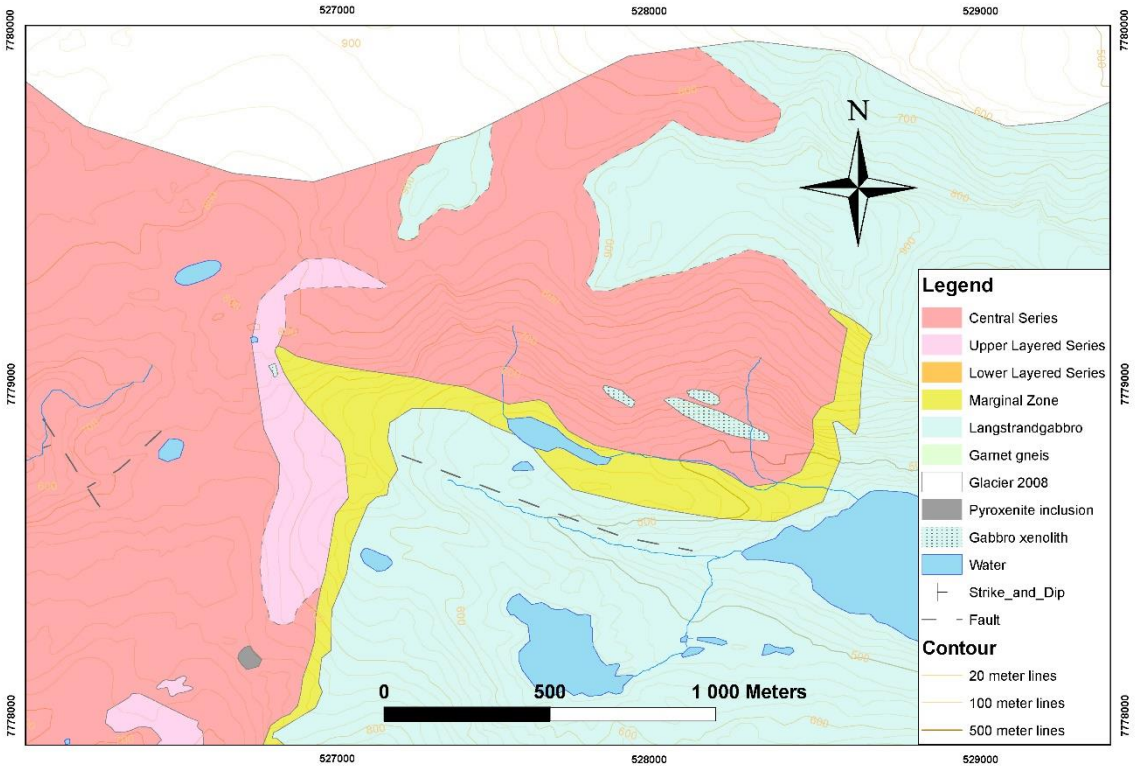

Figure 4.22: A zoomed in figure of the remapped NE part of the intrusion.

4.2.4 Southern parts of the intrusion

In the south and south east, minor revisions were conducted to the old maps (figure 4.25). The area south of Bonvikdalen in the south west, was not investigated and is based completely on the mapping by Emblin (1985). In the south east, field work proved that MZ is cut by the E-W striking fault in east (Figure 4.23 and Figure 4.24). This disagrees with previous work, as Emblin (1985) displaces the MZ and widens it while the fault goes straight up the mountain. Øen (2013) and Anker-Rasch (2013) also have the fault climbing straight up the mountain and show no displacement in the MZ south of the fault. Figure 4.23a) and b) contradicts this previous interpretation.

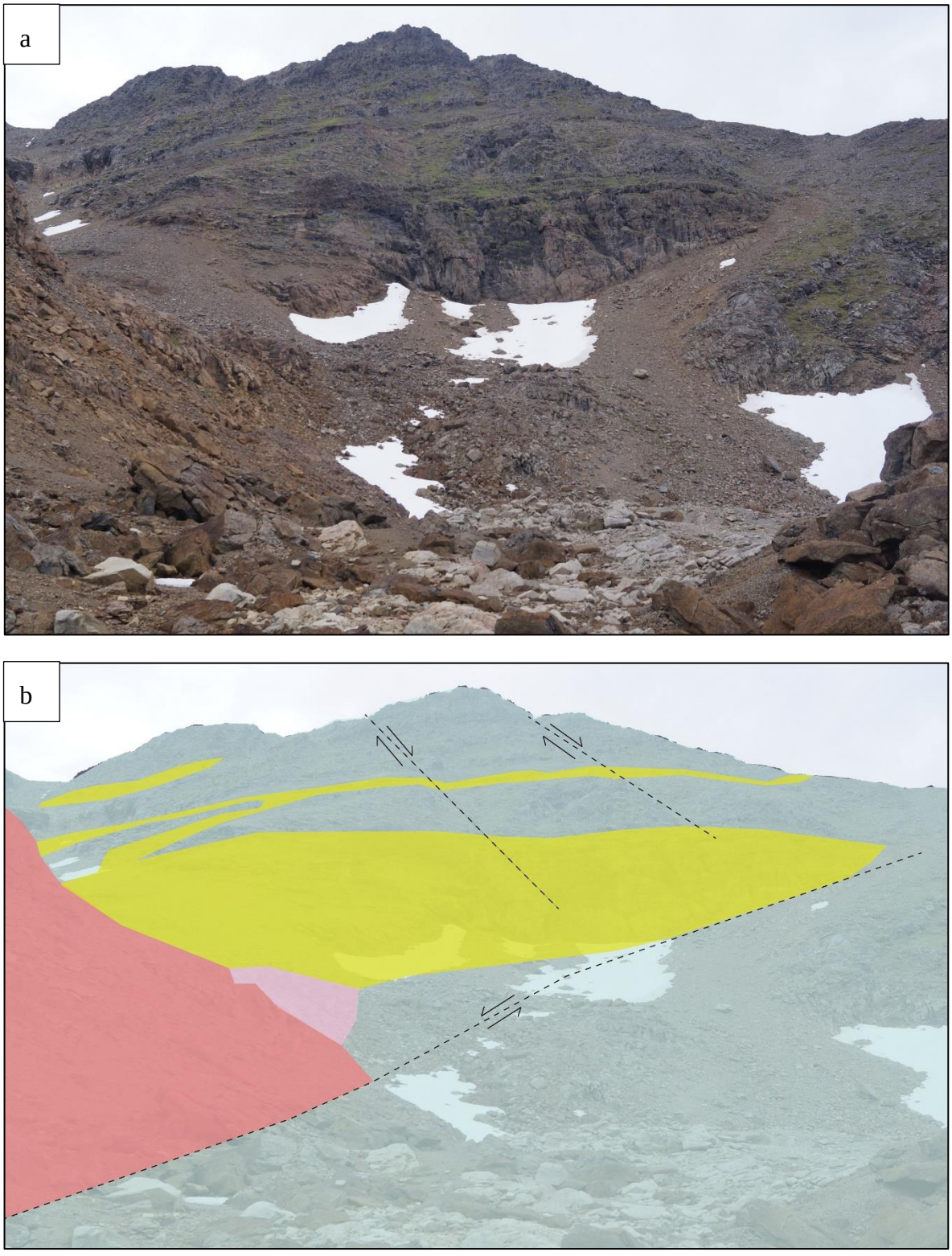

Figure 4.23: a) Photo is taken from fault showing the west facing mountain side where the MZ perforate into the gabbro with a thickness of 20+meters. b) Sketch of the photo, the major fault dips toward north while two minor fault dips south. Same legend as the map in Figure 4.17.

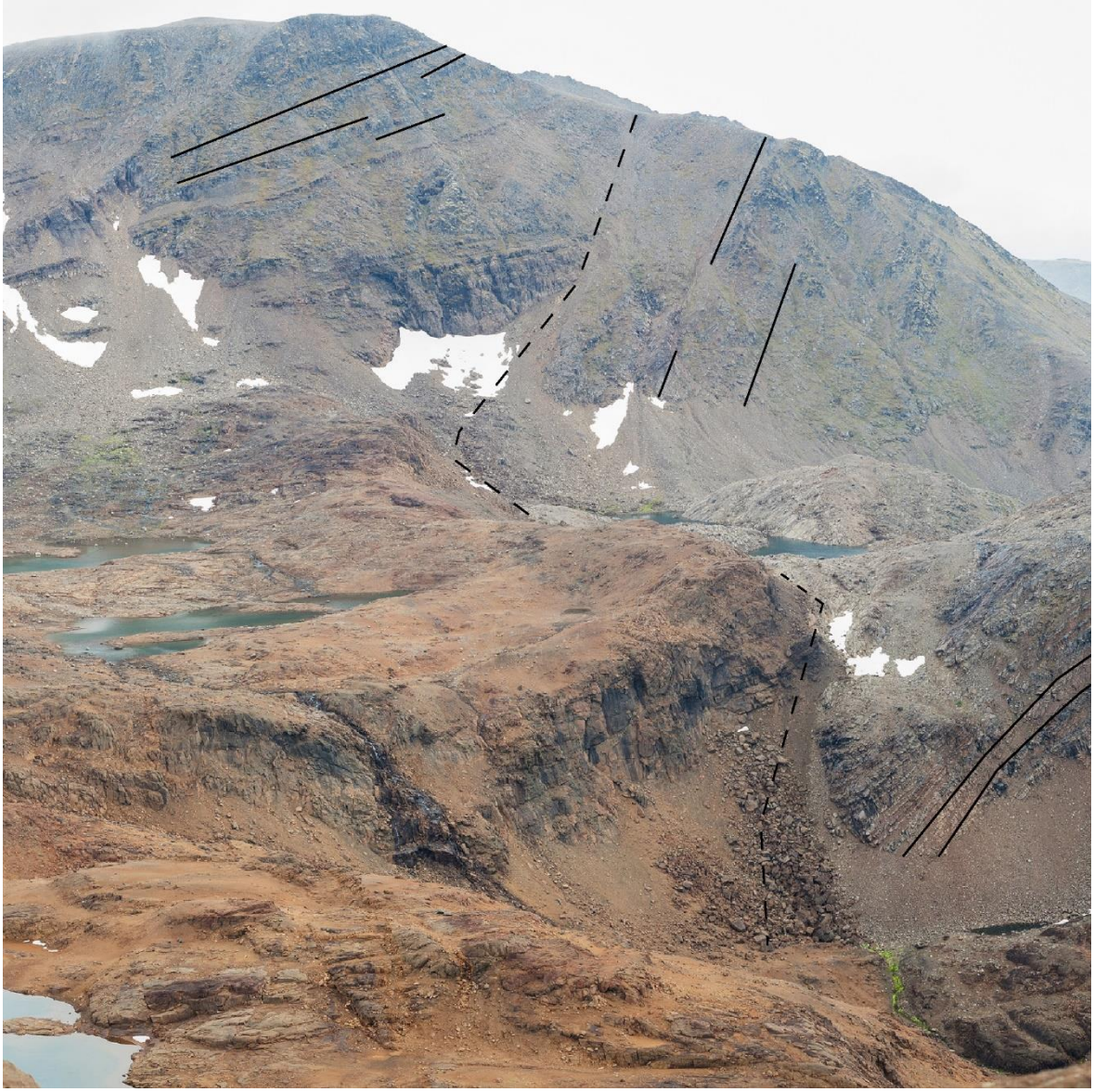

Figure 4.24: The south eastern part of the intrusion with the fault. The gabbro layering is marked to demonstrate the difference on each side of the fault, and the difference in the east compared to the western part. Down to the right the layering is dragged down into a curve indicating a normal fault. Seen towards ESE. (Photo Lars Anker-Rasch)

The north dipping fault is probably a normal fault, due to the angle that is 50-70° and the drag in the footwall gabbro marked in Figure 4.24. No field measurements were made to confirm this, due to lack of good surfaces. The closest cliff in Figure 4.24 show that the fault is covered in lose scree material.

Following the fault westwards, it is clear that this fault separates the ultramafic rocks from the gabbro and contrary to the rest of the intrusion, MZ is absent. There are two exceptions to this; that are the two small “tongues” of UM rock in this area. One located where the NW-SE faults

intersects are reinterpreted to MZ due to high plagioclase content (>10%), visible in hand samples. The one on the western side has not been investigated (Figure 4.26).

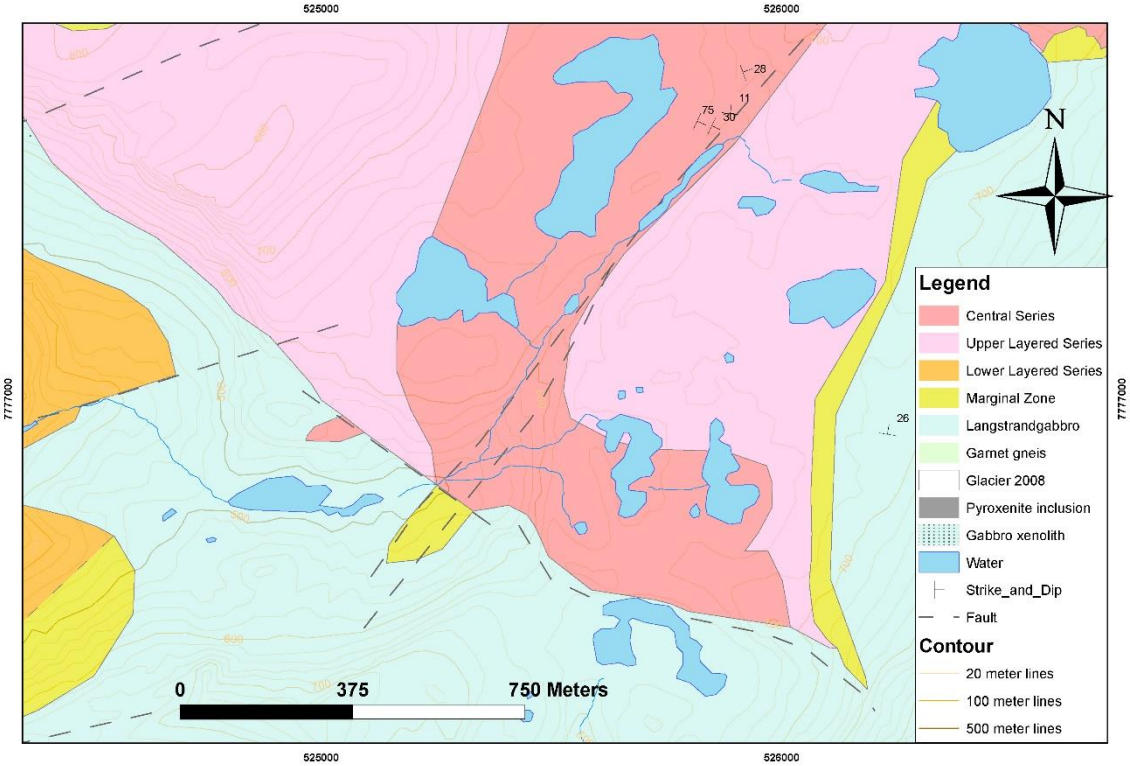

Figure 4.25: The southern part of the map. As mentioned previous, the south eastern fault is shifted into the gabbro to be visual, it is following the contact as seen on previous figures.

Figure 4.26: Figure from Øen (2013), that show the fault cutting the two small outcrops of MZ and CS, west fault presented. And that this fault continuous NW. Seen towards west.

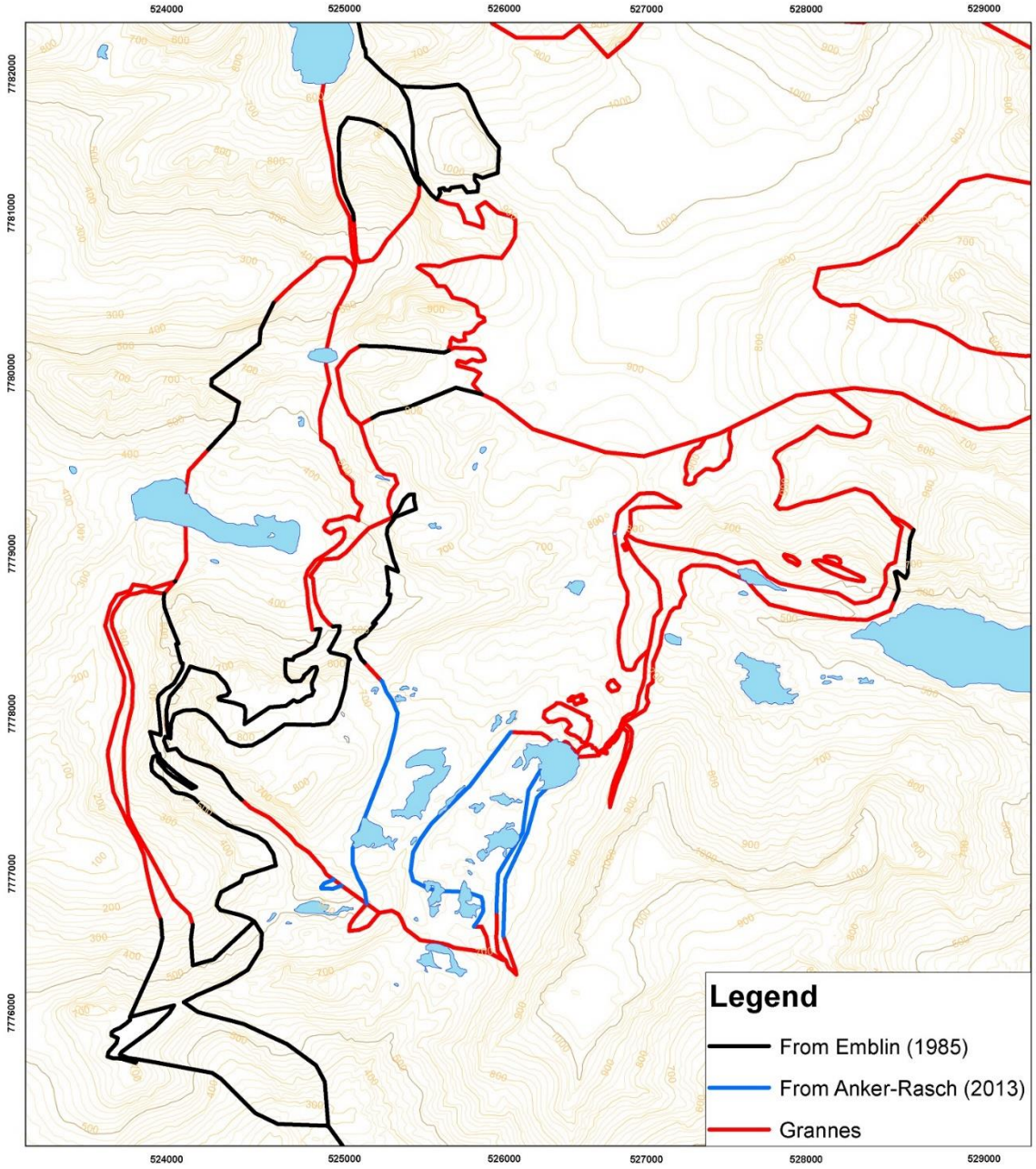

Figure 4.27: This map show the author of the boundaries in the intrusion. It give an indication of the area of the area that have been revised and remapped in this thesis.

4.3 Profiles

As the focus of this thesis is to understand the evolution of the intrusion and particularly the Central Series with the formation of ore-deposits, five cross sections throughout the intrusion were created. They disagree with the interpretations provided by Øen (2013). The profiles are based on the terrain model based on the contour data from the Norwegian Mapping Authorities, drill core data, field observations and geophysical survey conducted by Nordic Mining ASA. Interpretations were needed in areas where data is unavailable. To explain the intrusion in the best way possible four profiles were made roughly E-W direction Profile 5 has a SW-NE trend to tie the profiles together. Figure 4.28 shows where the profiles are located. Note the difference in scale on all profiles, it is intentionally done this way to present the data and relationships between the different lithologies. The difference in scale make some of the units appear thicker in the profile than reality.

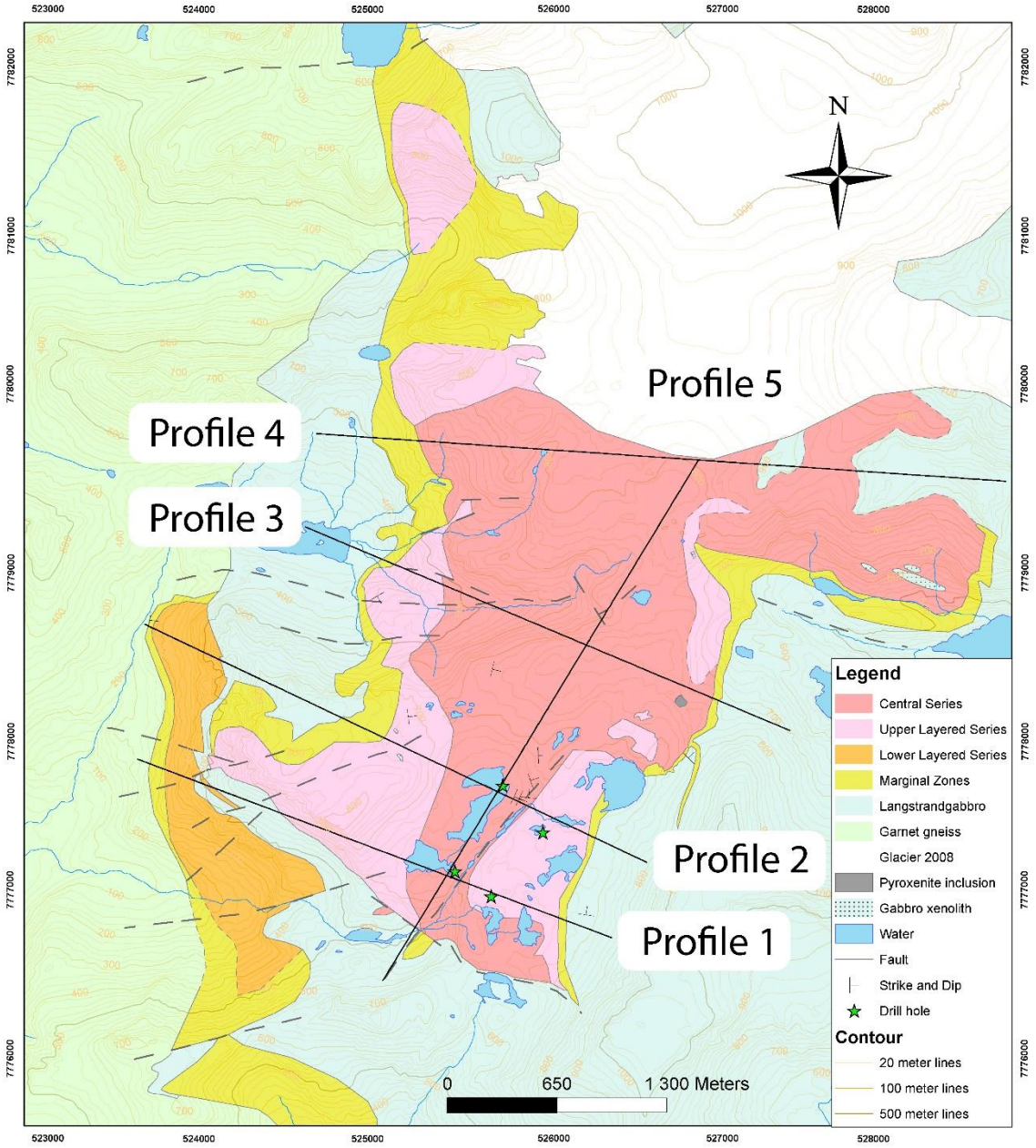

Figure 4.28: The location of the different profiles and the location of surface samples used to describe the CS and samples used in chapter 0 to describe the CS-Gabbro contact.

Profile 1

The first profile is from the south part of the intrusion and intersects the RF-1 and RF-2 drill cores. The RF-1 drill core consists of dunite (CS) with pyroxenite (ULS) in the top 30 meters. RF-2 consists of only Central Series (figure 4.29).

The LLS is seen in the cliff face as apophysis into the gabbro the same way seen with the CS on the plateau. The LLS is interpreted to exploit the gabbro-gneiss contact, and with no information in depth this contact is drawn sub vertical, but it might be sub horizontal and connected to the other UM rocks at depth.

Where the LLS is exploiting the gabbro gneiss contact, the ULS and CS have intruded through the gabbro and formed a sill south of the dyke swarm.. The CS-ULS contact is irregular because that is how it is observed in the field, but with no data at depth this is just an interpretation. The ULS in the west was described by Emblin to contain plagioclase, this could be from contamination from the wall rocks.

A MZ on the upper side of the LLS is believed to exist if it is not cut by faults.

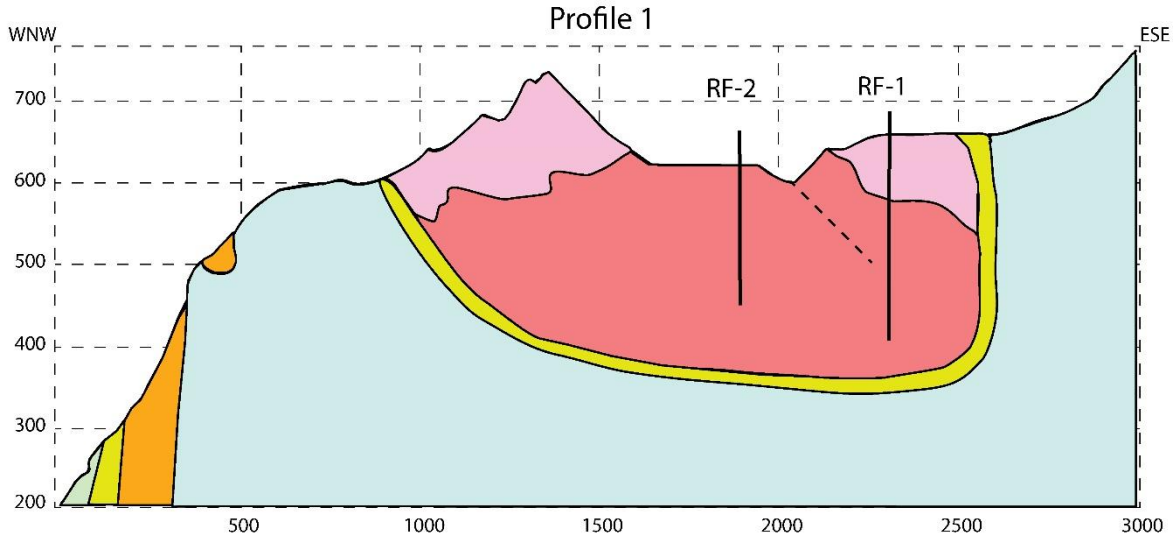

Figure 4.29: The southernmost profile showing the relationship between the UM and the host rock. For legend see Figure 4.28.

Profile 2

Profile 2 intersects with the longer RF-3 and RF-4 drill cores (figure 4.30). RF-3 show that the CS intersect and replace the ULS several times in the upper 100 meters of the drill core. RF-4 is pure dunite down to approximately 300 m.a.s.l. where large grained pyroxenite appears. This pyroxenite is interpreted as MZ due to many similarities with the MZ elsewhere in Reinfjord (discussed in chapter 5.2). The pyroxenite is consistent for over 50 meters, and may therefore represent the opening of the magma chamber and may represent the first UM melt emplaced into the gabbro (see chapter 4.4.1).

The western ULS is interpreted to lie underneath the MZ to compensate to the wide MZ in this area. Gabbro xenoliths found in this area might be from a second roof zone to the intrusion, discussed in chapter 5.1.

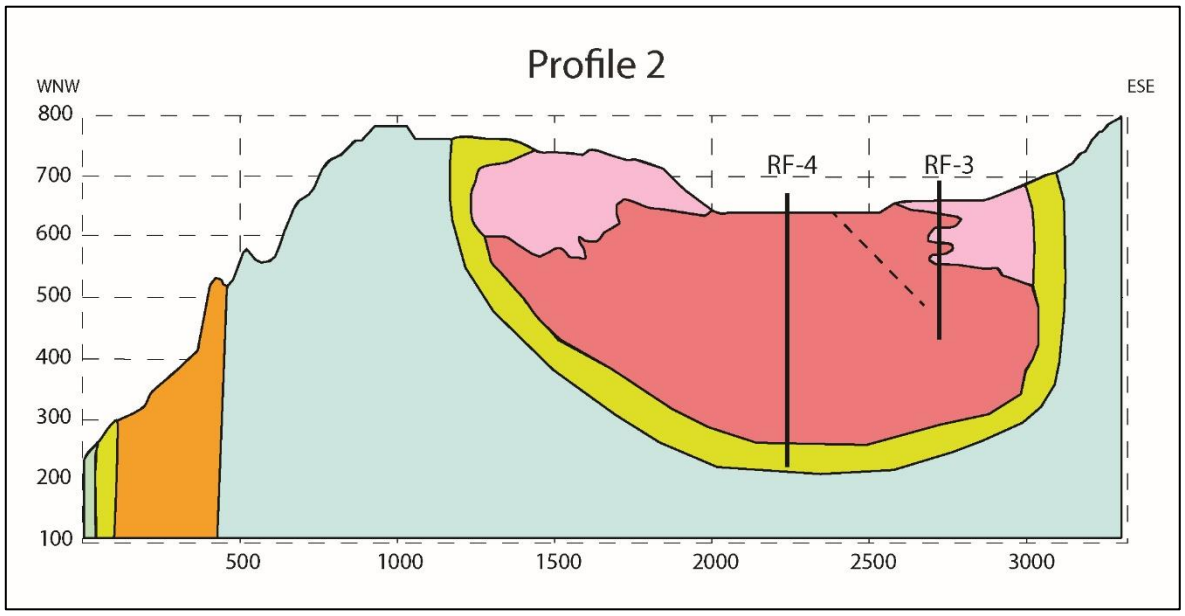

Figure 4.30: Profile intersecting with the RF-3 and RF-4 drill cores. For legend see Figure 4.28.

Profile 3

This profile is located across the dyke complex and close the replacive dunites which is located on the way up to the highest mountain ridge. This is where the believed conduit for the Reinfjord intrusion may be located (figure 4.31) (Grant et al, 2016). Drawing this cross section only surface data were used since no data exists at depth, therefore it is more uncertain than previous cross sections.

The CS is probably intruding the gabbro and the ULS in depth as we see elsewhere in the intrusion, especially along the eastern contact. This is not sketched since we have little to no data from this part of the intrusion. The lack off and little ULS is believed to be connected to the large amount of melt passing along the conduit system this profile represents.

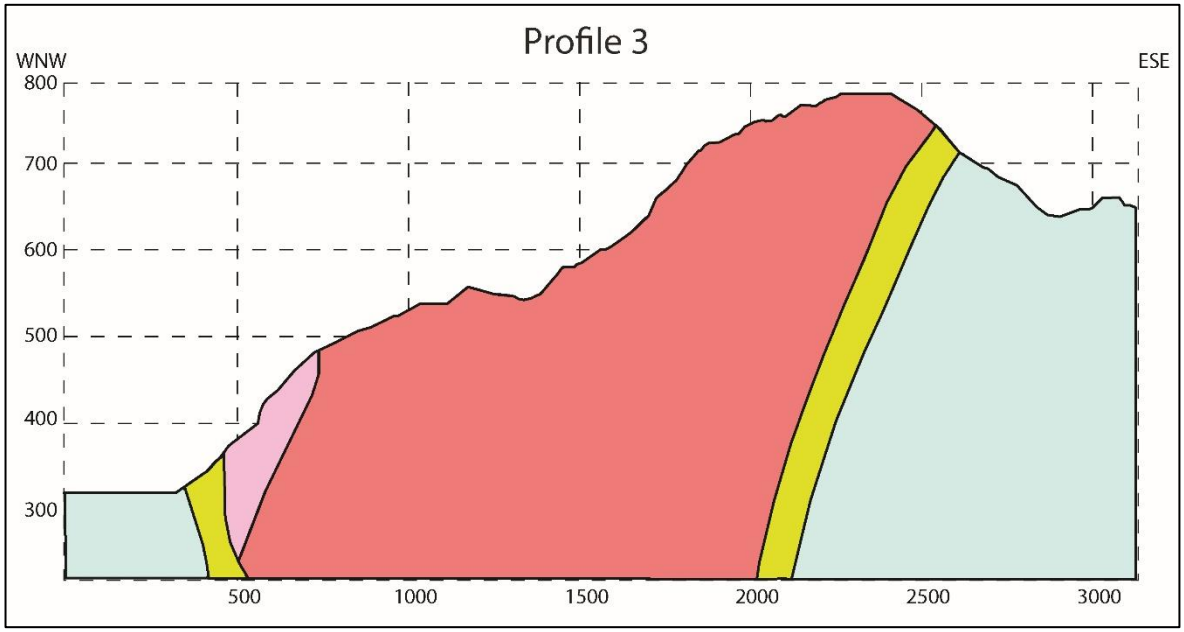

Figure 4.31: Profile over the dyke complex and what is believed to be conduit feeder for the parental melts. For legend see Figure 4.28.

Profile 4

This profile intersects the revised northern area and contains the e roof zone exposure. This is the profile with most uncertainty since the area close to the glacier is not mapped, and only one day of mapping was conducted in the eastern area of this profile before field work was aborted due to foul weather (figure 4.32).

In west, the contact is vertical as seen in the field where the gabbro-UM contact can be followed vertically down from the mountains close to Storvatnet. In the east the roof zone is sketched using an estimated elevation above the small depression, between the two mountain peaks. This was confirmed by the geophysical team during field work. Gabbro xenoliths observed in the cliff side presented under the roof zone is sketched on approximate elevation as observed in field. Due to scale of the figure and small size of the xenoliths, they are exaggerated in the figure.

The east side of this profile is interpreted to be a sill with a floor located somewhere between 300-500 m.a.s.l. This is uncertain due to little data, but the existence of pyroxenites in this area resembles the lower section of RF-4 and therefore might be an indication of a floor zone close by. The area is believed to resemble the south area, with a sill going north from the conduit system in profile 3 (see profile 5). The true depth of this sill is unknown, it is interpreted to be in the range 300-400 m.a.s.l.

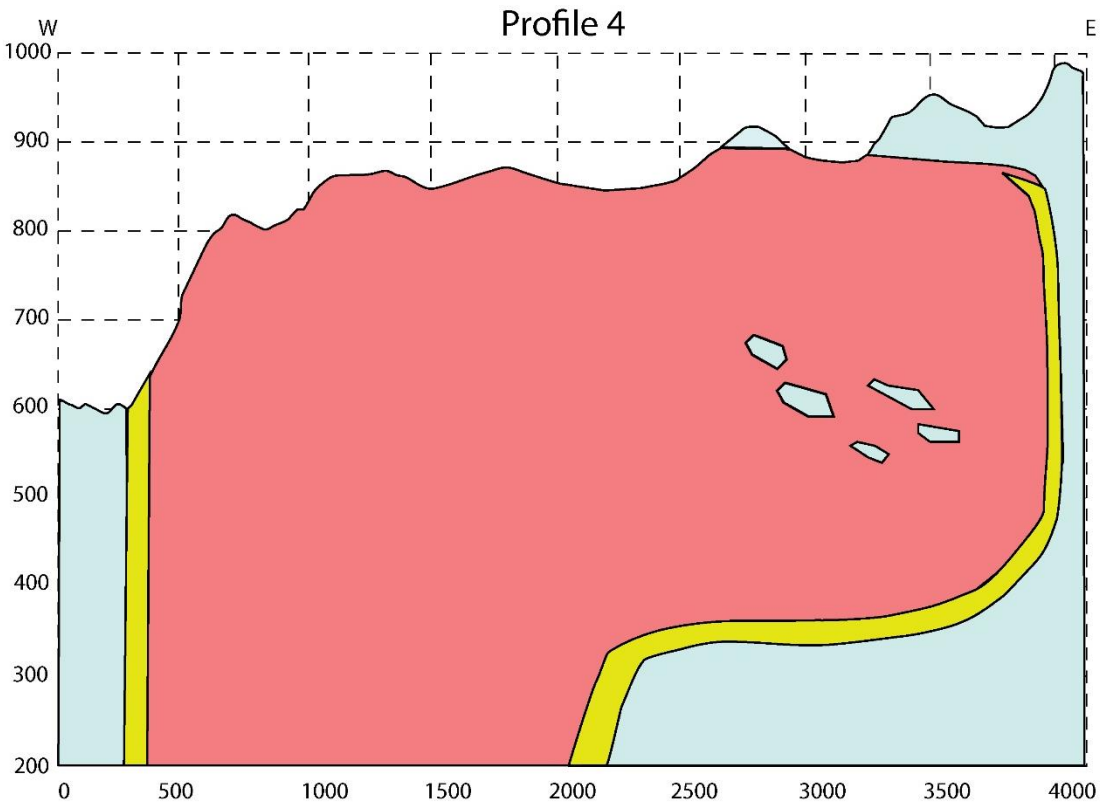

Figure 4.32: Profile over the northern part of the intrusion. For legend see Figure 4.28.

Profile 5

This profile follows the central parts of the intrusion along a N-S direction, intersecting with the RF-2 and RF-4 drill cores (figure 4.33). This is presented to tie all profiles together and present a complete interpretation of the intrusion.

The intrusion in south is cut by the fault previously presented. The depth of the southern part of the intrusion is estimated by the RF-2 and the RF-4 drill cores, with the feeder presented underneath the dyke complex (profile 3). The CS is believed to continue north under the glacier. The depth of the intrusion in north is uncertain, due to the pyroxenite observed in NE, it is interpreted to be more shallow than the southern depth.

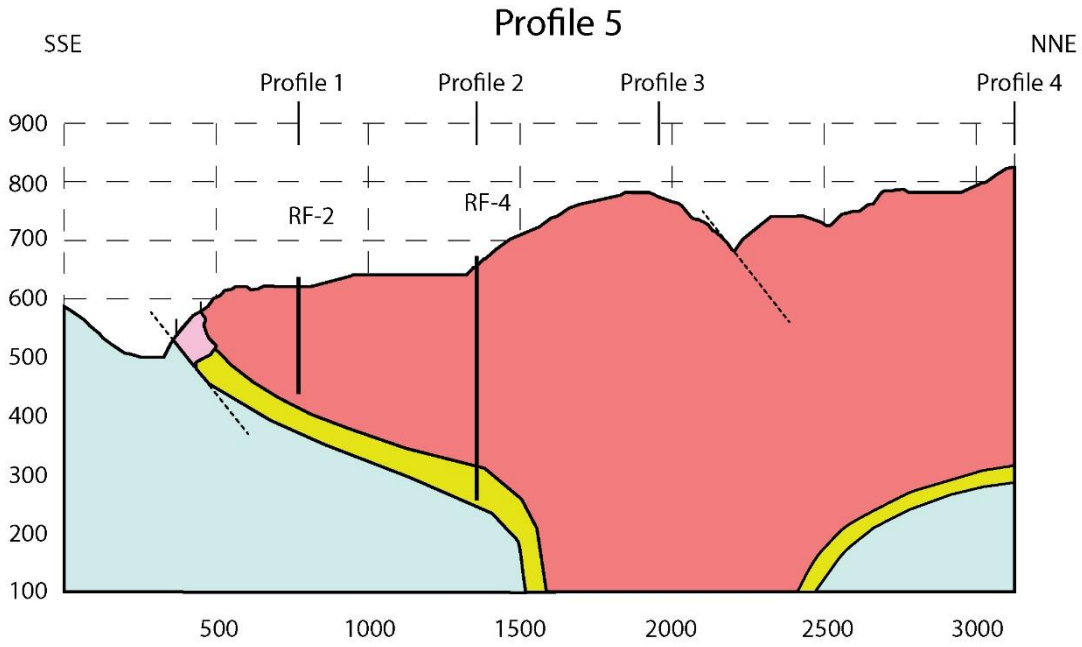

Figure 4.33: The N-S profile. Profile 1 to 4 is marked together with the RF-2 and RF-4 drill cores. For legend see Figure 4.28.

4.4 Chemical variation throughout the Central Series

To determine the chemical variations throughout the CS, the RF-4 drill core as well as 7 surface samples (KG14017 to KG14023) have been analysed for major and trace elements (for full dataset see digital appendix). Fourteen thin sections from the RF-4 drill core and 7 from the surface sample were investigated microscopically (see appendix A for sample list and locations). 18 samples were selected for EPMA, and a total of 493 data points were collected. XRD analyses were conducted on four of the drill core samples to quantify the modal mineralogy.

4.4.1 Whole-rock analysis

The RF-4 was sampled over 5m intervals. This makes local enrichments seem diluted compared to analyses of samples over shorter distances (smaller volumes), such as the surface samples and are therefore presented separately. The Mg# is presented as Wt% ratio and is calculated by [100Mg/(Mg + Fe)]. For Mg, Fe, Co, Cr, Pt, Pd and Au diagrams see appendix B.

RF-4

The RF-4 drill core mostly consists of fine to medium grained dunite with patches of wehrlite throughout the first 350m in the drill core and a medium- to coarse-grained clinopyroxenite in the lowest 50m.

The Mg# of the CS samples ranges from Mg# = 68 – 73,8, with maximum value at 430 m.a.s.l. While the pyroxenite in the lowest 50 meters of RF-4 has Mg# = 63 - 68. This lower 50 m is cut by two plagioclase rich veins that have Mg# of 37 and 44 (at 260 and 265 m.a.s.l.). In this type of environment cobalt is incompatible, compared to Cr, which is compatible in chromium spinel. Due to the high olivine content in the dunite, and therefore low content of other phases, the CS contains very few trace elements with concentration above the detection limit. The Co/Cr ratio and the Mg# show a strong correlation, where Mg# is high the ratio of Co/Cr are also high. Co/Cr peaks can most often be correlated with an increase or decrease in Mg#, indicating a magma recharge event.

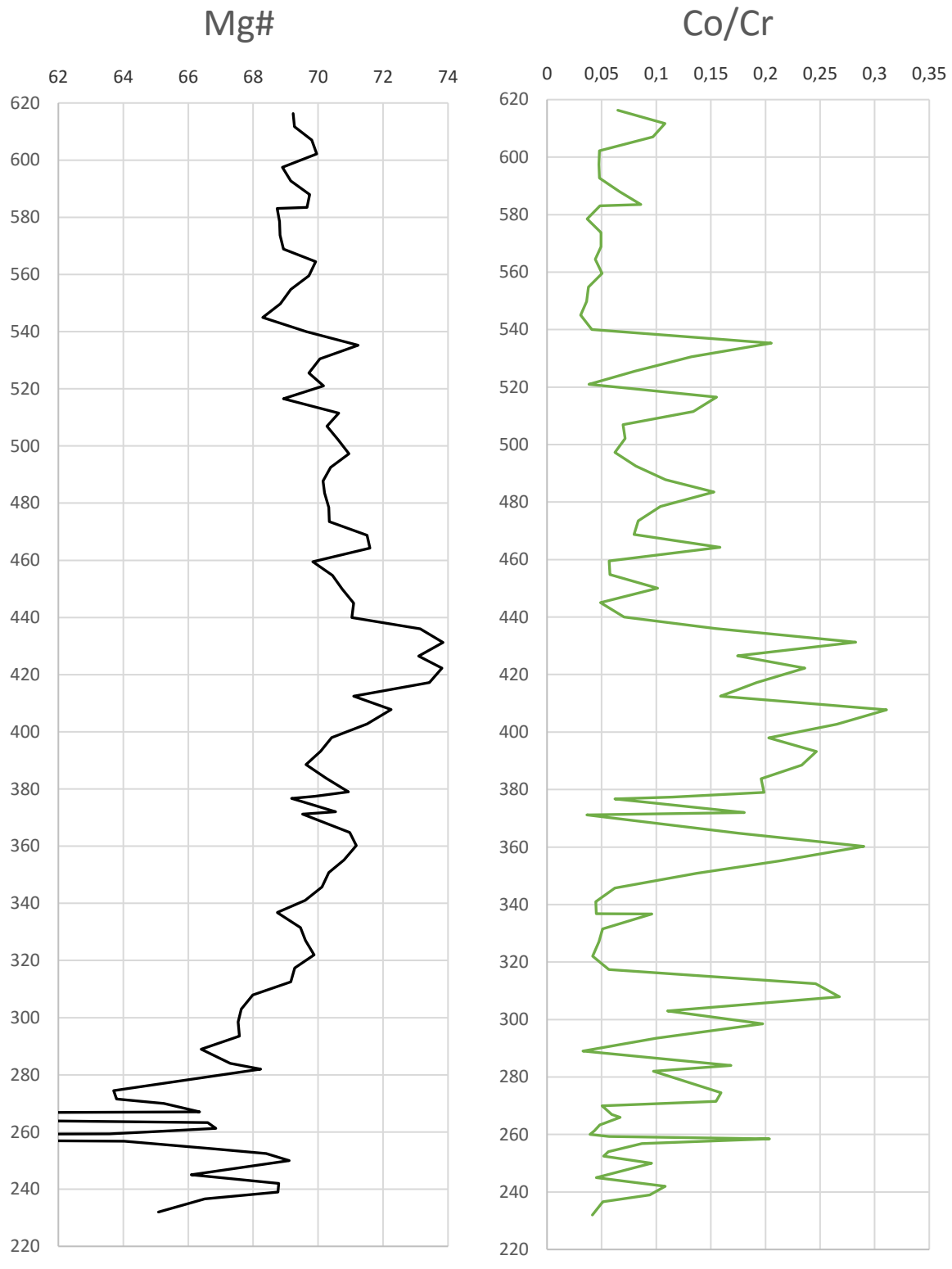

Figure 4.34: Bulk rock chemistry of Mg# and Co/Cr

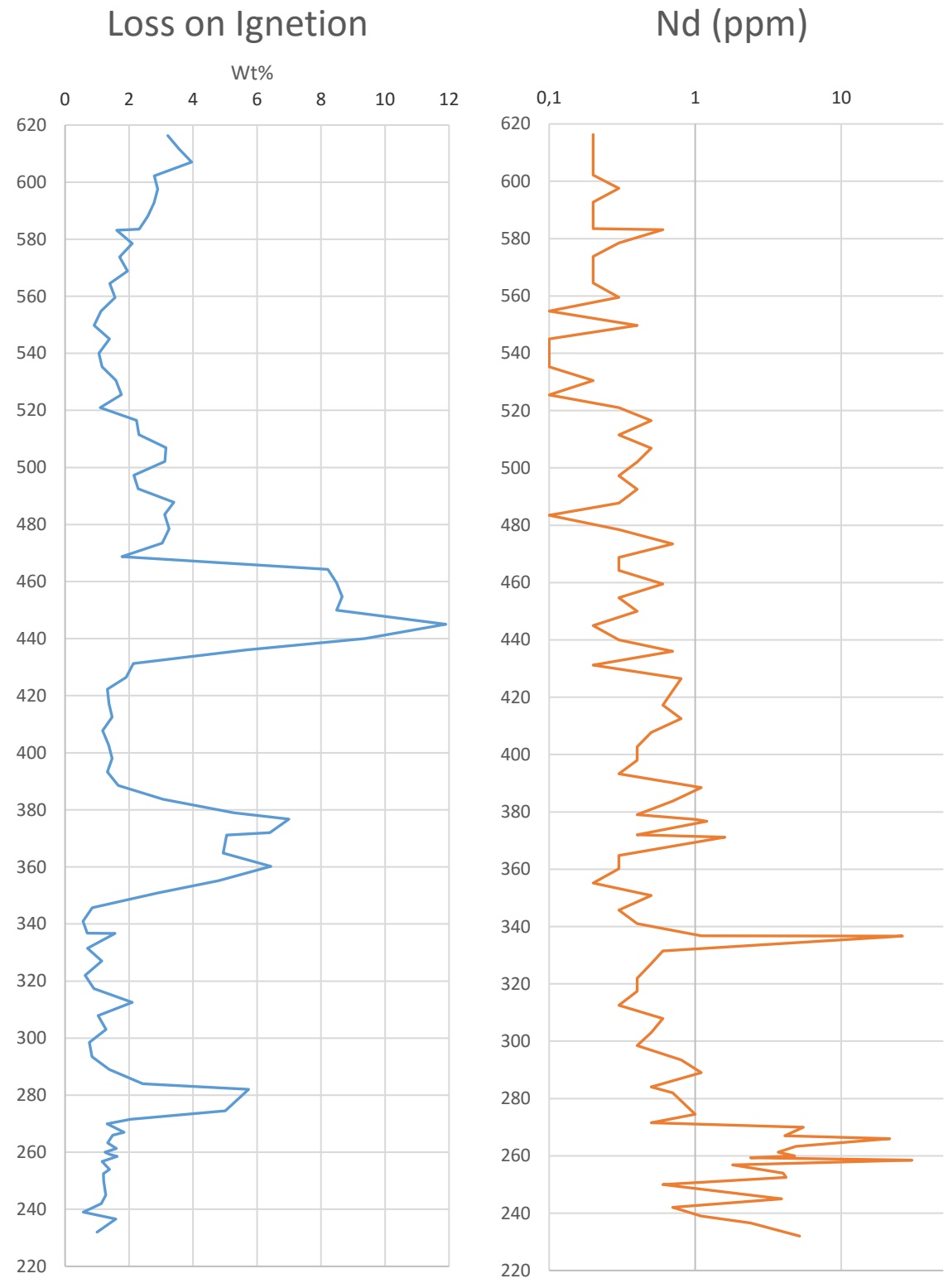

Figure 4.35: Loss on ignition (LOI) show the amount of volatiles (H_2O and CO_2) and Nd is a trace element, peaks (>10 ppm) correlates with observed veins.

At the base of the drill core the Mg# is vary, and show sudden and large variations that are indicative of cryptic layering. This lower section also has generally lower Mg# values than elsewhere in the drill core, crossing over with those of pyroxenites rather than dunite or wehrlite typical of the CS. Above this the Mg# steadily increases from 66,2 at 290 m.a.s.l. to 74 at 430 m.a.s.l. where it reaches the highest Mg# values observed in the drill core. Above this the Mg# steadily decreases to 68 at 550 meters, where it is steady for the rest of the drill core. The small variations from sample to sample within these major trends may be a result of cryptic and modal variations. Co/Cr values follow the same trend, but is more irregular and spiky in appearance. This can be argued with the appearance and disappearance of the coexisting chromium spinel.

Neodymium show a stable low content in the CS (< 1 ppm), averaging 0,5 ppm, with exception of the a plagioclase rich vein located at 335 m.a.s.l.. Where the pyroxenite appears, an increase ranging from 0,5 to 5,5 ppm is observed, averaging 3 ppm (not including the veins). This trend is reflected in other REE, which is presented later in chapter 4.5.2.

Loss on ignition (LOI) shows the amount of volatiles (i.e. H_2O and CO_2) present in the sample (figure 4.35). This might this give a rough indication of the amount of serpentinization, but with no knowledge of the chemistry of the volatiles, H_2O and CO_2, their ratio and origin is unknown.

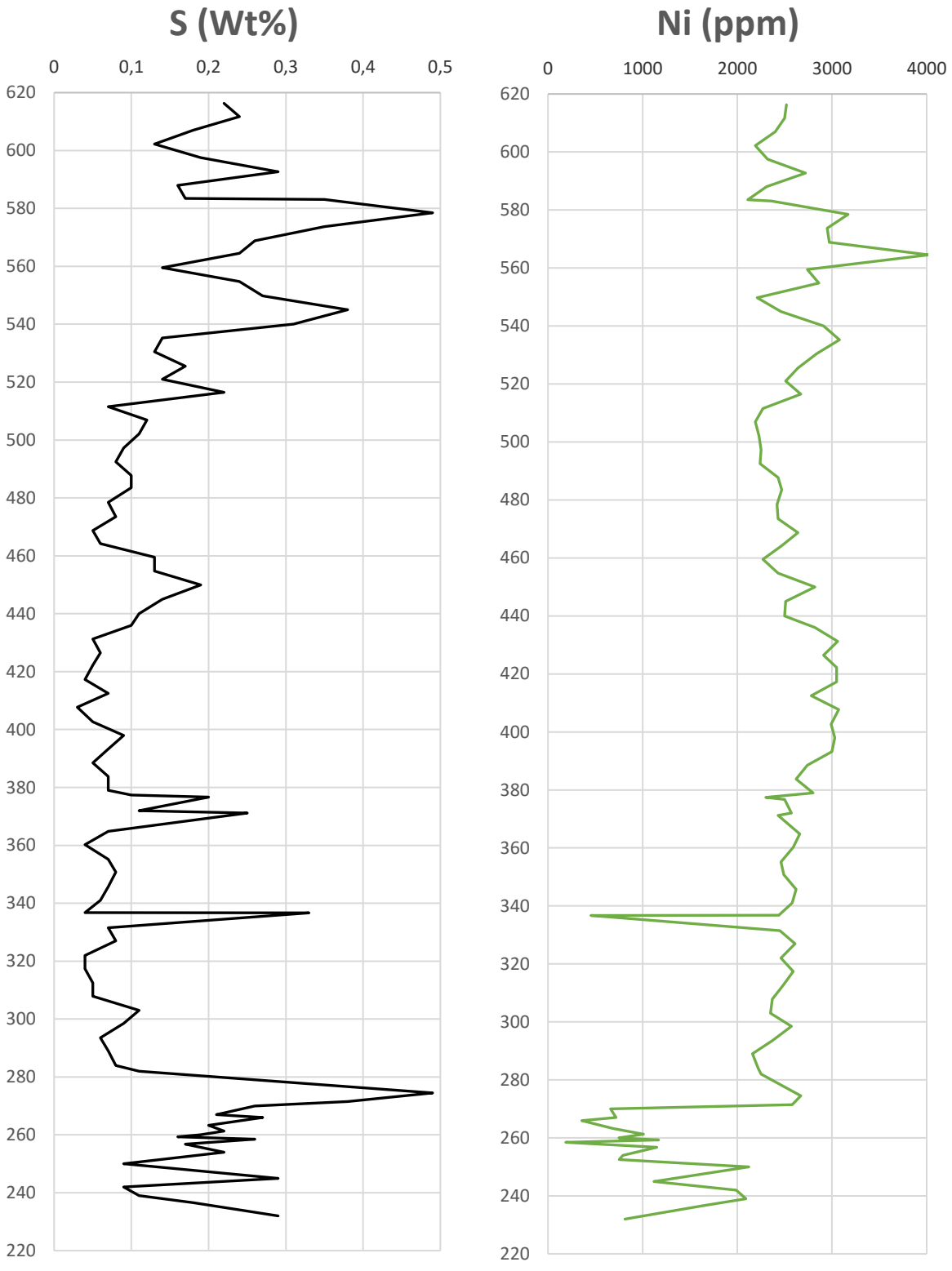

Figure 4.36: Bulk rock major element analysis of S (Wt%) and Ni (ppm).

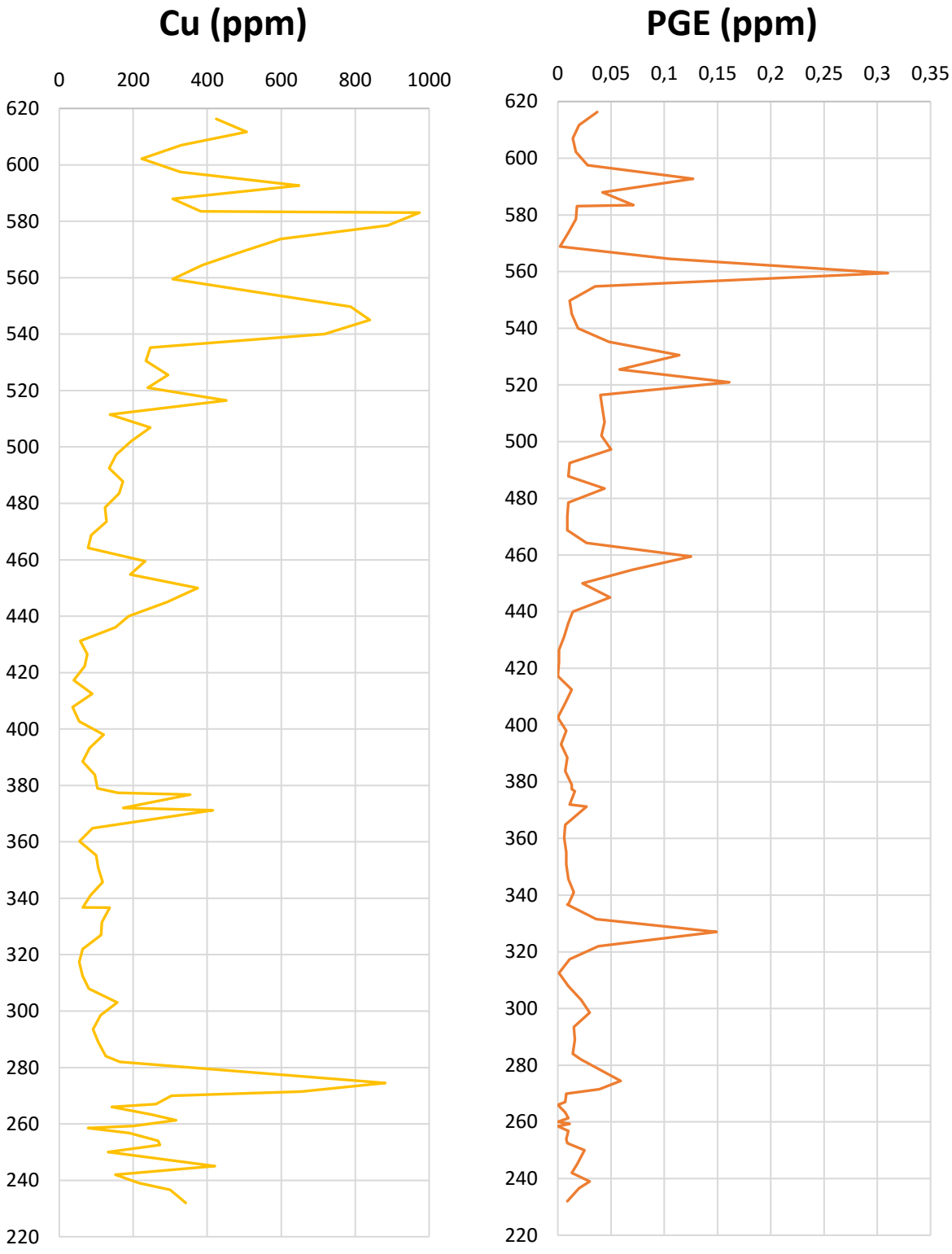

Figure 4.37: Bulk rock major element analysis of Cu (ppm) and PGE (ppm).

4.Result

The sulphide content range from 0,03 to 0,5 Wt%. Sulphide concentration may be classified into three groups; the first group is the highest peaks at 0,5 Wt%. The second group is with a sulphide content between 0,25 and 0,35 Wt% and the third group is with a sulphide concentration <0,25 Wt%.

In the CS, nickel concentrations range from 2100 to 4000 ppm, with an average nickel concentration of 2600 ppm. In the pyroxenite Ni values drop from 2000 ppm to 500ppm, with large fluctuations between samples. Note the highest nickel at 4020 ppm is in a zone with low sulphide (0,24 Wt%) between two sulphide peaks, 15m above or 20m below.

Copper concentrations reflect the concentration of sulphur in the CS. Except at 340 m.a.s.l. where a peak of 0,33 Wt% sulphur is marked with a decrease in Cu and Ni. Cu varying from 50 ppm to 200 ppm where the sulphide concentration is low. Where sulphur appears the copper concentrations increase.

The cryptically layered pyroxenite, copper and nickel content vary rhythmic increasing with depth. These changes in the pyroxenite may be correlated with the rhythmic changes in Mg# and Nd. Where Nd decreases with depth and Mg# increase. The copper content varies from 50-400 ppm, nickel varies from 250-2000 ppm.

Three of the copper peaks stand out, at 580, 545 and 275 m.a.s.l. These are marked by 0,5 Wt% S and 975 and 880 ppm Cu for the first and the second respectively, these are later referred to as Cu reefs . The second peak contains 0,35 Wt% sulphide with 840 ppm copper.

The PGE diagram consists of platinum (Pt), palladium (Pd) and gold (Au). Platinum and palladium have an almost 1:1 correlation, with the largest peak at 0,15 ppm each. Whereas gold has a lower concentration and peaks at 0,05 ppm located in a zone with low Pt-Pd (0,02-0,04 ppm) (appendix B.4 – B6).

The PGE peaks are always shifted compared to the copper and sulphide peaks (appendix B.7 – B.9). The highest PGE peak is located at 560 m.a.s.l., it consists of 0,03 ppm Au, 0,14 ppm Pt

and 0,15 ppm Pd. This peak is located in a zone of low sulphide and copper content, between two peaks of copper (presented above). This shift of metal enrichment is seen all over the drill core. Except at 592 (minor copper peak) and at the contact between the pyroxenite and the CS located at the275 m.a.sl.

Surface samples

Surface samples have smaller volumes compared to the drill core samples. This makes them unsuitable to compare drill-core samples, hence they are here presented separately.

The surface samples were collected east of the drill core, up the ridge in a northerly direction (appendix A.3). These samples continue upwards stratigraphically above the drill head. An estimate of the stratigraphic height for the samples was estimated (Table 4.1). The locations of the samples were transferred into a line going NE from the drill core. From here, the drop in stratigraphic elevation was estimated using a stratigraphic dip of 10° and 20°.

All plots are plotted at the stratigraphic elevation with an internal dip towards NE at 10° (estimated value), with an error at 10° dip towards NE.

Table 4.1: Estimates on the stratigraphic elevation for the surface samples.

Sample	Sample elevation	Latitude (X) distance from RF-4	Longitude (Y) distance from RF-4	Estimated stratigraphic elevation (10°)	Estimated stratigraphic elevation (20°)
KG14017	640	126 m	-89 m	640 m.a.s.l.	640 m.a.s.l.
KG14018	659	194 m	36 m	690 m.a.s.l.	720 m.a.s.l.
KG14019	693	240 m	177 m	745 m.a.s.l.	798 m.a.s.l.
KG14020	719	273 m	375 m	806 m.a.s.l.	894 m.a.s.l.
KG14021	746	270 m	475 m	849 m.a.s.l.	951 m.a.s.l.
KG14022	768	326 m	584 m	900 m.a.s.l.	1033 m.a.s.l.
KG14023	790	403 m	727 m	940 m.a.s.l.	1090 m.a.s.l.

The Mg# in these samples vary more than the drill core samples. This may be explained by the much larger gap between the samples, lateral variations within the CS and the fact that the samples represent only a fraction of the stratigraphy compared with the drill-core samples. The Mg# range from 66,3 to 69,5, where the average Mg# is 68,5. Sample KG14018 (690 m.a.s.l.) shows a significant drop in Mg# to 66,4, with a Co/Cr ratio at 0,5 (figure 4.38). Potentially indicating a magma recharge event.

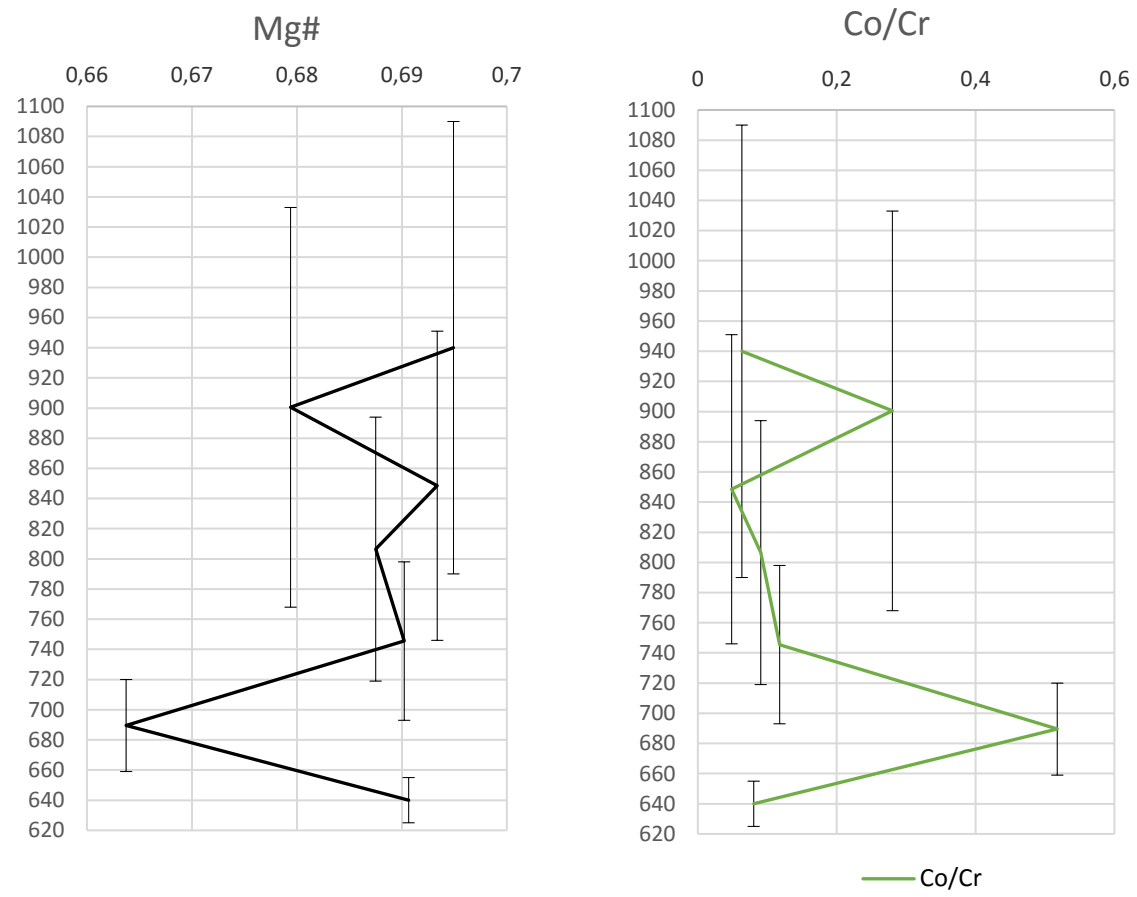

Figure 4.38: Bulk rock major elements, showing Mg# and Co/Cr evolution in the CS above RF-4.

These samples contain less nickel than in the drill core (figure 4.39). Except on 720 m.a.s.l. where sulphur (0,36 Wt%) and copper (1150 ppm) peaks and brings the nickel up to 3740 ppm. The LOI peaks at the same elevation as the drop Mg# and the peak in Co/Cr.

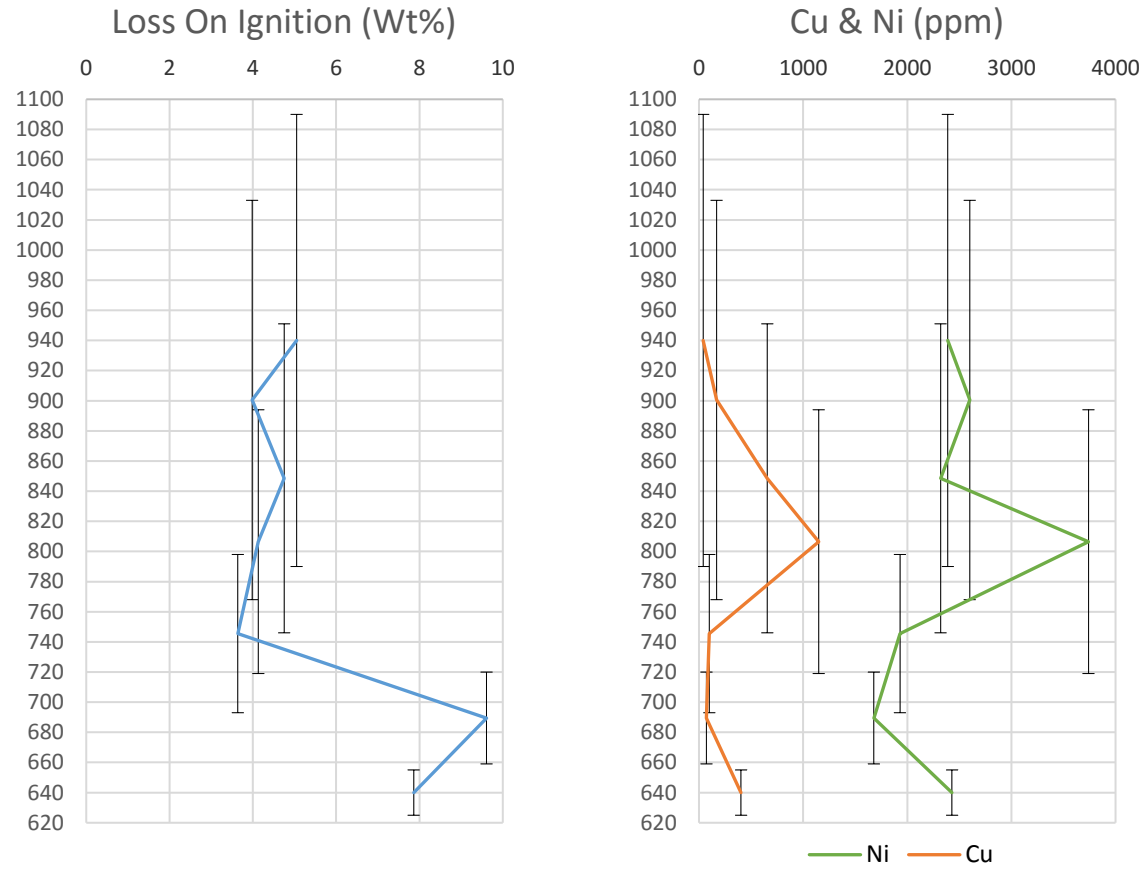

Figure 4.39: Volatiles shown in loss on ignition and base metal copper and nickel.

4.4.2 EPMA

14 thin sections from RF-4 and 4 surface samples were analysed by EPMA. Three samples were discarded for EPMA, due to massive serpentinization in these thin sections. Average data on all samples may be found in appendix C (see digital appendix for individual analysis), where they are presented in average composition for each sample with calculated standard derivation.

A list of detection limits, counting times and standards used for EPMA analyses is found in Table 3.1 and Table 3.2.

Olivine

Drill core samples and surface samples are plotted together. The surface samples are the same samples analysed for whole-rock analysis in chapter 4.4.1, and are plotted at the stratigraphic elevation calculated in Table 4.1. All points plotted are the average value from each sample and are plotted with the standard derivation as the error bars.

Forsterite compositions are calculated following Deer et al. (1992) end-member calculations for olivine. Forsterite is calculated by molar calculations: 100 Mg/ (Mg + Fe*), where Fe* is defined as $Fe^* = Fe^{2+} + Fe^{3+}$.

Chemically, the olivine types described by Grant et al. (2016), olivine type 1 ($Ol_{1)}$ and olivine type 2 (Ol_2) are indistinguishable.

The forsterite content in olivine varies $Fo_{82\text{-}85,6}$ in the CS, interstitial olivine in the pyroxenite in the drill hole have a forsterite value at Fo_{79} and $Fo_{80,2}$. Forsterite contents show the same trends as the bulk rock Mg#, with increasing Mg content up to 420 m.a.s.l. and decreasing above. The gap between the RF-4 samples and the surface samples in addition to the low sample density of the latter, make the evolution and history of the CS difficult to interpret above the RF-4. The uncertainty of the stratigraphic elevation and the possible horizontal variation of the surface samples make this even more complex

Nickel content in the olivine follow the same trends as the forsterite content. The nickel concentrations in olivine range from 0,2-0,42 Wt% NiO in the CS and 0,12 Wt% NiO in the pyroxenite. Calcium contents are low as it is an incompatible element in olivine. Calcium concentrations ranges from 0,005-0,02 Wt% CaO. The standard deviation is larger than the overall variation and therefore the values are treated as not valid (figure 4.41). The NiO/MnO diagram shows that this ratio is always >1 in the CS and between 0,5 and 0,6 in the pyroxenite. The NiO-MnO diagram and the NiO diagram show the same shape and trends, indicating a constant ratio of $D_{Ni}^{Ol/melt}$ and $D_{Mn}^{Ol/Melt}$. The only exceptions are the top two samples in RF-4.

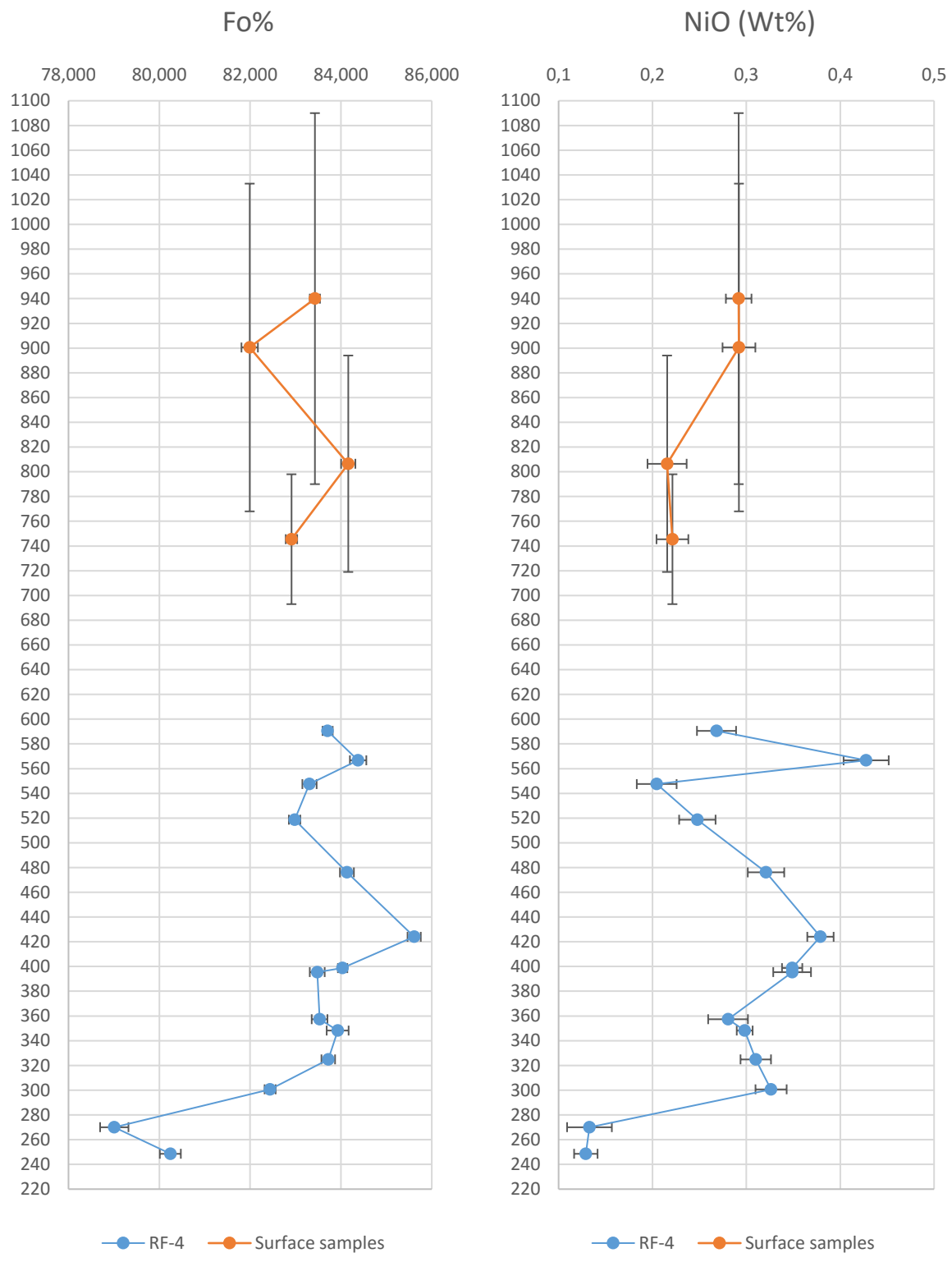

Figure 4.40: EPMA analysis showing the Fo content and NiO content in olivine

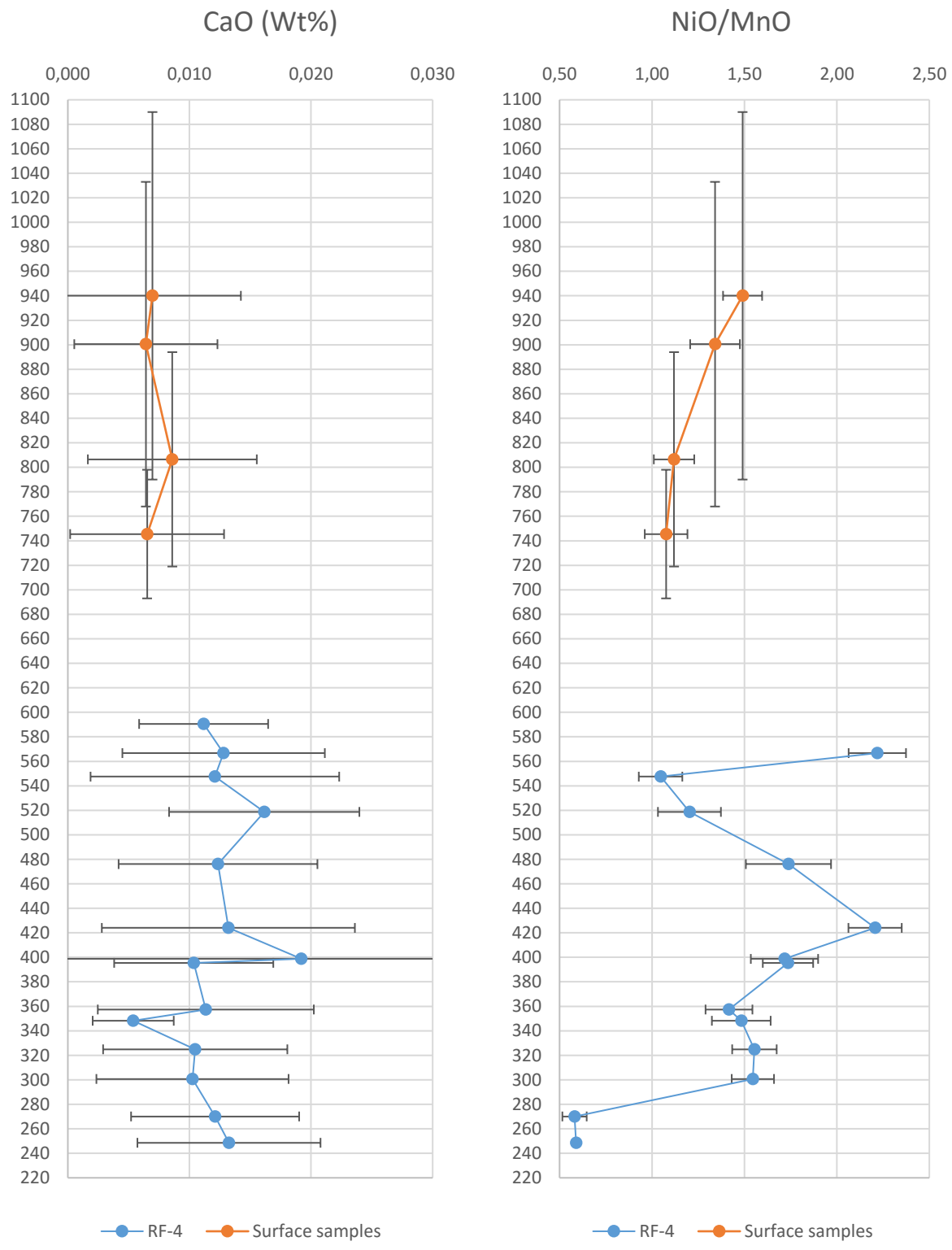

Figure 4.41: EPMA analysis showing the CaO content and NiO/MnO content in olivine

Clinopyroxene

8 of the drill core samples were analysed for pyroxene together with olivine. In the rest of the samples in RF-4 and the surface samples, pyroxene was absent. Only 7 points showed Opx compositions, therefore only Cpx are presented. But the Opx and the Cpx sample averages and calculated standard derivation can be viewed in appendix C.5-C.8. Points marked with yellow colour are from samples where only one grain was found and analysed with three separate EPMA points. This gives a total of two statistically representative samples for the CS and the pyroxenite in RF-4. The Mg# in the clinopyroxene range from 78,8 to 84,3 in the CS, and the two pyroxenite samples have 72,7 and 75,2. CaO contents in cpx decrease when going from pyroxenites in the bottom of the drill core to dunites in CS, but increase with stratigraphic height from there (figure 4.42). Clinopyroxene in the CS show a weak increase in Mg# and in CaO content. Cr_2O_3 content in the pyroxene in the pyroxenite range from 0,2-0,3 Wt%, while in the CS it is distinctively higher ranging from 0,6-1 Wt%. The SiO_2 show a slight increase from the pyroxenite to the CS (figure 4.43).

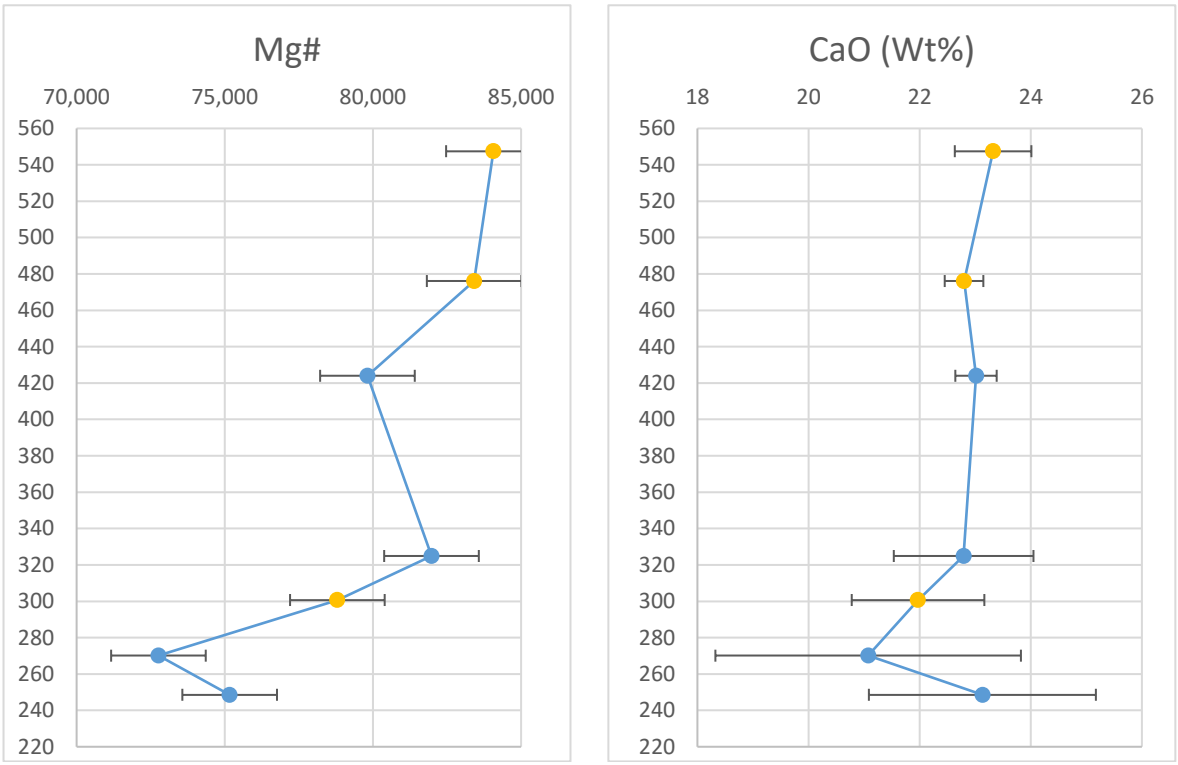

Figure 4.42: EPMA analysis showing the Mg# and CaO content in clinopyroxene. Points marked by yellow colour is analysed by one grain, therefore have low statistical significance

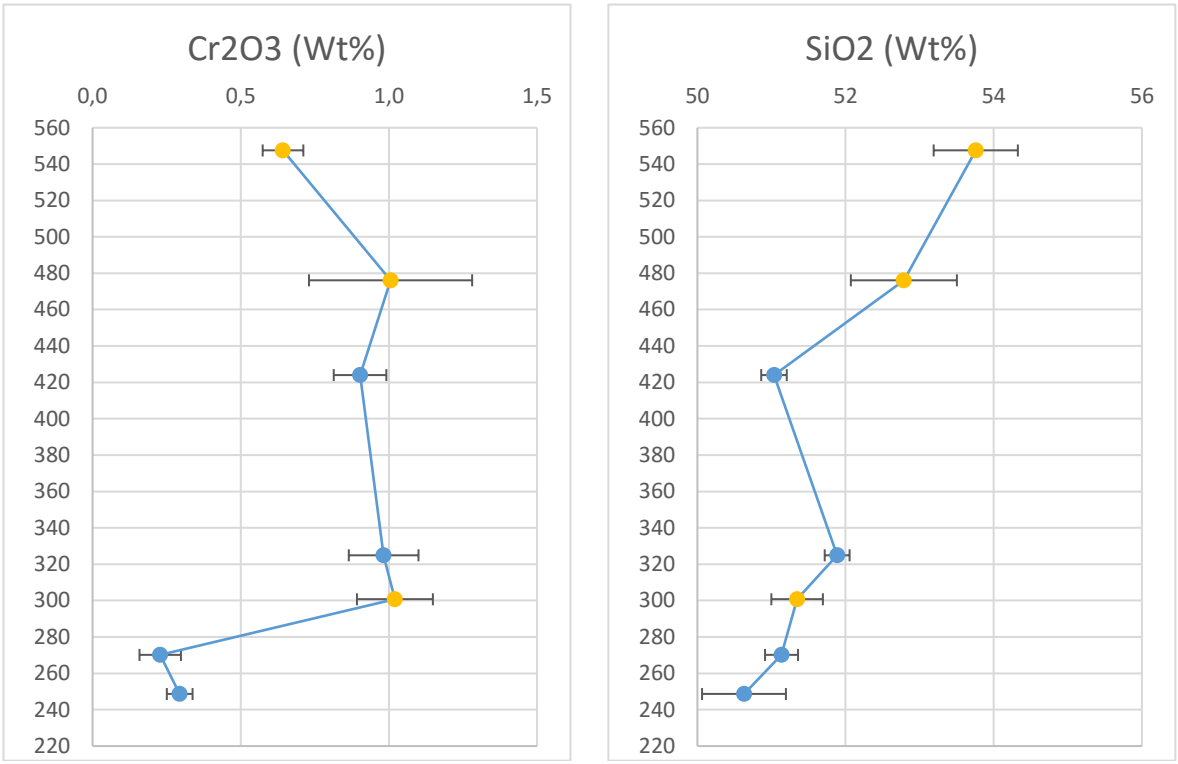

Figure 4.43 EPMA analysis showing the Cr_2O_3 content and SiO_2 content in clinopyroxene. Points marked by yellow colour is analysed by one grain, therefore have low statistical significance

The samples with statistical significance (more than three grains analysed) all Cpx is found as primocrysts. Samples from the CS with low statistical reliability, only the 4-7550 sample (550 m.a.s.l.), contains Cpx as primocrysts, whereas the other two contain interstitial Cpx.

4.4.3 Native copper

Optical microscopy revealed that the 4-7550 (547 m.a.s.l.) and 4-10430 (515 m.a.s.l.) samples contained native copper, together with minor amounts of chalcopyrite (ccp) (figure 4.44). These samples were therefore analysed using SEM, to describe the textures and mineralogical relationship between native copper and other phases.

Native copper often appears as elongated “grains” hosted within chalcopyrite or pyrrhotite. In sample 4-10430, native copper often appears with a rim of iron oxide

4-7550

Bulk majority of the copper found in this sample is found as scattered native copper. SEM-EDS analysis of the native copper show that it is 80-98 Wt% pure copper (see appendix D, for point analyses and spectrum), contamination from neighbouring minerals may explain the low Cu purity in some measurements. Copper alloys are found within the native copper grains. The alloys are copper rich (80-95 Wt%), copper-zinc and copper-iron alloys are common.

Sulphide phases are mainly pyrrhotite with pentlandite exsolutions, minor amounts of chalcopyrite and an altered unrecognizable darker phase (Figure 4.44b and d) is found in close proximity to the native copper. Observed chalcopyrite (Figure 4.44c) is often altered and replaced by digenite, chalcocite and magnetite. Most often in contact with serpentine, but also within sulphide grains. Pyrrhotite is seen reacting with serpentine veins, creating irregular boundaries (Figure 4.44b-d).

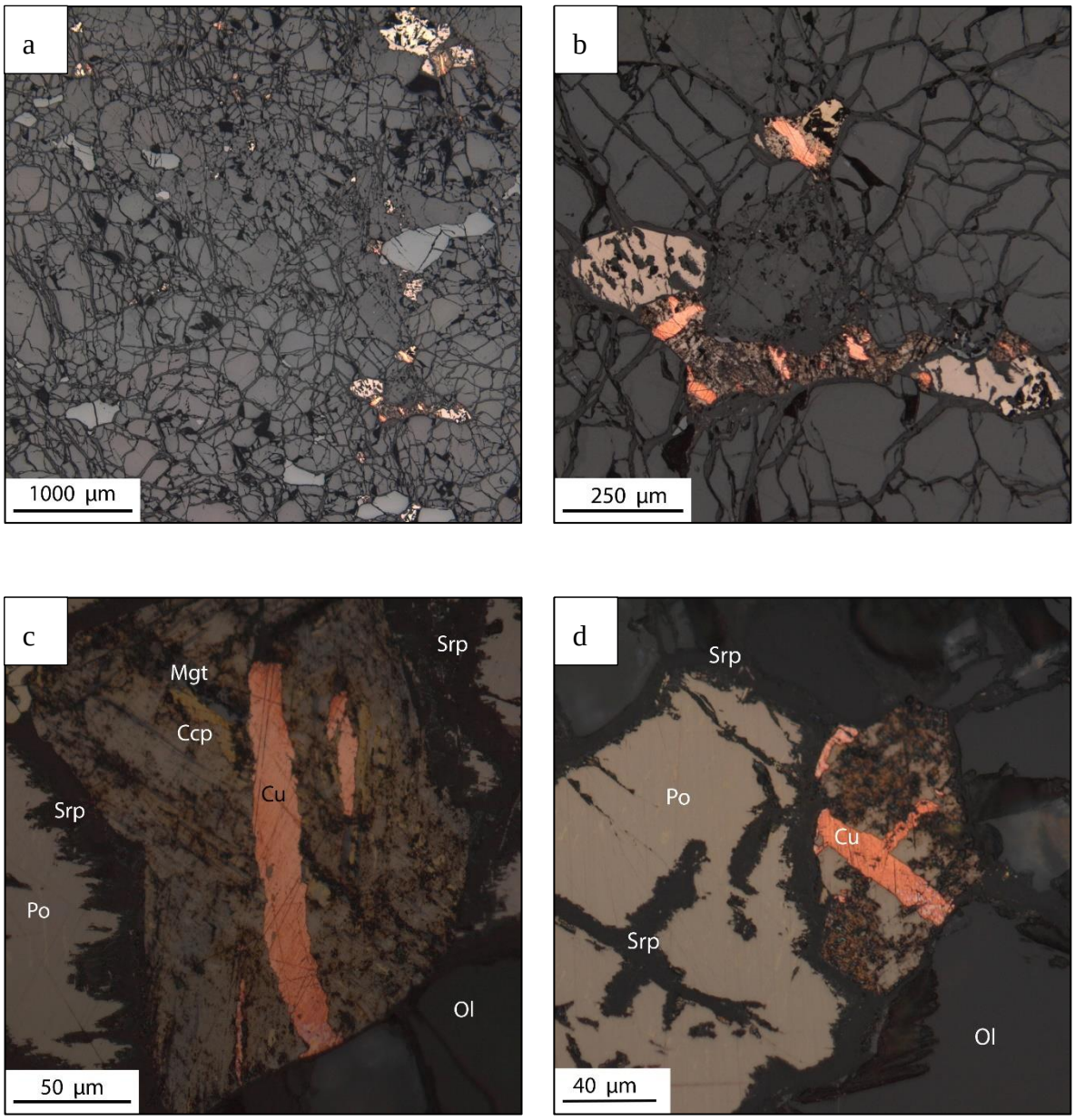

Figure 4.44: a) Overview of the riches part of the 4-7550 sample. b) Native copper hosted in fractured and altered pyrrhotite. c)Native copper hosted in a pyrrhotite and chalcopyrite grain surrounded by iron oxide. d) Pyrrhotite hosts the native copper and an altered copper-iron phase. It is part of a larger sulphide grain consisting of pyrrhotite with pentlandite exsolutions.

Native copper appears often as discontinuous elongated grains. The rectangular shaped native copper grains seem to have a preferred orientation, where the long axes are perpendicular to each other is the most common (Figure 4.44). A less common angle is 45° (Figure 4.45), this is only observed twice. Some of the native copper grains are irregular in this sample, this is most often the smallest of the grains (Figure 4.46).

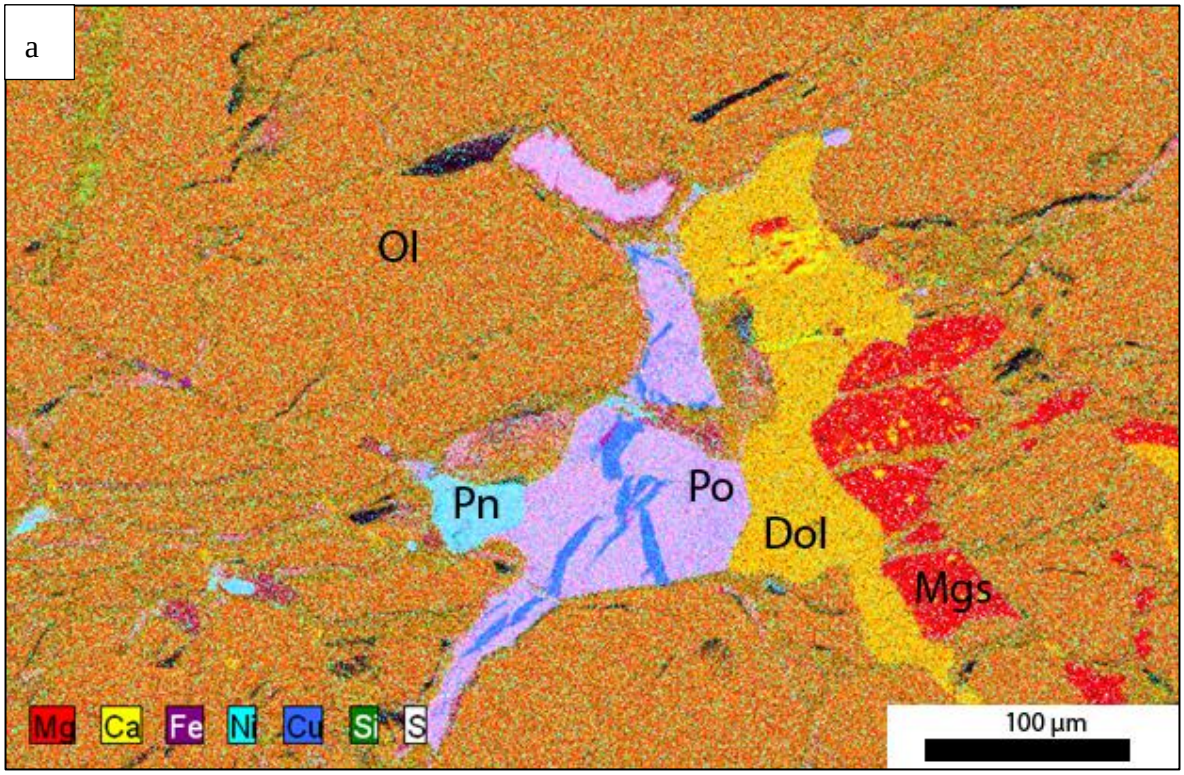

Figure 4.45: SEM-EDS element map showing how the blue native copper is situated within a pyrrhotite grain. Note the dark purple colour around sulphide grains, that is iron rich serpentine breaking down the sulphide. The yellow-red mix is dolomite, partially decomposing to brucite (red) and calcite (yellow).

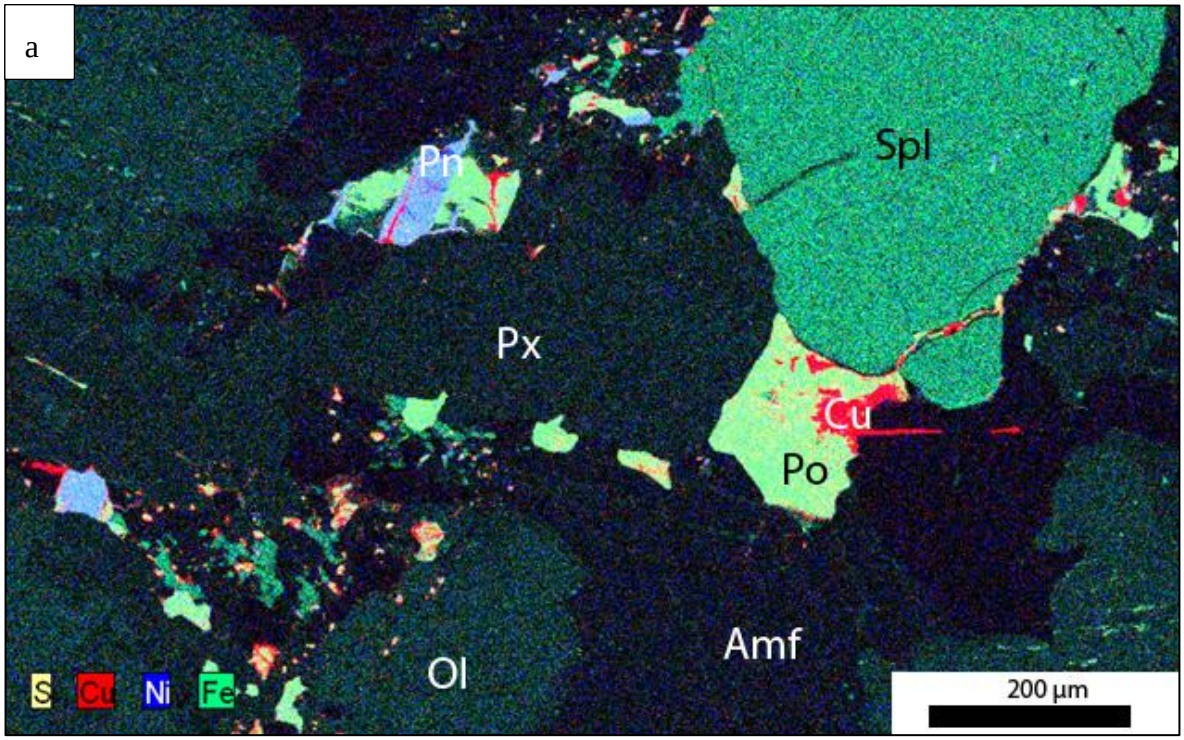

Figure 4.46: SEM-EDS element map showing sulphur, nickle, copper and iron. Showing how the Native copper and other sulphide minerals coexisit Pure red colours is native copper, red spots mixed with pale orange and green is chalcopyrite, blue is pentlandite and bright green is pyrrhotite.

4-10430

This sample contains much less native copper than 4-7550, which reflect the Cu observed in the whole-rock analysis (450 ppm Cu compared to 850 ppm Cu). The samplehave a large range of other copper bearing minerals, such as chalcopyrite, cubanite, covellite (maybe also chalcocite) and native copper. Compared to the 4-7550 sample, the sulphides and copper minerals are only observed in two areas, one large sulphide grain (Figure 4.47c and d) consisting of pyrrhotite, pentlandite, chalcopyrite and a large grain of native copper with rims of iron oxide. The second area is a pocket where copper minerals are scattered in a matrix of calcite-brucite and serpentine (Figure 4.47a, b and Figure 4.48a and b).

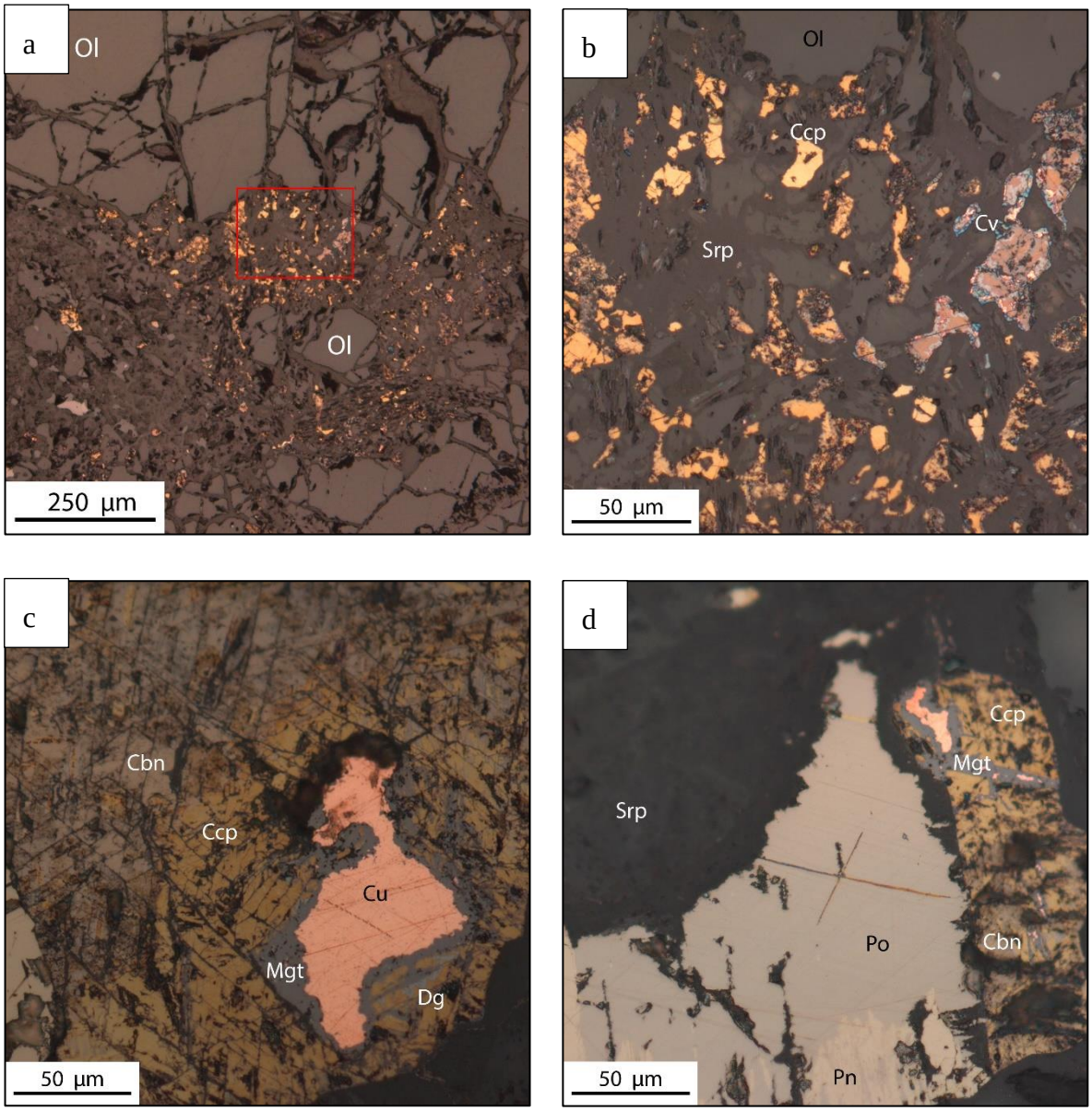

Figure 4.47: a-b) 2 cm pocket containing a wide range of copper minerals (Native copper, chalcopyrite, cubanite and covellite) and pyrrhotite in a matrix of serpentine, calcite and brucite. Red rectangle in a show the location of b. c-d)Large grain of native copper with a rim of iron oxide hosted in a fractured chalcopyrite. The chalcopyrite lies close to or is part of a larger grain of pyrrhotite with pentlandite exsolutions.

Figure 4.48a show the distribution of the brucite-calcite (green-blue) and serpentine (pink) matrix in the pocket, surrounded by olivine (bright green). Figure 4.48b show the distribution of the copper in the pocket.

Figure 4.48c show decomposition of interstitial dolomite to brucite and calcite close to the first area with the large grain of native copper. Left on the figure, dolomite is observed with brucite and calcite bellow.

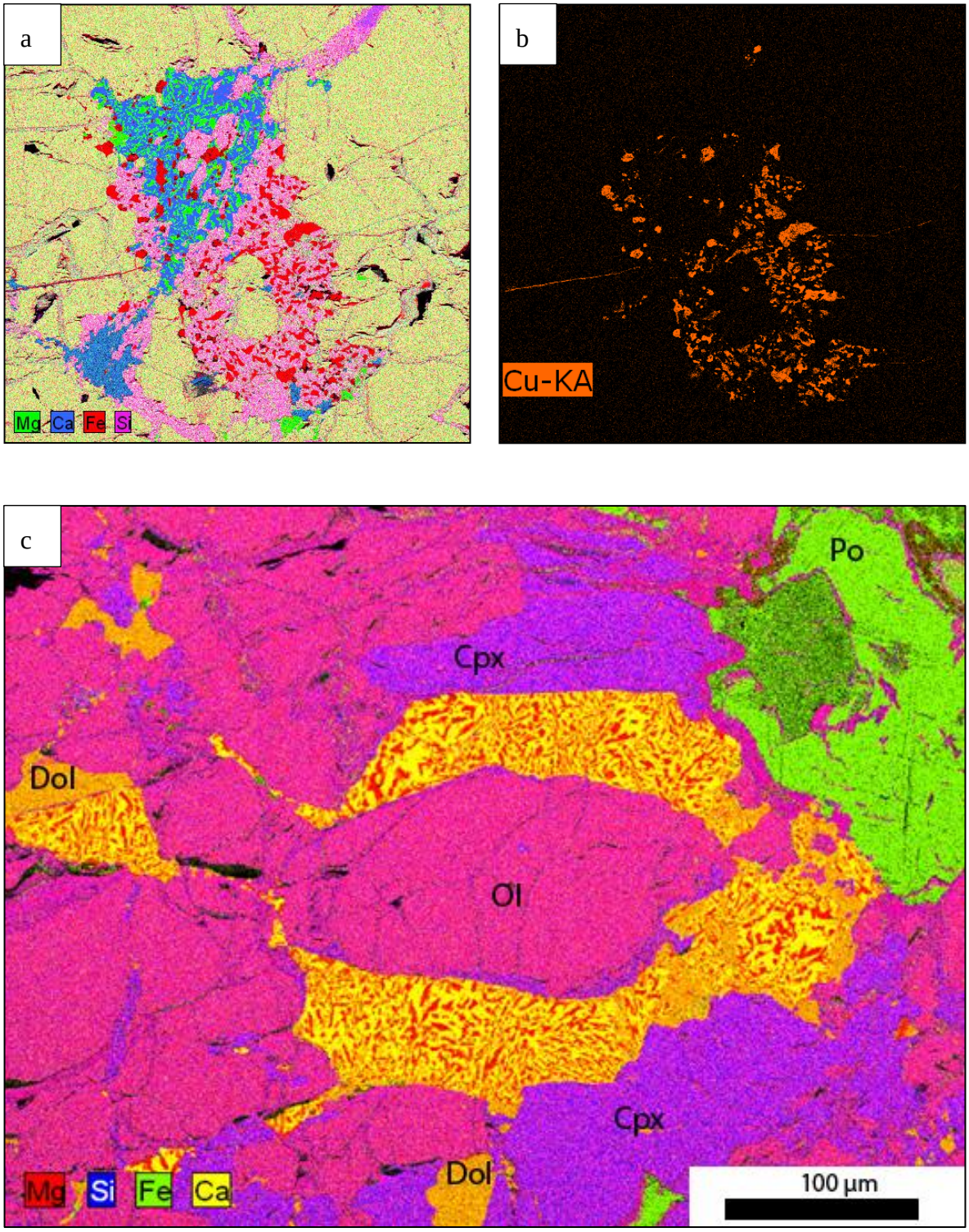

Figure 4.48: SEM-EDS maps. a) Shows the pocket of copper minerals pictured above. b) The same pocket showing how the copper is situated all over the pocket, green and blue colours show the total breakdown of dolomite to brucite (green) and calcite (blue) c) Breakdown of interstitial dolomite (mix of yellow and red) to brucite (red) and calcite (yellow) in olivine (pink) and clinopyroxene (purple). Pyrrhotite (green) grain is less than 0,5 cm from the native copper in Figure 4.47c is located.

4.4.4 XRD

XRD analyses were conducted to quantify the percentages of mineralogical phases in the top four thin section samples of the RF-4 drill core (for spectrums see appendix E). These samples give the modal mineralogy of barren CS and the deepest Cu reef, and the minor Cu enrichment (presented above).

The 4-3250 (590 m.a.s.l.) and 4-5630 (566 m.a.s.l.) samples (barren CS) both consist of 92% olivine and 8% serpentine. The latter also contains a detectable amount of chromium spinel, but too low quantify. The 4-7550 (547 m.a.s.l.) sample is collected from the second copper reef (>800 ppm, Figure 4.37). This sample contains less olivine (89%) and serpentine (6%) than barren CS, it does however contain dolomite (2%), and a detectable amount of Cpx (<3%), Ccp (<1%) and pure copper (<1%). The sample also detected calcite, brucite and pyrrhotite. The 4-10430 (519 m.a.s.l.) sample have low content of olivine (80%) and serpentine (5%) compared to other CS samples analysed. It contain 11% clinopyroxene, 3% amphibole and 1% dolomite. Plus small amounts of orthopyroxene, calcite and brucite were detected. Chromium spinel, chalcopyrite, pyrrhotite and native copper were only confirmed by other methods.

Table 4.2: XRD results of the four shallowest thin sections from the RF-4 drill core, showing the modal mineralogy. Minerals having <1% is present and detected, their concentration are is too small to be measured within the margin of error, data marked as detected were only confirmed present after use of other methods.

Sample	Ol	Srp	Chr	Cpx	Opx	Amp
4-3250 (Barren)	92%	8%				
4-5630 (Barren)	92%	8%	<1%			
4-7550 (Mineralised)	89%	6%	<1%	<3%		
4-10430 (Mineralised)	80%	5%	Detected	11%	<1%	3%

Sample	Dol	Cal	Brc	Ccp	Po	Cu
4-3250 (Barren)						
4-5630 (Barren)						
4-7550 (Mineralised)	2%	Detected	Detected	<1%	Detected	<1%
4-10430 (Mineralised)	1%	<1%	<1%	Detected	Detected	Detected

4.5 Contact zone between Central Series and the Langstrand Gabbronorite

The contacts between the CS and the gabbro has not been studied or described by previously authors. Before the 2014 field season, the only contact between these rocks was observed in the south where they are cut by faulting. Therefore, the contact zone 100 m north of the *finger* was investigated and sampled. Remapping of this contact revealed that we here have a direct contact between the CS-forming melts and the gabbro country rock, hence this may give a better understanding of the melt properties and the extent of gabbro assimilations.

4.5.1 Field observations

The CS in this part of the intrusion is close to the conduit system for the intrusion. The CS is observed to intrude the ULS and the gabbro to the south (rafts and the *finger*). North of the ridge, back-veining of gabbro-norite is observed into the CS, meaning that gabbroic melt separated as a dyke into the CS. The CS-Gabbro contact may be caused by CS melt replacing the ULS due to the large amount of melt that pass through the conduit system. The MZ in this contact is dominated by a gradual transition from dunite to a plagioclase bearing UM with substantial amounts of Cpx (15-20%). While the gabbro is dominated by partial melting of the gabbro, containing large pyroxene oikocrysts with a plagioclase rim (Figure 4.11d), plagioclase with pyroxene rims and Cpx with Opx rim (Figure 4.49). 80 meters into the gabbro, reaction rims are observed between plagioclase and pyroxene, these are much thinner than those in the MZ. The boundary between the plagioclase bearing UM and the partially melted gabbro is highly irregular (Figure 4.11c) and arguably resemble assimilation features. The entire contact zone and the MZ in this area is cut by vertical to sub vertical alkali dyke (Figure 4.11b).

Seven samples were collected along a profile stretching 150m from the gabbro, across the MZ into the CS. Two gabbro samples, three MZ samples and two CS samples make up the profile presented here.

Figure 4.49:The irregular gabbro-CS contact seen towards NE.

Mineralogical and textural descriptions.

The mineralogical phases change throughout the sample profile. The CS contain only olivine, while the MZ contain olivine as the most abundant phase together with clinopyroxene, plagioclase, orthopyroxene and ilmenite. The gabbro consists of plagioclase and clinopyroxene as major phases, together with minor amounts of ilmenite and orthopyroxene. For scanned pictures of the thin sections see appendix A.9-A.15.

The gabbro samples are fine-grained, with a mineralogy consisting of approximately 50% plagioclase, 30% clinopyroxene, 10-15% orthopyroxene and 5-10% ilmenite and biotite. Figure 4.50d show the gabbro sample closest to the contact.

The MZ is generally darker in colour than the CS with visible white plagioclase grains. It consists of 45-60% olivine, 10-20% plagioclase, 15-20% clinopyroxene and 5-10% orthopyroxene. Magnetite, biotite and amphibole is present as an accessory phases. Reaction rims around plagioclase and pyroxene grains are observed throughout the entire MZ. Figure 4.50a show a Opx rim around a clinopyroxene grain in contact with the olivine. Figure 4.50b

show a pyroxene rim (both Cpx and Opx rims observed) around a plagioclase grain in contact with olivine. The olivine in these three samples is strongly serpentinized and fractured, while the other phases are intact.

The CS samples consists of 70-80% olivine 15-25% clinopyroxene and minor amounts of orthopyroxene and magnetite. The olivine found in the samples, specially sample KG14015 is type 2 after Grant et al. (2016), smaller euhedral crystals with no or little internal deformation. Sample KG15016 contains some large olivine grains which is more irregular shaped, however very little internal deformation is observed in these samples. The olivine is more less serpentinized and fractured compared to the olivine in the MZ.

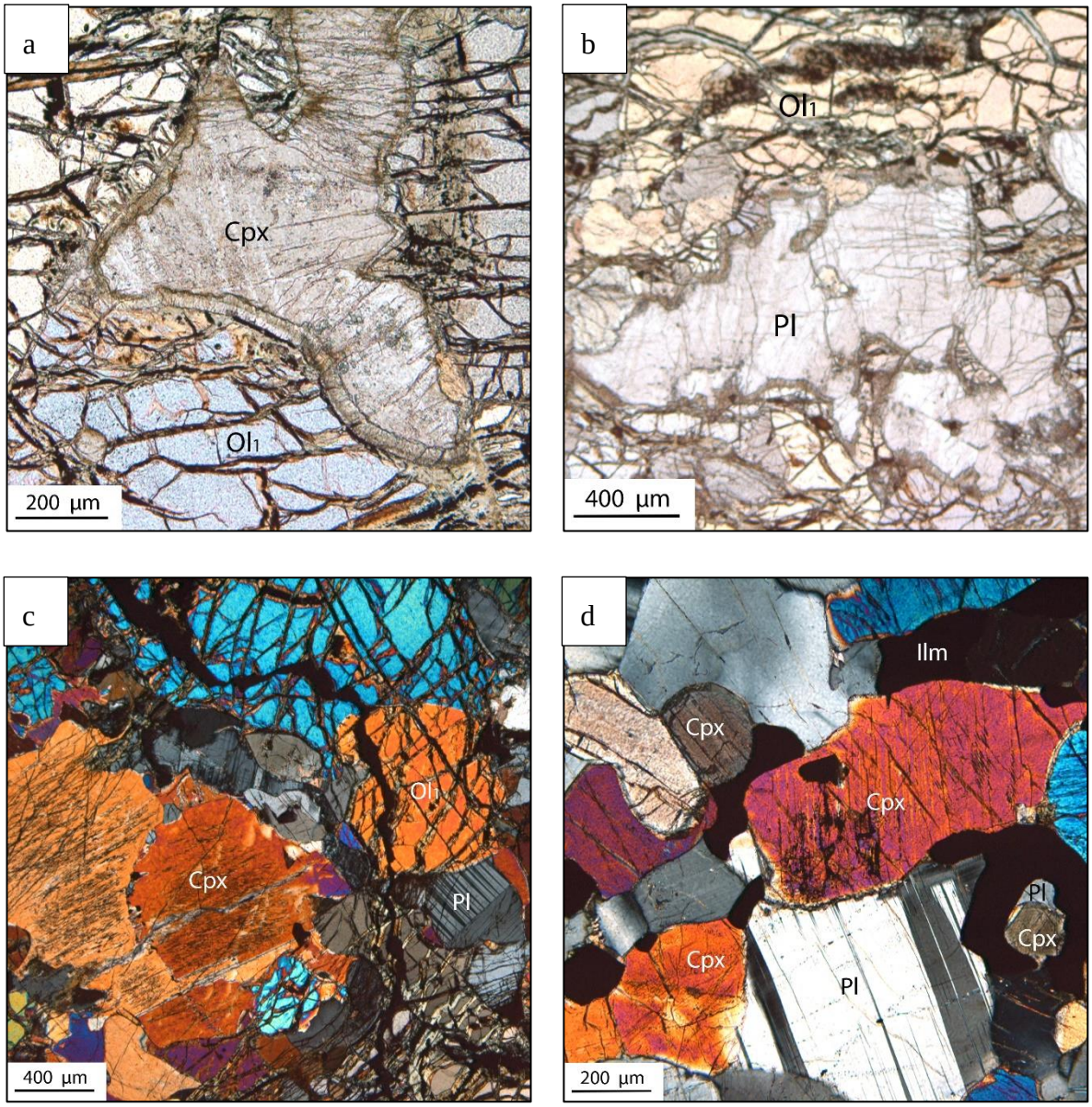

Figure 4.50: a) Cpx with a rim of Opx towards the Ol grains, seen in plane polarized light (ppl) in the MZ sample KG14012 15 meters from the gabbro contact. b) Plagioclase with a rim of pyroxene in the MZ sample closest to the gabbro contact (KG14012). c) Ol inclusions at Cpx grain contact, in the centre of the MZ (KG14013). d) Irregular grain contact between Cpx and Pl is observed in gabbro 15 meters from the contact (KG14011).

4.5.2 Whole-rock and trace element analysis

The seven samples used to describe the gabbro-CS contact are presented on the coming diagrams. The Mg#, presented is calculated by [100Mg/(Mg + Fe), Wt%]. For separate Mg and Fe diagrams see appendix. The contact is set as 0 on the x-axis, for the coming diagrams, with gabbro samples on the right side and CS samples to the left.

Mg# diagram (Figure 4.51) show how the Mg# is decreasing from the CS where it is 62,5%. To the MZ, where the Mg# drop from a value of 62,4 to 60,5 towards the gabbro over a distance of 23 meters. The gabbro has a Mg# = 34.

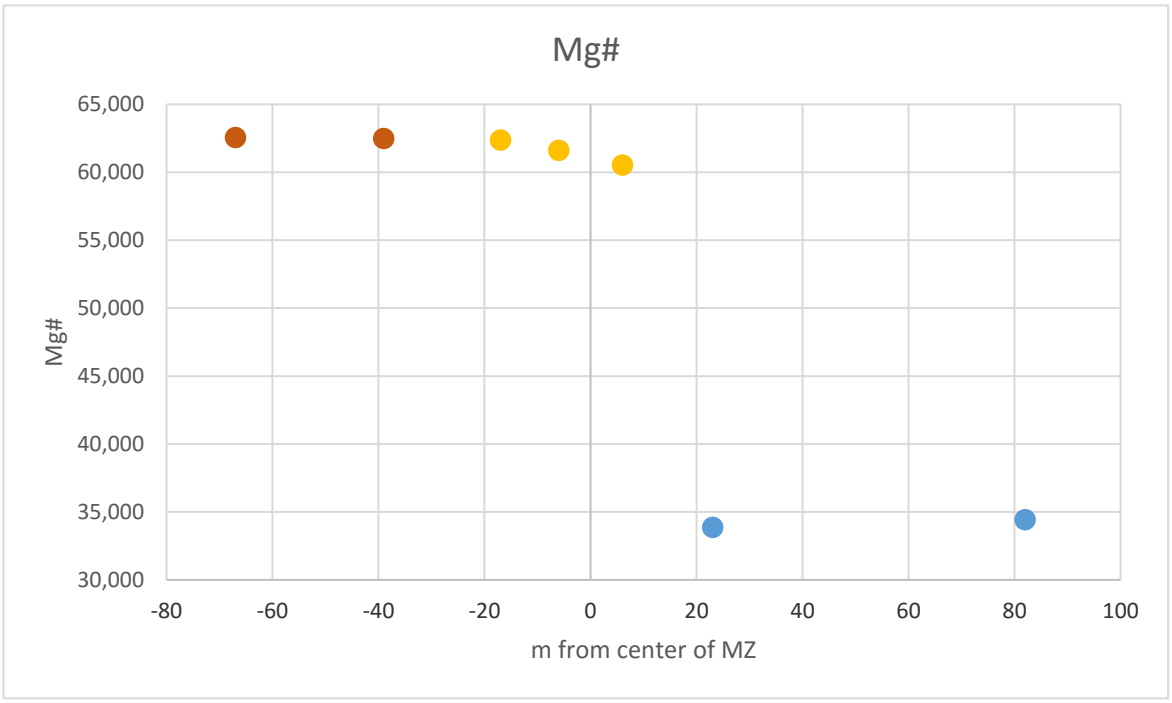

Figure 4.51: Bulk rock chemistry of Mg#. Blue points is gabbro, yellow points is MZ and red points is CS samples.

Trace element diagrams show the evolution of Sr, Eu and Cr as trace elements across the contact zone (figure 4.52). Sr and Eu show the same increasing trend from the CS through the MZ to the gabbro. The observed increase in Eu probably is Eu^{2+} due to the appearance and increase in plagioclase in the MZ and gabbro compared to the CS. Sr increase from 10 ppm in the CS to 140-150 ppm in the MZ and to 600-630 ppm in the gabbro. This indicate that the assimilation is restricted to the MZ, as suggested by Øen (2013) and Grant et al. (2016).

The Marginal Zone have the highest content in Cr, and show a decreasing trend from the samples close to the CS towards the gabbro. The values drop from 1940 to 1440 and to 1180 close to the gabbro contact. Cr content in the CS is 670 ppm in both samples, whereas the gabbro only contain 100 ppm. The low Cr is explained by the absence of chromium spinel, which is highest in the MZ.

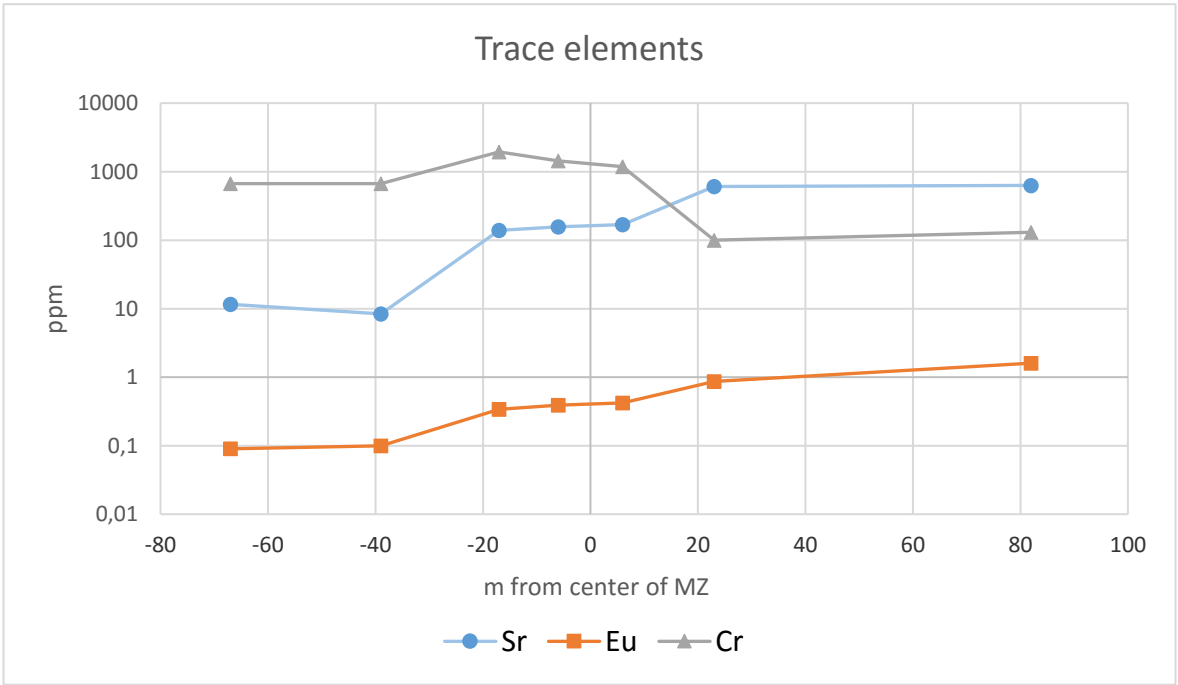

Figure 4.52: Trace elements over the CS-gabbro contact.

Trace elements and Rare Earth Elements (REE)

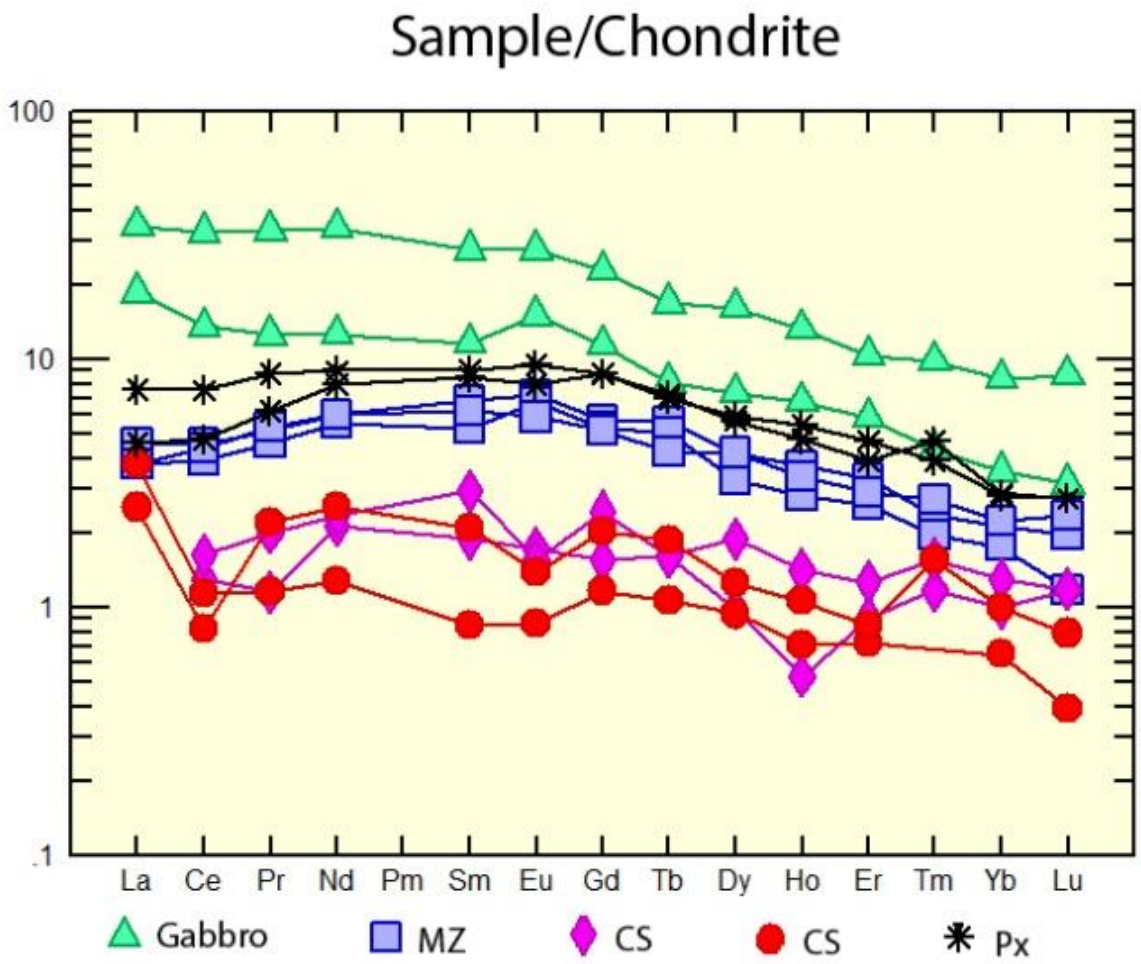

Figure 4.53: The samples are normalized to C1 chondrite and primitive mantle after Sun and McDonough (1989). Green, blue and pink samples are surface samples from the contact. The red samples are CS is from RF-4 (4-3950 and 4-24560), black is the pyroxenite in RF-4 (4-35970 and 4-36900).

Figure 4.53a show sample over C1 chondrite after Sun and McDonough (1989). The gabbro shows an enrichment in the REE, which decrease towards the contact, i.e. the most enriched gabbro sample is the one furthest away. The most enriched gabbro sample show an enrichment up to 30 times chondrite concentration for the LREE, with a steady decrease to the HREE, where the enrichment is 10 times the concentration of chondrite. The KG14011 sample goes from 20 times enriched in La towards only three times more enriched in Lu, this sample do show a small anomaly in Eu.

The three MZ samples (KG14012-KG14014) show minor enrichments in the LREE from 3-5 times the chondrite concentration in La to 7-8 times the concentration in Eu. From Eu the values decrease to 1-3 times the concentration in Yb and Lu.

The CS samples show the same decreaing trend from La to Lu as the other samples, however with near chondrite values. A small negative anomaly on Eu, before a steady decrease from Gd to Lu. One of the samples shows a negative Ho anomaly with 0,4 times the chondrite composition. The CS samples from the RF-4 drill cores were randomly selected 39,5 and 265,6 meter down the drill core. These samples shows a more steady decrease from La to Lu.

The pyroxenite from RF-4 show slightly elevated but essentially the same trend as MZ., with a slight increase in the LREE and Eu, from La to Eu (5-7 on La to 8-10 on Eu). The HREE decrease to 3 times chondrite content on Lu.

Enrichment of REE is dependent on the mineralogy and the composition of the parental melts forming the cumulates. For Eu the known Eu^{2+} fits into the atomic lattice of plagioclase where it substitutes Ca^{2+}. The high trace element content in the gabbro and pyroxenite from RF-4 compared to the CS, may be due to Cpx being more compatible for such elements than olivine. This is supported by the increase in trace elements with increasing Cpx content. The gabbro may have increase values due to the high Cpx and plagioclase content, but may also be enriched due to a less fractionated parent melt.

4.5.3 EPMA

7 thin sections from the profile were analysed with EPMA. Data averages with standard derivation for each samples is can be found in appendix C.9 – C.20. Detection limits, counting times and standards used analysing these samples are found in Table 3.1 and Table 3.2. Forsterite and anorthite numbers are calculated following Deer et al. (1992) end-member calculations for olivine and plagioclase.

The EPMA data show that clinopyroxene in the gabbro become more Mg-rich, and that the plagioclase becomes more Ca-rich towards the CS contact. The MZ samples show relatively

consistent Mg# ranging from 70,41 to 70,94. While in the CS Mg# drop from 73,2 to 72,5. The forsterite content in olivine ranges from 77,41 in the MZ sample closest to the gabbro to 78,52 in the CS.

The Mg# values of in Cpx and forsterite content in olivine, in the CS samples is low compared to the values observed in the RF-4 and surface samples collected in the central parts of the CS. This indicates that the CS is affected by chemical diffusion between the gabbro and CS. These values are low compared to the forsterite content in samples from central parts of the intrusion, which are 82-86 in the CS and 79-81 in the pyroxenite in RF-4.

Table 4.3: EPMA results showing the change in Mg# in Cpx, plagioclase and olivine composition throughout the gabbro-CS contact. Meters from centre of MZ in brackets.

Sample	**Rock type**	**Mg# (Cpx)**	**An%**	**Fo%**
KG14010 (82 meters)	Gabbro	61,05	81,99	
KG14011 (23 meters)	Gabbro	64,23	83,21	
KG14012 (6 meters)	MZ	70,43	86,34	77,41
KG14013 (-6 meters)	MZ	70,41	87,81	77,64
KG14014 (-17 meters)	MZ	70,94	90,02	77,82
KG14015 (-39 meters)	CS	73,23		78,52
KG14016 (-67 meters)	CS	72,50		78,38

4.5.4 Normative mineralogy

The CIPW normative calculation method is used to estimate a possible mineral assemblage of the contact zone. The CIPW norm data is calculated using spreadsheet by Kurt Hollocher (http://minerva.union.edu/hollochk/c_petrology/norms.htm, from 28.01.2016 accessed 05.05.2016). The CIPW data is estimated by calculating with idealized end member minerals crystalizing under equilibrium at low pressure, based on whole-rock data. The Reinfjord intrusion is emplaced under high pressure, 6-8 kbar (Grant et al., 2016), which might explain the low total% for the MZ and the CS (93,5-95,2%).

The CIPW estimation correlates best with observed modal mineralogy in the gabbro. The olivine estimates in the MZ and the CS are lower than observed, the pyroxene estimates however are larger than observed. An explanation for this might be that the olivine is calculated

as pure forsterite while the MZ and the CS contains $FO_{77\text{-}78,5}$ in these samples. The low totals will also have an effect on the results.

Table 4.4: CIPW normalized calculation after Hollocher, presented in percent. Meters from centre of MZ in brackets.

	KG 14010 (82 m)	**KG 14011** (23 m)	**KG 14012** (6 m)	**KG 14013** (-6 m)	**KG 14014** (-17 m)	**KG 14015** (-39 m)	**KG 14016** (-67 m)
Plagioclase	52,5	52,3	18,0	16,3	16,6	2,0	2,4
Diopside	16,0	18,2	16,1	16,8	20,1	6,2	7,5
Hypersthene	17,3	12,8	6,0	10,0	10,1	9,9	7,5
Olivine	3,5	4,1	50,0	48,1	45,1	73,2	69,5
Ilmenite	7,1	10,1	0,8	0,7	0,8	0,3	0,3
Magnetite	1,8	1,8	2,2	2,1	2,0	2,7	2,6
Orthoclase	1,5	0,9	0,3	0,1	0,2	0,0	0,1
Apatite	0,4	-	-	-	-	-	-
Chromite	-	-	0,2	0,2	0,3	0,1	0,1
Pyrite	0,3	0,3	0,2	0,1	0,1	0,1	0,1
Total	100,5	100,5	93,8	94,4	95,2	94,4	93,5

4.5.5 Finger

The Finger sill intrudes the Langstrand gabbro east of the lake district as previously described. The CS dyke is connected to the CS just south of the contact profile presented above. It intrudes into the gabbro and is outcropping for 200 meters from north to south, following the gabbro layering. It is between 15 meters thick in the opening and tapering to zero over 300 meters. Were samples were collected the thickness is between 5-10 meter.

As part of describing the contact zone the finger was investigated, 4 samples were collected and two of these analysed by EPMA. The KG14003 is located close to the KG14010 gabbro sample, while the KG14002 sample is located further away from the CS (Figure 4.54 and appendix A.4).

The KG002 contain olivine (30-35%), pyroxene (30-35%), biotite (15-25%) and plagioclase (5-10%), while the KG14003 sample contain olivine (50-60%), pyroxene (30%), plagioclase (5-10%), biotite (<5%) and ilmenite(<5%). Both samples show serpentinization as seen on the thin section scans in appendix.

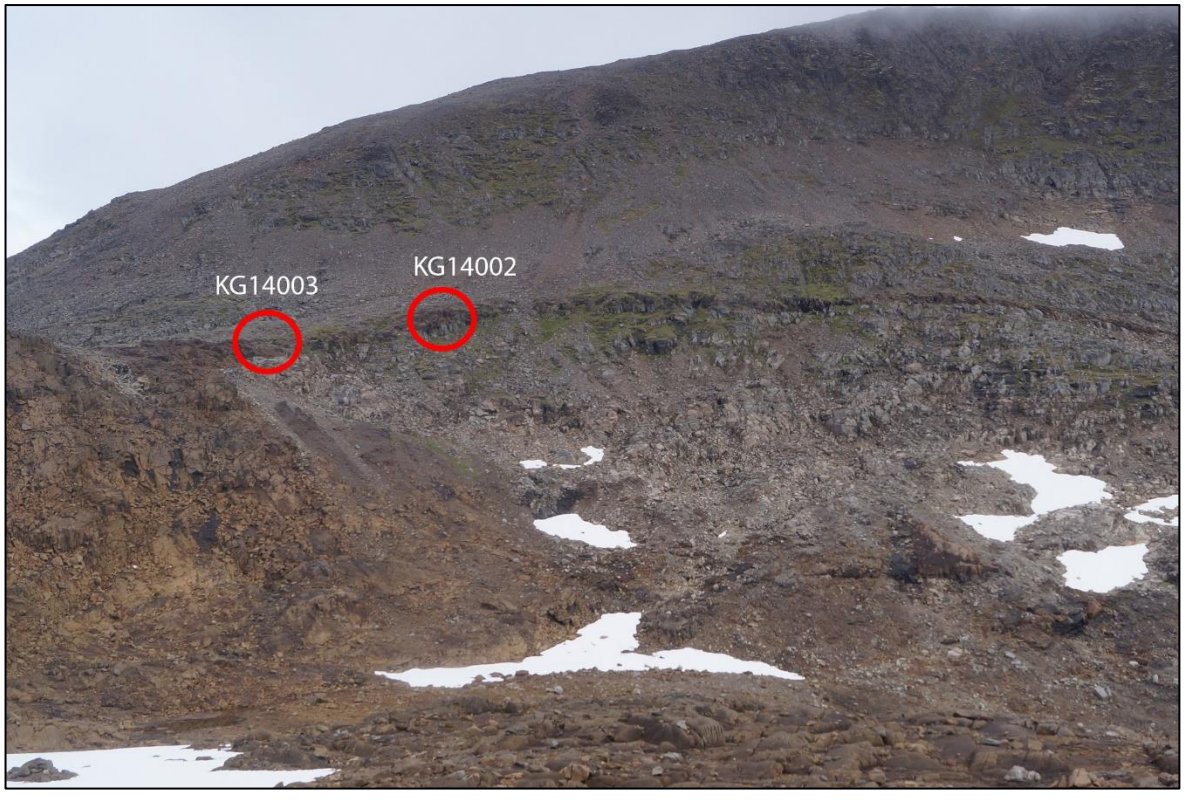

Figure 4.54: The “Finger” marked with sample locations.

The EPMA average analysis of the two samples analysed is presented in Table 4.5. This show a Mg# in Cpx at 68,15 for KG14002 and 67,33 for KG14003. The latter only one analysis were taken of the pyroxenite. The anorthite content in plagioclase show a minor increase from the KG14002 with 84,47 anorthite sample to the KG14003 sample with 87,62 anorthite. The forsterite content in olivine show a large variance in the two samples, a forsterite content at 74,79 for the KG14002 sample and 73,35 for the KG14003 sample.

Table 4.5: EPMA results showing the change in Mg# in Cpx, plagioclase and forsterite content in olivine. Average data with number of analysis is brackets.

Sample	Mg# (Cpx)	An%	Fo%
KG14002	68,15 (12)	84,47 (7)	74,79 (12)
KG14003	67,33 (1)	84,62 (7)	73,35 (9)

Comparing this with the MZ and the CS data show that the finger samples are more primitive with lower Mg# in clinopyroxene, lower anorthite content in plagioclase and lower forsterite content in olivine. Indicating rapid cooling (quenching) of the intrusive melt and low contamination and assimilation of contry rocks. Serpentinization and formation of biotite do show alteration and recrystallization, forming the hydrous minerals.

5 Discussion

5.1 Reinfjord ultramafic intrusion

The aim for the discursion is to give an better understanding of the CS evolution and the occurring ore-forming processes in the Reinfjord intrusion. In addition, present the new interpretation on syn- and post magmatic processes that have influenced the Reinfjord intrusion.

Some of the areas in this new map have not been remapped and is based on previous work by Emblin (1985), Anker-Rasch (2013) and Øen (2013). This is especially the case the Lake district and the western part of the plateau, our focus have been in the northern less explored areas.

The Marginal Zones around the complex share many common features that is unrelated to their position in the complex. The MZ is a hybrid zone that is determined by the type of UM melt and the type of host rock. Combining the Marginal Zones into one zone gives a more clear and correct approach of the MZ, compared to earlier interpretation of three or four separate zone.

Tectonic features

The Reinfjord Ultramafic complex have experienced post crystallization stress. Post-crystallization stress is seen as a ductile deformation phase occurring short after crystallization while the intrusion was still hot, and a brittle phase occurring after cooling.

The ductile deformation phase can be observed by ductile deformation of layering and magmatic veins (Figure 4.7). Ductile deformation is less profound than the later brittle phase.

Brittle faulting postdate the ductile deformation. Faulting have provided permeability for fluids and have resulted in strongly serpentinized zones. Emblin (1985) classified this brittle deformation into; a SW-NE striking fault system, a system with little or no displacement and a E-W trending fracture system which cut and displaces the former. Little work have been conducted and published on the fault systems, however Grant, Larsen and Sørensen (T. Grant,

R.B. Larsen and B.E. Sørensen 2016, personal communication, 14 Mars) is working on a theory that the large faults within NE-SW trending fault systems do show vertical displacement. The E-W trending fracture system presented in Emblin (1985) displaces the earlier NE-SW system and hence is a later phase. His fracture systems is based on the large fault from Storvatnet. If these connected faults by Storvatnet can be connected to the large fault in south that separates the intrusion from the gabbro. This fault system is rather striking SE-NW.

The SE-NW striking fault in south need significant displacement for the MZ to be lacking and to cause the drag observed in the gabbro close to the fault (Figure 4.24). The angle and the drag in the gabbro indicate a large normal fault. The displacement of this fault is probably larger than 50 meters, this based on that the marginal zone (between 50 and 100m wide) is lacking.The connected faults found by Storvatnet stretches for several km into the intrusion eastwards, they are also found east of the intrusion (either the same fault or part of the a set of connected faults). It is therefore likely that the southern SE-NW fault, follows the entire UM-gabbro contact northwest in Bonnvikdalen. (Figure 5.1 and Figure 5.3). This will explain why the entire southern contact lack the Marginal Zones.

Figure 5.1:Possible faulting separating the ULS and gabbro in south-west.

The SE-NW striking fault in the south show little or no serpentinization compared to the Storvatnet faults. This may be explained by that the northern SE-NW striking faults is close to the conduit system and that these faults worked as a permeable path for late magmatic fluids. The southern fault show no signs of fluid flow, this may be due to low permeability.

A possible fault that where not mapped is a SW-NE striking fault located by Storvatnet. This possible fault goes from the gabbro-LLS contact south of Storvatnet, to a small lake north of Storvatnet (figure 5.3). This fault was not investigated in field, as the observations were first connected later. It is therefore not mapped due to the uncertainty. The fault is believed to exist on the basis of the observation seen in Figure 4.3a and Figure 5.2 and depressions in relief by Storvatnet. Figure 4.3a show the gabbro layering on the left and fractured or faulted LLS on the right. Figure 5.2 show the northern observation, where the gabbro show a fracture zone. East of the possible fault the gabbro is darker and have rusty colour (Figure 4.16 and figure 5.2).

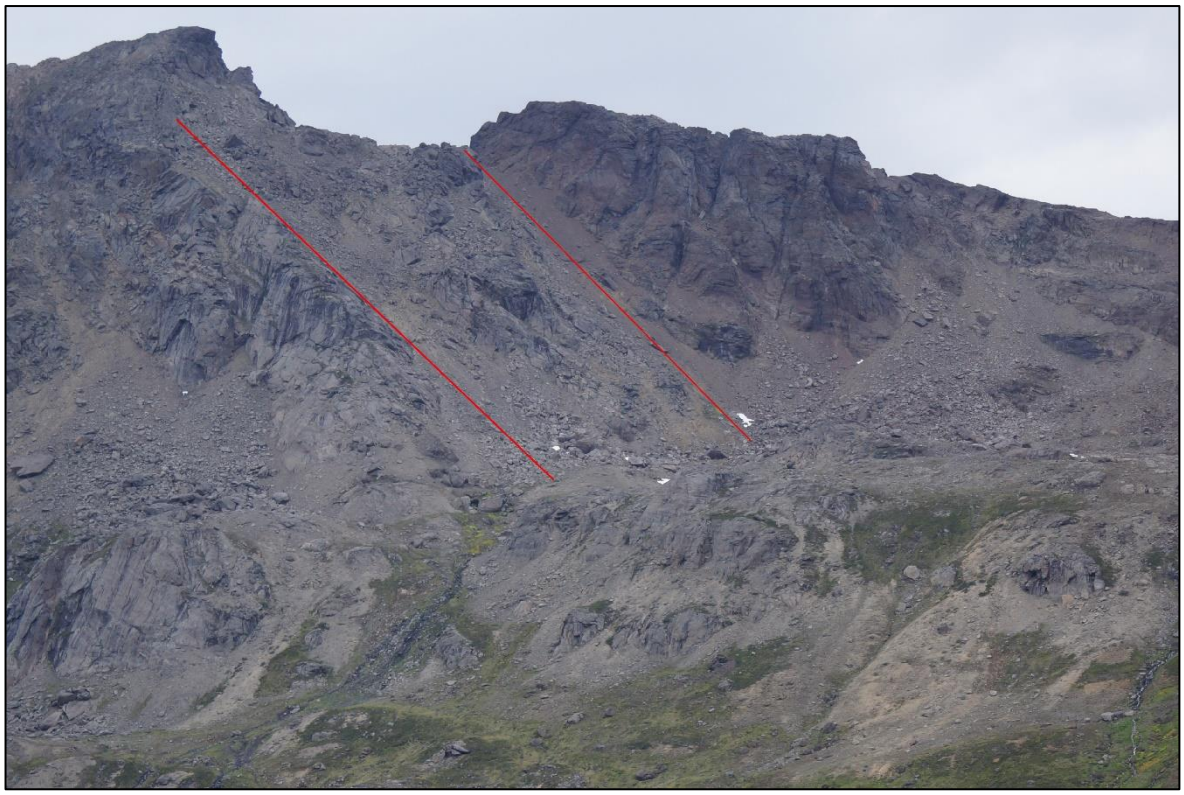

Figure 5.2: Possible NE-SW striking fault north of Storvatnet in the gabbro. Gabbro is rusted east of the possible fault.

If the displacement in the fault systems are significant this will have a major impact on the understanding of the intrusion. As the NE-SW and the SE-NW fault systems are dipping towards SE and NE respectively, and the fault systems is most likely a normal fault (at least the

SE-NW fault system). This implies that the LLS may have been faulted into closer contact with the plateau intrusion.

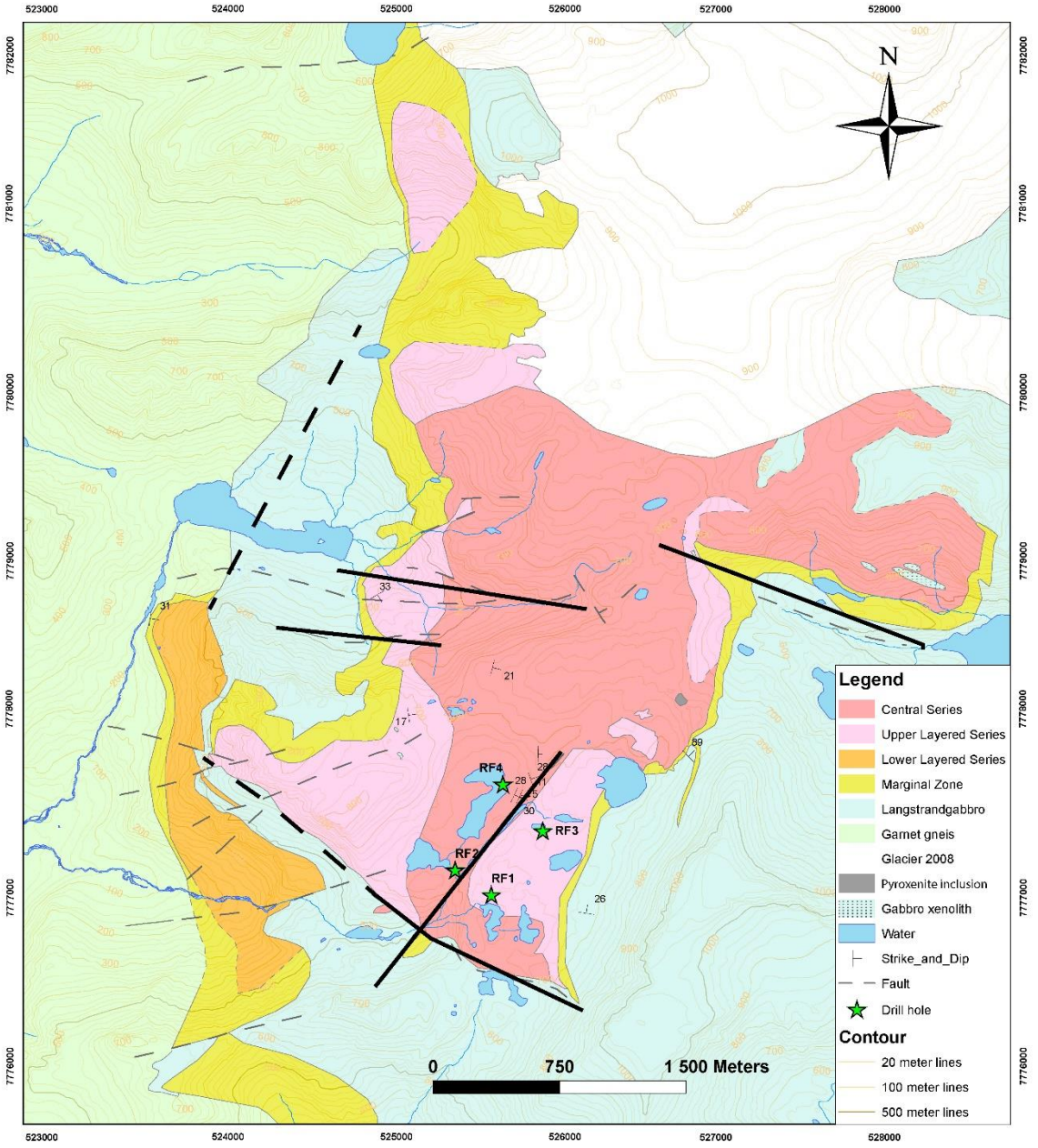

Figure 5.3: Major faults and possible major fault in the Reinfjord intrusion.

In later years, receding of the icecap that previously were covering the top of the complex revealed a conspicuous roof zone at 900 m.a.s.l.. This zone show sub horizontal gabbro dipping towards NE, lie on top of the CS. Numerous gabbro xenoliths are observed in the south facing cliff underneath this zone. Most of these xenoliths are shaped as sheets oriented with the layering of the CS. The shape and location of these xenoliths can be explained by either as the

residue of an earlier roof zone which were penetrated and enclosed by the intruding UM melt. Or by settling from the roof zone due to density contracts compared to the intruding melt.

In the ULS in southwest, just north of Bonvikdalen, on the mountain located east of the LLS, large amount of gabbro xenoliths are observed (Figure 5.4). These xenoliths resembles the xenoliths found in NE with sheetlike shapes oriented within the layering of the ULS. They are smaller but more abundant than what is observed in NE. The xenoliths have reacted with the ULS melt and are partly assimilated, all xenoliths are enriched in pyroxene. Often covered with a rim of almost pure pyroxene.

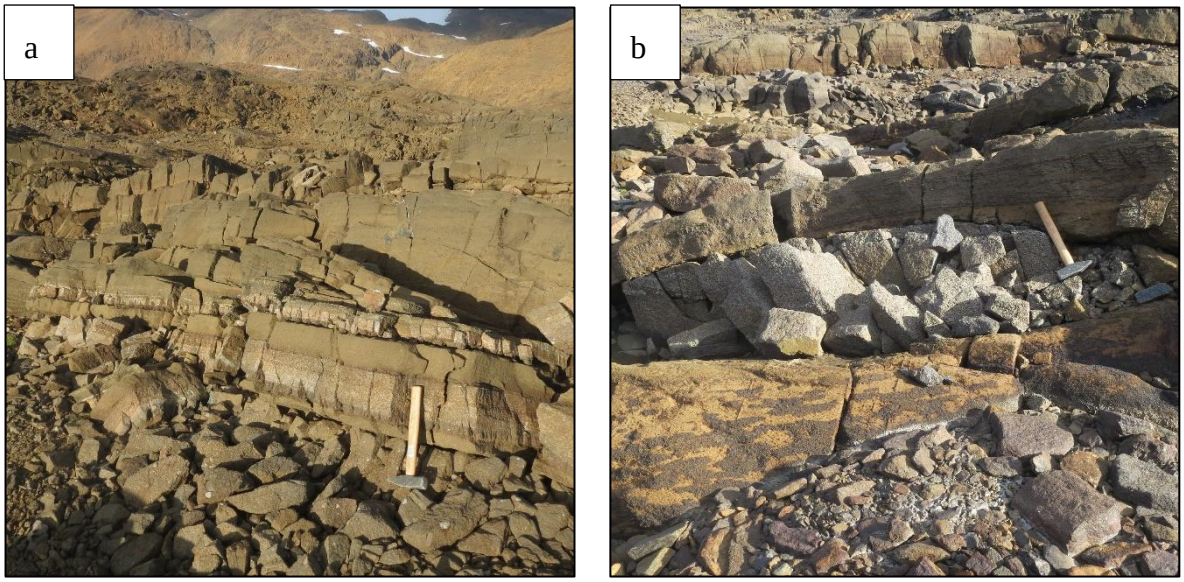

Figure 5.4: Xenoliths hosted within the layering of the ULS, located in SW.

The area with the xenoliths in the ULS is in the same area where Emblin (1985) observed plagioclase in the otherwise plagioclase free ULS (Figure 5.5). The appearance of plagioclase and large amounts of gabbro xenoliths indicate that the ULS melts were in close proximity to the gabbro. He suggest that assimilation of gabbro by the ULS melts resulted in contamination, and hence the plagioclase bearing ULS. He further suggest that the contamination of the ULS melt come from assimilation of the gabbro screen observed underneath the ULS. If this gabbro-ULS contact is faulted as presented earlier, the source of the plagioclase is most likely from a local roof zone as observed in NE. Contamination from the wall is not likely, as the plagioclase is observed 300 from the contact (Figure 5.5).

5.Discussion

Contamination from a roof zone best explain large amount of gabbroic xenoliths and plagioclase observed in this area. This author will introduce three theories on the roof zone origin and emplacement in the ULS. The roof might have existed just above the mountain on 800 m.a.s.l. which is only 50 meters away from where the xenoliths are observed. Or the xenoliths may be located far from the roof as seen in NE where sheet shaped xenoliths are found hundreds of meters beneath the roof itself. The shape of the xenoliths imply that the intruding ULS melt intruded into the gabbro roof utilizing the internal layering in the gabbro forming sheet shaped xenoliths. So the second possibility is that these xenoliths are then the residue from the roof which are assimilated and expanded upwards by the continuous influx of large amount of UM melts into the magma chamber. Third possibility is that the roof is located higher up with xenoliths dropping in the melt due to density contrasts. The xenoliths is then assimilated by the ULS forming the plagioclase bearing ULS.

Of these possibilities, the second option is more likely as correlates best with the observations from the NE roof zone. The roof zones are likely only local roof zones which prevent the magma locally. This is supported by the elevation of the roof zones, where the northern lies at approximately 900 m.a.s.l. while the possible SW is located at 800 m.a.s.l..

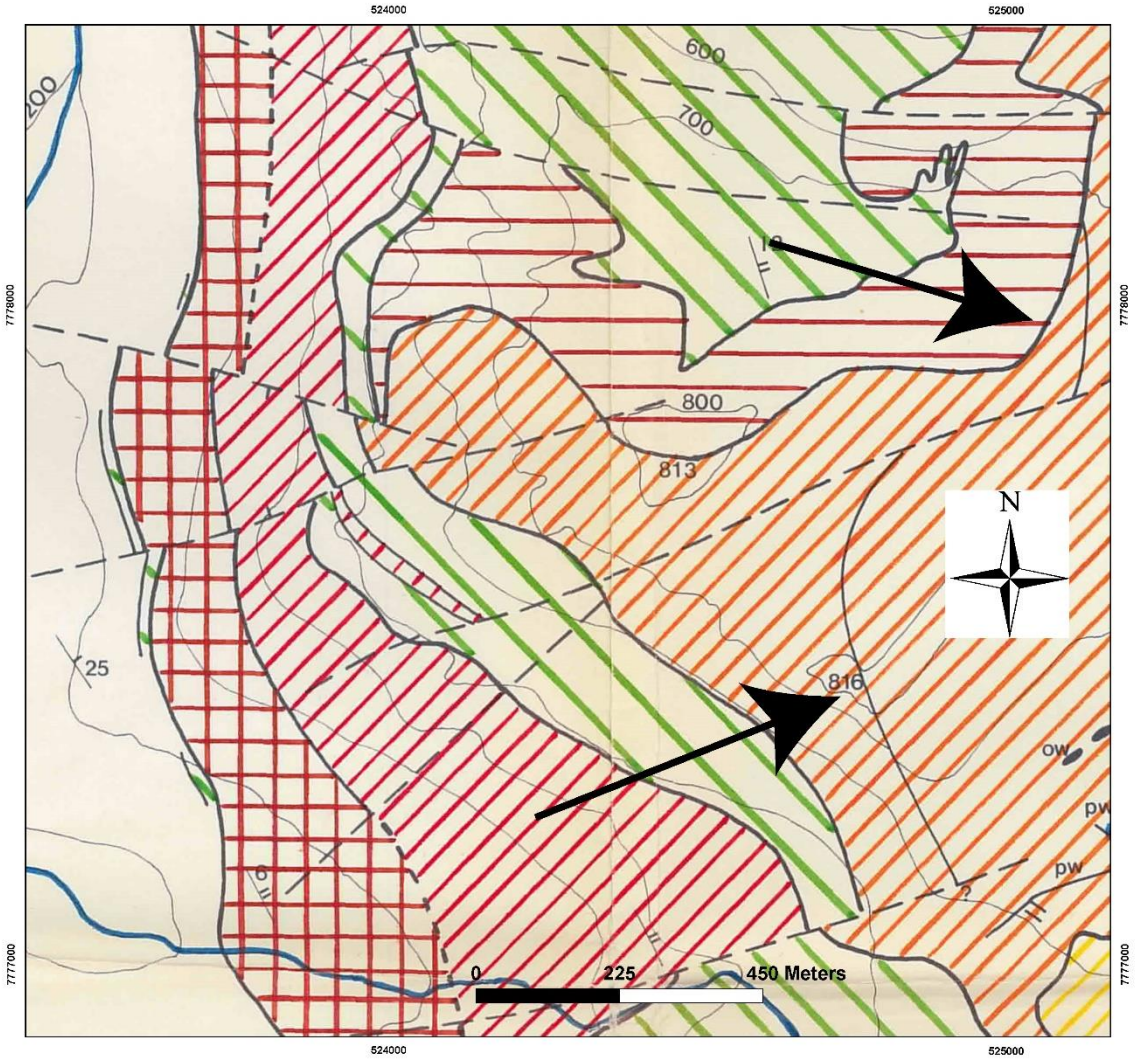

Figure 5.5: Part of the map by Emblin (1985). Where he observed plagioclase left of the thin line marked by arrows, in the plagioclase free ULS (orange diagonal lines).

Slumping (Figure 4.6a) is observed in this area, this is a magmatic process formed by density contrasts in crystal mush. This process may have been caused by influx of new more primitive UM melt or crystal mush over a contaminated plagioclase bearing ULS mush. Density contrasts between the different crystal mush may have caused the slumping to occur.

5.2 Evolution of Central Series

The central series shows evidence of continuous new pulses of magma entering the magma chamber. Co/Cr ratio and Mg# show a minimum of 10 magma recharge events, in the CS from RF-4. As many as 15 magma recharge events can be argued to exist. The large abrupt changes in chemical composition suggests low interaction between new melt and the cumulus pile (Grant et al., 2016).

Bennett et al. (1986) presents in his summary of the ultramafic intrusions in Seiland that all mafic-ultramafic complexes in the Seiland Intrusive Province show "reverse fractional crystallization". Where the magma crystalizes in the reverse order than what would be expected by a fractionating magma. Such an event is observed in the CS, where the CS becomes enriched in Mg# and forsterite content in olivine from 290 m.a.s.l. to 440 m.a.s.l.. From 440 m.a.s.l. the Mg# and forsterite content decreases, which for an fractionating magma, with decreasing Mg# and forsterite content in olivine.

There are several possible reasons for this "reverse fractional sequence", Bennett et al. (1986) suggests a upward migrating magma chamber, such that new cumulates will be emplaced beneath earlier emplaced cumulates. This theory is unlikely as the CS shows the expected trend for an fractionating magma above 440 m.a.s.l.. He also suggest that the successive tapping of a vertical zoned deep-situated magma chamber. Other theories is presented by Irvine (1974) which suggest that the rising magma may be heated from the latent heat created by previous magma rising through the conduit system or that the mantle source have been enriched in olivine due to episodes of partial melting. Grant et al. (2016) suggests melt-rock reactions, caused by replenishment of new more primitive magma into the cumulus pile, where it interacts and replaces previous cumulates with olivine. This replacive dunite in the ULS is observed in figure 4.8a, where olivine replaces the ULS cumulates. They suggest channelized flow as the dominant mechanism for melt transport (Figure 4.19) (Grant et al., 2016).

The change from increasing to decreasing Mg# and forsterite content (i.e. from reverse fractional sequence to what is expected from an fractionating melt) require a change a change in conditions. What this is dependent on the reason for the "reverse fractional sequence". However if the parent melt became more and more primitive in the first place, stabilizing the

intruding melt with regards to its composition and allow this melt to fractionate, this may cause a reversal in the Mg#. However as Grant et al. (2016) suggest, the cumulates have been affected by more complex processes than simple fractional crystallization.

Above 550 m.a.s.l. the Mg# and forsterite content stabilize around Mg# at 70 and Fo_{83-84}. This may be explained by large influx of magma passing in the system from a compositional stable parent melt that experience the same amount of fractionation.

Fractional crystallization

As fractional crystallization is documented to have occurred in the Reinfjord Intrusion (Bennett, 1971, Bennett, 1973, Bennett et al., 1986), this thesis will try and estimate the amount of fractionation in the upper part of RF-4 from 440 m.a.s.l. and up.

Picritic melt is suggested as the parental magma for the ultramafic complexes in the SIP, with up to 20 Wt% MgO with temperature around 1450°C (Bennett et al., 1986). Griffin et al. (2013) suggest another parent melt; a dunite with 40 Wt% MgO and temperature at 1650°C as the parent melt for the Nordre Bumannsfjord complex. Forming the mafic intrusions in the SIP is based on massive assimilation of gabbros. This is considered too drastic, so the melt concentration used for the calculations is based on the on picritic dykes from Robins (1975).

Mn melt concentration is based on picrite dykes sample 1752 in Robins (1975), and gives a Mn concentration in the melt on 0,21 Wt%. Nickel concentration in the melt is not reported in Robins (1975). This is therefore estimated from the most primitive sample in RF-4, which is the RF-4-19900 sample from 440 m.a.s.l.. Melt concentration is calculated from the partition coefficient of nickel in olivine, $D_{Ni}^{Olivine/melt}$ being 4,5, based on the partition coefficients from Matzen et al. (2013) with a temperature of 1450°C. Giving a melt concentration of nickel: 0,37895/4,5 = 0,084 Wt%. The partition coefficient of Mn in olivine is dominated by the degree of polymerization of the melt (NBO/T). It is set to $D_{Mn}^{Olivine/Melt}$ 0,85 and 0,9 after Kohn and Schofield (1994) using the data with a temperature on 1450°C from Watson (1977).

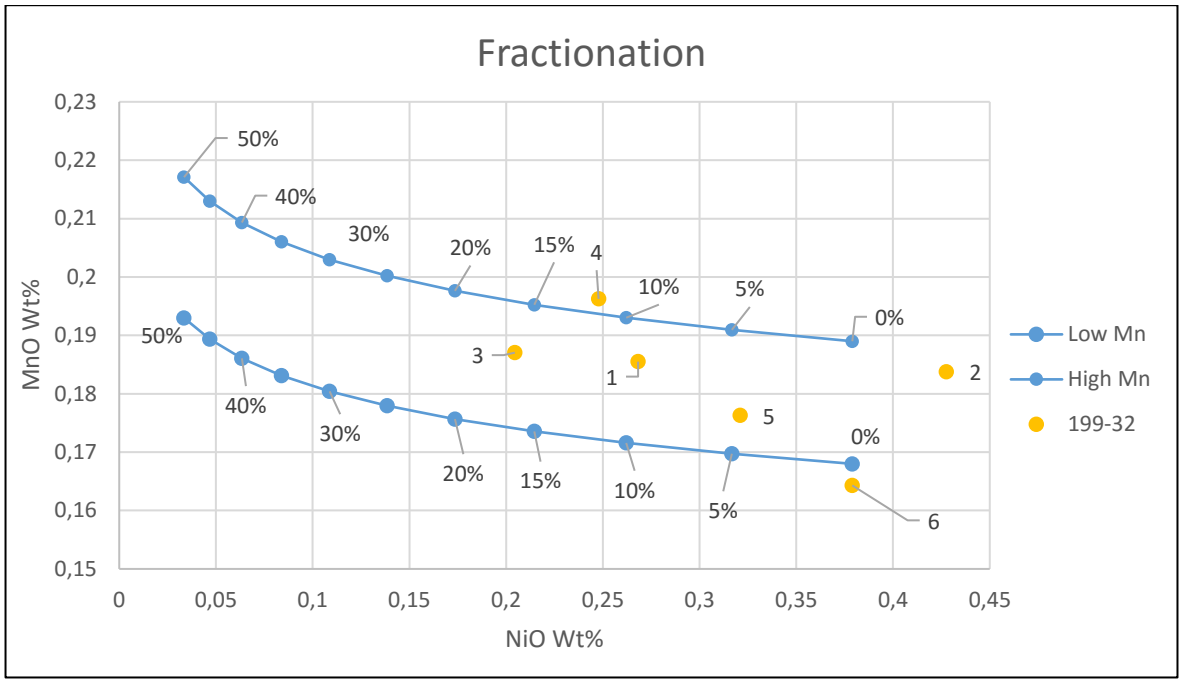

Figure 5.6: Fractionation of the CS from 440 to 590 m.a.s.l.. Numbered after depth from top down.

Grant et al. (2016) and Figure 5.6 show variation from simple fractional crystallization, this suggest more complex evolution than only fractional crystallization. This may be caused by replenishment of more primitive melt, replacement or melt-rock reaction by recharge of new melt into the cumulus pile or by migration of interstitial liquids (Grant et al., 2016). Other uncertainties is the parent melt composition and partition coefficient used in the calculation. The NiO melt concentration is an estimate, calculated from the most primitive cumulate olivine composition. Kohn and Schofield (1994) argue that the Mn partition coefficient in the melt may vary with changing MgO concentration in the melt. Post-magmatic alteration may have affected the composition of the olivine cumulates. From the XRD and SEM we know that the CS have been affected by serpentinization. Hydrothermal breakdown of chalcopyrite to native copper is present in two of the samples used to calculate the fractional crystallization. All this bring inaccuracy to the calculations.

However, fractional crystallization is likely to have occurred. And Figure 5.6 show that the most fractionated magma will have fractionated between 15-20%. This indicates that the conduit system of the Reinfjord ultramafic complex did continue upwards with large amount of melts.

Pyroxenite

The pyroxenite in RF-4 (232-274 m.a.s.l.) is the only large scale pyroxenite found outside the pyroxenite layers in the LLS. Other pyroxenites are found in small patches in the MZ and as patches of pegmatite in the ULS. The LLS pyroxenite is documented by Emblin (1985), where pyroxenite is found as units in the modally layered LLS. The drill core were examined and sampled before the chemical results were ready. Therefore only two samples were collected and analysed (Figure A. 16 and Figure A. 17). These samples consists mostly large Cpx grains (up to several cm in size) with bands and pockets of olivine, mainly olivine type 2 (recrystallized grains with little to no internal deformation) (Figure 5.7).

Analysis of the pyroxenites show that the RF-4 pyroxenite is chemically different than the LLS pyroxenite. As it contains lower amounts of Cr_2O_3, 0,2 to 0,3Wt% compared to 0,6-0,8 Wt% in the LLS (one sample containing 0,38 Wt%) (Emblin, 1985). It also contains less TiO_2 and more CaO, compared to the LLS pyroxenite. Figure 4.34 and Figure 4.36 show that the pyroxenite is cryptically layered. Mg# decrease from 68 in the lower data points to 64 by the CS contact. Ni content decrease steady from 2000 ppm in the second to last data point to 500 ppm at the contact. Figure 4.40 show that olivine (type 2 - Ol_2) have Fo_{79-80}, which is distinct lower than the olivine composition in the CS ($Fo_{82-85,7}$).

The enrichment in trace elements and C1 chondrite normalized REE (Figure 4.53) compared to the CS and the MZ, may be explained by contamination from assimilation of gabbro. If the pyroxenite is the first UM melt intruding and opening the magma chamber. Assimilation of gabbro during emplacement, contaminates the melt which become enriched in trace elements and REE.

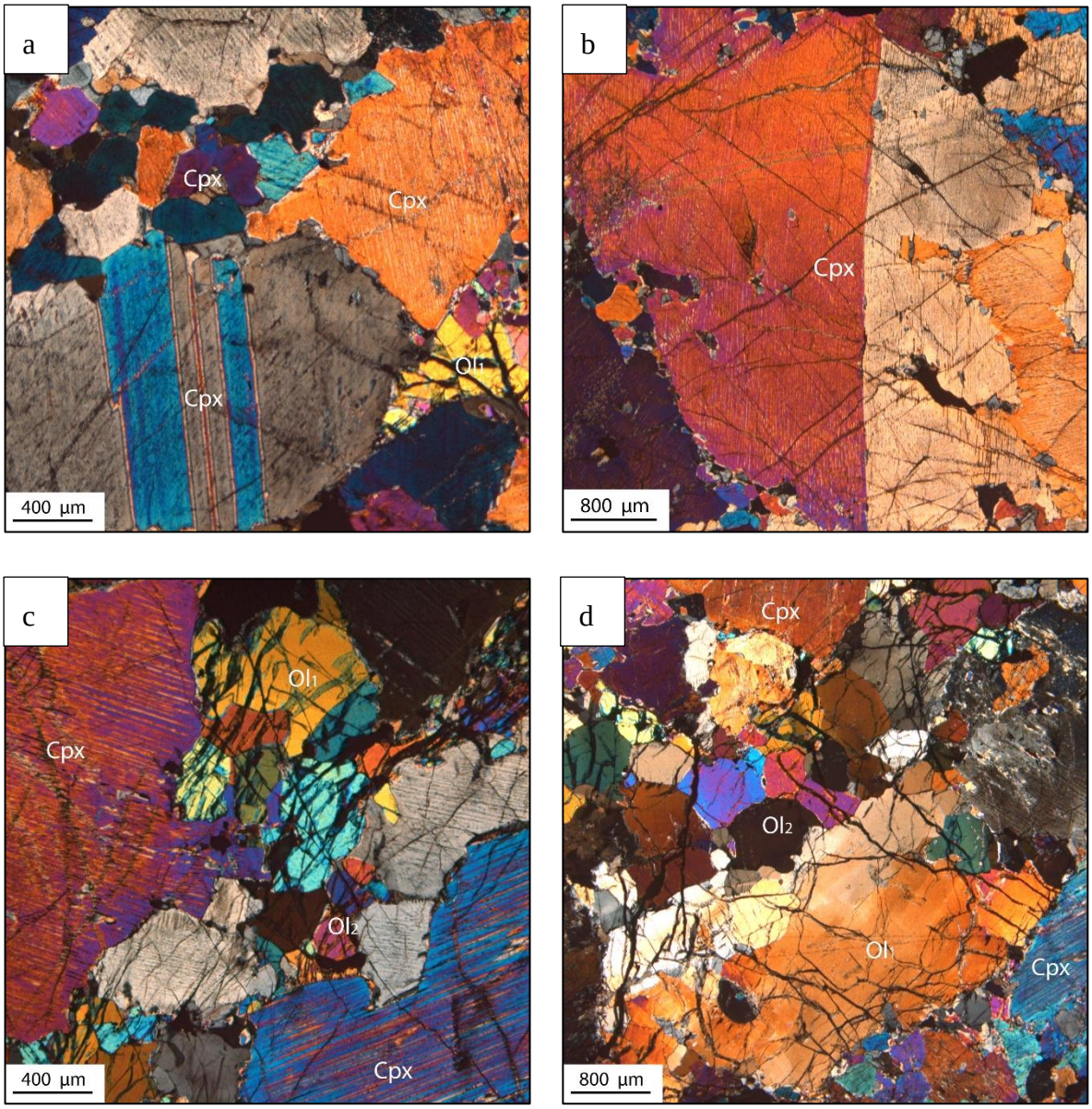

Figure 5.7: a) Large grained Cpx with twinning, and recrystallized Ol_2. (sample 4-37440) b) 3-4 cm large Cpx twinned grain. (sample 4-35290) c) Band of recrystallized olivine in the pyroxenite (sample 4-35290) d) Interstitial ol_2 with Cpx and Ol cumulates(sample 4-37440).

Mineralization

The first mineral deposits in Reinfjord complex were first described by Hansen (1971) in the western contact between the LLS and the garnet gneiss. Helicopter-borne Transmission Electron Magnetic (TEM) survey conducted by Nordic Mining ASA in 2012 found a large conductive field (600x600 meters). The conductive field is located on a depth between 60 and 110 meters beneath the Lake District gently dipping towards NE (Figure 5.8). This was later confirmed by drilling (RF-1 - figure 5.3), where they found a 9 meters thick PGE reef containing 0,64 ppm Pt+Pd+Au and a Ni-Cu-PGE reef containing 0,38 Wt% Ni and 0,12 Wt% Cu (Iljina, 2013). Øen (2013) showed that sulphides hosting the reefs in RF-1 originated from a mantle source with some minor contamination from the gabbro host.

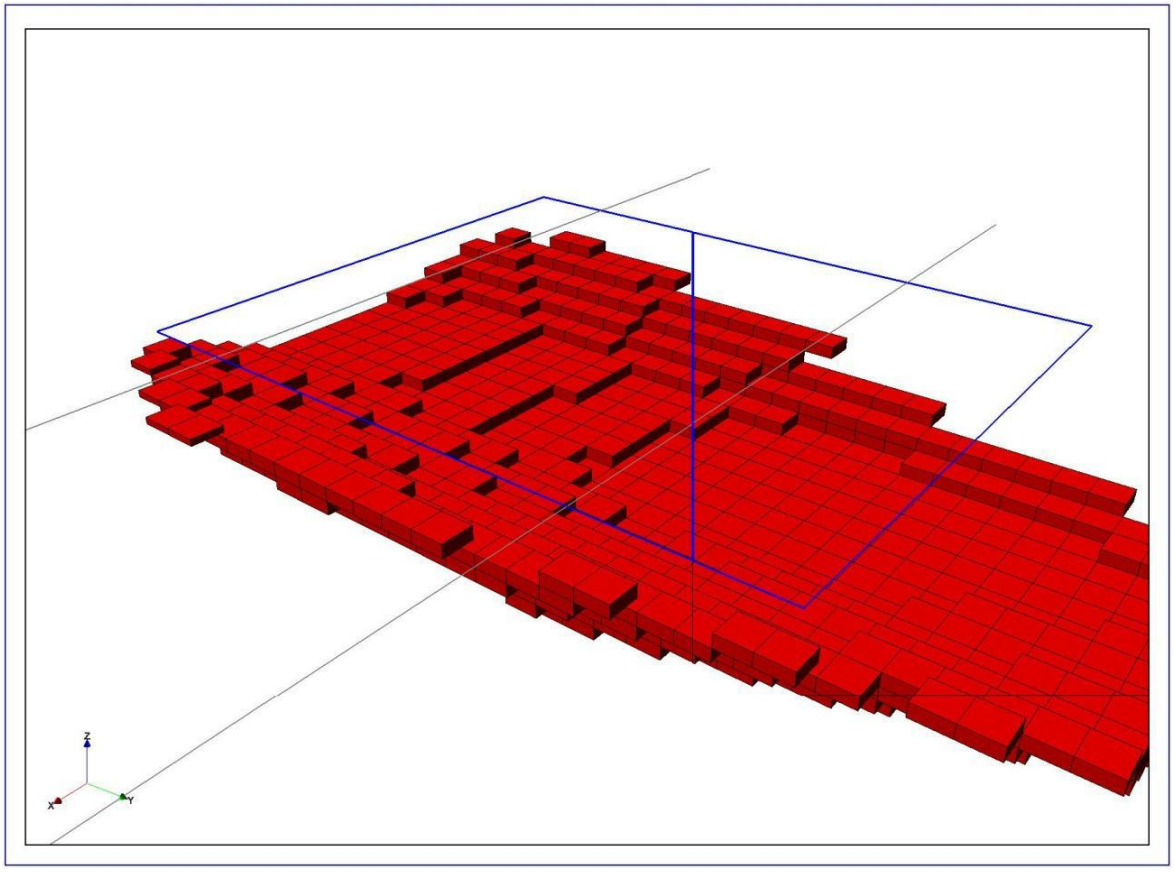

Figure 5.8: 3D model of the conductive field under the lake district, from the survey report by THUNEHED (2012) to Nordic Mining ASA.

Whole-rock analysis of RF-4 (figure 4.36-4.37) show the economic elements hosted within the CS, that is Cu, Ni, PGE (Pd, Pt and Au). These diagrams show up to 5 possible Cu-Ni-PGE sulphide deposits. Figure B.7-B.9 in appendix B compare these diagrams showing their evolution with depth in the same diagrams. These diagrams show that copper content is

proportional with sulphide content, while Ni and PGE enrichments are shifted compared to the Cu and S peaks.

The upper 100 meters of RF-4 contains three enrichments that may turn out to be economic grade deposits. This include one Cu reef with 0,5 Wt% S and 0,1 Wt% Cu over a ten meter zone, one Cu reef containing 0,35 Wt% sulphide and 800 ppm Cu in a 15 meter wide zone. Between these two Cu reefs a low sulphide Ni-PGE reef containing 0,4 Wt% Ni and 0,3 ppm PGE with a thickness less than 5 meters. These three Cu and Ni-PGE reefs are all separated with 20 meters and located between 540 and 580 m.a.s.l.. The native copper presented in chapter 4.4.3 is from the lower copper reef (4-7550) and from a minor copper peak located at 515 m.a.s.l. containing 375 ppm Cu and 0,2 Wt% S. The formation and origin of the native copper is discussed later in chapter 5.4. One other ore-deposit is found in RF-4, this is located at the contact between the CS and the pyroxenite, this is a Cu reef containing 0,5 Wt% S and 850 ppm Cu with traces of PGE and Ni.

The upper Cu reef and the Ni-PGE reef correlates with the Cu-Ni and Ni-PGE reefs found in the CS from RF-1, reported in the drilling report for Nordic Mining by Iljina (2013). Where they report the finding of two reefs separated by 20 meters of barren dunite. The Ni-PGE reef contain 0,64 ppm PGE and 0,27 Wt% Ni, and the Cu-Ni reef contain 0,38 Wt% Ni and 0,12 Wt% Cu. The major difference from these deposits to the RF-4 deposits is that they are not hydrothermally altered, however the upper Cu-reef is not sampled and may be unaltered. Also their Cu-Ni reef contains significantly more nickel compared to RF- 4 (this is discussed later).

The Cu-Ni reef observed in RF-1 is located at 560 m.a.s.l., this is 20 meters lower compared to the possible same reef in RF-4. However, if this is the same reefs,. The RF-1 reefs should be located much deeper due to the NE-dip of the intrusion (Figure 5.3). This may be explained by the NE-SW fault located between the drill holes. This fault may also explain the origin of the hydrous fluids observed in the RF-4 (footwall). The RF-1 (hanging wall) do not contain the deepest of the two Cu reefs (540 m.a.s.l.) found in RF-4. This may be explain by hydrothermal remobilization occurred in RF-4 and not RF-1, or that the RF-1 and RF-4 is separate reefs with limited extent. However, the helicopter-borne TEM survey conducted for Nordic mining

suggest a coherent conductor dipping towards NE. This conductor is described as open in NE, which mean it may continue towards the conduit system.

The overall nickel content in the CS is stable around 2500 ppm. Nickel content show an upward increase towards 440 m.a.s.l. and decrease from 440 to 520 m.a.s.l.. This reflects the Mg# and forsterite content in olivine, indicating that $D_{Ni}^{Olivine/Melt}$ increased with Mg# content and increasing forsterite content (Li et al., 2007). In some of the minor sulphur peaks, small enrichment in Ni concentration is observed. $D_{Ni}^{sulphide/Melt}$ suggested to be 500 in Peach and Mathez (1993) is approximate 100 times larger than $D_{Ni}^{Olivine/Melt}$ (which is 4,5 at 1450°C (Matzen et al., 2013)), this suggest that sulphide immiscibility happened after much of the nickel already had partitioned into olivine.

Microprobe data of olivine show that NiO concentration vary between 0,2 and 0,43 Wt% in the CS (Figure 4.40). From XRD analysis we know that the CS consists of over 90% olivine. This give an expected Ni content 2000-4000 ppm in the bulk rock. This mean that the Ni observed in RF-4 most likely is hosted in olivine. The Ni-PGE reef presented earlier is then most likely only a PGE reef, as the nickel are hosted in olivine (i.e. non-economic).

Copper concentration in the CS is proportional with the sulphide concentration. This is understandably in the CS, as copper is incompatible in olivine. Therefore would be enriched by crystallization of olivine. The PGE reef in RF-1 was investigated in the master thesis by Nikolaisen (2016). He observed that Pd and Pt is found as alloys with Te. The observed enrichment of Pd and Pt is believed have magmatic origin, and is connected to pyrrhotite and pentlandite. Au however is believed to be connected to carbonatitic fluids (Nikolaisen, 2016)

5.3 Relationship of Central Series and Langstrandgabbro

The contact between the CS and the gabbro-norite is an irregular magmatic contact. In the contact zone, CS melt is observed to intrude into the gabbro-norite (i.e. the finger), a zone of gabbroic melt or gabbro xenoliths that have been separated by the intruding melt, forming a dyke into the CS are observed (figure 4.49). The contact zone range from uncontaminated CS to the hybrid MZ and further to partial melted gabbro.

The CS becomes gradually more and more contaminated towards the contact, this is seen by the increasing amount of poikilitic plagioclase and clinopyroxene. The first occurrence of plagioclase in the CS (which marks the start of the hybrid MZ) is observed 50 meters from the contact. Rafts of recrystallized gabbro are common in the partial melted gabbro and lie sub-parallel to the layering (Grant et al., 2016). The MZ is cut by variating amount of sub vertical plagioclase veins, 1 to 10 cm wide.

The Nordre Bumannsfjord pluton, is another ultramafic intrusion in the Seiland Igneous Province. The Nordre Bumannsfjord and Reinfjord intrusions show many similarities with respect to contamination and assimilation of their gabbro host. Griffin et al. (2013) suggest that all mafic and ultramafic intrusions in the SIP are caused by massive assimilation of the host gabbro with hot mantle plume parent melt arriving from the core-mantle boundary. Grant et al. (2016) show that the CS and ULS are unlikely to be contaminated by assimilation of the gabbro-norite outside the hybrid MZ zone. This is supported in the master thesis by Øen (2013), he show that the sulphide isotopes found in the CS (δ^{34}S (VCDT) = -4) are distinct different from sulphides found in the gabbro (δ^{34}S (VCDT) = +2) and the gneiss (δ^{34}S (VCDT) = +10). If the UM series had formed from massive assimilation of the gabbro the sulphides should have the same signature. As they do not, Øen (2013) suggests that the sulphur originate from a mantle source. However the MZ (δ^{34}S (VCDT) = 0), are likely to have been formed by assimilation.

However, the intrusions show similarities on contamination in the contact zones. The least contaminated dunites in Nordre Bumannsfjord have a olivine composition of Fo_{80-81} and the contaminated peridotite have Fo_{76-79} (Griffin et al., 2013). The contaminated MZ in Reinfjord have somewhat higher forsterite compositions, the CS olivine composition range from $Fo_{82-85,5}$ in RF-4, where most analysis have between Fo_{83-84}. The MZ and the CS located close to the

contact are lower, $Fo_{77,4-78,4}$ olivine composition (table 4.3), which correlates with the contaminated peridotite in Nordre Bumannsfjord. The Mg# in clinopyroxene in the MZ and the CS is Mg# = 70,5-71 for the MZ and Mg# = 73 for the CS, this is lower than Griffin et al. (2013) observe in Nordre Bumannsfjord, where the dunite and peridotite is reported to be uniform at Mg# = 81-83 for Cpx. This difference may be connected to the high anorthite content in the plagioclase xenocrysts in the gabbro ($An_{82-83,2}$) and the MZ ($An_{86,3-90}$), compared to the gabbro (An_{72-76}) and peridotite ($An_{75-82,5}$) in Nordre Bumannsfjord.

REE plot (figure 4.53) of the gabbro-CS contact samples, show that the CS samples collected 50 and 80 meters from the contact contain the same amount of trace elements as the RF-4 samples. This implies that the this they not or low degree of contamination. Which restricts the width of the MZ to 50-60 meter.

5.4 Origin of the native copper

The formation of native copper have not been a focus in this thesis. as this is not part of the primary magmatic processes. However the hydrothermal alteration that form the native copper and other phases, may help explain the reef formations observed in the drill core and in the aeromagnetic analysis (Iljina, 2013).

Formation of serpentine and dolomite, as observed in the native copper rich part of the intrusion may be formed these possible reactions:

Eq. 3: Formation of serpentine from breakdown of olivine.

$$Forsterite + SiO_2 + Fluid \rightarrow Serpentine$$

$$3Mg_2SiO_4 + SiO_2 + H_2O \rightarrow 2Mg_3Si_2O_5(OH^-)_4$$

Eq. 4:Formation of serpentine and dolomite.

$$Forsterite + Fluids + Ca^{2+} \rightarrow Lizardite + Dolomite + H_{2(g)}$$

$$4Mg_2SiO_4 + 6H_2O + 4CO_2 + 2Ca^{2+} \rightarrow 2Mg_3Si_2O_5(OH^-)_4 + 2CaMg(CO_3)_2 + 6H_2$$

Eq. 4 require calcium for the formation of the observed dolomite. This Ca^{2+} could have come from the aqueous fluids or have been leached from the cumulus pile as the fluids migrate up.

The native copper is observed in the CS at lower Cu reef found at 540 and at minor copper enrichment at 520 m.a.s.l. Native copper is found as massive native copper replacing chalcopyrite in the primary sulphide (Figure 4.47c-d), as disseminated grains in serpentine veins (Figure 4.47a-b) and as disseminated grains in along chalcopyrite cleavage or fracture zones where chalcopyrite is broken down to digenite and magnetite (Figure 5.9). All these occurrences of native copper is in close proximity to serpentine veins, indicating its importance for the breakdown of chalcopyrite to native copper.

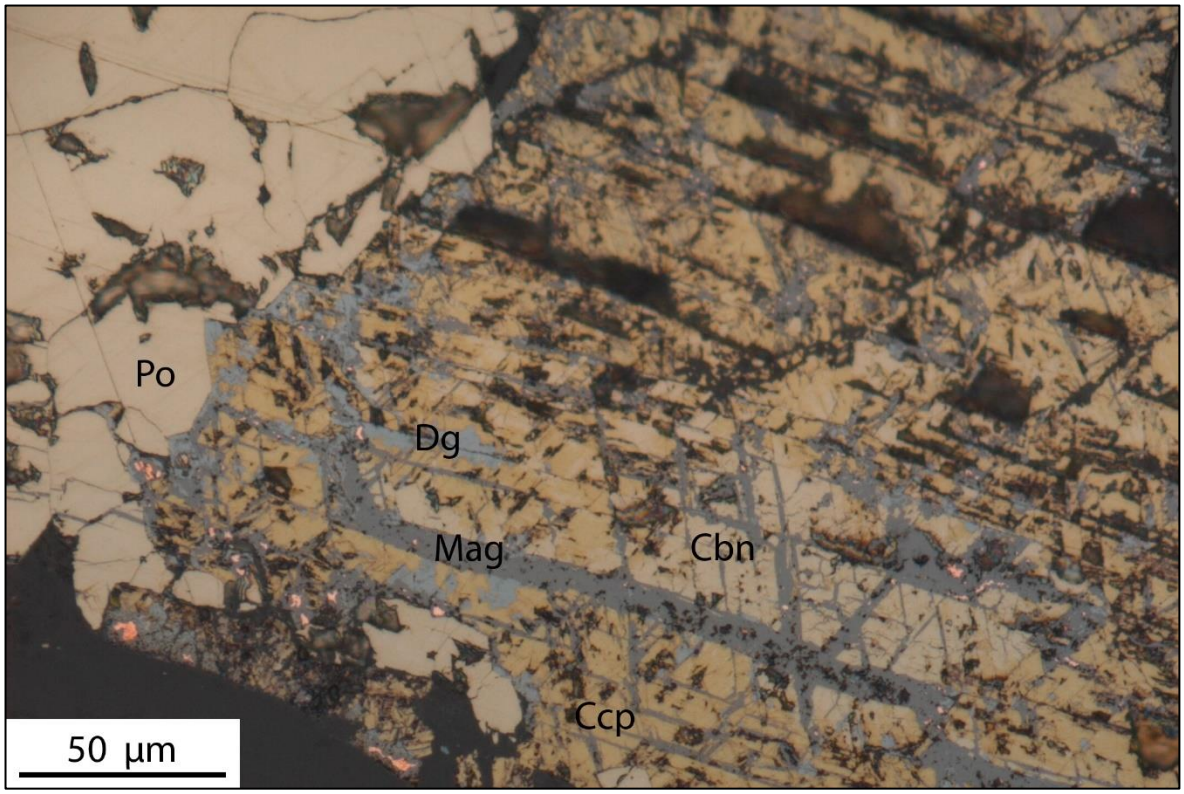

Figure 5.9: Native copper formation along cleavage or fracture planes in Chalcopyrite

Breakdown of chalcopyrite is a result of serpentinization, and it is replaced by digenite, native copper and magnetite (figure 5.9). Associated phases in these samples is amphibole, pyrrhotite and dolomite. Eq. 5 show a possible reaction for the breakdown of chalcopyrite, the reaction is not balanced due to varying content of native copper, digenite and magnetite between grains. This is the same reactions as Lorand (1988) describe formation of native copper in the Maqsad district, Sumali ophiolite, Oman. He observes a rim of magnetite (Mt) having formed round the native copper, this as a reaction between serpentine veins and breakdown of chalcopyrite and pyrrhotite. He suggests that low oxygen and sulphur fugacity reflect the strongly reducing conditions needed to form base metal alloys. This again is caused by the production of H_2 gas, which will consume S_2 from the sulphides and form H_2S.

Figure 4.44c show a reaction between pyrrhotite and serpentine, where pyrrhotite is replaced/assimilated by serpentine. From the low occurrence of pyrrhotite and pentlandite in these samples, this suggest that breakdown of pyrrhotite and pentlandite also occurred.

Eq. 5: Breakdown of chalcopyrite forming native copper, digenite and magnetite. Reaction is not balanced.

$$Chalcopyrite + fluid \rightarrow Magnetite + Digenite + Native\ copper + Hydrogen\ sulphide$$

$$CuFeS2 + H_2O \rightarrow 0{,}33Fe3O4 + Cu9S5 + Cu + H_2S$$

Breakdown of dolomite to brucite and calcite is observed in the Cu reefs, within close proximity to breakdown of chalcopyrite (Figure 4.45 and Figure 4.48Figure 4.47). For this a possible reaction may be Eq. 6:

Eq. 6: Breakdown of dolomite to brucite and calcite.

$$Dolomite + H_2O \rightarrow Calcite + Brucite + CO_2$$

$$CaMg(CO_3)_2 + H_2O \rightarrow Ca(CO_3) + Mg(OH^-)_2 + CO_2$$

The reefs in RF-1 drill core show no sign of hydrothermal alteration, this show that the Central Series were enriched by magmatic processes. Øen (2013) show by sulphur isotopes that the mantle is the most likely source of the sulphides observed in Reinfjord. He also show that the sulphide found in MZ is contaminated by gabbro assimilation. RF-4 show later hydrothermal remobilisation of copper. The hydrous alteration and remobilization of copper, explain why the copper deposits are so sulphide poor.

From the data and observations presented, this possible evolution of the melt may explain the formations of the reefs. During ascent of melt sulphide immiscibility did not occur due to high temperatures and drop in pressure. The melt is emplaced into the magma chamber, where fractional crystallization of olivine lowers the solubility of sulphur and deplete the melt of Ni. When sulphide immiscibility occur, copper partition into the sulphide liquid forming the Cu reefs observed in RF-1. Post magmatic fluids enter the magma chamber, this may be connected with faulting which increase permeability. This leads to a phase of minor remobilization of copper, with low degree of hydrous breakdown of copper (sample 4-10430 – minor copper peak). Sample 4-7550 (The deepest Cu-reef) show the last phase, where very little sulphides is preserved, the copper is present as native copper or digenite. The last phase is also where most of the native copper is found as small thin grains with preferred orientation. The orientation of native copper grains is always perpendicular if intergrown. Separate grains in the 7550 sample

show rotation of the preferred orientation, indicating rotation and remobilization of native copper.

5.Discussion

6 Conclusions

Detailed fieldwork resulted in an updated geological map, with an entirely new interpretation of the NE part of the intrusion. Fieldwork also unveiled a roof zone for the CS in the NE-parts of the intrusion, with a sub horizontal gabbro cap the CS. A possible roof zone for the ULS in SW may also be argued. The pyroxenite found in RF-4 may be part of the MZ and represents the floor of the magma chamber, this is likely as trace elements and REE show similar concentrations in both these and that the thickness lies within the observed width of the MZ. If the pyroxenite is indeed part of the MZ, an estimate of the total volume of the Reinfjord intrusion may be obtained.

Field evidence shows that the two fault systems (NE-SW and SE-NW) may be more significant than earlier work suggested. The lack of a MZ around the intrusion in south and evidence of drag in the adjacent gabbro suggests that there is a significant displacement in the SE-NW fault system. The NE-SW fault system may be the source of the hydrous fluids forming native copper in RF-4. Displacement along the NE-SW fault is likely, but no data yet exists on this. This implies that the LLS may be faulted into closer contact with the ULS and CS, this however will need further investigation.

The evolution of the CS is presented, with an increasing Mg# and forsterite content from the base up to 440 m.a.s.l., From 440 m.a.s.l. and up the Mg# and forsterite content decreases, before bulk rock Mg# stabilize at Mg# = 68-70. The decreasing Mg# and forsterite content is likely caused by fractional crystallization, while the “reverse fractional sequence” is likely caused by new melt interacting with the earlier emplaced cumulates. Field and geochemical data show multiple replenishment events of melt in the CS.

Four possible deposits are found in RF-4 hosted in CS, two Cu reefs, one PGE reef and one Cu-PGE contact deposit. The three upper reefs are separated with 20 each from 540 to 580 m.a.s.l.. The copper reefs are found to contain 0,1 Wt% Cu and 800 ppm Cu over 10 and 15 meters respectably. The PGE reef found between these Cu reefs contains 0,3 ppm Pt+Pd, over a 5 meter interval. A 10 meter thick Cu contact deposit towards the pyroxenite, contain 900 ppm Cu and traces of PGE. The absence of nickel in the sulphide reefs indicate that the sulphide immiscibility occurred after crystallization of olivine, which depleted the melt in nickel. The

uppermost Cu reef and the PGE reef may be connected with the reefs found in RF-1. The lower Cu reef is altered by hydrous fluids forming native copper.

The new data together with Grant et al. (2016) show that the CS melts were influenced by other processes as well as fractional crystallization. New calculations on the amounts of fractional crystallization show this, and indicate that the most fractionated samples experienced a crystal fractionation between 15% and 20%. This means that large amount of melts past through the conduit system en route to shallower levels within a large igneous province. This supports the theory that the Reinfjord ultramafic intrusion is a deep situated magma chamber, and a conduit system for mantle derived melt. This may explain the sporadic appearance ULS and the replacive CS close to the conduit system. As the large amount of melt passes through the system, earlier unconsolidated cumulates become replaced by melt-rock reactions.

The hybrid MZ are formed by contamination of the UM melt by assimilation of the partial melted gabbro-norite host. The contamination is restricted to a 50-100 wide zone of the UM cumulates, where poikilitic plagioclase and plagioclase xenocrysts have increasing amounts towards the contact zone. The zone is later cut by sub-vertical plagioclase veins 1-20 cm wide, these veins are believed to be related to melting of the host gabbro-norite.

6.Conclusions

New field observations and geochemical data give the following geological history of the Reinfjord ultramafic complex:

- Emplacement of the Langstrand gabbro-norite in the metasediments forming the garnet gneiss.
- Emplacement of the first UM melts in the partly consolidated gabbro. This melt is contaminated through assimilation of the gabbro as it intrudes and opens the magma chamber. This may be the pyroxenite observed in the RF-4 drill core.
- Emplacement of the ULS.
- Emplacement of the CS expanding the magma chamber and replacing earlier cumulates. Only local contamination from the gabbro in the Marginal zones.
- Magmatic enrichment of Cu-Ni-PGE by sulphides.
- Dykes and fluids intrude into the cumulus pile. Hydrothermal alteration and hydrous enrichment and breakdown of Cu, forming native copper under reducing conditions.
- Faulting by the NE-SW fault system. Providing permeability for fluids, this is seen by large amount of serpentine in the fault zone. This system is later cut by the SE-NW fault system. This system shows a large displacement cutting the intrusion in the south.

This excludes the LLS, as it is still unknown if it is connected to the main intrusion or if it emplaced as separate magma chamber/dyke/sill close to the main intrusion.

Further work:

- Further mapping in the Reinfjord intrusion should be conducted, particularly in the northern areas close to the glacier, as these areas have not been investigated by this or previous authors.
- A detailed study on the fault systems should be conducted to determine the displacement and its connection to the post magmatic fluids.
    - A study on the southern contact should be conducted to determine if the E-W fault is in contact with the gabbro scree above LLS.
- Investigate if the mineralization's found in RF-4, if can be found on the surface, as this is not observed in the RF-2 drill core. Using 10 degrees dip to NE on the CS layering an outcrop may be found on the southern side of the lake between RF-2 and RF-4. Sulphides were observed in this area during fieldwork.
- Detailed sampling throughout the reefs to accurate determine the true thickness and grade of the reefs. This will make a correlation with the RF-1 drill core deposits possible.
- An investigation on the pyroxenite in RF-4 should be conducted to establish if it is part of the MZ or new ultramafic series not described before.

7 References

ANKER-RASCH, L. 2013. Magmatiske malmdannende prosesser i Reinfjord, Seiland magmatiske provins : En studie av kjemisk sammensetning av olivin i forbindelse med ultramafisk magmatisk aktivitet. *MSc, Norwegian University of Science and Technology,*.

BENNETT, M. 1971. The Reinfjord ultramafic complex. *Norges geologiske undersøkelse Bull,* 269**,** 165-171.

BENNETT, M., EMBLIN, S., ROBINS, B. & YEO, W. 1986. High-temperature ultramafic complexes in the North Norwegian Caledonides: I—regional setting and field relationships. *Norges geologiske undersøkelse Bull,* 405**,** 1-40.

BENNETT, M. C. 1973. *The geology and petrology of the Reinfjord ultramafic complex, Troms, North Norway.* University College of Swansea.

BENNETT, M. C. 1974. The emplacement of a high temperature peridotite in the Seiland province of the Norwegian Caledonides. *Journal of the Geological Society,* 130**,** 205-226.

BOUDREAU, A. 1999. Fluid fluxing of cumulates: the JM reef and associated rocks of the Stillwater Complex, Montana. *Journal of Petrology,* 40**,** 755-772.

CAMPBELL, I. & NALDRETT, A. 1979. The influence of silicate: sulfide ratios on the geochemistry of magmatic sulfides. *Economic Geology,* 74**,** 1503-1506.

CAWTHORN, R. G. 2015. The Bushveld Complex, South Africa. *In:* TEGNER, C., NAMUR, O., CHARLIER, B. & LATYPOV, R. (eds.) *Layered intrusions.* Springer.

DEER, W., HOWIE, R. & ZUSSMAN, J. 1992. *An introduction to the rock-forming minerals,* Longman Scientific Technical, Harlow, United Kingdom.

EMBLIN, S. 1985. *The Reinfjord ultramafic complex, Seiland province: Emplacement history and magma chamber model.* University of Bristol.

GRANT, T. B., LARSEN, R. B., ANKER-RASCH, L., GRANNES, K. R., ILJINA, M., MCENROE, S., NIKOLAISEN, E., SCHANCHE, M. & ØEN, E. 2016. Anatomy of a deep crustal volcanic conduit system; The Reinfjord Ultramafic Complex, Seiland Igneous Province, Northern Norway. *Lithos,* 252–253**,** 200-215.

GRIFFIN, W., STURT, B., O'NEILL, C., KIRKLAND, C. & O'REILLY, S. Y. 2013. Intrusion and contamination of high-temperature dunitic magma: the Nordre Bumandsfjord pluton, Seiland, Arctic Norway. *Contributions to Mineralogy and Petrology,* 165**,** 903-930.

HANSEN, T. S. 1971. *En undersøkelse av nikkel-kopper mineraliseringer i Reinfjord-Jøkkelfjord området.* MSc, NTH/NTNU.

HEREDIA, B. D., TEGNER, C. & WAIGHT, T. E. 2008. Assimilation and fractional crystallization constraints in the upper zone of Hasvik layered intrusion, Norway; Sr-crystal isotope stratigraphy in plagioclase. *International Geological Congress, Abstracts = Congres Geologique International, Resumes,* 33.

HOOPER, P. 1971. The mafic and ultramafic intrusions of SW Finnmark and North Troms. *Norges Geol. Unders,* 269**,** 147.

ILJINA, M. 2013. Reinfjord drilling and mapping campaigns in 2012 — geochemical observations, discussion on ore genesis and exploration implications. Report for Nordic Mining ASA.

IRVINE, T. 1974. Petrology of the Duke Island ultramafic complex southeastern Alaska. *Geological Society of America Memoirs,* 138**,** 1-244.

IRVINE, T. 1977. Origin of chromitite layers in the Muskox intrusion and other stratiform intrusions: a new interpretation. *Geology,* 5**,** 273-277.

IRVINE, T. 1982. Terminology for layered intrusions. *Journal of Petrology,* 23**,** 127-162.

KINNAIRD, J. A. 2005. The Bushveld large igneous province. *Review Paper, The University of the Witwatersrand, Johannesburg, South Africa, 39pp*.

KLEMM, D., HENCKEL, J., DEHM, R. & VON GRUENEWALDT, G. 1985. The geochemistry of titanomagnetite in magnetite layers and their host rocks of the eastern Bushveld Complex. *Economic Geology,* 80**,** 1075-1088.

KOHN, S. C. & SCHOFIELD, P. F. 1994. The importance of melt composition in controlling trace-element behaviour: an experimental study of Mn and Zn partitioning between forsterite and silicate melts. *Chemical Geology,* 117**,** 73-87.

KRILL, A. G. & ZWAAN, K. 1987. Reinterpretation of Finnmarkian deformation on western Sørøy, northern Norway. *Norsk Geologisk Tidsskrift,* 67**,** 15-24.

LI, C., NALDRETT, A. J. & RIPLEY, E. M. 2007. Controls on the Fo and Ni Contents of Olivine in Sulfide-bearing Mafic/Ultramafic Intrusions: Principles, Modeling, and Examples from Voisey's Bay. *Earth Science Frontiers,* 14**,** 177-183.

LORAND, J. 1988. Fe-Ni-Cu sulfides in tectonite peridotites from the Maqsad district, Sumail ophiolite, southern Oman: Implications for the origin of the sulfide component in the oceanic upper mantle. *Tectonophysics,* 151**,** 57-73.

MATZEN, A. K., BAKER, M. B., BECKETT, J. R. & STOLPER, E. M. 2013. The temperature and pressure dependence of nickel partitioning between olivine and silicate melt. *Journal of Petrology,* 54**,** 2521-2545.

NALDRETT, A. J. 2004. *Magmatic sulfide deposits: geology, geochemistry and exploration,* Springer Science & Business Media.

NAMUR, O. E. A. 2015. Igneous Layering in Basaltic Magma Chambers. *In:* TEGNER, C., NAMUR, O., CHARLIER, B. & LATYPOV, R. (eds.) *Layered Intrusion.*

NASLUND, H. R. & MCBIRNEY, A. R. 1996. Mechanisms of Formation of Igneous Layering. *In:* RICHARD GRANT, C. (ed.) *Developments in Petrology.* Elsevier.

NIELSEN, T. F. 2004. The shape and volume of the Skaergaard intrusion, Greenland: implications for mass balance and bulk composition. *Journal of Petrology,* 45**,** 507-530.

NIKOLAISEN, E. S. 2016. Platinum Group Elements in the Reinfjord Ultramafic Complex. *MSc, Norwegian University of Science and Technology,.*

OOSTEROM, M. G. 1963. The ultramafites and layered gabbro sequences. *Leidse Geologische Mededelingen,* 28**,** 177-296.

PEACH, C. & MATHEZ, E. 1993. Sulfide melt-silicate melt distribution coefficients for nickel and iron and implications for the distribution of other chalcophile elements. *Geochimica et Cosmochimica Acta,* 57**,** 3013-3021.

ROBB, L. 2009. *Introduction to ore-forming processes,* John Wiley & Sons.

ROBERTS, R., CORFU, F., TORSVIK, T., ASHWAL, L. & RAMSAY, D. 2006. Short-lived mafic magmatism at 560–570 Ma in the northern Norwegian Caledonides: U–Pb zircon ages from the Seiland Igneous Province. *Geological Magazine,* 143**,** 887-903.

ROBERTS, R. J. 2008. *The Seiland Igneous Province, northern Norway: age, provenance, and tectonic significance.*

ROBINS, B. 1975. Ultramafic nodules from Seiland, northern Norway. *Lithos,* 8**,** 15-27.

ROBINS, B. & GARDNER, P. 1974. Synorogenic layered basic intrusions in the Seiland petrographic province, Finnmark. *Norges geologiske undersøkelse,* 312**,** 91-130.

ROBINS, B. & GARDNER, P. M. 1975. The magmatic evolution of the Seiland province, and Caledonian plate boundaries in northern Norway. *Earth and Planetary Science Letters,* 26**,** 167-78.

SALMONSEN, L. P. & TEGNER, C. 2013. Crystallization sequence of the Upper Border Series of the Skaergaard Intrusion: revised subdivision and implications for chamber-scale magma homogeneity. *Contributions to Mineralogy and Petrology,* 165**,** 1155-1171.

SUN, S.-S. & MCDONOUGH, W. 1989. Chemical and isotopic systematics of oceanic basalts: implications for mantle composition and processes. *Geological Society, London, Special Publications,* 42**,** 313-345.

SØRENSEN, B. E. 2013. A revised Michel-Lévy interference colour chart based on first-principles calculations. *European Journal of Mineralogy,* 25**,** 5-10.

TEGNER, C., CAWTHORN, R. G. & KRUGER, F. J. 2006. Cyclicity in the Main and Upper Zones of the Bushveld Complex, South Africa: crystallization from a zoned magma sheet. *Journal of Petrology,* 47**,** 2257-2279.

TEGNER, C., ROBINS, B., REGINIUSSEN, H. & GRUNDVIG, S. 1999. Assimilation of crustal xenoliths in a basaltic magma chamber: Sr and Nd isotopic constraints from the Hasvik Layered Intrusion, Norway. *Journal of Petrology,* 40**,** 363-380.

THUNEHED, H. 2012. TEM-survey at Reinfjord – survey and interpretation report.

U.S. GEOLOGICAL SURVEY. 2016. *USGS Global Positioning Application and Practice* [Online]. http://water.usgs.gov/. Available: http://water.usgs.gov/osw/gps/ [Accessed 02.05 2016].

WAGNER, L. & DEER, W. 1939. Geological investigation in East Greenland. Part III. The petrology of the Skaergaard Intrusion, Kangerdluqssuaq, East Greenland. Meddelser om Grønland 105:1-352.

WATSON, E. B. 1977. Partitioning of manganese between forsterite and silicate liquid. *Geochimica et Cosmochimica Acta,* 41**,** 1363-1374.

WHITNEY, D. L. & EVANS, B. W. 2010. Abbreviations for names of rock-forming minerals. *American mineralogist,* 95**,** 185.

WILL, G. 2006. *Powder diffraction: The Rietveld method and the two stage method to determine and refine crystal structures from powder diffraction data,* Springer Science & Business Media.

WINTER, J. D. 2010. *Principles of Igneous and Metamorphic Petrology,* Prentice Hall.

YEO, W. 1984. *The Melkevann ultramafic complex, Seiland Igneous Province, North Norway: Intrusive mechanisms and petrological evolution.* Doctor of Philosophy, University of Bristol

ØEN, E. N. 2013. Dannelse av sulfidforekomster i Reinfjord og Lokkarfjord, Seiland magmatiske provins. *MSc, Norwegian University of Science and Technology,.*

7.References

Appendices

Appendix A **Sample list and pictures**

Appendix B **Whole rock data**

Appendix C **EPMA analysis**

Appendix D **SEM analysis**

Appendix E **XRD analysis**

Digital appendix can also be found at http://daim.idi.ntnu.no/.

Appendices

Appendix A: Sample list and pictures

Surface sample list

Figure A. 1: List of surface samples:

Sample	Rock type	Coordinates	Thin section	Whole-rock analysis	EPMA
KG14001	MZ	0526908 7777784	X	X	
KG14002	MZ	0526913 7777838	X	X	
KG14003	MZ	0526881 7777906	X	X	
KG14004	MZ	0526867 7777949	X	X	
KG14005	CS	0525402 7776925	X	X	
KG14006	CS	0525433 7776980	X	X	
KG14007	CS	0525498 7777047	X	X	
KG14008	CS	0525515 7777267	X	X	
KG14009	CS	0526835 7777913	X	X	
KG14010	Gabbro	0526942 7777905	X	X	X
KG14011	Gabbro	0526909 7777966	X	X	X
KG14012	MZ	0526885 7777964	X	X	X
KG14013	MZ	0526870 7777973	X	X	X
KG14014	MZ	0526877 7777991	X	X	X
KG14015	CS	0526873 7778014	X	X	X
KG14016	CS	0526878 7778047	X	X	X
KG14017	CS	0525859 7777588	X	X	

KG14018	CS	0525927 7777713	X	X	
KG14019	CS	0525973 7777854	X	X	X
KG14020	CS	0526006 7778052	X	X	X
KG14021	CS	0526003 7778152	X	X	
KG14022	CS	0526059 7778261	X	X	X
KG14023	CS	0526136 7778404	X	X	X
KG14024	CS	0525450 7777115	X	X	
KG1501	MZ	0525153 7781128	X	X	
KG1502	ULS	0525177 7781128			
KG1503	ULS	0525187 7780869			
KG1504	Gabbro	0525083 7779081			
KG1505	MZ	0523671 7778655			
KG1506	LLS	0523671 7778610			
KG1507	LLS	0523784 7778591			
KG1508	LLS	0523647 7777729			
KG1509	LLS	0523708 7777664			
KG15010	LLS	0523813 7777272			
KG1511	MZ	0523780 7777291			
KG1512	MZ (Sulphide)	0526232 7776934			
KG1513	Gabbro	0526232 7776934	X	X	

KG1514	MZ	0528004 7778682	X	X	
KG1515	MZ	0527158 7778889	X	X	
KG1516	MZ	0524978 7778820			
KG1517	MZ	0527158 7778889	X	X	

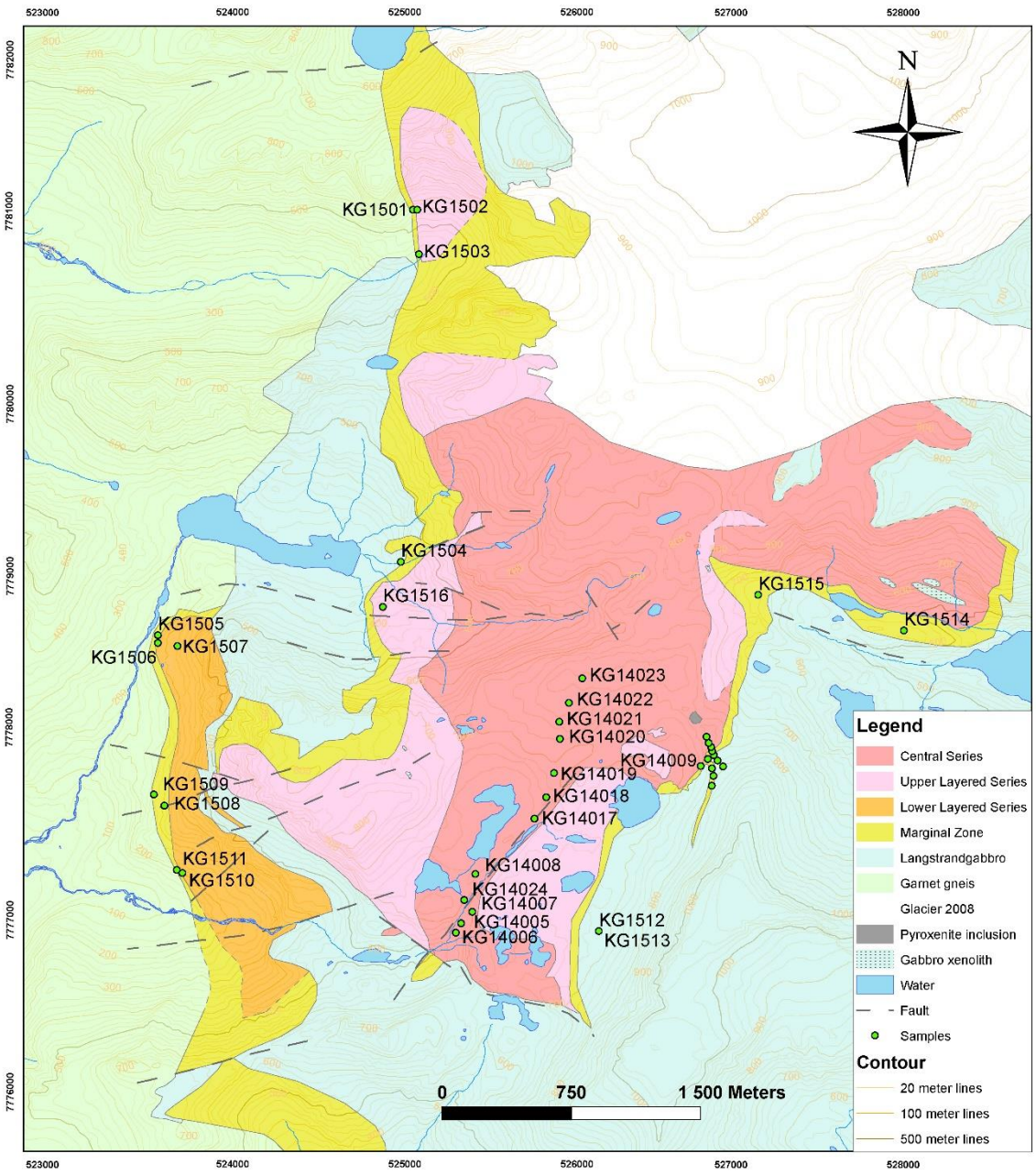

Figure A. 2: New map with sample locations.

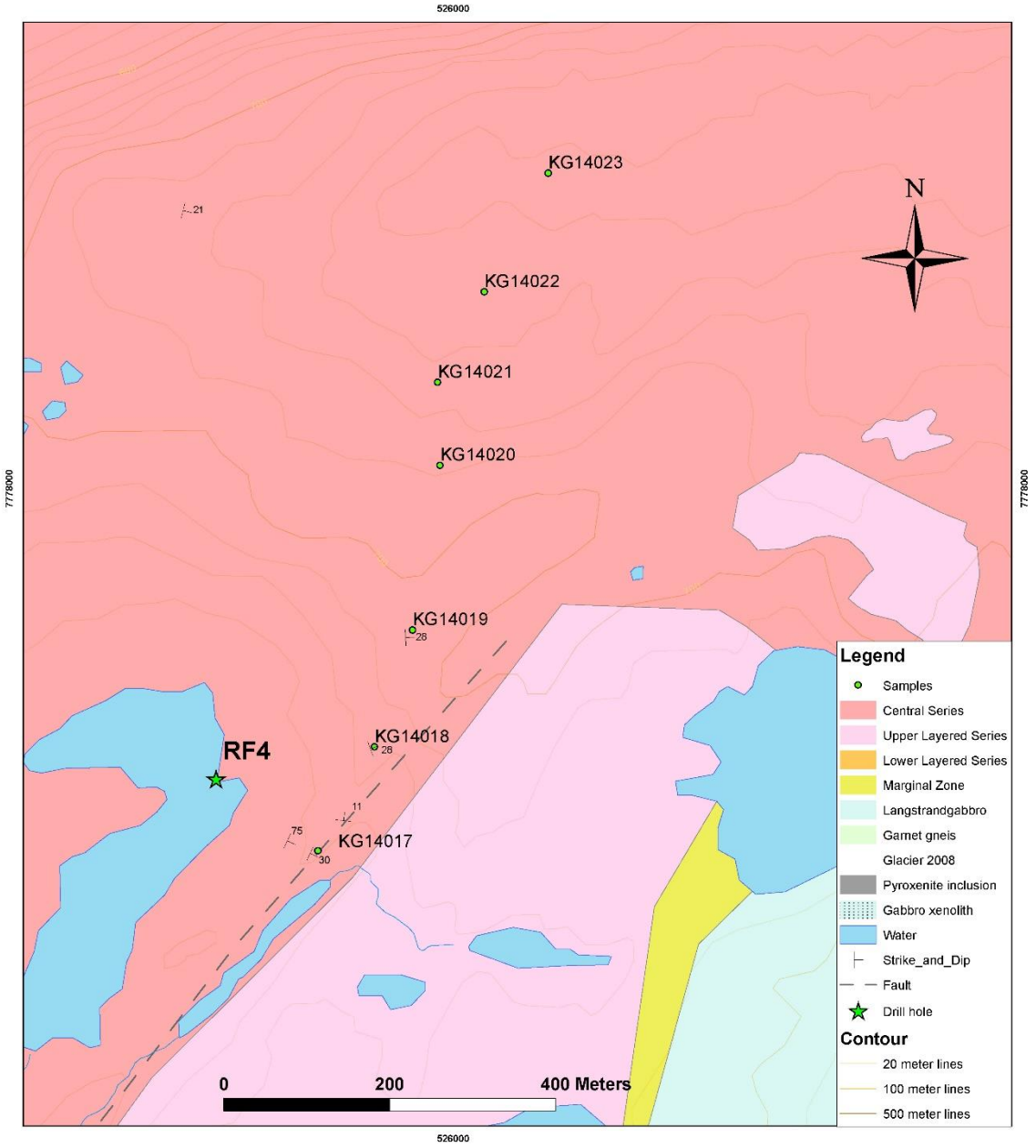

Figure A. 3: Location of samples used to describe the evolution of the CS

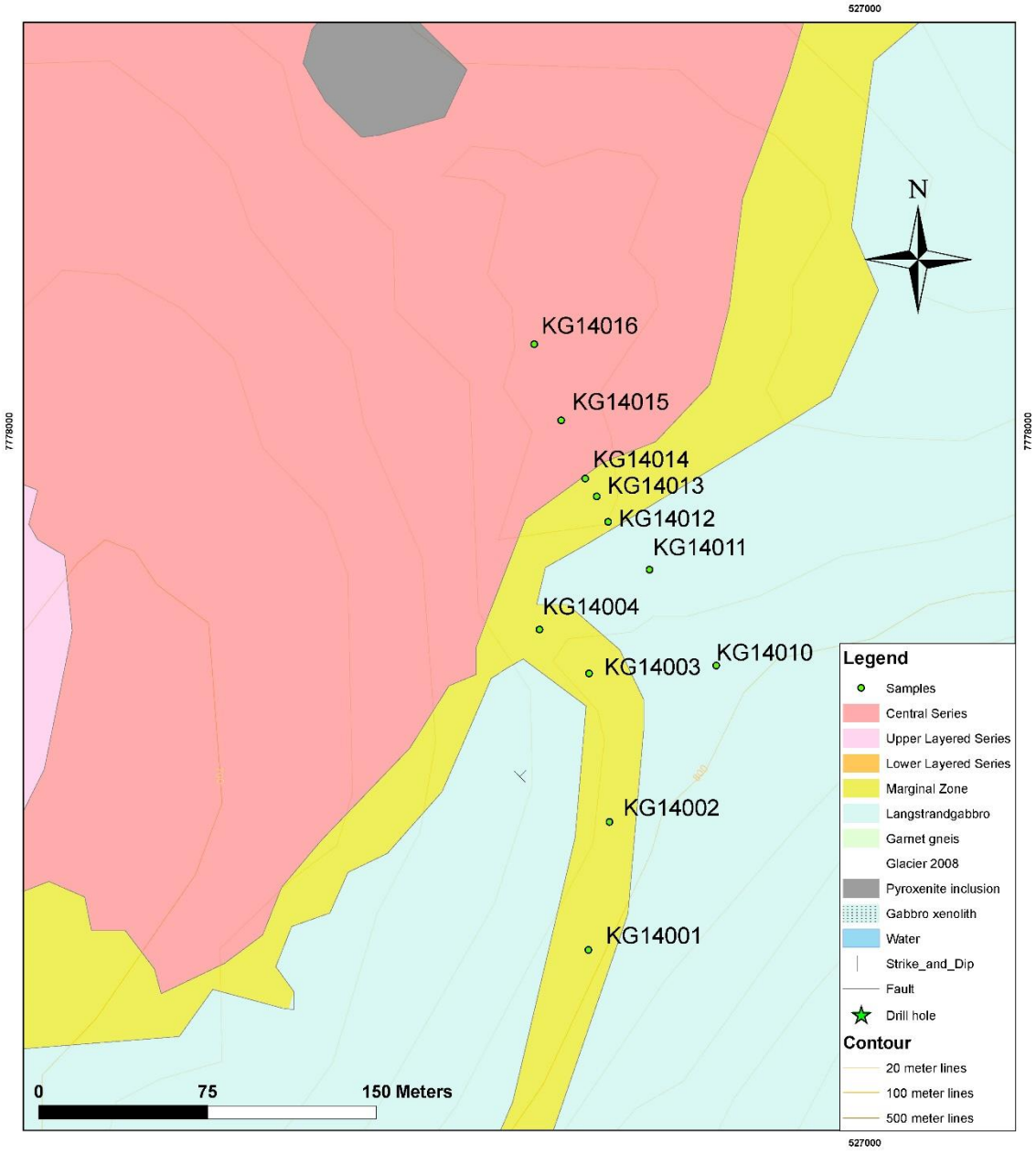

Figure A. 4: Location of samples used to describe the CS-Gabbro contact

Figure A. 5: Scanned photos of the KG14001 sample

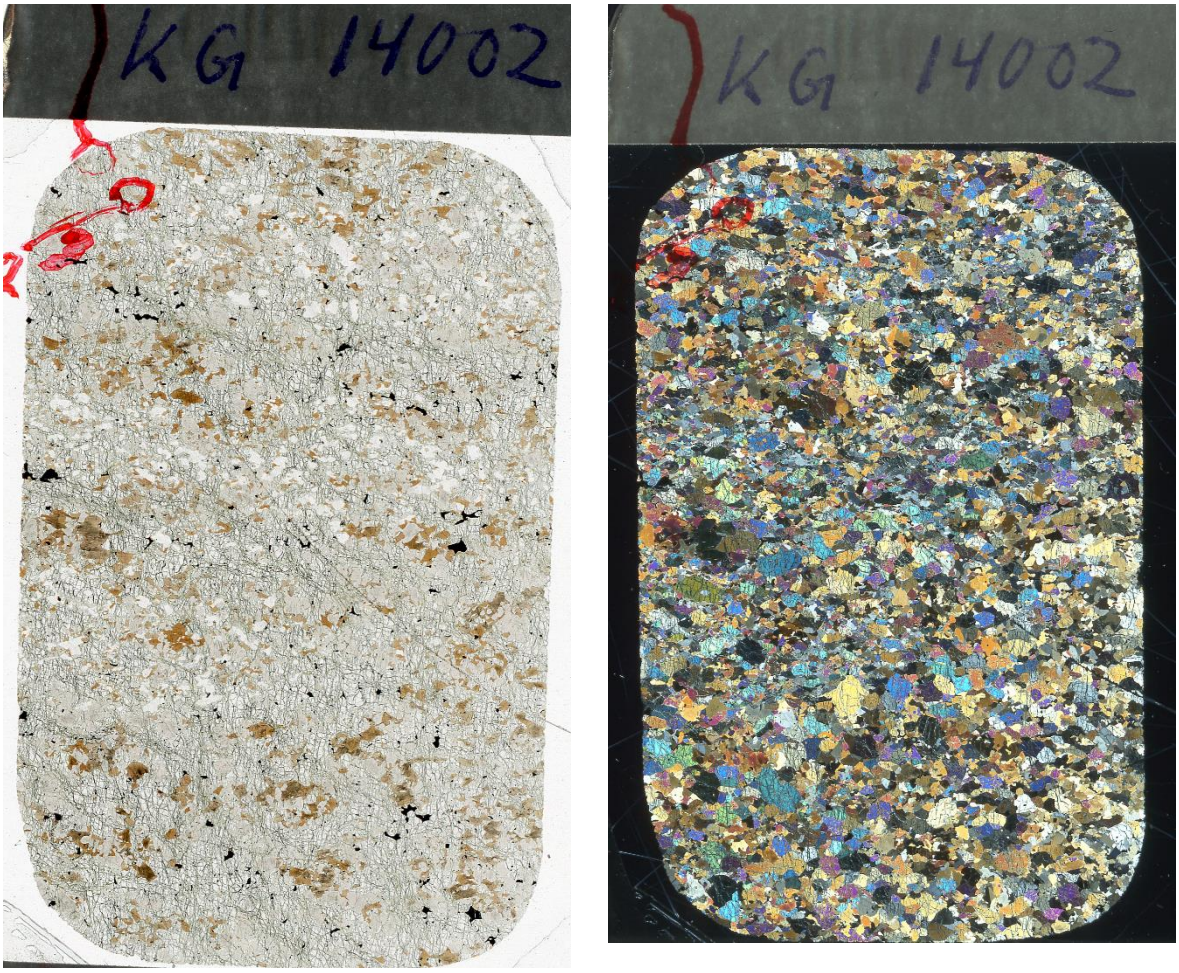

Figure A. 6: Scanned photos of the KG14002 sample

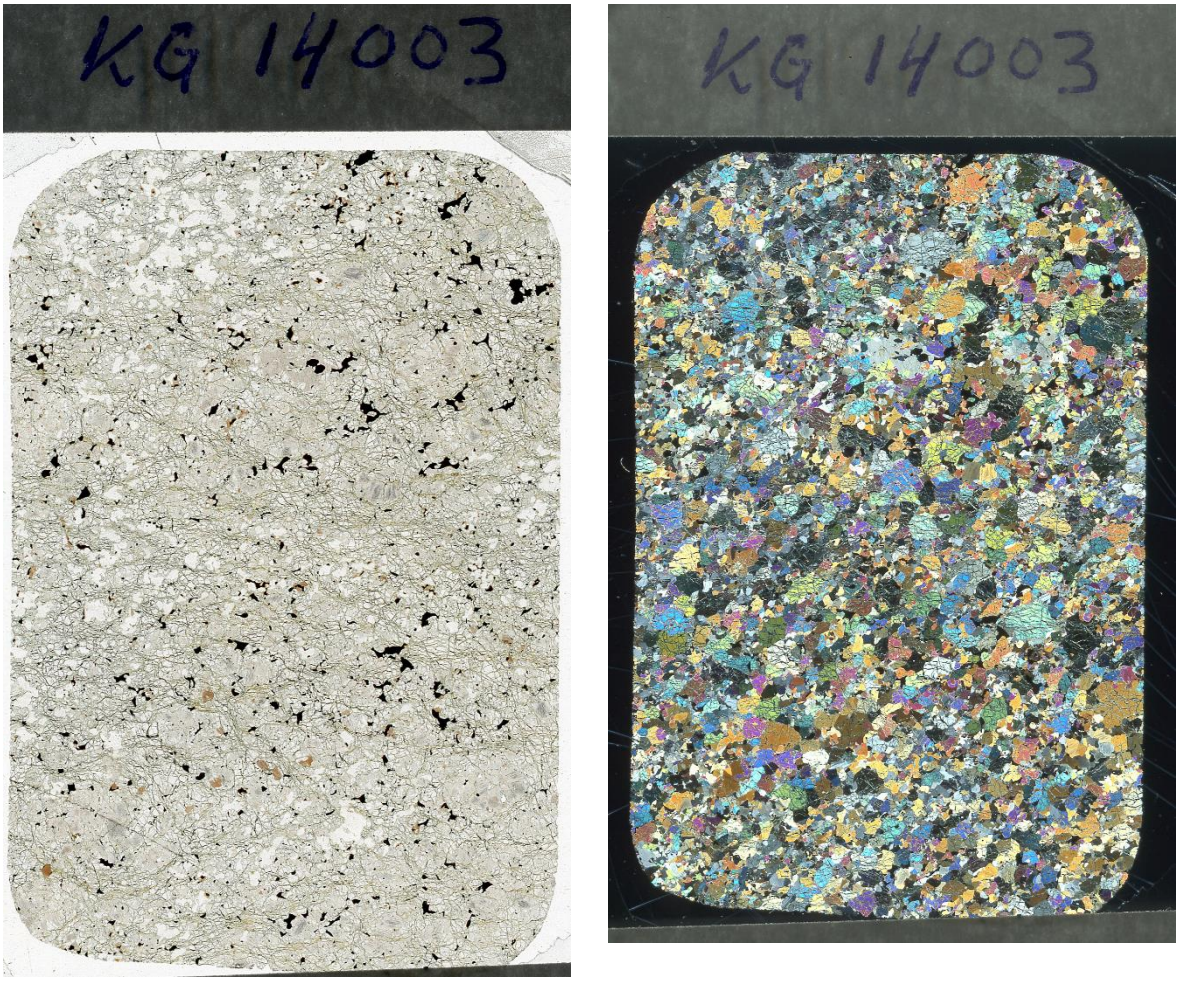

Figure A. 7: Scanned photos of the KG14003 sample

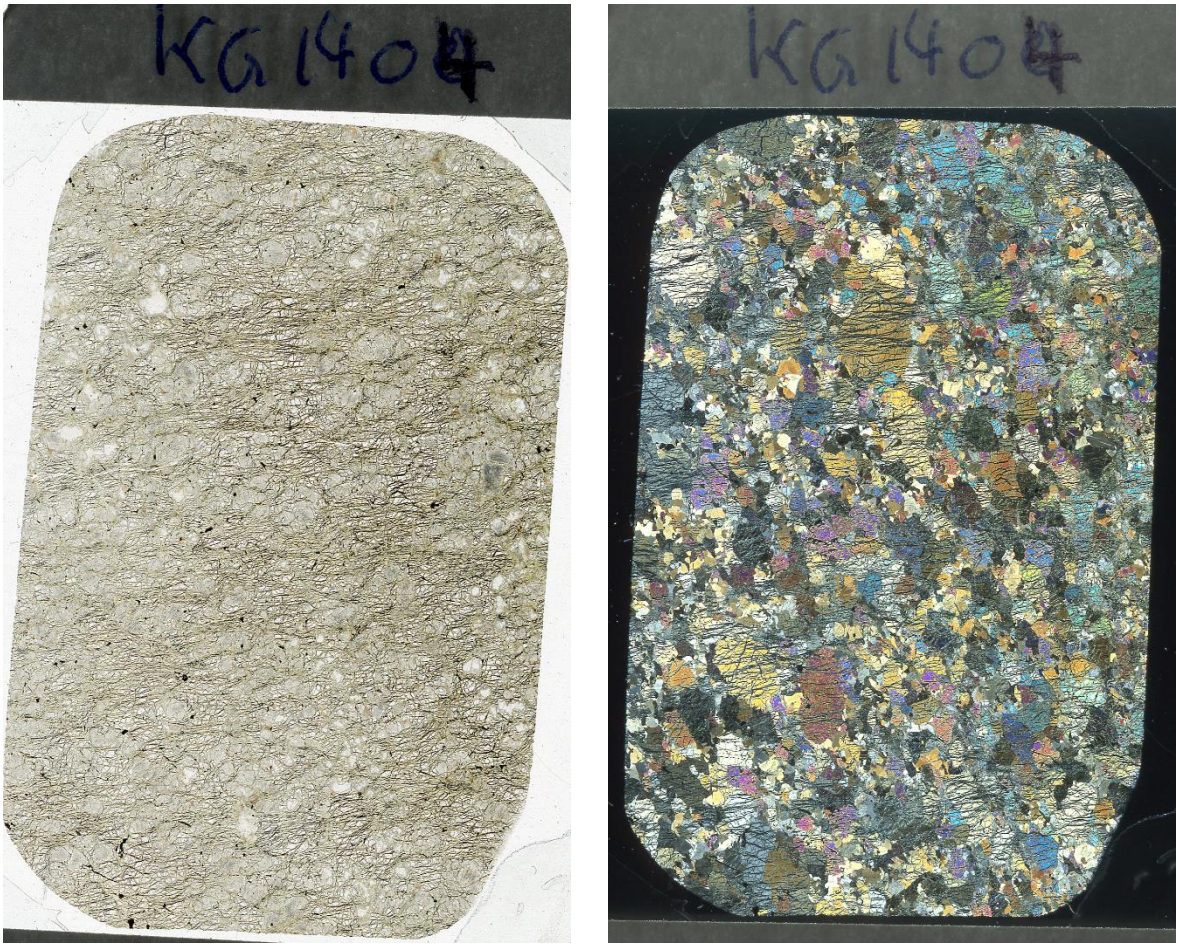

Figure A. 8: Scanned photos of the KG14004 sample

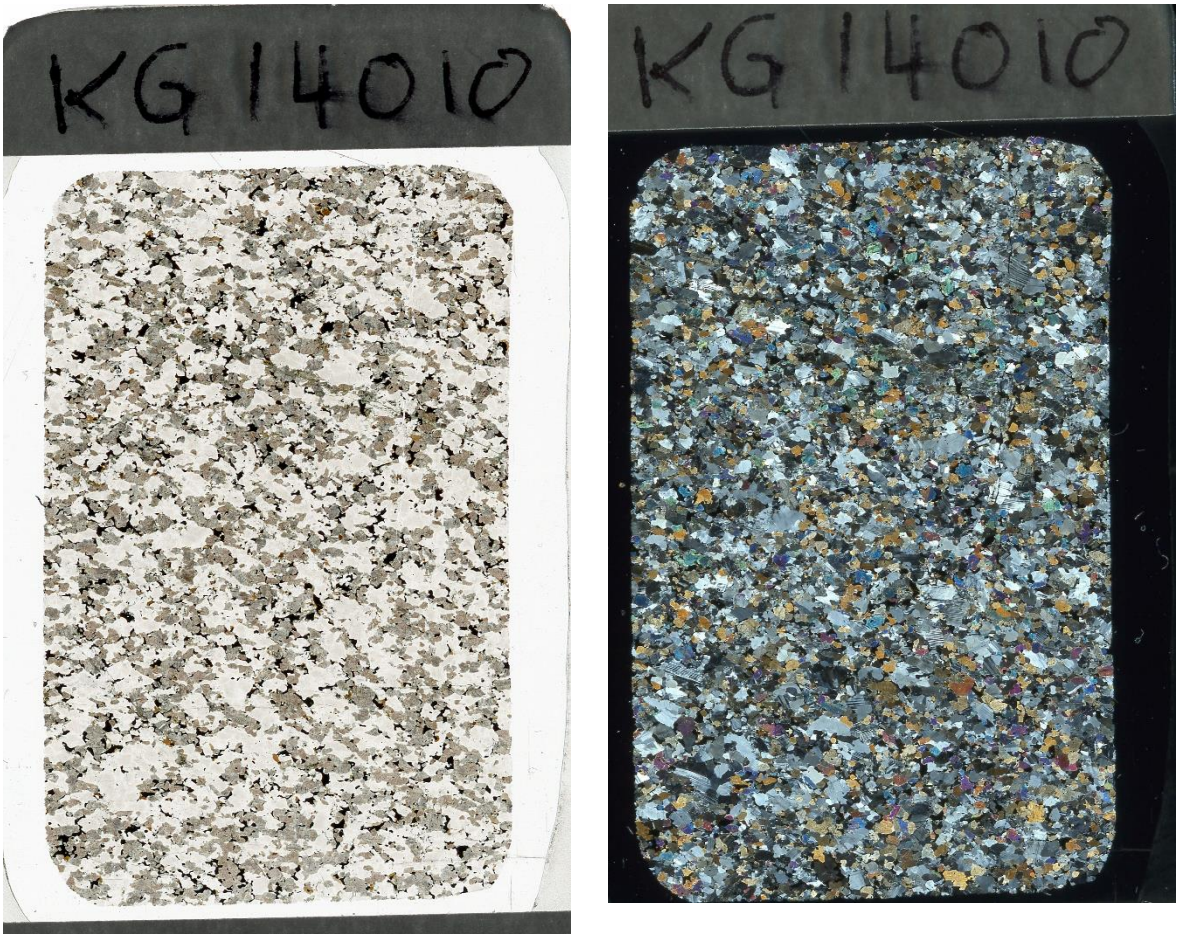

Figure A. 9: Scanned photos of the KG14010sample

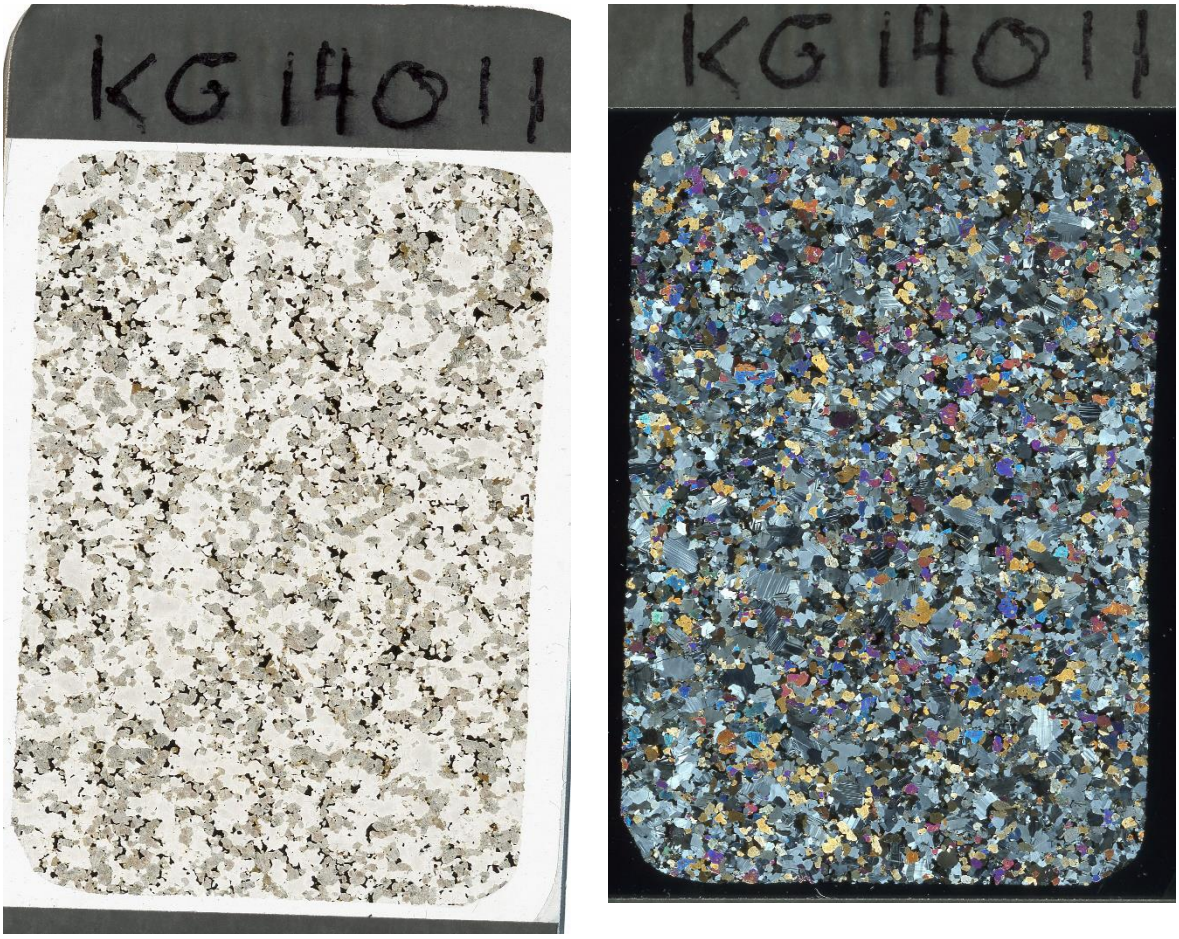

Figure A. 10: Scanned photos of the KG14011 sample

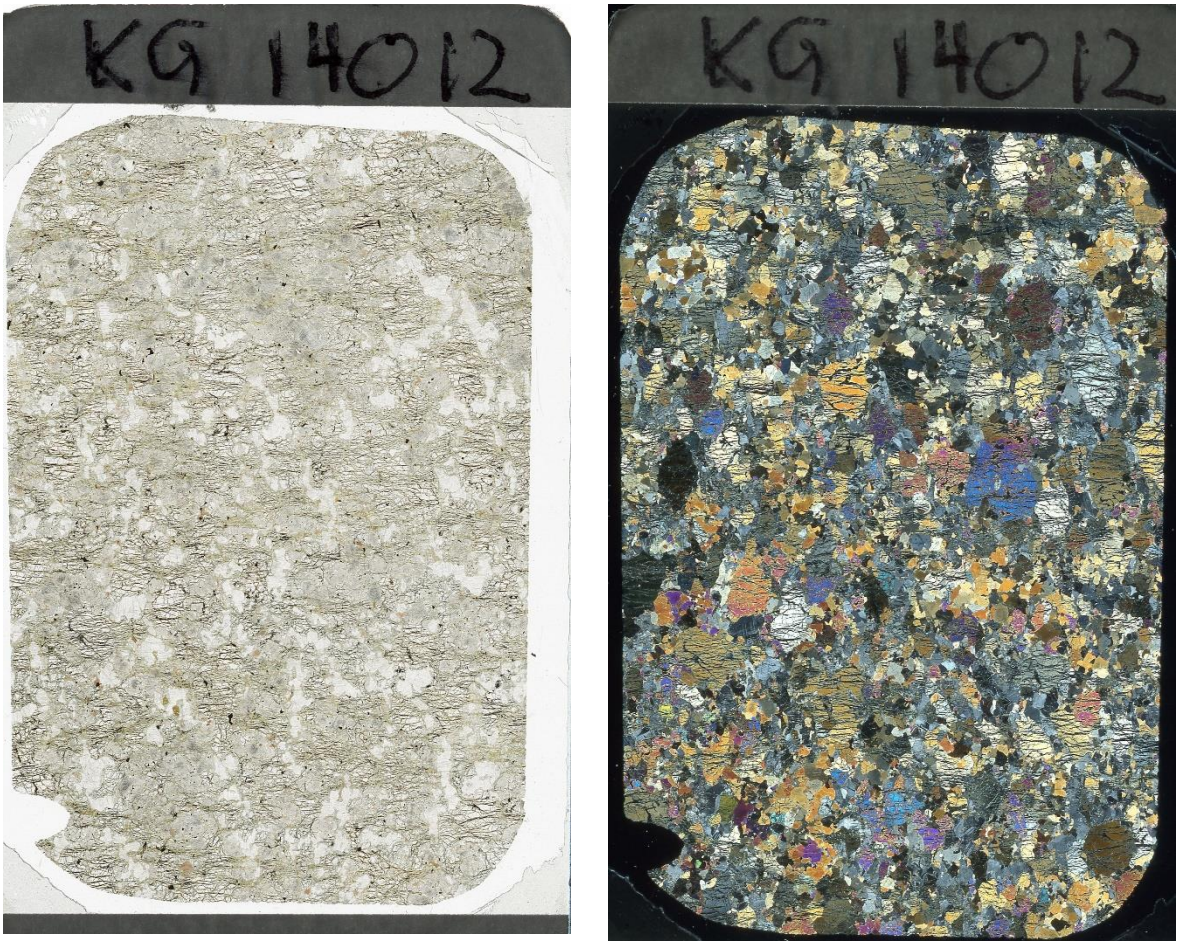

Figure A. 11: Scanned photos of the KG14012 sample

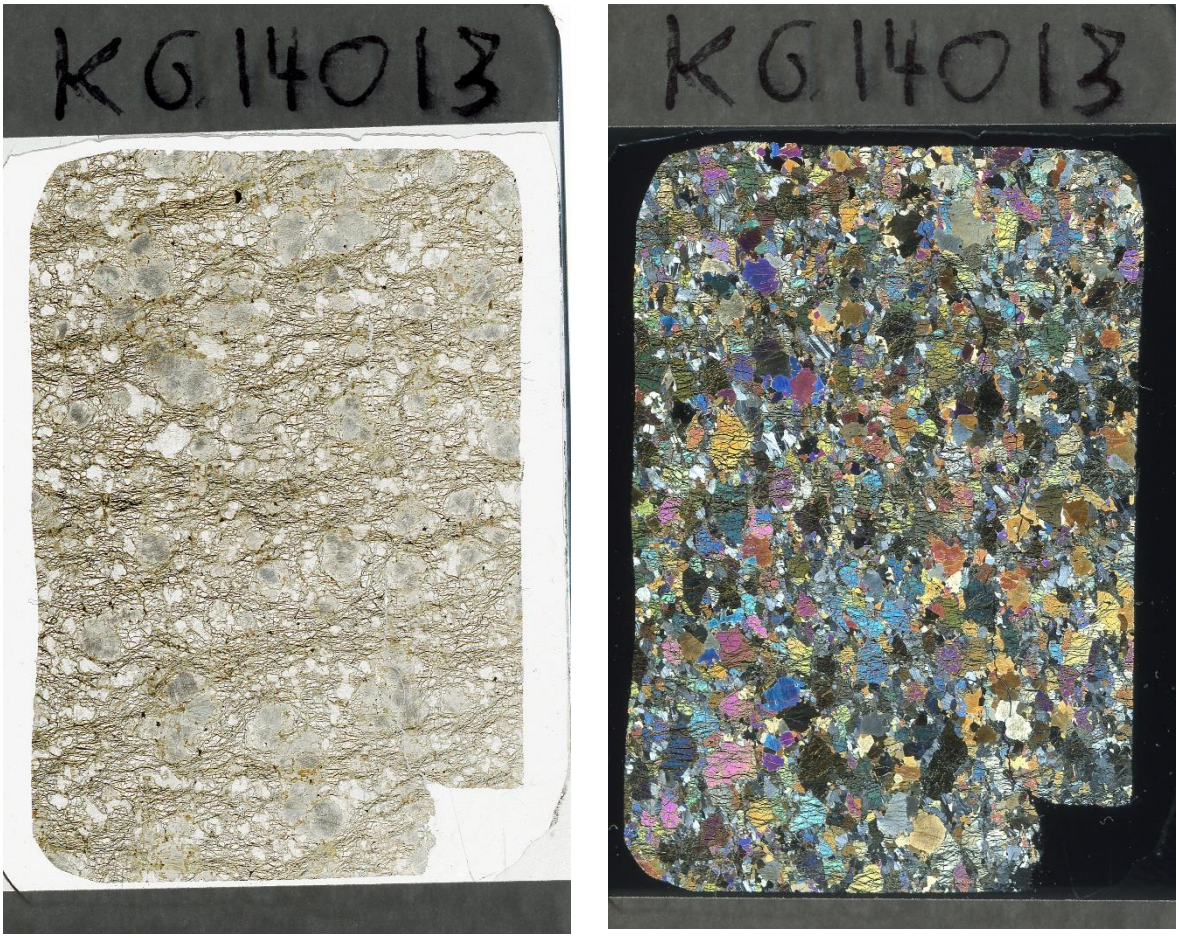

Figure A. 12: Scanned photos of the KG14013 sample

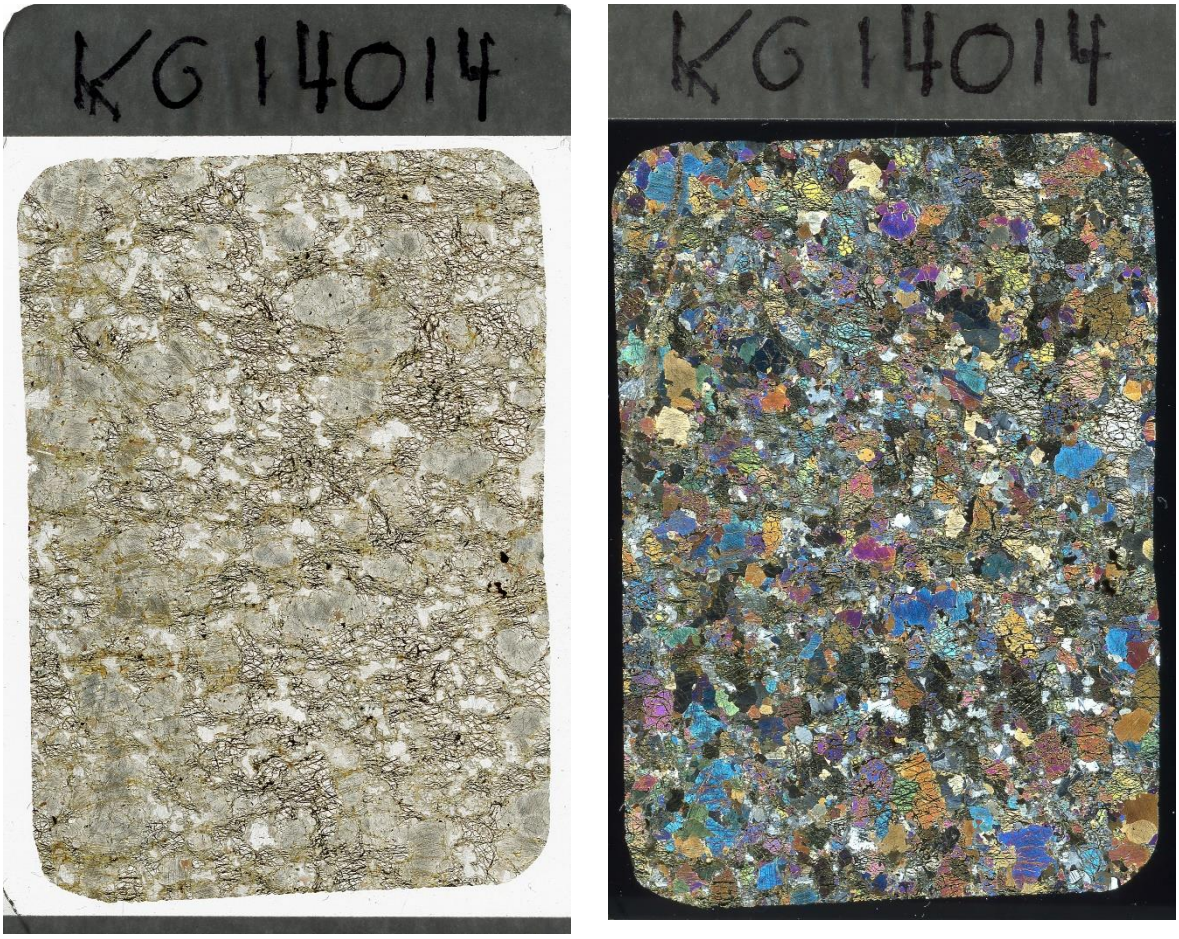

Figure A. 13: Scanned photos of the KG14014 sample

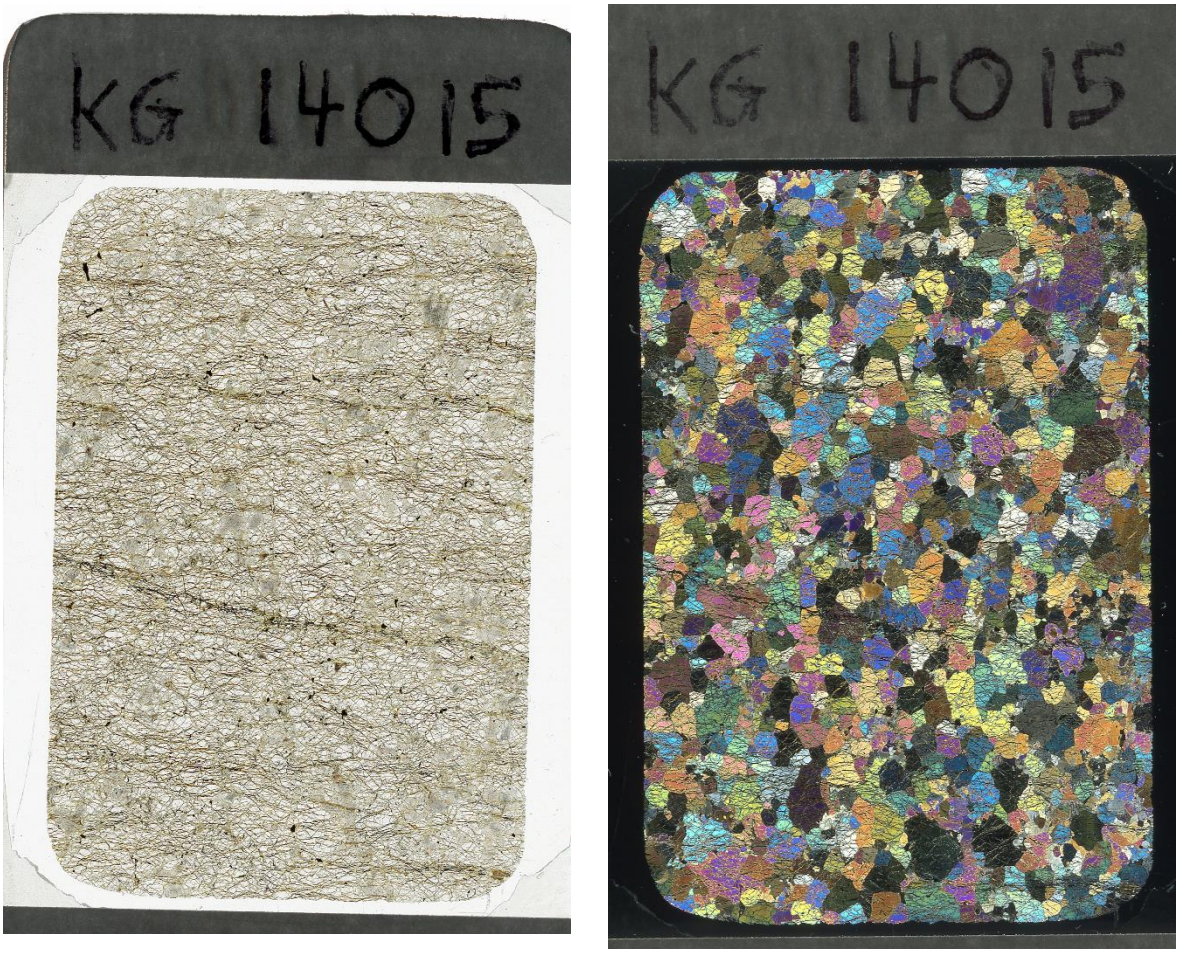

Figure A. 14: Scanned photos of the KG14015 sample

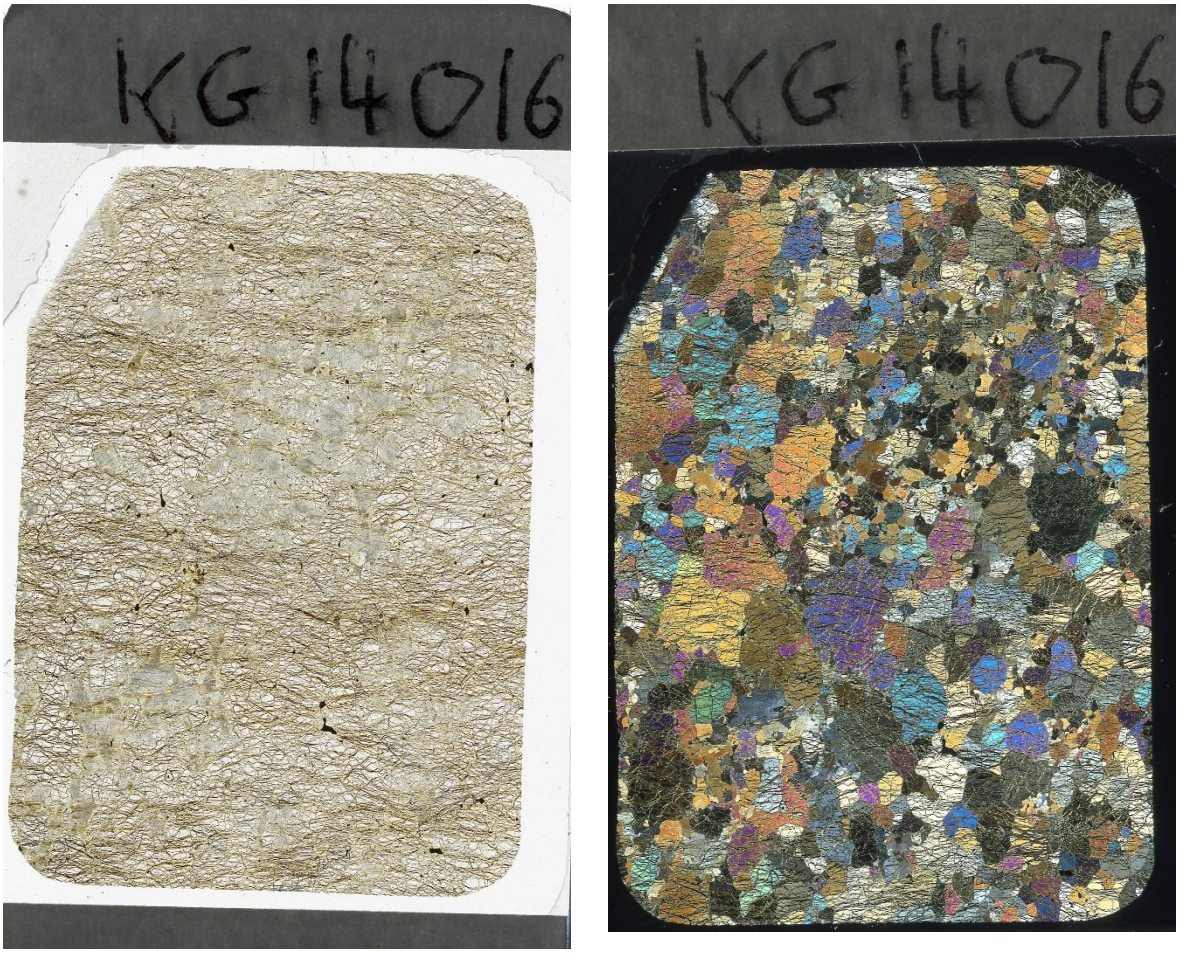

Figure A. 15: Scanned photos of the KG14016 sample

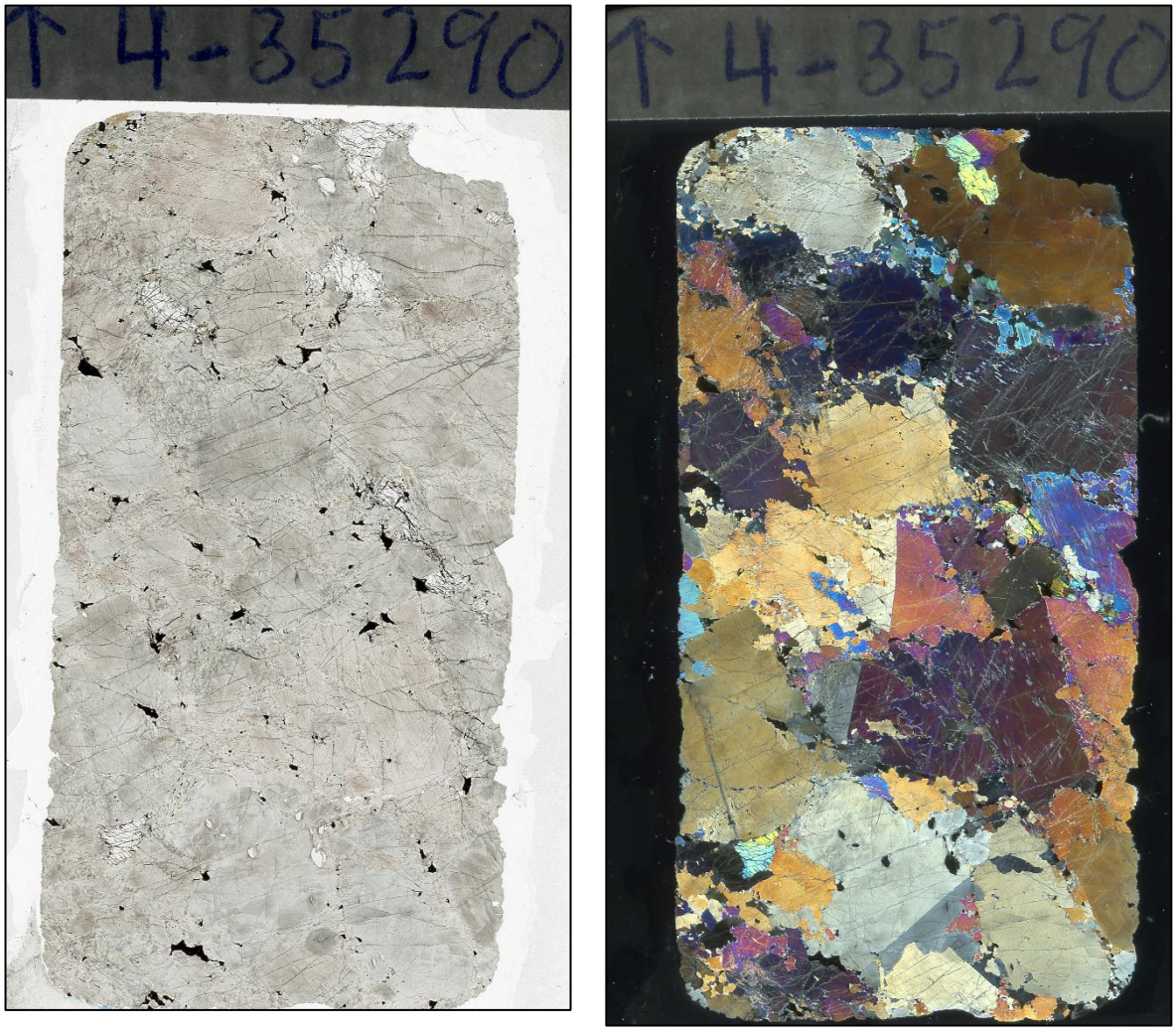

Figure A. 16: Scanned photos of the 4-35290 sample.

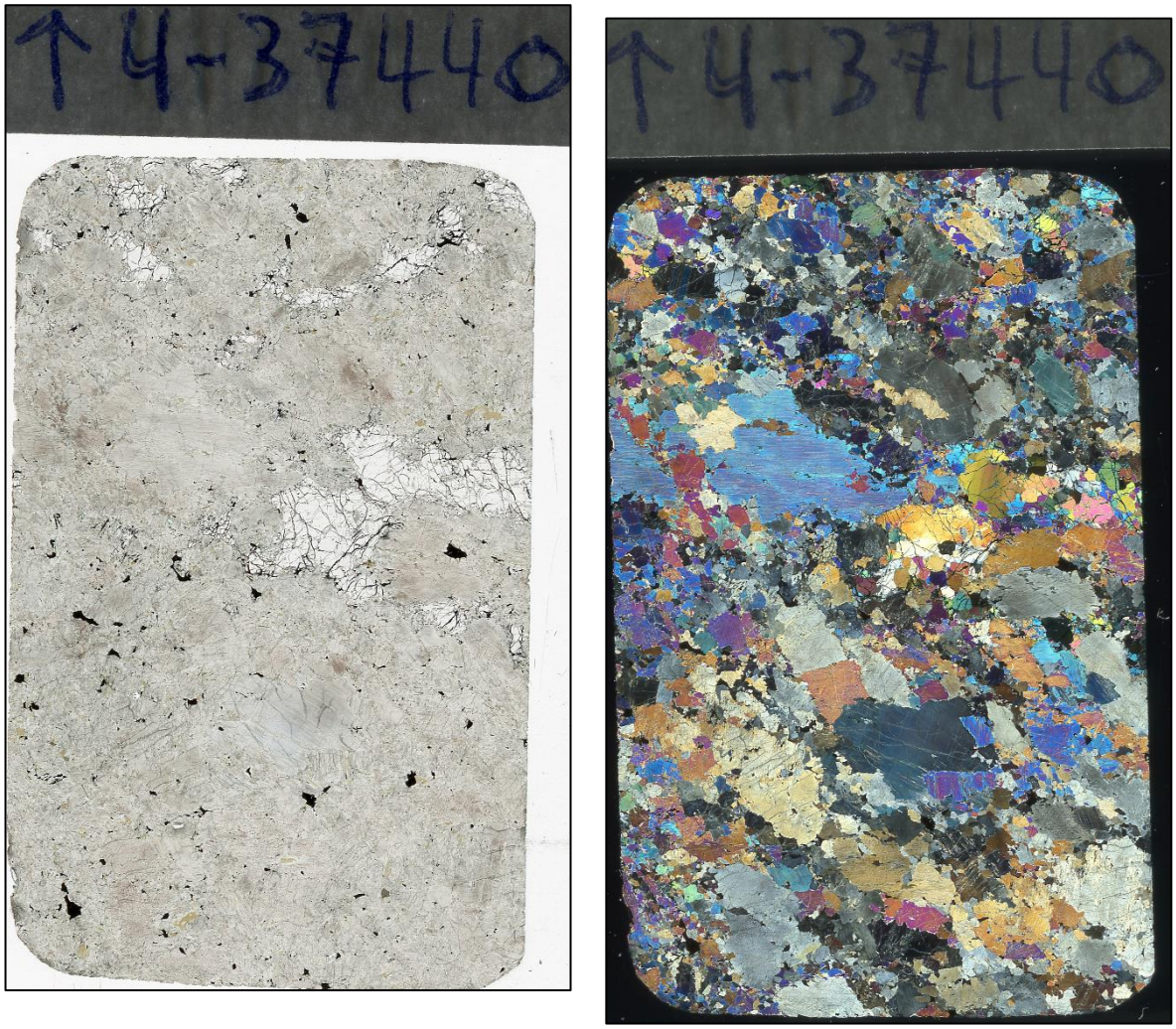

Figure A. 17: Scanned photos of the 4-37440 sample.

Appendix B: Whole-rock

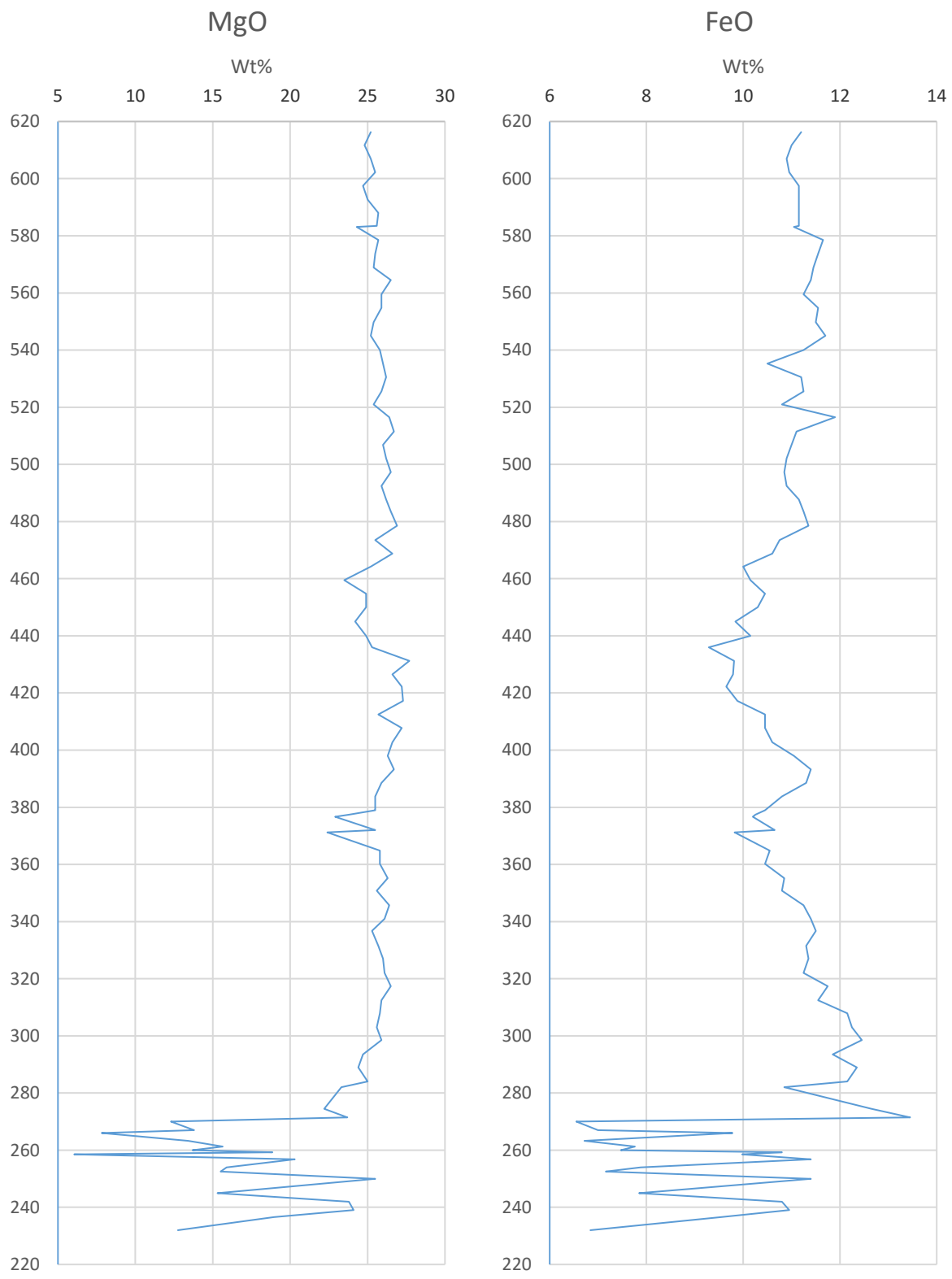

Figure B. 1: Mg and Fe whole-rock analysis of the RF-4 drill core

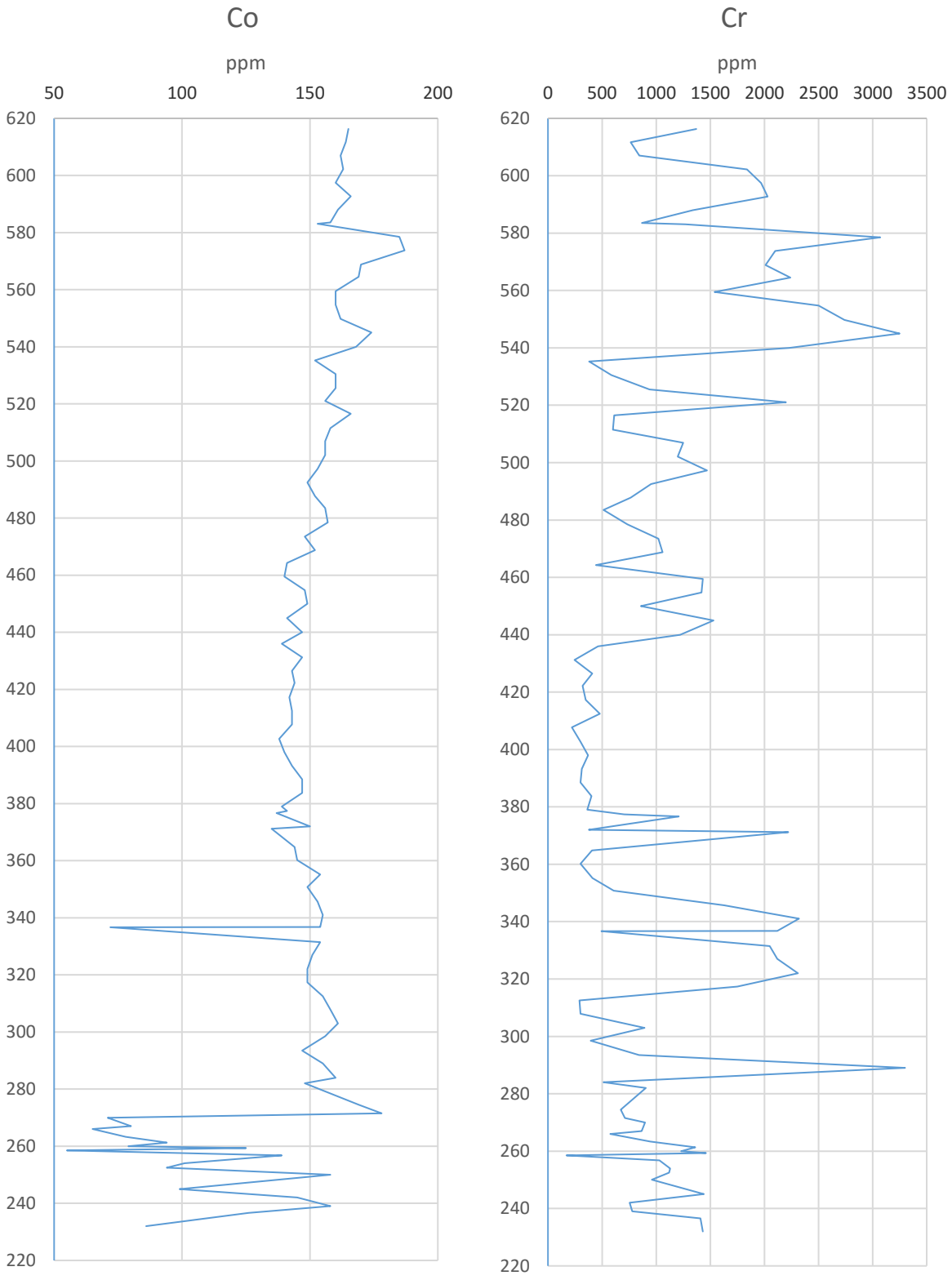

Figure B. 2: Co and Cr whole-rock analysis of the RF-4 drill core

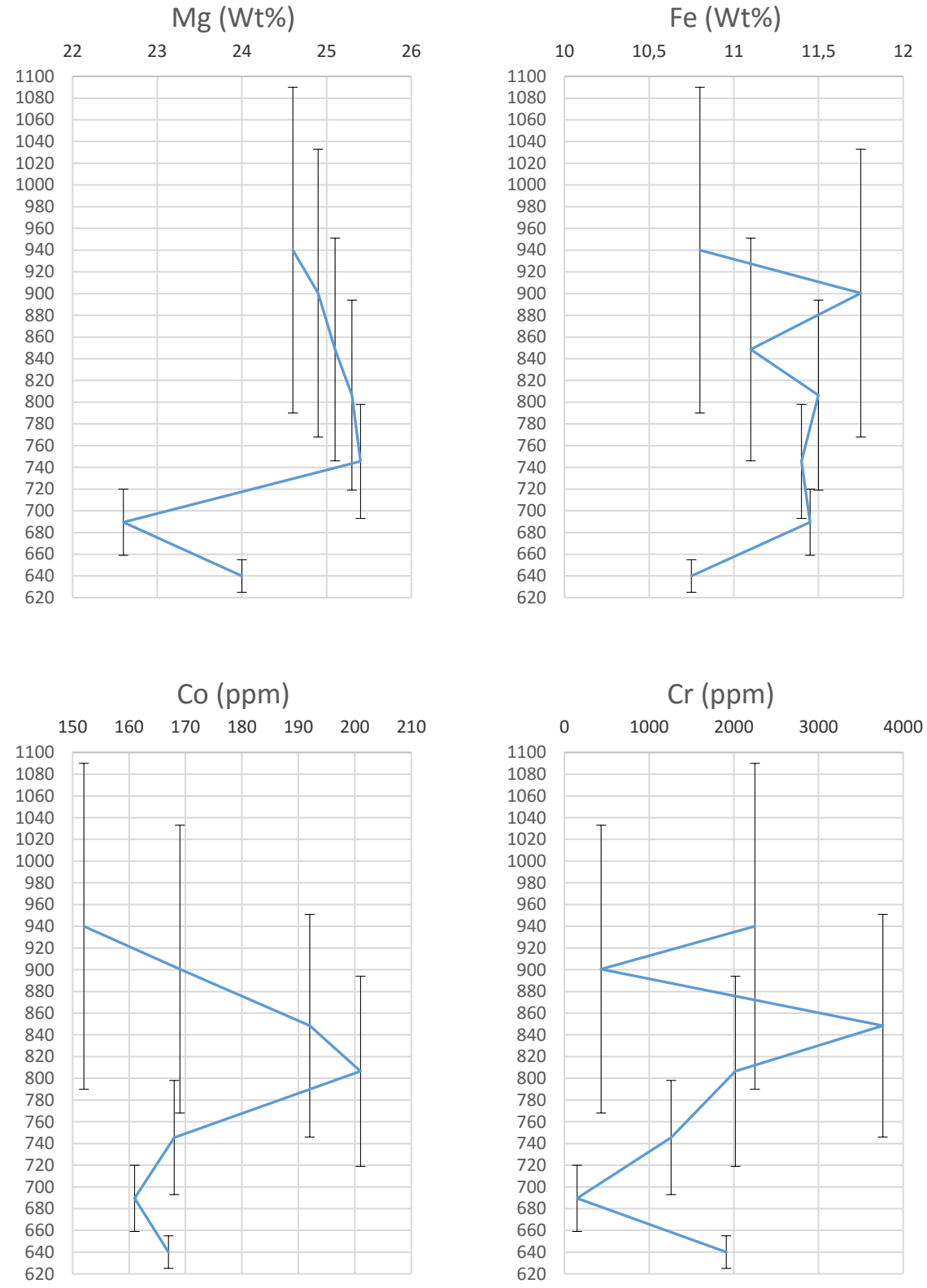

Figure B. 3: Mg, Fe, Co and Cr whole-rock analysis of the CS surface samples

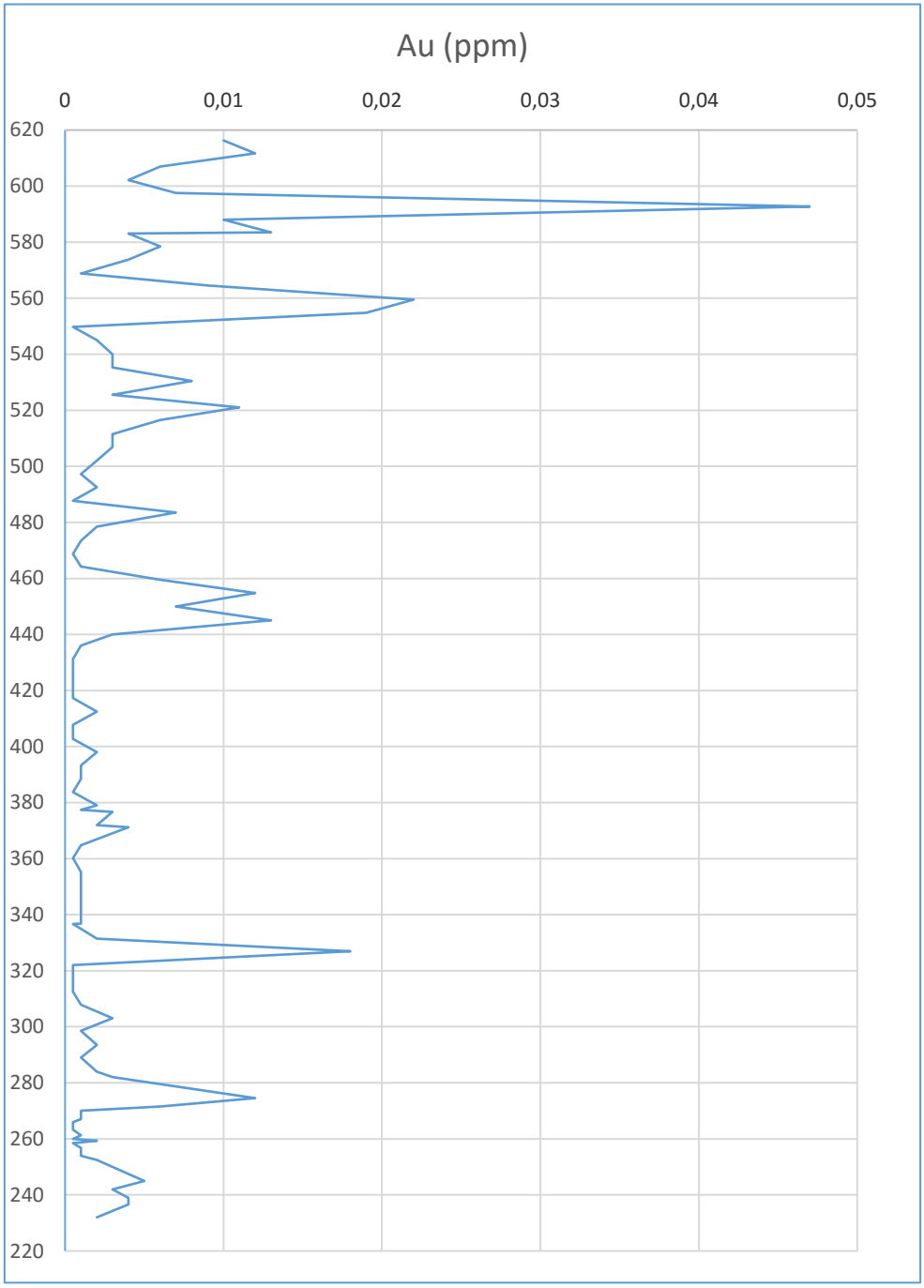

Figure B. 4: Au trace element analysis of the RF-4 drill core

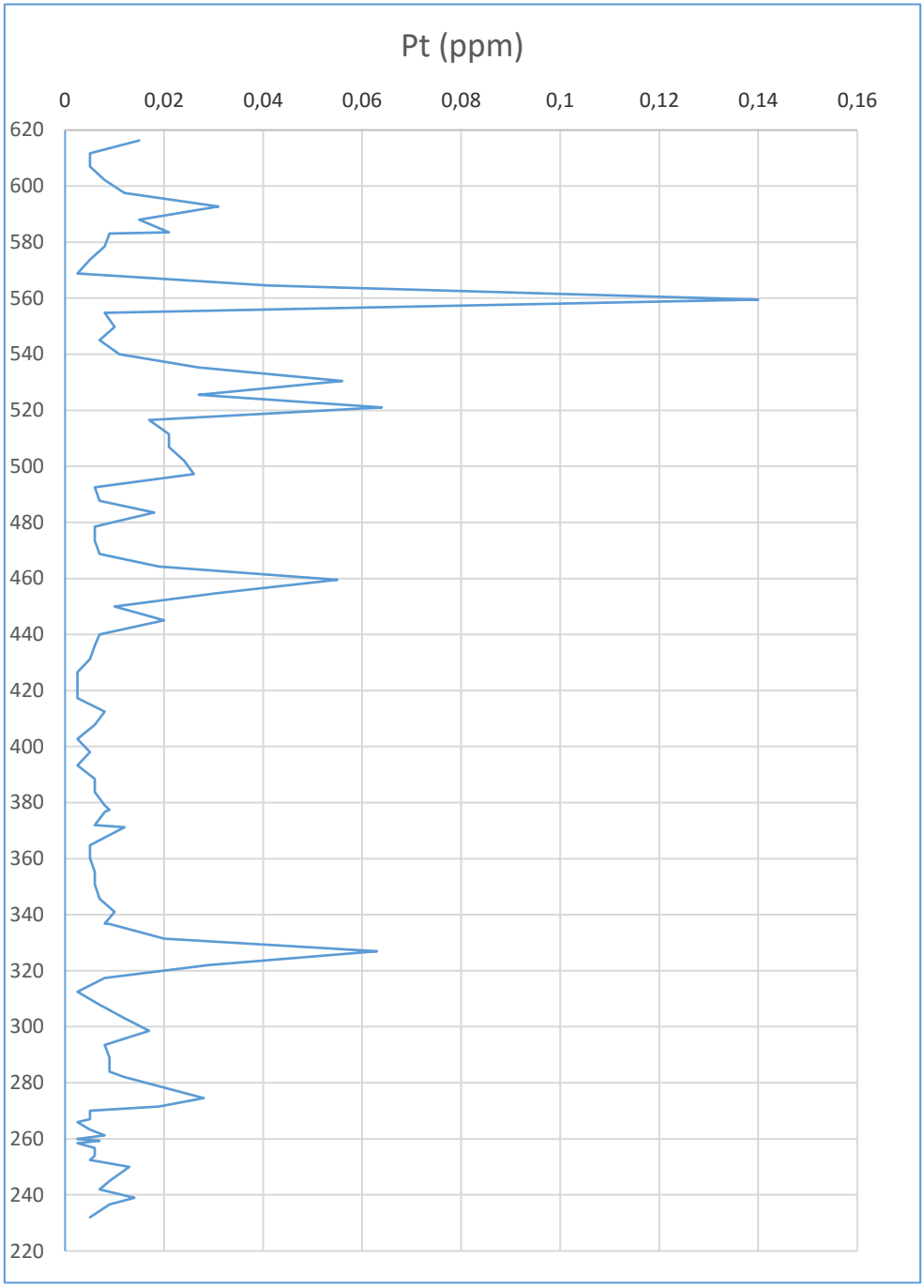

Figure B. 5: Pt trace element analysis of the RF-4 drill core

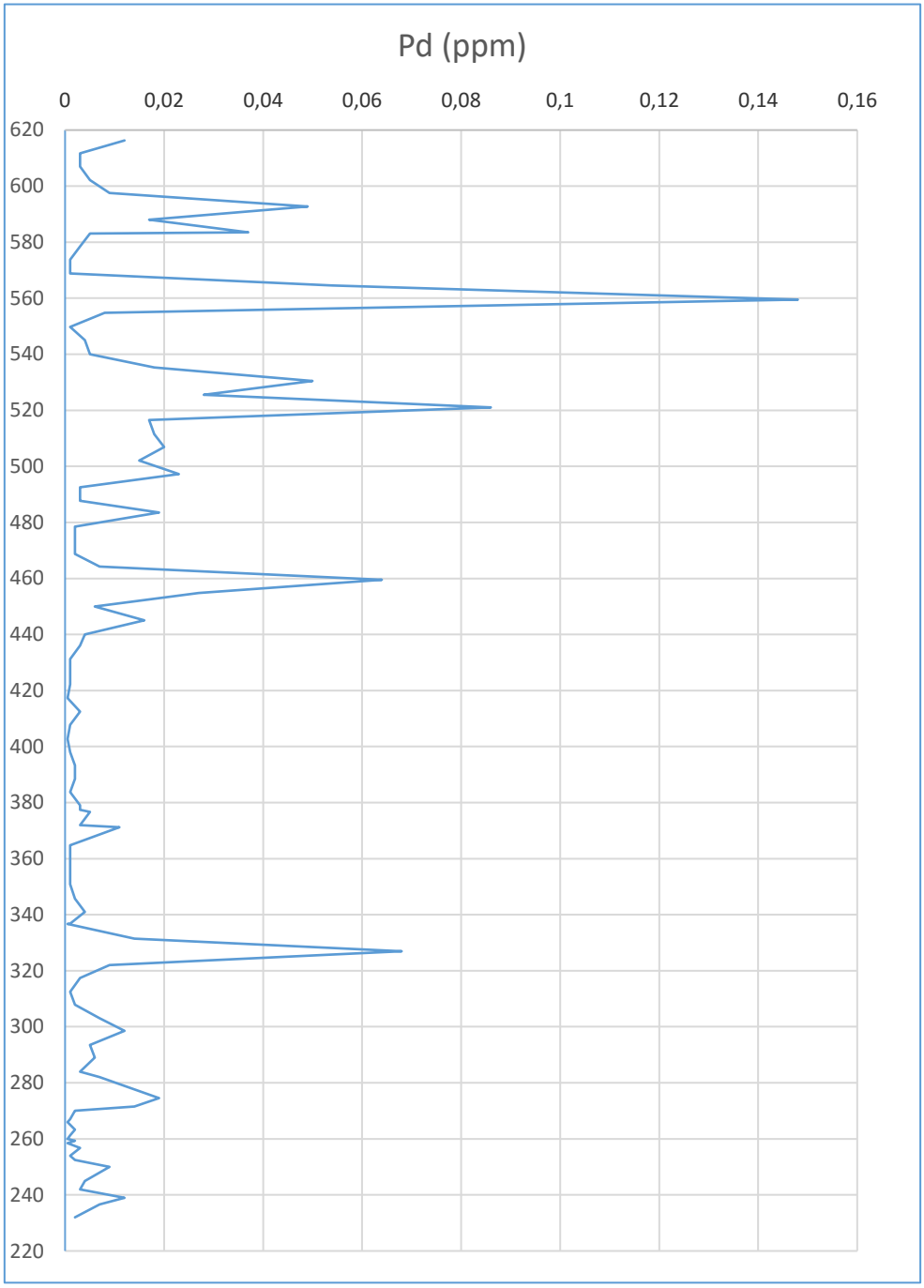

Figure B. 6: Pd trace element analysis of the RF-4 drill core

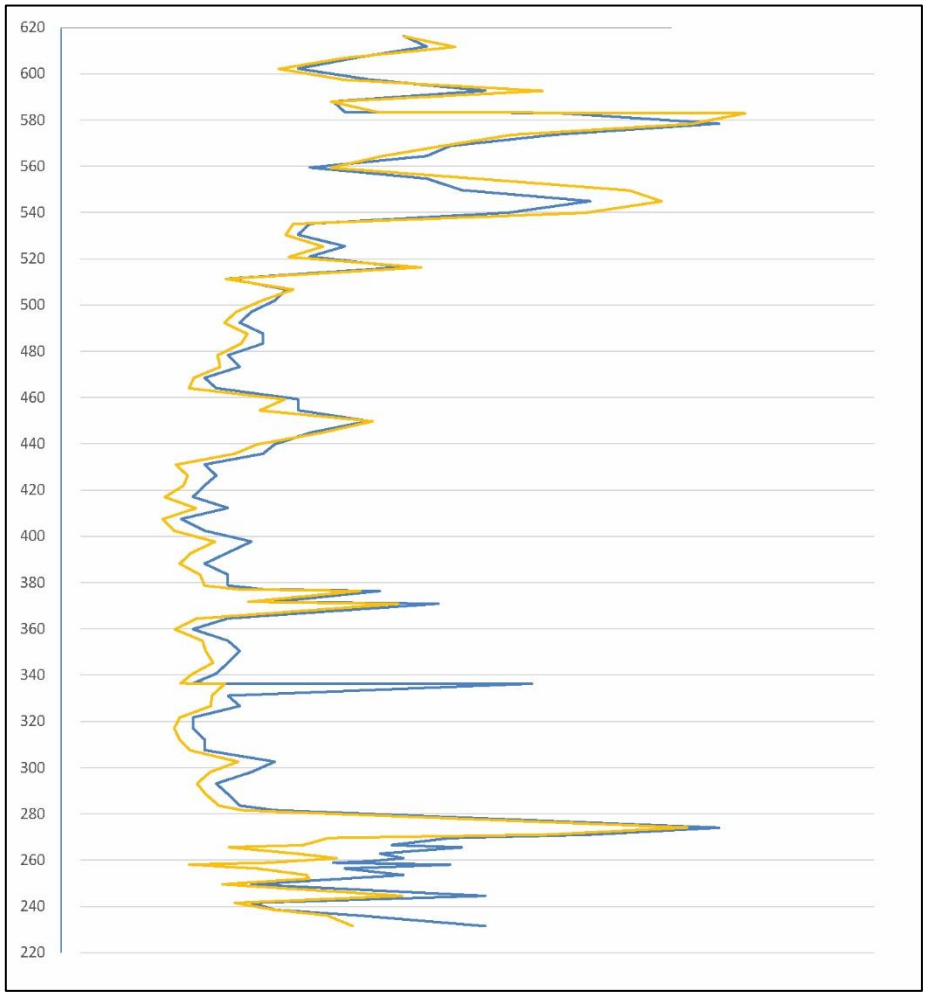

Figure B. 7: Diagram showing the evolution of Cu (Yellow) and S (Blue) with depth

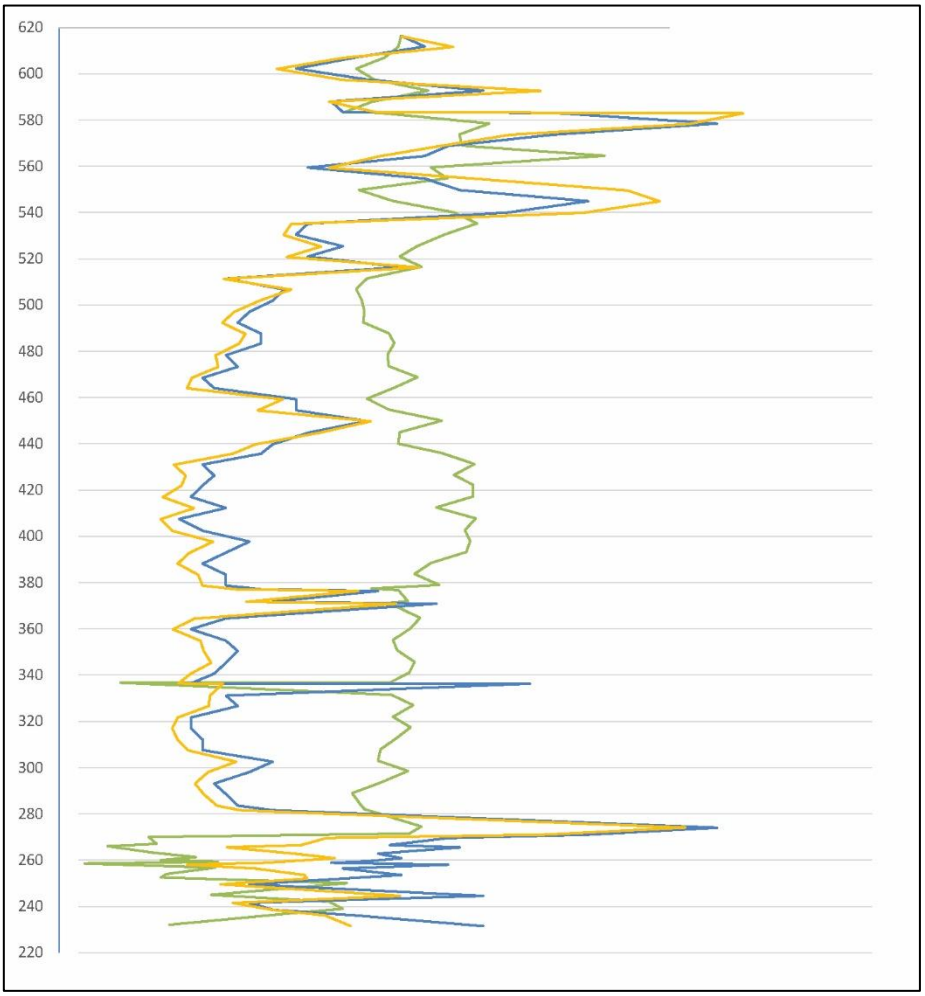

Figure B. 8: Diagram showing the evolution of Cu (Yellow), Ni (Green) and S (Blue) with depth

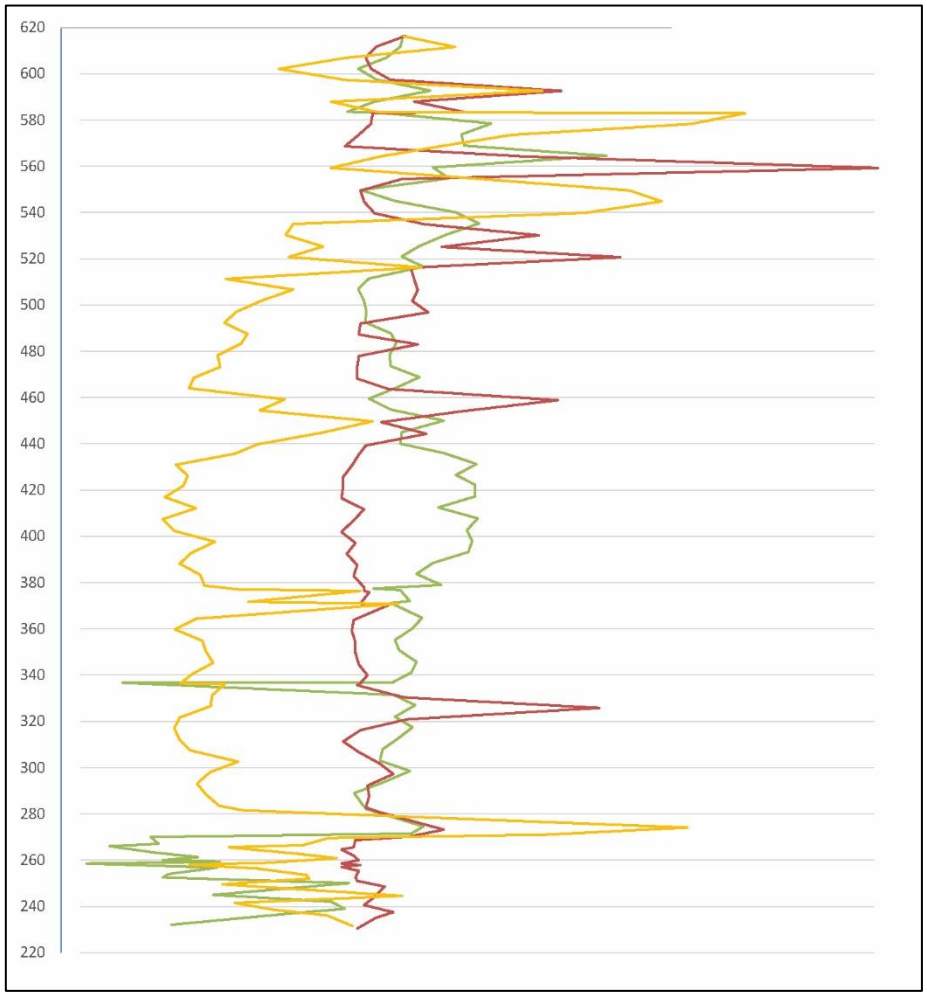

Figure B. 9: Diagram showing the evolution of Cu (Yellow), Ni (Green) and PGE (red) with depth

Appendix C: EPMA

Olivine

Figure C. 1 Olivine EPMA analysis. Presented in Wt%, part 1/2

Sample	m.a.s.l.	MgO	Na_2O	K_2O	MnO	SiO_2
KG14023	940	44,95	0,00	0,00	0,19	40,00
KG14022	900,5	44,04	0,01	0,00	0,21	39,86
KG14020	806,5	45,52	0,01	0,01	0,18	40,40
KG14019	745,5	44,75	0,01	0,00	0,20	40,16
32,5	590,5	42,91	0,01	0,01	0,19	39,93
56,3	566,7	44,58	0,01	0,00	0,18	39,35
75,5	547,5	43,99	0,01	0,00	0,19	39,11
104,3	518,7	43,47	0,00	0,00	0,20	39,41
146,9	476,1	43,71	0,00	0,00	0,18	39,96
199,0	424	44,19	0,00	0,00	0,16	40,23
224,3	398,7	44,76	0,01	0,01	0,19	40,04
227,5	395,5	43,29	0,00	0,00	0,19	39,92
265,6	357,4	43,13	0,00	0,01	0,19	39,92
274,8	348,2	44,88	0,00	0,00	0,19	39,93
298,1	324,9	44,28	0,00	0,00	0,19	39,44
322,3	300,7	43,30	0,00	0,00	0,20	38,52
352,9	270,1	41,44	0,01	0,01	0,22	37,72
374,4	248,6	42,23	0,00	0,00	0,21	38,24

Figure C. 2 Olivine EPMA analysis. Presented in Wt%, part 2/2

Sample	Al_2O_3	CaO	FeO	NiO	Total	Fo#
KG14023	0,00	0,01	15,92	0,29	101,36	83,43
KG14022	0,00	0,01	17,24	0,29	101,67	81,99
KG14020	0,00	0,01	15,27	0,22	101,62	84,16
KG14019	0,00	0,01	16,44	0,22	101,79	82,91
32,5	0,00	0,01	14,89	0,27	98,21	83,71
56,3	0,00	0,01	14,71	0,43	99,28	84,38
75,5	0,00	0,01	15,71	0,20	99,23	83,31
104,3	0,00	0,02	15,89	0,25	99,24	82,98
146,9	0,00	0,01	14,69	0,32	98,88	84,13
199,0	0,01	0,01	13,24	0,38	98,22	85,61
224,3	0,00	0,02	15,16	0,35	100,54	84,04
227,5	0,00	0,01	15,27	0,35	99,04	83,48
265,6	0,00	0,01	15,16	0,28	98,71	83,53
274,8	0,00	0,01	15,32	0,30	100,63	83,93
298,1	0,00	0,01	15,35	0,31	99,58	83,72
322,3	0,01	0,01	16,44	0,33	98,81	82,44
352,9	0,00	0,01	19,63	0,13	99,17	79,01
374,4	0,00	0,01	18,54	0,13	99,37	80,24

Figure C. 3: Standard derivation on olivine EPMA analysis, part 1/2

Sample	m.a.s.l.	MgO	Na_2O	K_2O	MnO	SiO_2
KG14023	940	0,221	0,008	0,006	0,013	0,352
KG14022	900,5	0,120	0,008	0,006	0,010	0,149
KG14020	806,5	0,146	0,015	0,017	0,013	0,150
KG14019	745,5	0,141	0,008	0,006	0,014	0,154
32,5	590,5	0,231	0,009	0,009	0,011	0,101
56,3	566,7	0,336	0,011	0,006	0,011	0,257
75,5	547,5	0,204	0,006	0,004	0,013	0,254
104,3	518,7	0,163	0,006	0,005	0,009	0,147
146,9	476,1	0,268	0,006	0,004	0,012	0,083
199,0	424	0,211	0,005	0,004	0,013	0,085
224,3	398,7	0,085	0,008	0,008	0,004	0,072
227,5	395,5	0,256	0,005	0,005	0,016	0,136
265,6	357,4	0,344	0,008	0,011	0,014	0,140
274,8	348,2	0,246	0,006	0,007	0,010	0,069
298,1	324,9	0,440	0,005	0,004	0,013	0,340
322,3	300,7	0,188	0,009	0,006	0,013	0,235
352,9	270,1	0,286	0,012	0,024	0,015	0,265
374,4	248,6	0,201	0,005	0,002	0,012	0,298

Figure C. 4: Standard derivation on olivine EPMA analysis, part 2/2

Sample	Al_2O_3	CaO	FeO	NiO	Total	Fo#
KG14023	0,003	0,007	0,168	0,014	0,631	0,139
KG14022	0,003	0,006	0,160	0,017	0,304	0,143
KG14020	0,004	0,007	0,130	0,021	0,320	0,121
KG14019	0,003	0,006	0,124	0,017	0,252	0,132
32,5	0,006	0,005	0,137	0,021	0,371	0,112
56,3	0,004	0,008	0,128	0,024	0,294	0,181
75,5	0,004	0,010	0,138	0,021	0,206	0,157
104,3	0,004	0,008	0,112	0,019	0,176	0,126
146,9	0,007	0,008	0,107	0,019	0,247	0,153
199,0	0,008	0,010	0,152	0,014	0,295	0,146
224,3	0,006	0,025	0,123	0,011	0,175	0,103
227,5	0,003	0,007	0,127	0,020	0,292	0,164
265,6	0,006	0,009	0,121	0,021	0,360	0,173
274,8	0,001	0,003	0,202	0,008	0,157	0,242
298,1	0,004	0,008	0,154	0,016	0,793	0,150
322,3	0,007	0,008	0,131	0,017	0,224	0,121
352,9	0,005	0,007	0,267	0,024	0,346	0,312
374,4	0,006	0,008	0,202	0,013	0,310	0,231

Pyroxene

Figure C. 5: Pyroxene (white-Cpx, green-Opx) EPMA analysis. Presented in Wt%, part 1/2

Sample	M.a.s.l.	N	SiO2	Na2O	K2O	Cr2O3	MgO
75,50	547,50	3	53,757	0,607	0,002	0,643	16,674
146,90	476,10	7	52,787	0,698	0,010	1,006	16,204
199,00	424,00	3	51,034	0,754	0,006	0,903	14,986
298,10	324,90	15	51,886	0,649	0,006	0,982	15,986
322,30	300,70	3	51,346	0,766	0,002	1,020	15,704
352,90	270,10	14	51,135	0,411	0,005	0,228	16,154
374,40	248,60	20	50,629	0,424	0,007	0,294	15,081
104,3	518,7	3	56,930	0,019	0,013	0,031	32,662
227,5	395,5	1	57,156	0,000	0,011	0,073	33,077
35290	270,1	2	54,630	0,011	0,006	0,027	29,372
37440	248,6	1	53,024	0,154	0,000	0,197	23,455

Figure C. 6: Pyroxene (white-Cpx, green-Opx) EPMA analysis. Presented in Wt%, part 2/2

Sample	Al2O3	CaO	MnO	TiO_2	FeO	Total	Mg#
75,50	2,558	23,322	0,089	0,399	3,160	101,211	84,067
146,90	4,243	22,799	0,108	0,753	3,222	101,829	83,416
199,00	6,464	23,014	0,080	1,196	3,790	102,227	79,815
298,10	3,603	22,791	0,107	0,569	3,515	100,095	81,976
322,30	4,216	21,971	0,124	0,584	4,225	99,957	78,800
352,90	4,293	21,073	0,121	0,850	6,047	100,318	72,761
374,40	4,892	23,129	0,108	0,959	4,983	100,505	75,165
104,3	1,547	0,119	0,239	0,027	10,289	101,876	76,045
227,5	1,039	0,265	0,224	0,041	9,837	101,723	77,077
35290	1,946	0,341	0,230	0,098	13,029	99,688	69,272
37440	4,083	6,701	0,234	0,319	11,889	100,056	66,362

Figure C. 7: Standard derivation on pyroxene (white-Cpx, green-Opx) EPMA analysis, part 1/2

Sample	M.a.s.l.	N	SiO2	Na2O	K2O	Cr2O3	MgO
75,50	547,50	3	0,716	0,185	0,002	0,275	0,544
146,90	476,10	7	0,173	0,077	0,007	0,089	0,290
199,00	424,00	3	0,168	0,037	0,008	0,118	0,314
298,10	324,90	15	0,348	0,083	0,007	0,128	0,693
322,30	300,70	3	0,223	0,124	0,003	0,070	0,662
352,90	270,10	14	0,566	0,064	0,007	0,043	1,419
374,40	248,60	20	0,599	0,049	0,011	0,018	1,032
104,3	518,7	3	0,547	0,017	0,011	0,022	0,442
227,5	395,5	1	0,000	0,000	0,000	0,000	0,000
35290	270,1	2	0,045	0,011	0,006	0,005	0,088
37440	248,6	1	0,000	0,000	0,000	0,000	0,000

Figure C. 8: Standard derivation on pyroxene (white-Cpx, green-Opx) EPMA analysis, part 1/2

Sample	Al2O3	CaO	MnO	TiO_2	FeO	Total
75,50	1,149	0,689	0,011	0,195	0,380	0,391
146,90	0,177	0,348	0,011	0,094	0,105	0,187
199,00	0,283	0,372	0,012	0,058	0,227	0,289
298,10	0,357	1,257	0,014	0,079	0,397	0,382
322,30	0,190	1,194	0,010	0,011	0,732	0,315
352,90	0,443	2,750	0,026	0,228	1,253	0,640
374,40	0,433	2,043	0,020	0,331	0,907	0,404
104,3	0,991	0,026	0,019	0,020	0,167	0,151
227,5	0,000	0,000	0,000	0,000	0,000	0,000
35290	0,013	0,002	0,013	0,023	0,039	0,055
37440	0,000	0,000	0,000	0,000	0,000	0,000

Contact Zone

Olivine

Figure C. 9: Olivine EPMA analysis. Presented in Wt%, part 1/2

Sample	N	MgO	Na_2O	K2O	MnO	SiO2
KG14012	15	39,913	0,003	0,003	0,248	38,368
KG14013	12	40,027	0,006	0,0002	0,238	38,459
KG14014	15	41,443	0,003	0,003	0,228	39,123
KG14015	18	41,920	0,001	0,002	0,237	39,197
KG14016	21	41,594	0,010	0,004	0,238	38,945
KG14002	12	38,516	0,008	0,012	0,268	38,373
KG14003	9	37,795	0,005	0,304	0,304	38,071

Figure C. 10: Olivine EPMA analysis. Presented in Wt%, part 2/2

Sample	Al2O3	CaO	FeO	NiO	Tot	Fo%
KG14012	0,001	0,009	20,763	0,135	99,442	77,41
KG14013	0,005	0,015	20,550	0,160	99,462	77,64
KG14014	0,001	0,008	21,055	0,168	102,031	77,82
KG14015	0,002	0,009	20,435	0,184	101,986	78,52
KG14016	0,005	0,011	20,447	0,173	101,427	78,38
KG14002	-	0,021	23,139	0,168	100,514	74,79
KG14003	-	0,007	24,472	0,165	100,839	73,35

Figure C. 11: Standard derivation on olivine, part 1/2

Sample	N	MgO	Na_2O	K2O	MnO	SiO2
KG14012	15	0,098	0,006	0,005	0,010	0,213
KG14013	12	0,161	0,006	0,004	0,014	0,124
KG14014	15	0,166	0,005	0,004	0,013	0,095
KG14015	18	0,199	0,004	0,002	0,012	0,097
KG14016	21	0,254	0,012	0,006	0,013	0,186
KG14002						
KG14003						

Figure C. 12: Standard derivation on olivine, part 2/2

Sample	Al2O3	CaO	FeO	NiO	Tot	Fo%
KG14012	0,003	0,007	0,244	0,017	0,354	0,002
KG14013	0,005	0,011	0,156	0,014	0,116	0,002
KG14014	0,003	0,007	0,192	0,016	0,276	0,002
KG14015	0,004	0,006	0,194	0,015	0,233	0,002
KG14016	0,006	0,008	0,329	0,016	0,257	0,004
KG14002	-					
KG14003	-					

Pyroxene

Figure C. 13: Cpx EPMA analysis. Presented in Wt%, part 1/2

Sample	N	SiO2	Na2O	K2O	Cr2O3	MgO
KG14010	14	49,865	0,620	0,007	0,024	13,526
KG14011	9	49,915	0,730	0,005	0,014	13,963
KG14012	11	48,902	0,801	0,011	0,570	13,768
KG14013	12	48,972	0,747	0,004	0,693	13,988
KG14014	16	49,665	0,739	0,006	0,701	13,823
KG14015	12	49,589	0,700	0,004	0,676	14,085
KG14016	15	49,754	0,689	0,005	0,698	14,327
KG14002	14	49,494	0,633	0,008	7,169	14,879
KG14003	1	49,203	0,808	0,000	7,325	13,603

Figure C. 14: Cpx EPMA analysis. Presented in Wt%, part 2/2

Sample	Al2O3	CaO	MnO	TiO2	FeO	Total
KG14010	5,803	21,032	0,199	0,947	8,630	100,652
KG14011	6,102	21,272	0,164	1,169	7,778	101,111
KG14012	7,434	22,288	0,132	1,492	5,782	101,180
KG14013	7,125	22,148	0,136	1,336	5,692	100,947
KG14014	7,260	22,508	0,141	1,295	5,662	101,799
KG14015	7,340	22,869	0,123	1,373	5,149	101,907
KG14016	6,991	22,245	0,126	1,277	5,435	101,548
KG14002	0,419	20,296	0,167	1,418	6,953	101,468
KG14003	0,338	21,772	0,161	1,393	6,599	101,262

Figure C. 15: Standard derivation for Cpx EPMA analysis. Presented in Wt%, part 1/2

Sample	N	SiO2	Na2O	K2O	Cr2O3	MgO
KG14010	14	0,291	0,090	0,008	0,012	0,545
KG14011	9	0,360	0,066	0,006	0,009	0,803
KG14012	11	0,347	0,043	0,010	0,050	0,851
KG14013	12	0,645	0,103	0,005	0,125	1,915
KG14014	16	0,407	0,051	0,010	0,083	0,320
KG14015	12	0,251	0,067	0,004	0,078	0,315
KG14016	15	0,265	0,042	0,007	0,062	0,547

Figure C. 16: Standard derivation for Cpx EPMA analysis. Presented in Wt%, part 2/2

Sample	Al2O3	CaO	MnO	TiO2	FeO	Total
KG14010	0,239	1,615	0,022	0,098	1,184	0,420
KG14011	0,495	2,020	0,027	0,195	1,489	0,492
KG14012	0,363	1,337	0,021	0,123	0,966	0,292
KG14013	0,496	2,859	0,031	0,167	1,456	0,442
KG14014	0,408	0,642	0,019	0,126	0,407	0,553
KG14015	0,283	0,607	0,015	0,097	0,371	0,186
KG14016	0,242	0,984	0,013	0,092	0,452	0,262

Plagioclase

Figure C. 17: Plagioclase EPMA analysis. Presented in Wt%, part 1/2

Sample	N	MgO	Na2O	K2O	MnO	SiO2
KG14010	15	0,015	5,172	0,188	0,008	54,954
KG14011	15	0,005	4,962	0,130	0,003	54,535
KG14012	13	0,004	4,321	0,058	0,006	52,910
KG14013	12	0,005	3,961	0,074	0,004	52,551
KG14014	17	0,005	3,394	0,022	0,007	50,843
KG14002	7	0,011	4,758	0,071	0,005	54,482
KG14003	7	0,010	4,751	0,043	0,005	54,586

Figure C. 18: Plagioclase EPMA analysis. Presented in Wt%, part 2/2

Sample	Al2O3	CaO	FeO	TiO2	Total	AN#
KG14010	28,400	10,919	0,083	0,046	99,785	81,99
KG14011	28,786	11,320	0,064	0,045	99,850	83,21
KG14012	29,698	12,462	0,024	0,040	99,522	86,34
KG14013	30,252	13,077	0,043	0,037	100,004	87,81
KG14014	31,248	14,210	0,033	0,024	99,786	90,02
KG14002	29,288	11,825	0,037	0,057	100,534	84,47
KG14003	29,338	11,894	0,053	0,071	100,750	84,62

Figure C. 19: Standard derivation for plagiocalse EPMA analysis. Presented in Wt%, part 2/2

Sample	N	MgO	Na2O	K2O	MnO	SiO2
KG14010	15	0,049	0,169	0,030	0,008	0,432
KG14011	15	0,005	0,063	0,020	0,005	0,214
KG14012	13	0,008	0,107	0,017	0,008	0,380
KG14013	12	0,007	0,124	0,012	0,006	0,291
KG14014	17	0,012	0,890	0,013	0,007	1,846
KG14002						
KG14003						

Figure C. 20: Standard derivation for plagiocalse EPMA analysis. Presented in Wt%, part 2/2

Sample	Al2O3	CaO	FeO	TiO2	Total	AN#
KG14010	0,293	0,339	0,030	0,027	0,561	0,95
KG14011	0,113	0,086	0,022	0,027	0,174	0,22
KG14012	0,177	0,110	0,017	0,013	0,374	0,37
KG14013	0,169	0,189	0,030	0,012	0,203	0,47
KG14014	1,202	1,438	0,021	0,024	0,245	2,91
KG14002						
KG14003						

Appendix D: SEM

4-7550 – Cu reef

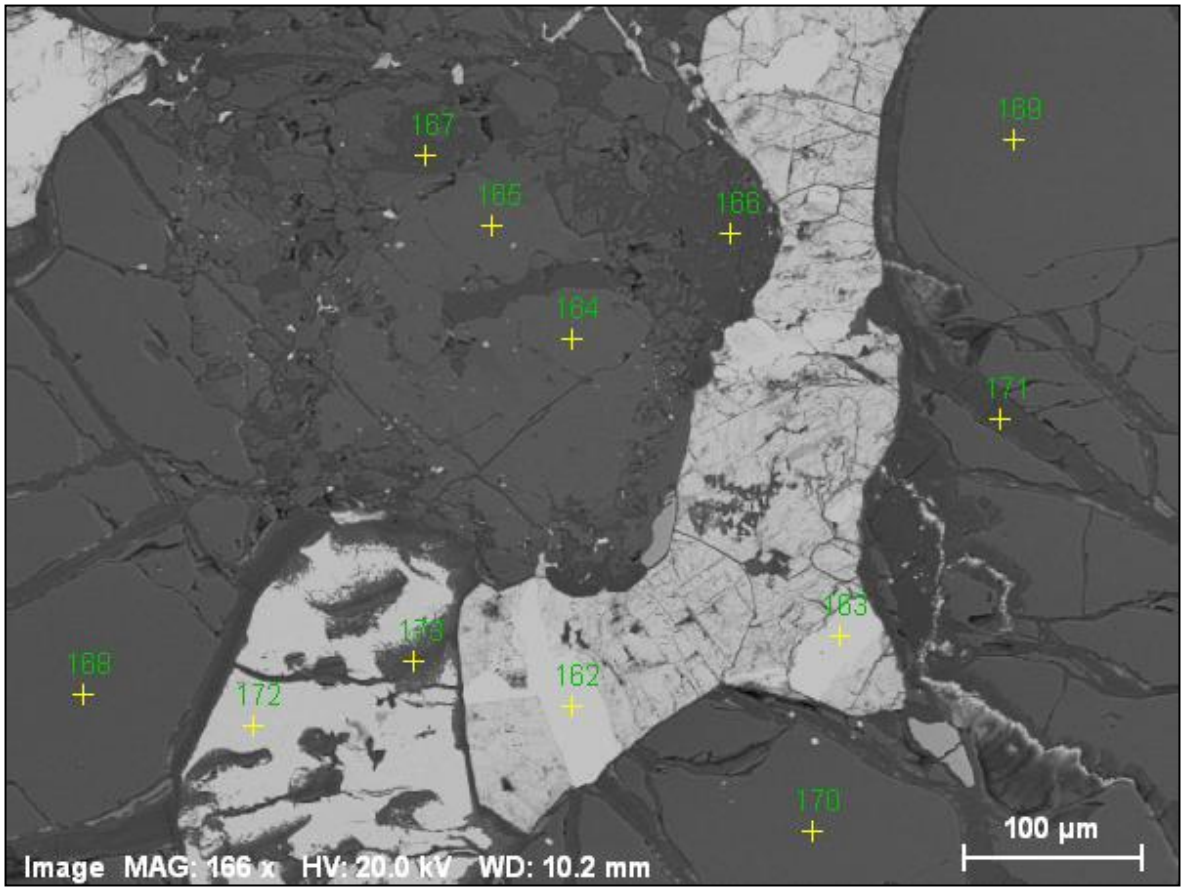

Figure D. 1: Picture of copper phases, with selected SEM spot analysis on the next pages.

Spectrum: 162

El	AN	Series	unn. C [wt.%]	norm. C [wt.%]	Atom. C [at.%]	Compound	Comp. C [wt.%]	norm. Comp. C [wt.%]	Error (1 Sigma) [wt.%]
Cu	29	K-series	84.34	94.01	84.05		94.01	84.34	2.29
O	8	K-series	2.35	2.62	9.30		0.00	0.00	0.57
Al	13	K-series	1.23	1.37	2.88	Al2O3	2.59	2.32	0.09
Mg	12	K-series	0.77	0.86	2.01	MgO	1.43	1.28	0.08
Si	14	K-series	0.53	0.59	1.20	SiO2	1.27	1.14	0.05
Fe	26	K-series	0.50	0.55	0.56	FeO	0.71	0.64	0.04
C	6	K-series	0.00	0.00	0.00		0.00	0.00	0.00
		Total:	89.72	100.00	100.00				

q

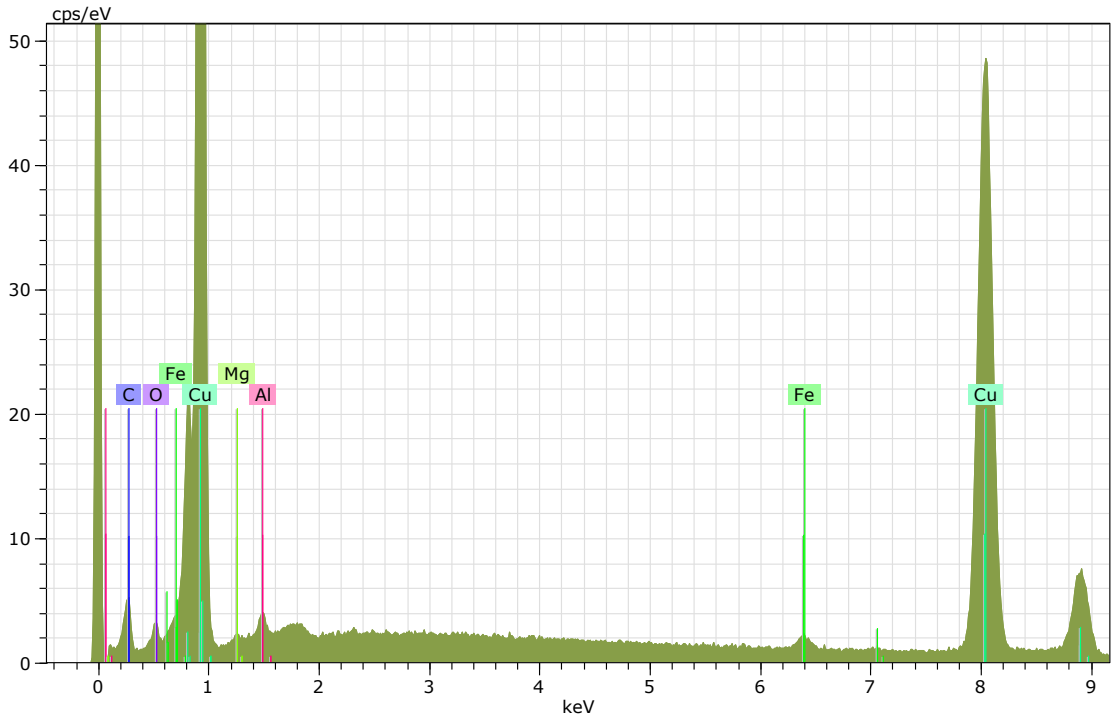

Spectrum: 163

El	AN	Series	unn. C [wt.%]	norm. C [wt.%]	Atom. C [at.%]	Compound	Comp. C [wt.%]	norm. Comp. C [wt.%]	Error (1 Sigma) [wt.%]
Cu	29	K-series	85.15	94.78	86.41		94.78	85.15	2.31
O	8	K-series	1.87	2.08	7.54		0.00	0.00	0.41
Al	13	K-series	1.25	1.39	2.99	Al2O3	2.63	2.37	0.09
Mg	12	K-series	0.83	0.93	2.21	MgO	1.54	1.38	0.08
Fe	26	K-series	0.73	0.81	0.84	FeO	1.05	0.94	0.05
C	6	K-series	0.00	0.00	0.00		0.00	0.00	0.00
		Total:	89.84	100.00	100.00				

Spectrum: 167

El	AN	Series	unn. C [wt.%]	norm. C [wt.%]	Atom. C [at.%]	Compound	Comp. C norm. [wt.%]	Comp. C [wt.%]	Error (1 Sigma) [wt.%]
O	8	K-series	21.01	32.37	50.00		0.00	0.00	2.70
Ca	20	K-series	27.43	42.26	26.05	CaO	59.13	38.37	0.83
Mg	12	K-series	14.38	22.16	22.53	MgO	36.74	23.85	0.82
Fe	26	K-series	2.08	3.21	1.42	FeO	4.13	2.68	0.09
C	6	K-series	0.00	0.00	0.00		0.00	0.00	0.00
		Total:	64.90	100.00	100.00				

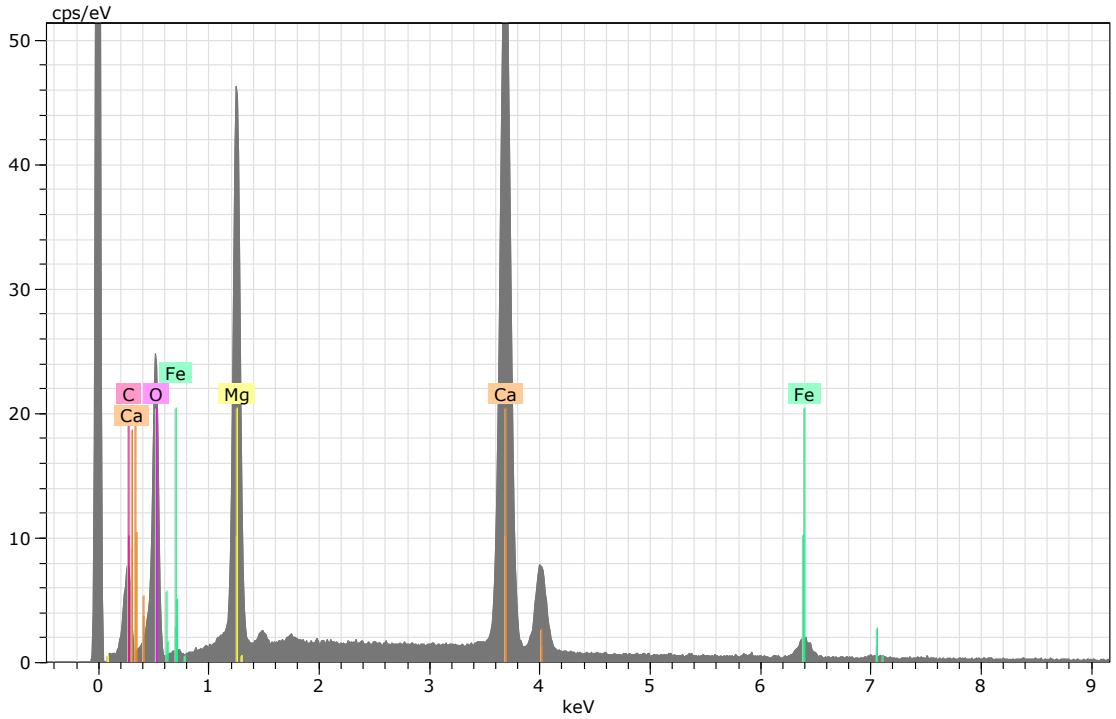

Spectrum: 168

El	AN	Series	unn. C [wt.%]	norm. C [wt.%]	Atom. C [at.%]	Compound	Comp. C [wt.%]	norm. Comp. C [wt.%]	Error (1 Sigma) [wt.%]
O	8	K-series	36.43	41.68	56.47		0.00	0.00	4.39
Mg	12	K-series	25.07	28.69	25.59	MgO	47.57	41.58	1.40
Si	14	K-series	14.66	16.77	12.94	SiO2	35.88	31.36	0.65
Fe	26	K-series	11.24	12.86	4.99	FeO	16.55	14.46	0.33
C	6	K-series	0.00	0.00	0.00		0.00	0.00	0.00
		Total:	87.40	100.00	100.00				

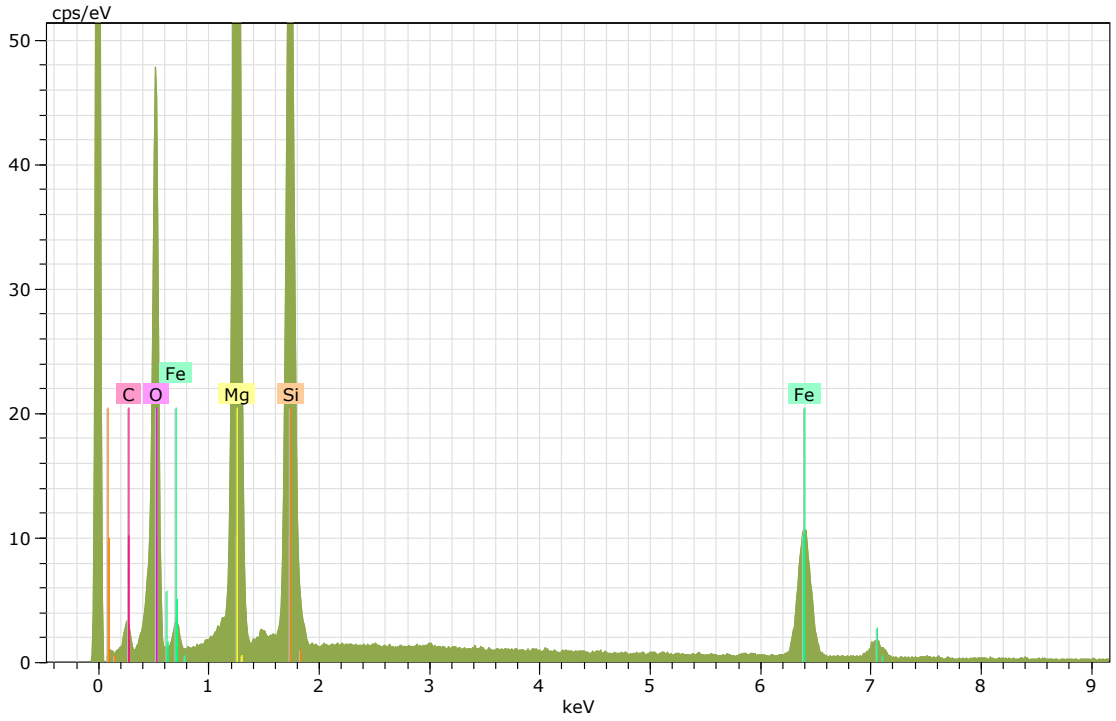

Spectrum: 171

El	AN	Series	unn. C [wt.%]	norm. C [wt.%]	Atom. C [at.%]	Compound	Comp. C norm. [wt.%]	Comp. C [wt.%]	Error (1 Sigma) [wt.%]
O	8	K-series	31.64	43.11	57.48		0.00	0.00	3.77
Mg	12	K-series	19.76	26.93	23.63	MgO	44.65	32.77	1.11
Si	14	K-series	14.46	19.70	14.97	SiO2	42.15	30.93	0.64
Fe	26	K-series	7.53	10.25	3.92	FeO	13.19	9.68	0.24
C	6	K-series	0.00	0.00	0.00		0.00	0.00	0.00
		Total:	73.38	100.00	100.00				

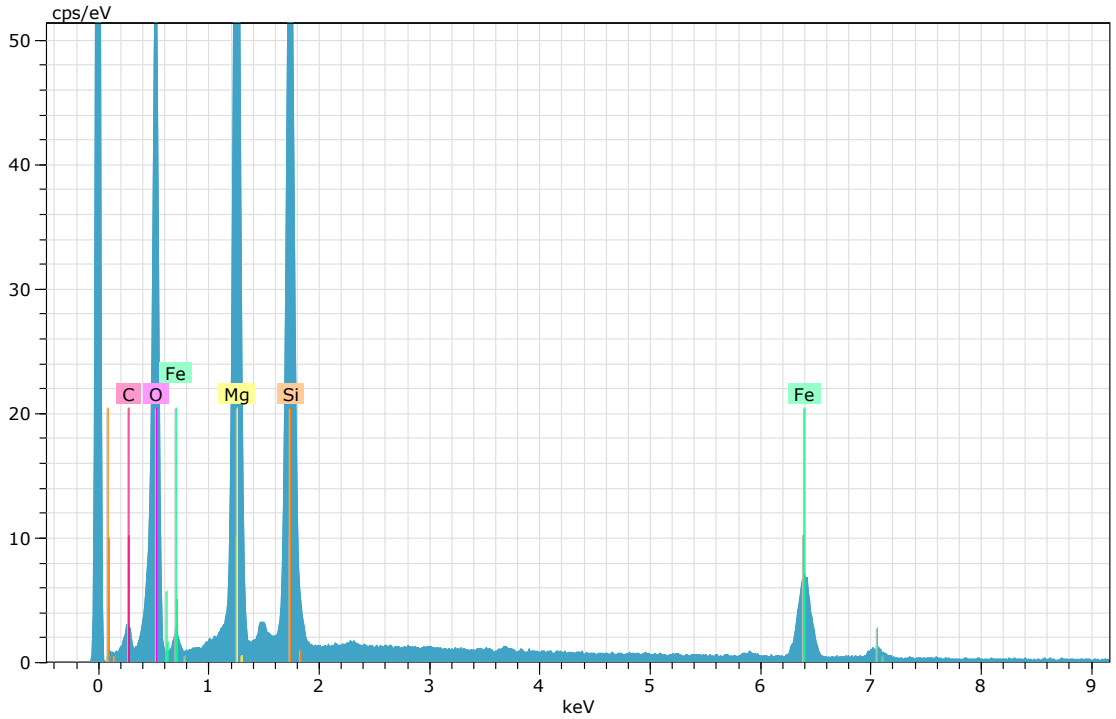

Spectrum: 172

El	AN	Series	unn. C [wt.%]	norm. C [wt.%]	Atom. C [at.%]	Compound	Comp. C [wt.%]	norm. Comp. C [wt.%]	Error (1 Sigma) [wt.%]
O	8	K-series	44.87	40.36	65.59		0.00	0.00	10.42
Fe	26	K-series	44.94	40.42	18.82	FeO	52.00	57.81	1.22
S	16	K-series	21.37	19.22	15.59	SO3	48.00	53.37	0.79
C	6	K-series	0.00	0.00	0.00		0.00	0.00	0.00
		Total:	111.18	100.00	100.00				

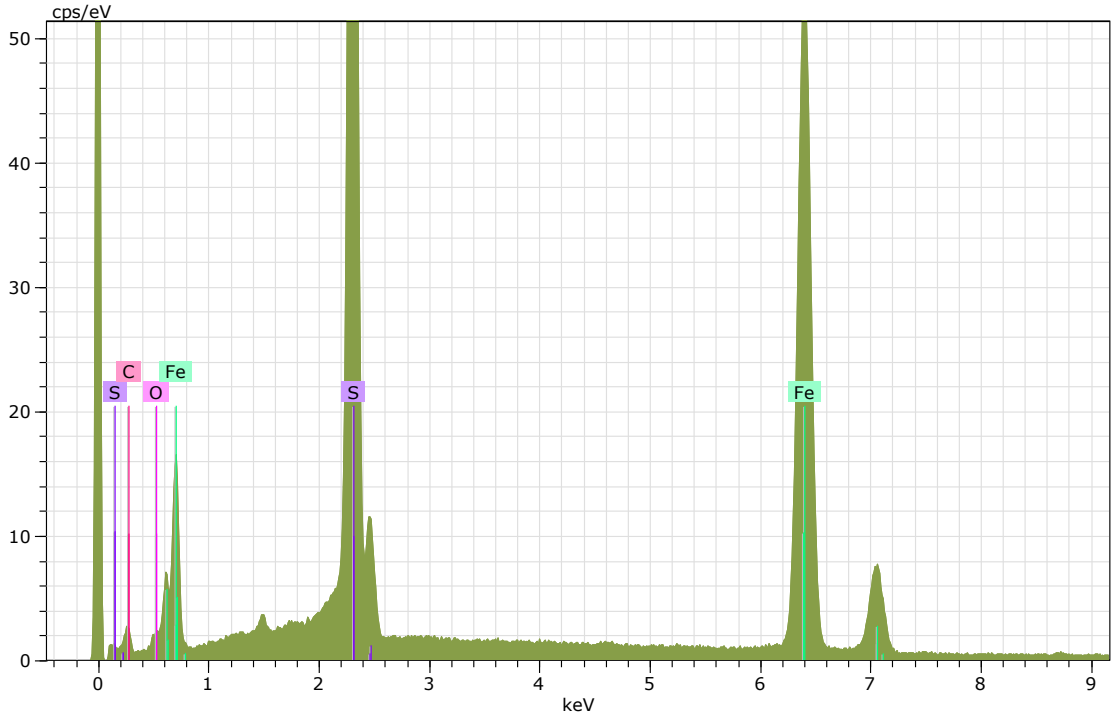

Spectrum: 173

El	AN	Series	unn. C [wt.%]	norm. C [wt.%]	Atom. C [at.%]	Compound	Comp. C [wt.%]	norm. Comp. C [wt.%]	Error (1 Sigma) [wt.%]
O	8	K-series	32.15	41.20	57.03		0.00	0.00	3.81
Mg	12	K-series	19.20	24.61	22.42	MgO	40.81	31.84	1.08
Si	14	K-series	13.91	17.83	14.06	SiO2	38.15	29.76	0.62
Fe	26	K-series	12.76	16.36	6.49	FeO	21.05	16.42	0.37
C	6	K-series	0.00	0.00	0.00		0.00	0.00	0.00
		Total:	78.03	100.00	100.00				

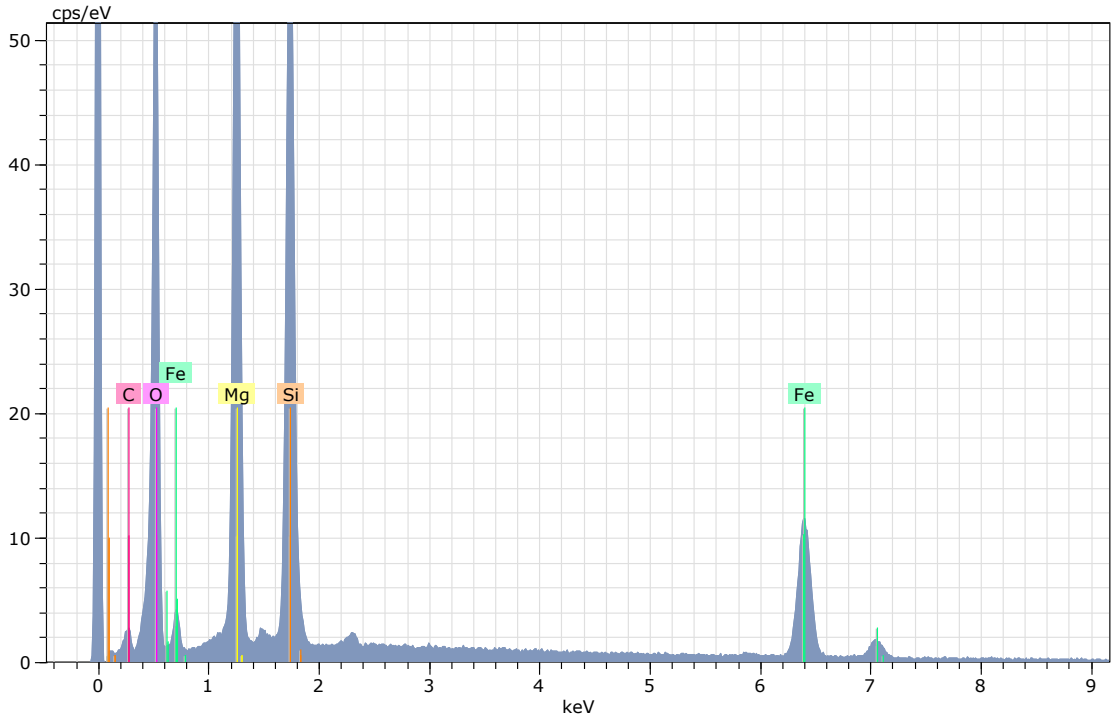

4-10430

Figure D. 2: Picture of copper phases, with selected SEM spot analysis on the next pages.

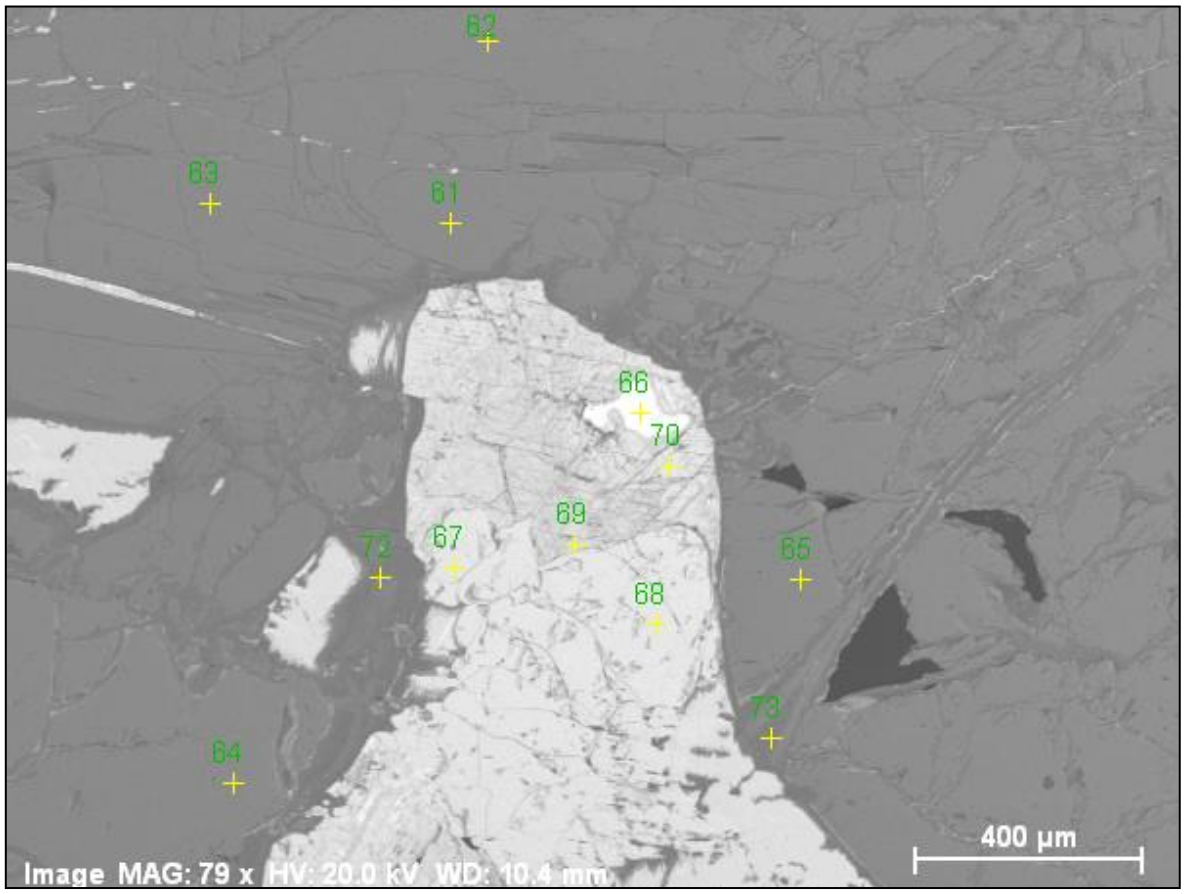

Spectrum: 61

El	AN	Series	unn. C [wt.%]	norm. C [wt.%]	Atom. C [at.%]	Compound	Comp. C [wt.%]	norm. Comp. C [wt.%]	Error (1 Sigma) [wt.%]
O	8	K-series	35.12	44.99	59.37		0.00	0.00	4.24
Si	14	K-series	18.94	24.27	18.25	SiO2	51.92	40.53	0.83
Mg	12	K-series	16.28	20.86	18.12	MgO	34.58	26.99	0.92
Fe	26	K-series	6.16	7.89	2.98	FeO	10.15	7.92	0.20
Al	13	K-series	1.01	1.29	1.01	Al2O3	2.43	1.90	0.08
Mn	25	K-series	0.55	0.71	0.27	MnO	0.91	0.71	0.05
C	6	K-series	0.00	0.00	0.00		0.00	0.00	0.00
		Total:	78.06	100.00	100.00				

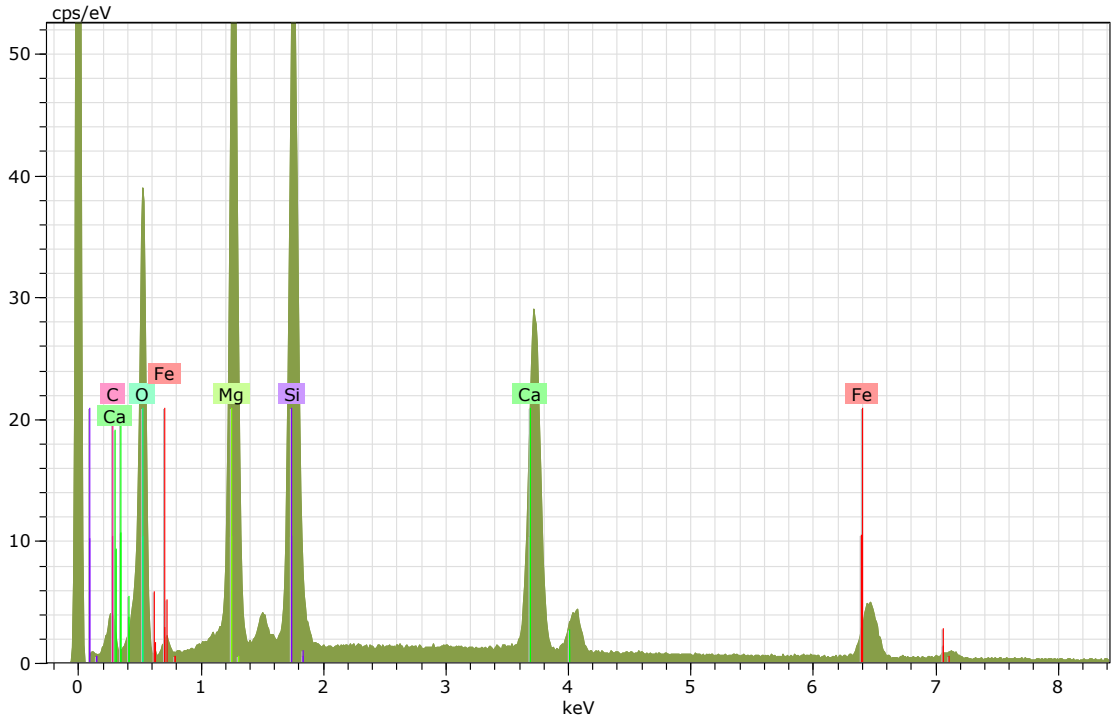

Spectrum: 62

El	AN	Series	unn. C [wt.%]	norm. C [wt.%]	Atom. C [at.%]	Compound	Comp. C [wt.%]	norm. Comp. C [wt.%]	Error (1 Sigma) [wt.%]
O	8	K-series	27.26	40.74	56.47		0.00	0.00	3.34
Mg	12	K-series	14.53	21.72	19.82	MgO	36.02	24.10	0.82
Si	14	K-series	10.97	16.40	12.95	SiO2	35.08	23.47	0.50
Ca	20	K-series	10.10	15.10	8.36	CaO	21.13	14.14	0.32
Fe	26	K-series	4.05	6.05	2.40	FeO	7.78	5.20	0.14
C	6	K-series	0.00	0.00	0.00		0.00	0.00	0.00
		Total:	66.91	100.00	100.00				

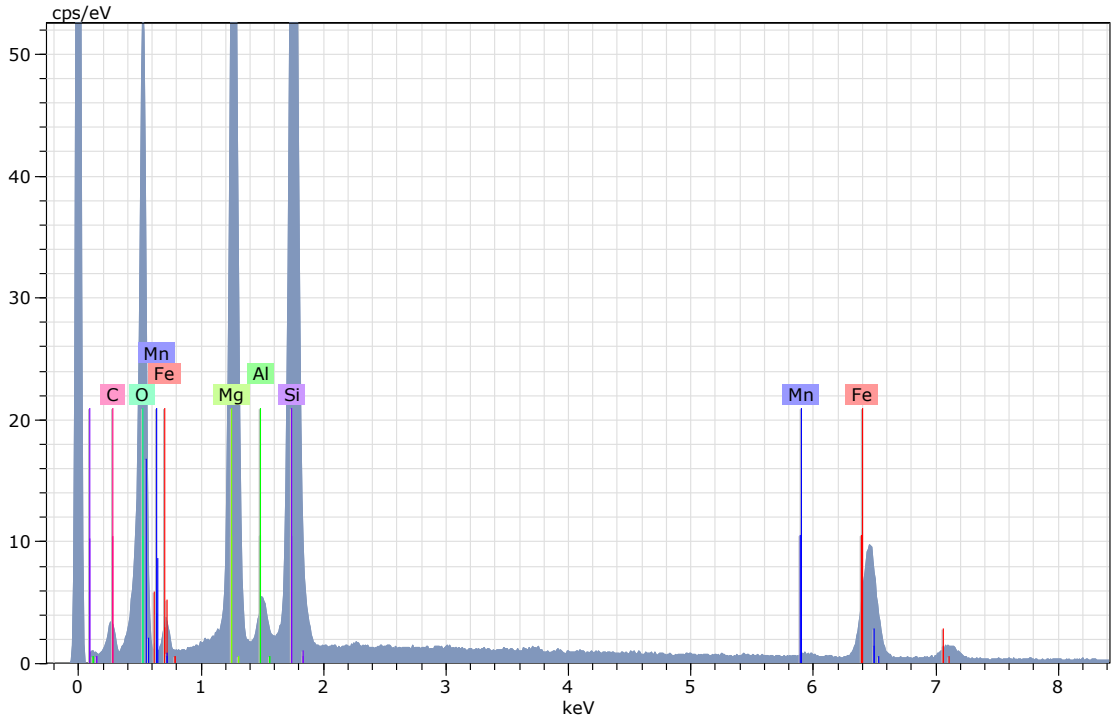

Spectrum: 65

El	AN	Series	unn. C [wt.%]	norm. C [wt.%]	Atom. C [at.%]	Compound	Comp. C [wt.%]	norm. Comp. C [wt.%]	Error (1 Sigma) [wt.%]
O	8	K-series	32.83	41.74	56.51		0.00	0.00	3.97
Mg	12	K-series	22.53	28.65	25.53	MgO	47.50	37.37	1.26
Si	14	K-series	13.27	16.87	13.01	SiO2	36.10	28.40	0.59
Fe	26	K-series	9.18	11.66	4.52	FeO	15.01	11.80	0.28
Mn	25	K-series	0.85	1.08	0.42	MnO	1.39	1.09	0.06
C	6	K-series	0.00	0.00	0.00		0.00	0.00	0.00
		Total:	78.66	100.00	100.00				

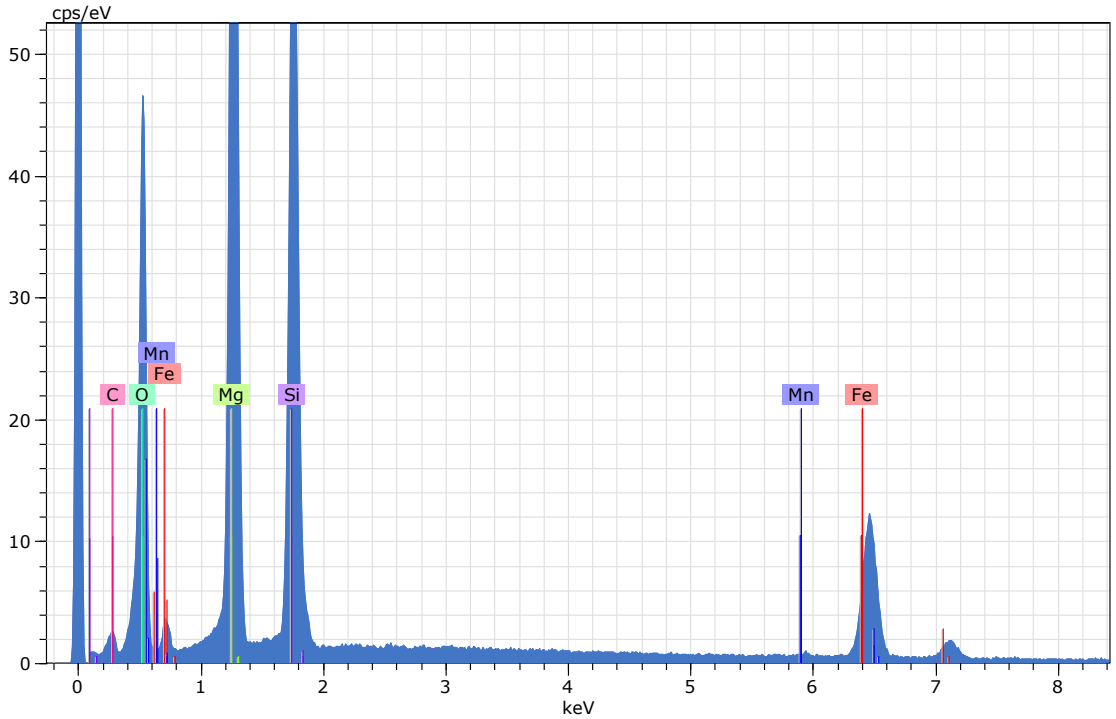

Spectrum: 66

El	AN	Series	unn. C [wt.%]	norm. C [wt.%]	Atom. C [at.%]	Error (1 Sigma) [wt.%]
Cu	29	K-series	62.26	99.27	97.16	1.70
O	8	K-series	0.46	0.73	2.84	0.14
C	6	K-series	0.00	0.00	0.00	0.00
		Total:	62.72	100.00	100.00	

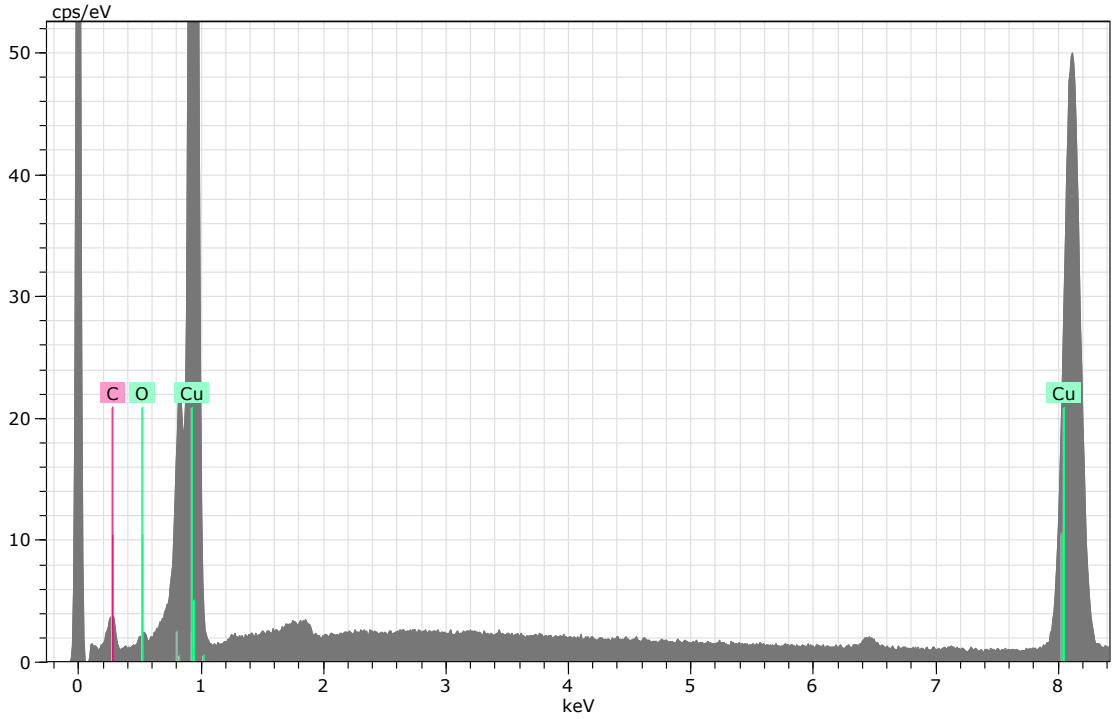

Spectrum: 67

El	AN	Series	unn. C [wt.%]	norm. C [wt.%]	Atom. C [at.%]	Compound	Comp. C norm. [wt.%]	Comp. C [wt.%]	Error (1 Sigma) [wt.%]
O	8	K-series	36.76	40.55	65.91		0.00	0.00	8.33
S	16	K-series	17.78	19.62	15.91	SO3	48.98	44.40	0.66
Fe	26	K-series	21.03	23.20	10.80	FeO	29.84	27.05	0.59
Ni	28	K-series	15.09	16.64	7.37	NiO	21.18	19.20	0.44
C	6	K-series	0.00	0.00	0.00		0.00	0.00	0.00
		Total:	90.65	100.00	100.00				

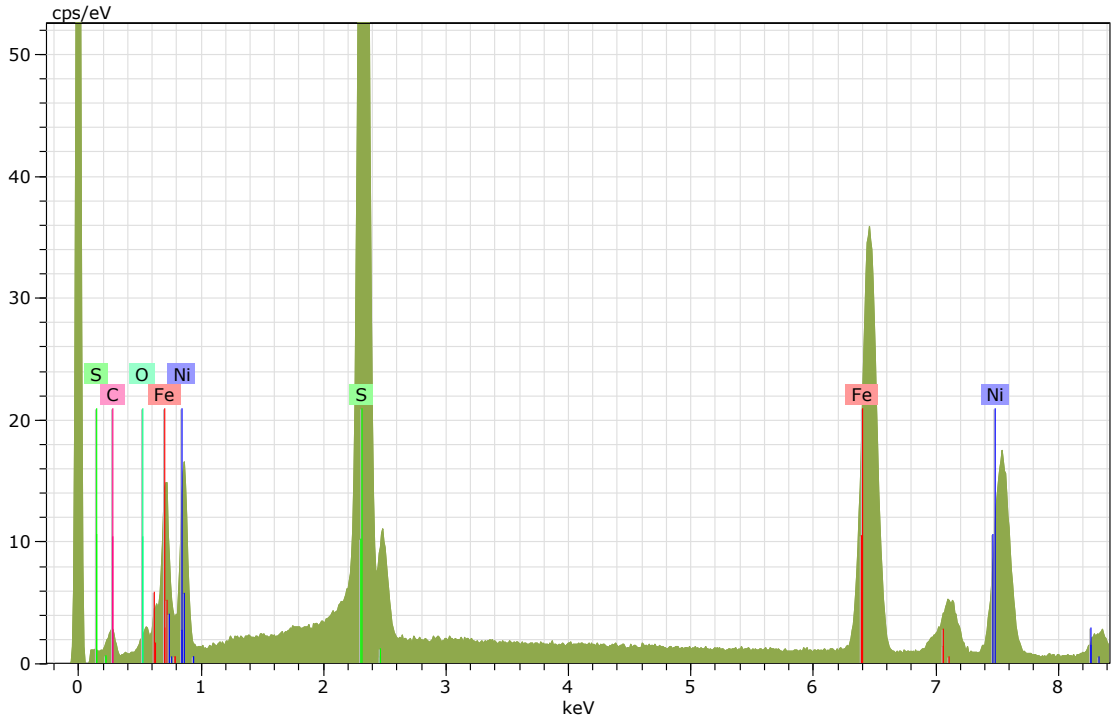

Spectrum: 68

El	AN	Series	unn. C [wt.%]	norm. C [wt.%]	Atom. C [at.%]	Compound	Comp. C [wt.%]	norm. Comp. C [wt.%]	Error (1 Sigma) [wt.%]
O	8	K-series	36.85	40.46	65.91		0.00	0.00	8.43
S	16	K-series	17.83	19.57	15.91	SO3	48.87	44.52	0.66
Ni	28	K-series	19.22	21.10	9.37	NiO	26.85	24.45	0.55
Fe	26	K-series	17.19	18.88	8.81	FeO	24.28	22.12	0.49
C	6	K-series	0.00	0.00	0.00		0.00	0.00	0.00
		Total:	91.09	100.00	100.00				

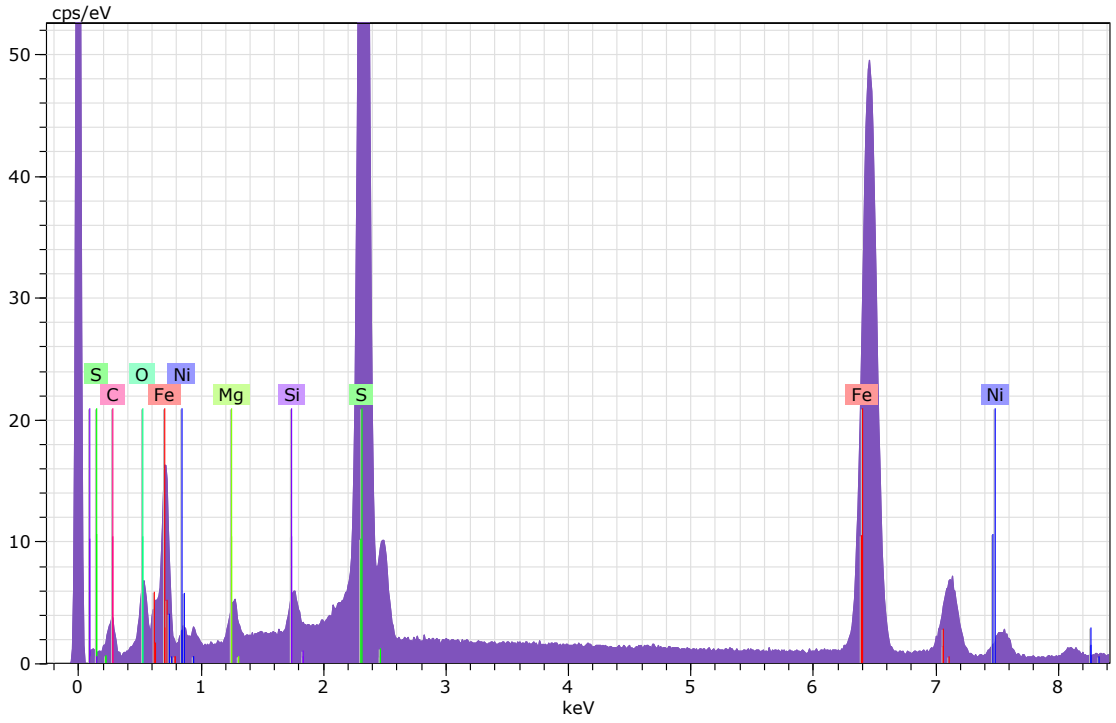

Spectrum: 69

El	AN	Series	unn. C [wt.%]	norm. C [wt.%]	Atom. C [at.%]	Compound	Comp. C [wt.%]	norm. Comp. C [wt.%]	Error (1 Sigma) [wt.%]
O	8	K-series	37.19	41.68	66.06		0.00	0.00	5.86
S	16	K-series	17.88	20.04	15.85	SO3	50.03	44.63	0.67
Fe	26	K-series	30.90	34.63	15.73	FeO	44.56	39.75	0.85
Ni	28	K-series	2.00	2.25	0.97	NiO	2.86	2.55	0.09
Mg	12	K-series	0.82	0.92	0.96	MgO	1.53	1.36	0.08
Si	14	K-series	0.43	0.48	0.43	SiO2	1.03	0.92	0.05
C	6	K-series	0.00	0.00	0.00		0.00	0.00	0.00
		Total:	89.21	100.00	100.00				

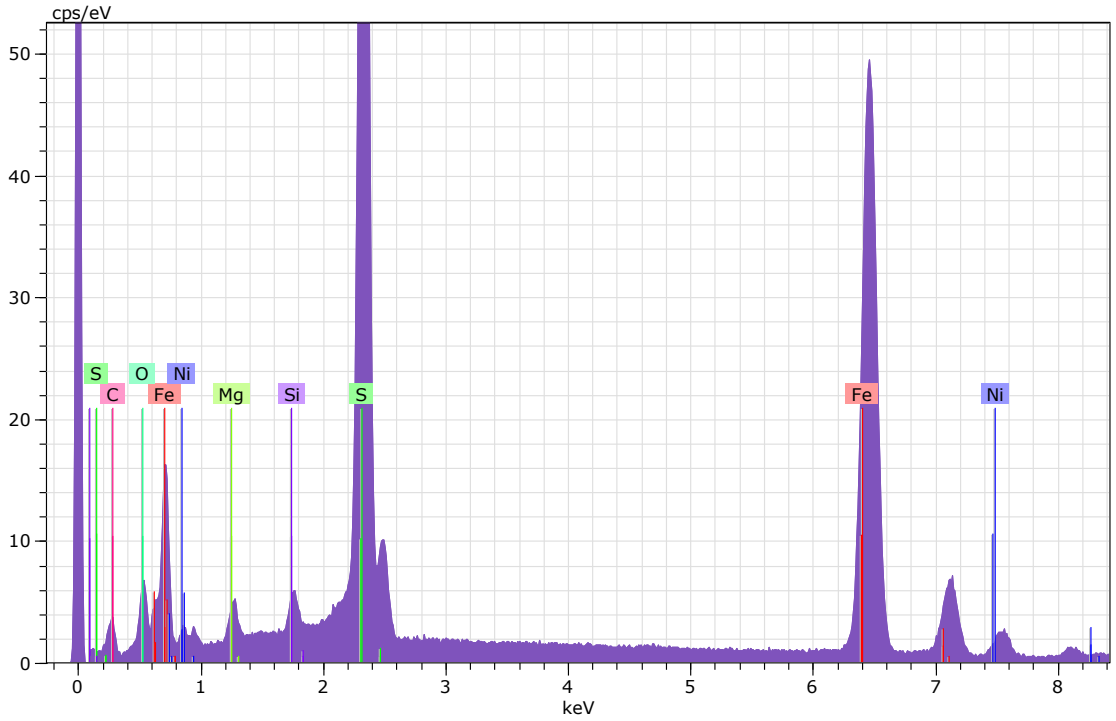

Spectrum: 70

El	AN	Series	unn. C [wt.%]	norm. C [wt.%]	Atom. C [at.%]	Compound	Comp. C [wt.%]	norm. Comp. C [wt.%]	Error (1 Sigma) [wt.%]
O	8	K-series	31.32	36.31	62.31		0.00	0.00	5.22
S	16	K-series	16.80	19.48	16.68	SO3	48.64	41.95	0.63
Fe	26	K-series	18.42	21.35	10.50	FeO	27.47	23.69	0.52
Cu	29	K-series	17.44	20.22	8.74		20.22	17.44	0.51
Mg	12	K-series	0.71	0.83	0.93	MgO	1.37	1.18	0.07
Ni	28	K-series	1.56	1.81	0.85	NiO	2.30	1.99	0.08
C	6	K-series	0.00	0.00	0.00		0.00	0.00	0.00
		Total:	86.26	100.00	100.00				

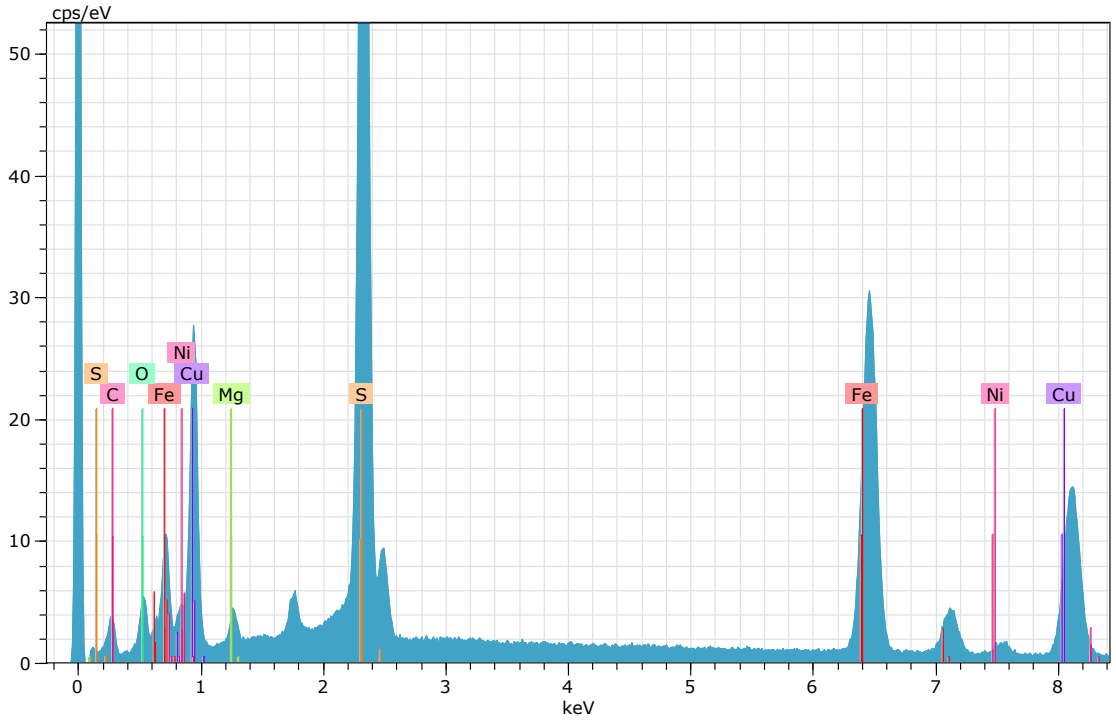

Appendix E: XRD

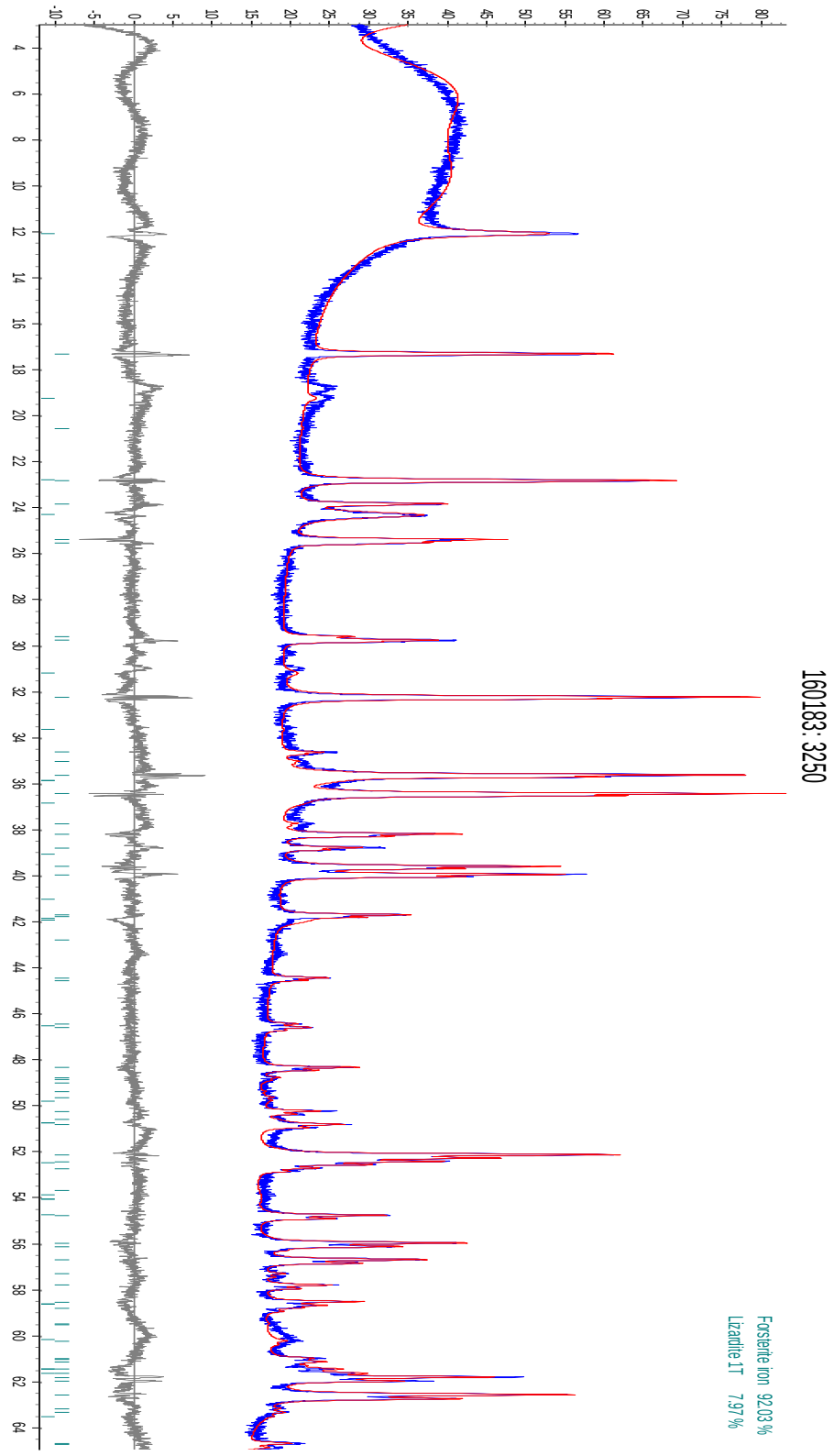

Figure E. 1: XRD analysis of the 3250 sample

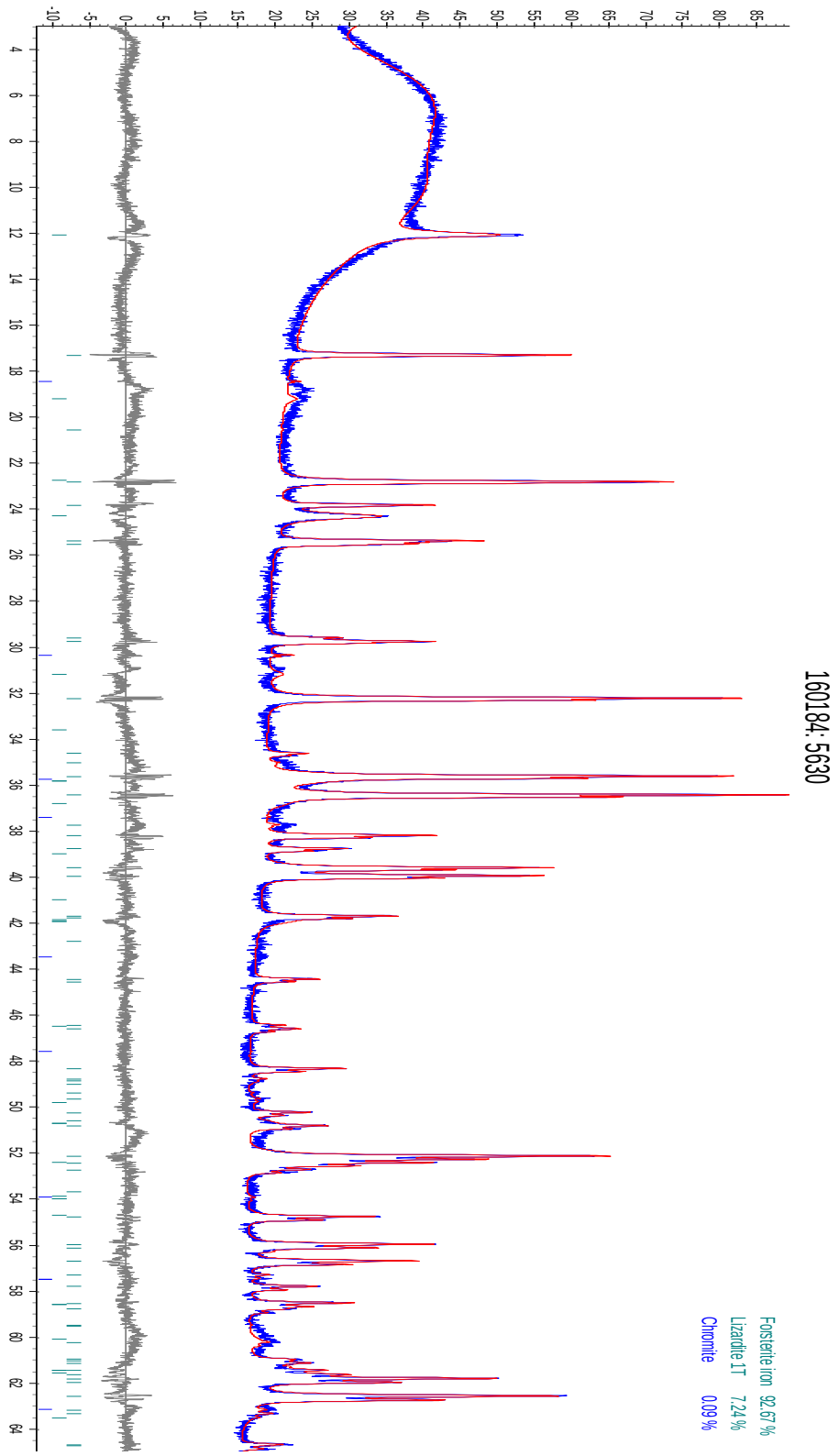

Figure E. 2: XRD analysis of the 5630 sample

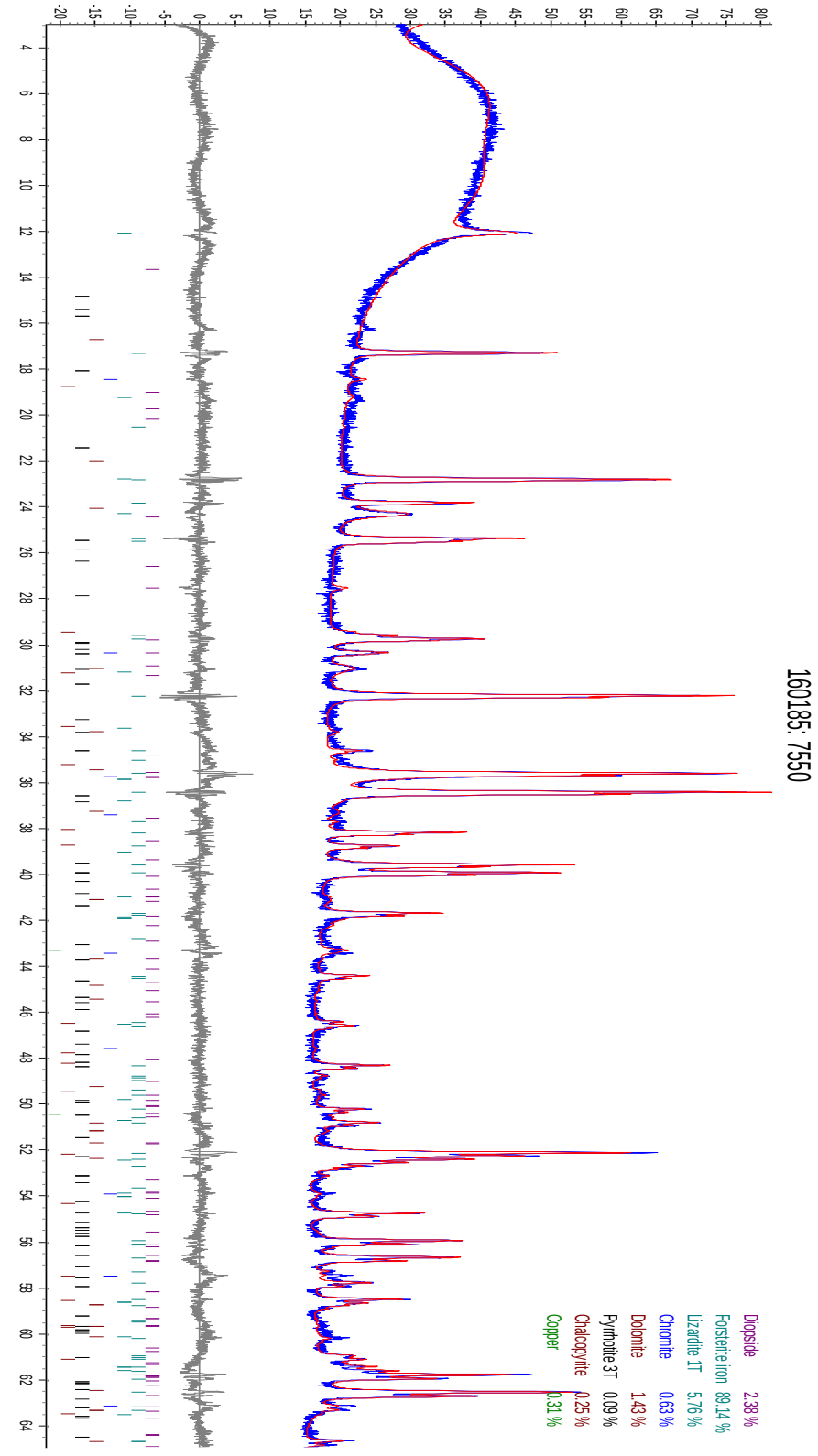

Figure E. 3: XRD analysis of the 7550 sample

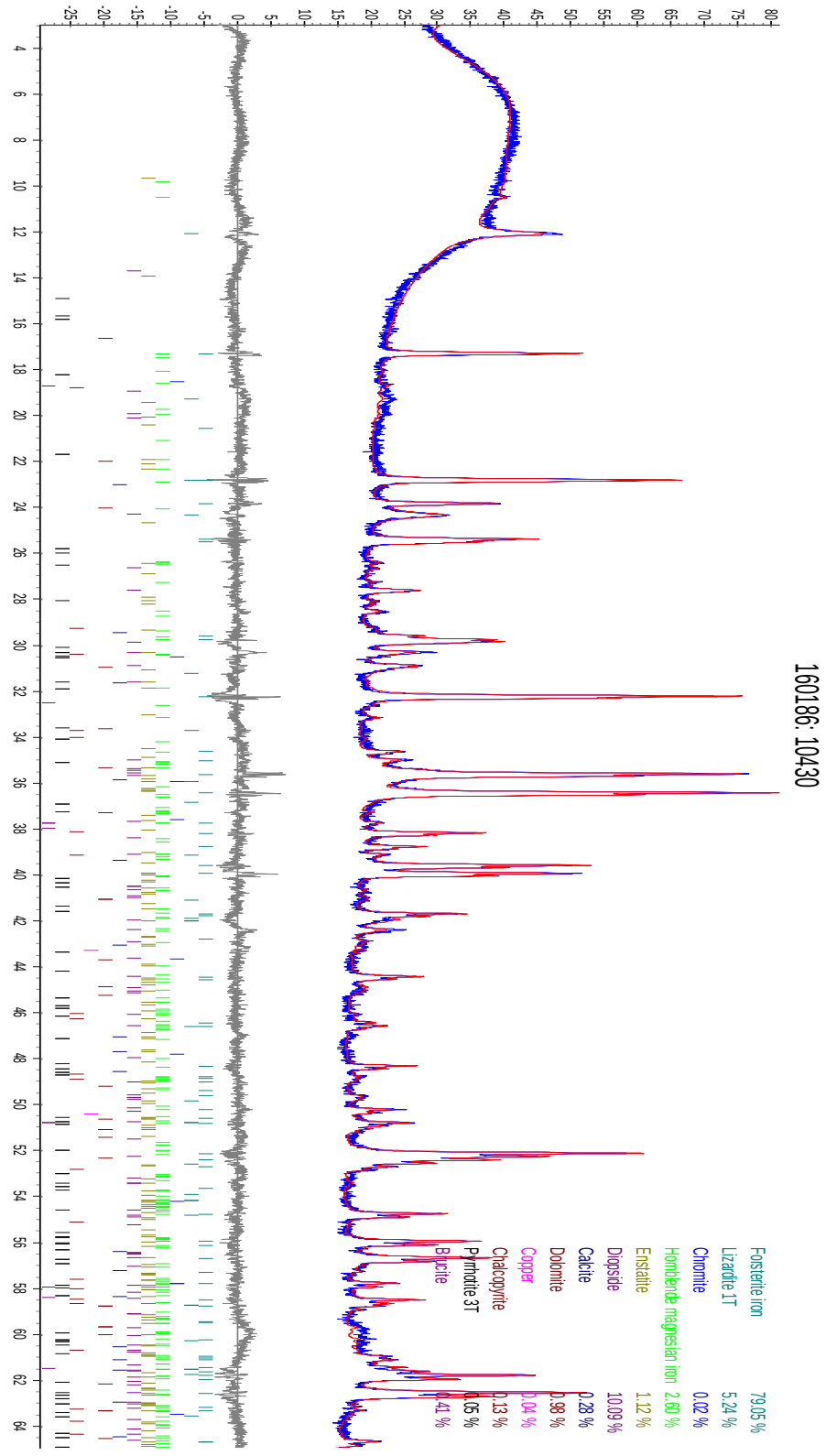

Figure E. 4: XRD analysis of the 10430 sample